UNIVERSIDAD DE CHILE
FACULTAD DE CIENCIAS FÍSICAS Y MATEMÁTICAS
DEPARTAMENTO DE FÍSICA

Waves called Fronts

Marcel G. Clerc

SANTIAGO DE CHILE
September 2020

Contents

Chapter 1

Fronts in nature

In our daily lives, we are accustomed to propagation phenomena; admittedly, the most common ones that have fascinated us are light, sound, mechanical, and water waves (cf. Fig. 1.1). For its simplicity, the waves of pools, rivers, lakes, or seas are those that first take a rational consciousness. For example, when the water is stagnant, still, or flowing slowly, it seems to us that it does not move. Then, we know that it is in equilibrium. When one disturbs the surface of the water, propagative rings emerge (see the top snapshot of the left panel Fig. 1.1). This type of propagative ring is what we call waves. The waves correspond to the transmission of energy in matter or space. In the case of water, by disturbing its surface, one concentrates the energy

Figure 1.1: Waves in nature: the left and right panels account for waves in water and light.

of the disturbance in a region, which subsequently propagates on the surface at a well-defined speed. Waves are oscillations or vibrations of a physical medium or a field around relatively fixed locations. The waves on the surface of the water generated by a disturbance are characterized by the fact that when the rings cross, they overlap and intersect each other. This type of wave is classified as *linear waves*.

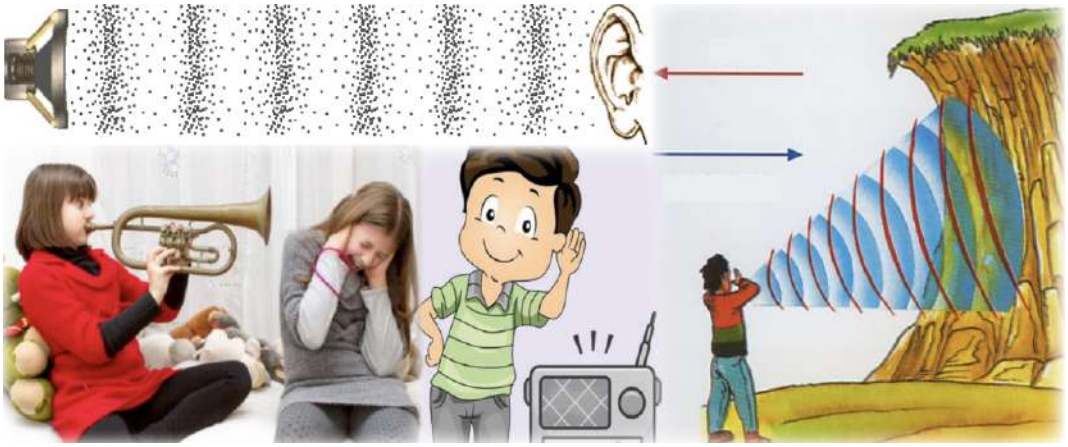

Figure 1.2: Sound waves, schematic representation of sound waves.

The sound waves are a similar phenomenon but much more challenging to conceive. The sound is the propagation of disturbances in the air; more precisely, it is the local compression of the air (pressure waves, see Fig. 1.2). Inevitably, the first time one becomes aware that it is phenomenally propagative is when one hears their echo. An echo is a reflection of sound that arrives at the listener with a delay after the direct sound. The right cartoon on Fig. 1.2 schematically illustrates the echo process. Sound waves are a typified phenomenon of the linear wave type. However, large disturbances of the air, for example, explosions or very abrupt movements, generate a propagative phenomenon of a different nature called *shock waves*. This wave moves faster than the local speed of sound in a fluid media. Like an ordinary or lineal wave, a shock wave carries energy and can propagate through a medium; however, it is characterized by an abrupt, nearly discontinuous change in pressure, temperature, and density of the medium. Even these waves transmit mass. Figure 1.3 illustrates different shock

waves. Due to a large amount of energy released, these waves are characterized by the connection of two thermodynamic states, one of low and high temperature, as illustrated in the right diagram of Fig. 1.3. This type of phenomenon generated by large perturbations in wave media creates propagation waves that are called *fronts* to distinguish them from linear waves.

Figure 1.3: Shock waves, snapshots of shock waves when an airplane exceeds the speed of sound, the explosion of an atomic bomb and cannons. This type of wave corresponds to fronts. The right panel shows two snapshots of a nuclear explosion and a scheme of the pressure in the different regions.

The concept of fronts will be used broadly as waves connecting two states of equilibrium. The pedestrian use of the concept of the front in our daily life is associated with weather fronts, which are boundaries separating two masses of air of different densities and temperatures. Figure 1.4 depicts a weather front.

An interesting front is observed when one takes water supercooled; that is, the water is below the temperature of solidification. Physically, this corresponds to an unstable state or meta state of water. When disturbed, the supercooled liquid is propagated to a state corresponding to frozen water. Hence, the perturbation generates the propagation of a solidification front. Figure 1.5a shows a solidification front in supercooling water. Note that, on average, the interface between the frozen and liquid state spreads with a well-defined speed. The possibility of having fronts between different states is generic, for example, one can observe the burning of a candle, where the states that are connected correspond to the burned and unburned state or the propagation of a combustion reaction. Figure 1.5 shows fronts observed in these chemical contexts. Note

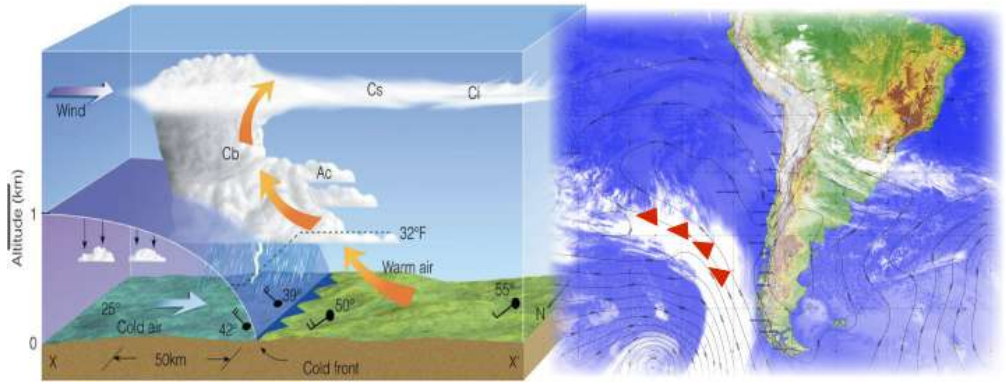

Figure 1.4: Schematic representation of a weather front, which is boundaries separating two masses of air of different densities and temperatures.

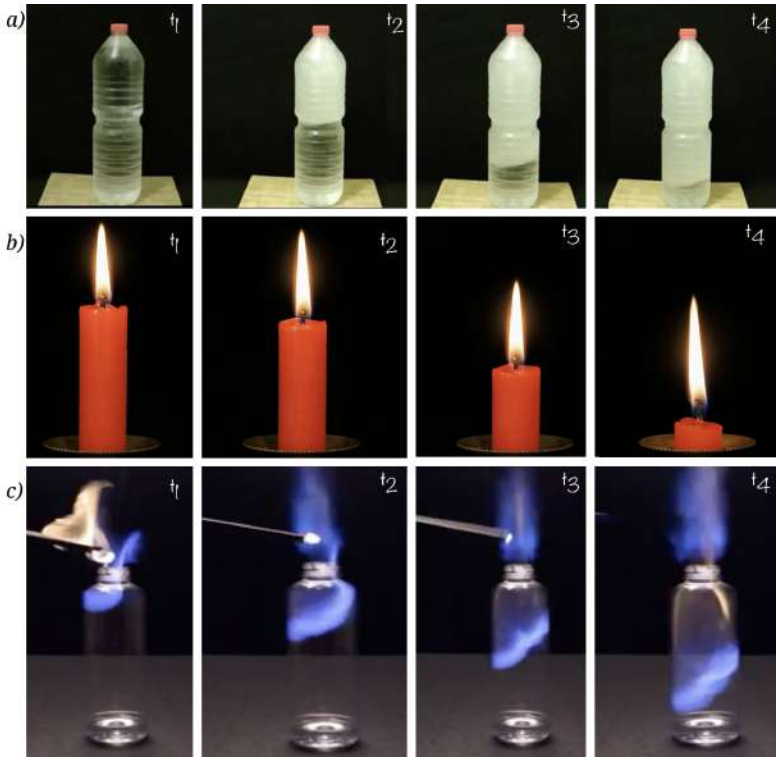

Figure 1.5: Front propagation between different equilibria. The temporal sequence of snapshots of (a) a bottle with supercooled water disturbed by a hit with the floor, the different states correspond to liquid-solid water, respectively, (b) a burning of a candle, and (c) a combustion reaction with different states corresponding to burned and unburned ($t_1 < t_2 < t_3 < t_4$).

that there is a clear similarity between these physical phenomena. One of the objectives will be to present a unified description of this robust phenomenon. Hence, fronts are responsive to how one state invades another.

The systems out of equilibrium can present a great variety of states like homogeneous, oscillatory, chaotic, patterns, and so forth. The characterization of all possible equilibrium states for spatial systems is still an open question of nonlinear science. Patterns are solutions that are characterized by having specific representative lengths. Figure 1.6 shows ripples that one observes in shallow waters, typically at the edges of the sea or lakes. Likewise, one observes that in other shallow waters, there are no ripples. Then, one intuits that as a function of the movement of the fluid, both states are at equilibrium, and then we can have fronts between these states of equilibrium. Figure 1.6 shows the propagation of ripples in a homogenous state. Therefore, each time one ob-

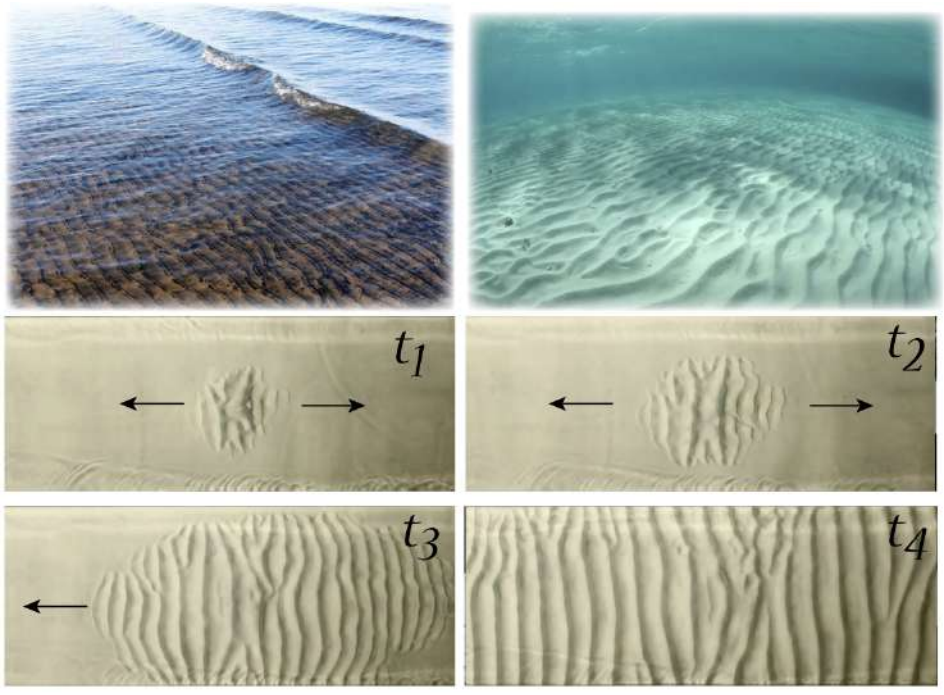

Figure 1.6: Sand ripples: pattern formation under water due to fluid oscillations. Bottom panels account for a snapshot of sand ripples propagation into a homogeneous state in a tank fluid experiment ($t_1 < t_2 < t_3$).

serves a given equilibrium by changing the parameters that control the system under observation, it can be invaded by another equilibrium.

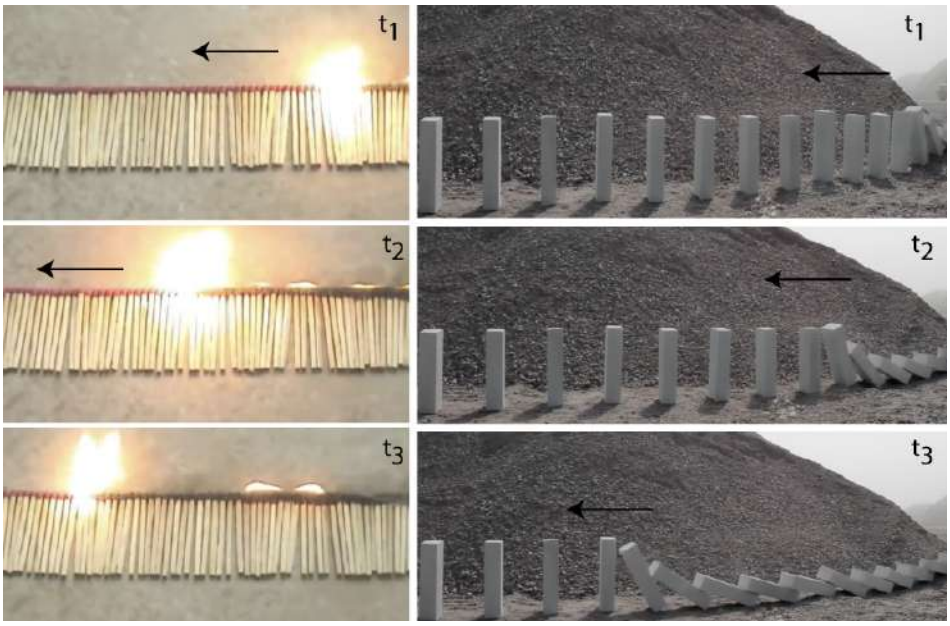

Figure 1.7: Propagation of fronts in coupled systems. Left and right panels illustrate front propagation in a line of matches and a chain of dominoes, respectively ($t_1 < t_2 < t_3$).

A natural question that emerges from the previous phenomenon is whether it is due to the continuous nature in the space of the observed front propagation. The answer is that in discrete systems, the fronts are observed; for example, if one considers a line of matches, the propagation of the combustion can be found when one match is ignited. Figure 1.7 depicts the front propagation in a chain of matches and a line of dominoes. Clearly, both systems have a well-defined speed of propagation. The propagation of dominoes or *domino effect* is one of the first playful experiences of wave propagation. This phenomenon corresponds to the progressive destabilization of vertical dominoes due to the fall of neighboring dominos; the propagation of energy characterizes this constant process at a well-defined speed. The experience with dominoes shows us that the mass does not spread but that what is propagated is the kinetic energy generated by the movement of dominoes. Besides, one learns that regardless of how one disturbs

the domino after a moment, it always propagates in the same way; that is, the shape and speed with which the domino is spread is an attractor. Unlike linear waves, when two fronts collide, the propagation is stopped.

This monograph is consecrated to the propagation of the nonlinear waves that connect two states of equilibrium.

Chapter 2

Out of equilibrium macroscopic systems

2.1 Robust phenomena

On the physical scale where humans perform daily life—meters, seconds, and kilograms—matter is made up of many microscopic constituents (atoms and molecules), typically in the Angstrom scale domain. Moreover, the matter is in permanent contact with other macroscopic objects with a constant exchange of energy, momentum, and particles. It is important to note that this is the natural context in which life develops. Under these conditions of permanent exchange, the matter is referred to *out of equilibrium* or *Non-equilibrium thermodynamics* [129, 78, 21], the origin of this concept is in contrast to the macroscopic systems in thermodynamic equilibrium. Which corresponds to a transient behavior of the universe as a whole. However, our human scale is, in good approximation, a permanent dynamical behavior. Statistical physics and nonlinear physics are devoted to studying matter out of equilibrium.

The description of macroscopic matter is usually done using a small number of coarse-grained or macroscopic variables such as matter density, polarization, elastic tensor, charge density, magnetization, and so forth. When spatial inhomogeneities are consid-

ered, these variables are spatiotemporal fields whose evolution is determined by deterministic partial differential equations. This reduction is possible due to a separation of time scales, which allows a description in terms of the slowly varying macroscopic variables, which are in fact fluctuating variables due to the elimination of a large number of fast variables whose effect can be modeled including suitable stochastic terms in the partial differential equations (*stochastic differential equations*). In the previous chapter, we noticed that the fronts were observed in diverse contexts, such as climatology, explosions, combustion processes, and crystalline growth; therefore, they are a generic phenomenon of many physical systems. When a phenomenon is observed in different contexts, it is called a *robust phenomenon*. To understand this concept and the out-of-equilibrium system that follows, we will study a simple system that exhibits

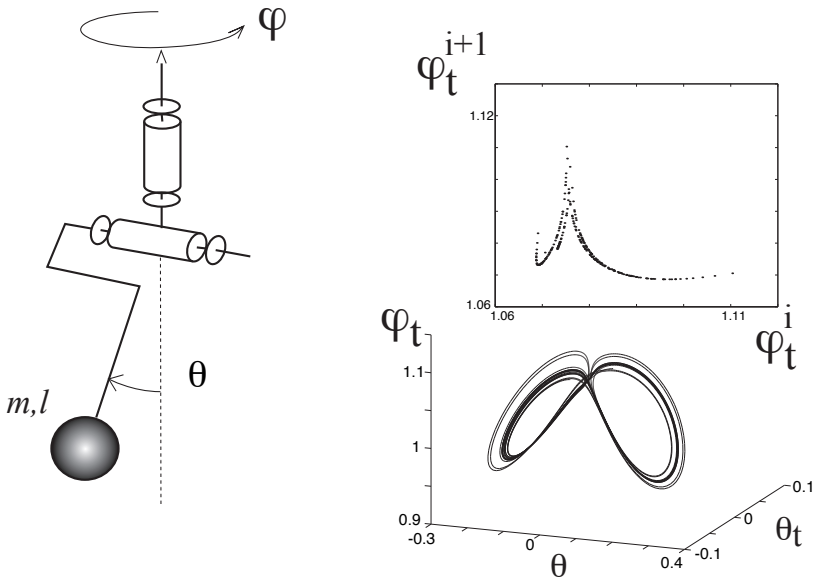

Figure 2.1: Lorenz pendulum, schematic representation of Lorenz pendulum. The insets account for the characteristic Lorenz map (top panel) and the phase space trajectory (bottom panel) obtained from numerical simulation of Eqs. (2.1) [42]. The Lorenz model approximates this physical system for small displacements.

robust phenomena.

Let us consider a simple mechanical system out of equilibrium composed by a spherical pendulum immersed in the air with an engine that applies a torque on the azimuth axis, the Lorenz pendulum [42]. Figure 2.1 shows a schematic representation of the system in consideration. This is a rotating spherical pendulum that consists of a horizontal support (represented by the horizontal cylinder in Fig. 2.1), which can rotate around a vertical axis with angular velocity $\dot{\varphi}$ and a pendulum formed by a punctual mass m at a distance l from the support, which oscillates in a vertical plane fixed with respect to the support (cf. Fig. 2.1), forming an angle $\theta(t)$ with the vertical. The system will dissipate energy by friction in the contacts and by the motion of the mass m in the air through Stoke's law [25]. It is injected energy through a constant torque τ applied to the horizontal support. In dimensionless variables the equations of this system are ($I = \frac{I'}{ml^2}$, where I' is the inertial moment of the support)

$$\begin{aligned} \ddot{\theta} &= \frac{\sin(2\theta)}{2}\dot{\varphi}^2 - \sin(\theta) - \nu\dot{\theta}, \\ \left(I + \sin^2(\theta)\right)\ddot{\varphi} &= -2\sin(\theta)\cos(\theta)\dot{\varphi}\dot{\theta} - \tilde{\mu}(\dot{\varphi} - \Omega) \\ &\quad -\nu\dot{\varphi}\sin^2(\theta), \end{aligned} \tag{2.1}$$

where $\tilde{\mu}$ and ν are the damping coefficients (ν is related to Stoke's law) and written the torque $\tau = \tilde{\mu}\Omega$. Indeed, the system is driven to have an azimuthal angular velocity Ω. The system is described by four variables (θ, $\dot{\theta}$, $\dot{\varphi}$, φ), but φ is absent in Eqs. (2.1) due to the system's rotation invariance. Indeed, the Lorenz pendulum is then a three-dimensional dynamical system. The quantity $P = \left(I + \sin^2(\theta)\right)\dot{\varphi}$ is the total angular momentum with respect to the vertical axis, which is conserved in the absence of dissipation and forcing, i.e., if $\tilde{\mu} = \nu = 0$ (notice that since $\tau = \tilde{\mu}\Omega$ the applied torque vanishes with the dissipation) in which case the system is reversible with respect to the time reversal transformation $t \to -t$, $\theta \to \theta, \dot{\theta} \to -\dot{\theta}$, $\dot{\varphi} \to \dot{\varphi}$. It is also an integrable system, since P is constant and Eqs. (2.1) reduces to (conservative limit)

$$\ddot{\theta} = \frac{\sin(2\theta)}{2\left(I + \sin^2(\theta)\right)^2}P^2 - \sin(\theta). \tag{2.2}$$

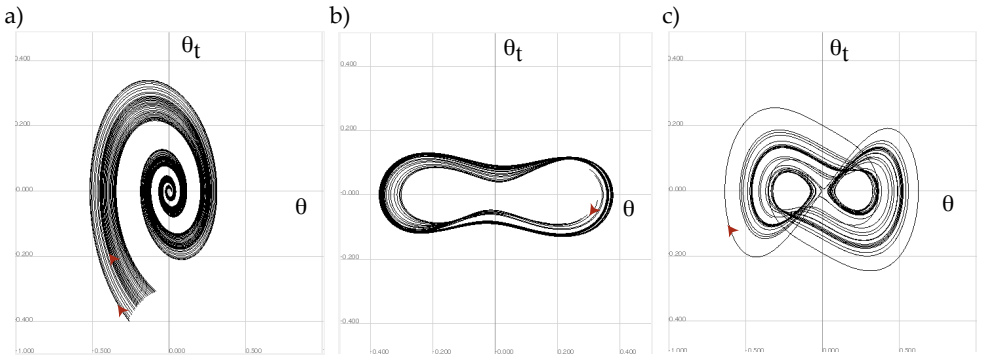

Figure 2.2: Robust phenomena in Lorenz pendulum for different values of the parameters. a) the origin corresponds to a focus; then the trajectories are attracted to the origin in a spiral manner $\Omega < 1$. b) limit cycle, $\Omega > 1$, then the trajectories are attracted to this close orbit. c) Strange attractor corresponding to a chaotic trajectory in the phase space [42].

Then, in this limit, the system corresponds to a particle that slides on a rotating ring [18]. Namely, the above model describes a flat pendulum under the effect of a centrifugal force.

This simple macroscopic system, Eqs. (2.1), is subjected to injection of energy by the torque and dissipation through the opposing force generated by the surrounding air.

We will examine the type of dynamic behaviors displayed by this out-of-equilibrium system. A natural equilibrium of this system corresponds to a vertical pendulum ($\theta = \dot{\theta} = 0, \dot{\varphi} = \Omega$) . Note that for $\Omega < 1$, this equilibrium is stable. The trajectories in phase portrait are characterized by spirally converging to this equilibrium corresponding to a *focus state*. Figure 2.2a shows the typical trajectories observed in portrait space.

Increasing the torque magnitude, the vertical position of the pendulum becomes unstable, and it is marginal for $\Omega = 1$. This instability occurs because the centripetal force overcomes the gravitational one. To a specific region of parameters, the system exhibits as a steady state an attractive periodic solution, which corresponds to a *limit cycle*. Figure 2.2b shows the typical trajectories observed in portrait space in the region of parameters where the system exhibits a limit cycle. From a geometric point of view, both equilibria—the fixed point and the limit cycle—have an integer dimension. Indeed, the

dimension of a fixed point and a limit cycle correspond to zero and one, respectively. However, in another region of parameters, the system displays more complex permanent dynamical behaviors, the *strange attractor*. That is, the system presents chaotic dynamics. Figure 2.2c shows the observed strange attractor. The exponential sensitivity to the initial conditions characterizes this type of dynamic behavior; that is, a slight modification of the initial conditions generates large differences in the evolution. Idea envisaged by the works of H. Poincaré in the understanding of the dynamics of the celestial bodies [134]. Likewise, James Clerk Maxwell visualized the idea of sensitivity to initial conditions and non-predictability in the dynamics of collisions of elements in gases, Perhaps Maxwell was the first to visualize the chaotic behavior of systems with many elements [90]. Notice that the dimension of the strange attractor in the phase portrait is fractional [150, 92]. From a geometric point, permanent states exhibited by the Lorenz pendulum have integer or non-integer dimensions. There is no other possibility dimension, and therefore, this covers all possible attractors. In general, any dynamic system of finite variables can only display three permanent dynamical behaviors, *robust phenomena*, equilibria (fixed points), attractive periodic or quasi-periodic orbit, and chaos.

One can define a robust phenomenon as a dynamic behavior common to different physical contexts that do not depend on the underlying physics. Hence, the obvious question that emerges, *which are robust permanent equilibrium type phenomena in systems with infinite variables (fields)*? The answer to this question is unknown. Today, it is the central research theme in the so-called nonlinear science. In this monograph, we will focus on understanding a robust phenomenon in field theory, the nonlinear waves called fronts.

2.2 Extended systems

An extended system is a macroscopic system consisting of a simple dynamic system that is replicated several times and is coupled. Figure 2.3 shows a schematic representation

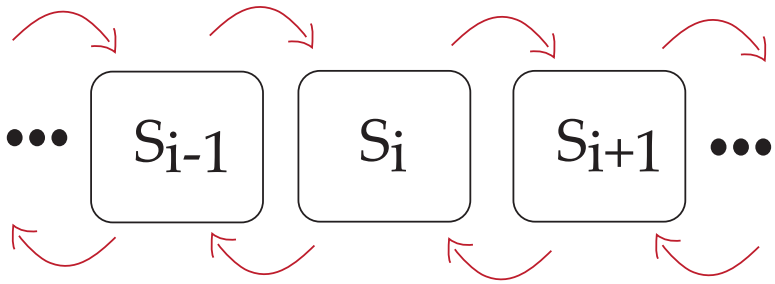

Figure 2.3: Schematic representation of an extended system. S_i is a dynamic system at i-th position. The arrows account for the coupling between different identical systems.

of an extended system. S_i accounts for a simple single dynamic system. An example of an extended system is a chain pendula, which is constituted by a coupled planar pendulum (each pendulum corresponds to a microscopic system), described by (*the dissipative Frenkel-Kontorova model* [35])

$$\ddot{\theta}_i = -\omega^2 \sin\theta_i - \mu\dot{\theta}_i + \kappa(\theta_{i+1} - 2\theta_i + \theta_{i-1}), \tag{2.3}$$

where $\theta_i(t)$ is the angle formed by the pendulum and the vertical axis in the i-position at time t, i is the index label the i-th pendulum, ω is the pendulum natural frequency, μ accounts for damping coefficient, and κ stands for the strength of interaction between near pendulums. Notice that in the previous chain, the pendulums were only coupled to their first neighbors. Of course, one can consider systems coupled with more distant neighbors. The distance between consecutive pendulums is dx. When $dx \to 0$ and $\kappa \to \infty$, the system becomes in a continuous medium, the dissipative sine-Gordon equation [60]. Figure 2.4a shows a scheme of the chain of dissipative coupled pendula. In the conservative or Hamiltonian limit, $\mu = 0$, the above model is well-know as the Frenkel-Kontorova equation [35], which describes the dynamics of a chain of particles interacting with the nearest neighbors in the presence of an external periodic potential. This model is used to describe the dynamics of atoms and atom layers adsorbed on crystals surfaces, incommensurate phase in dielectric, domain wall in the magnetic domain, fluxon in Josephson transmission lines, rotational motion of the DNA bases,

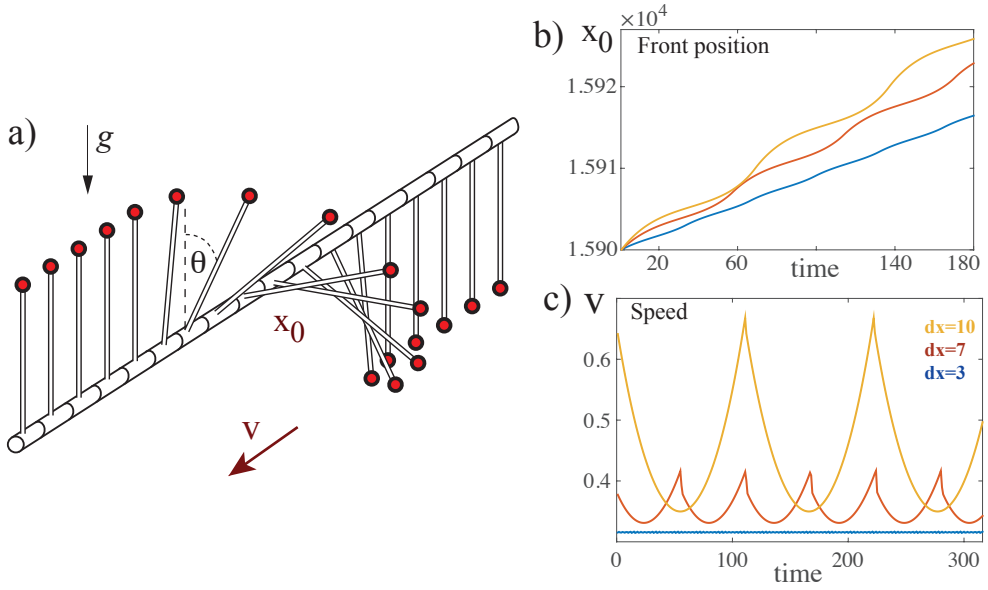

Figure 2.4: Chain of dissipative coupled pendula [10]. a) Schematic presentation of a chain of dissipative coupled pendula. Temporal evolution of b) front position ($x_0(t)$ and c) front speed ($\dot{x}_0(t)$). Each curve is the data for the front position or the front speed, with $\omega = 1.0$ and $\mu = 6$. The upper (yellow), middle (orange), and lower curves (blue) correspond to $dx = 10$, $dx = 7$, and $dx = 3$, respectively.

and plastic deformations in metals (see textbook [35] and references therein). Therefore, model Eq. (2.3) is a paradigmatic model with application to several physical contexts. Note that equation (2.3) can rewrite in the following manner

$$\mu\dot{\theta}_i = -\frac{\delta F}{\delta\theta_i}, \tag{2.4}$$

where the Lyapunov functional F has the form

$$F \equiv \sum_{i=0}^{N}\left[\frac{\dot{\theta}_i^2}{2} - \omega^2\cos\theta_i + \kappa(\theta_{i+1}-\theta_{i+1})^2\right]. \tag{2.5}$$

Hence, the dynamics of Eq. (2.3) is characterized by the minimization of function F when $\mu \neq 0$. Since using Eq. (2.3), one obtains

$$\frac{d\mathcal{F}}{dt} = \sum_i \frac{\partial\mathcal{F}}{\partial\theta_i}\frac{\partial\theta_i}{\partial t} = -\sum_i\left(\frac{\partial\mathcal{F}}{\partial\theta_i}\right)^2. \tag{2.6}$$

2.2.1 Continuous limit of extended system

Considering that the extended system is composed of tiny constituent systems that interact with a strong coupling, the variables and their ordinary differential equations describing the extended system becomes in physical fields, and their models become in partial differential equations. For example chain of pendulums Eq. (2.3) reads in this limit as (sine-Gordon equation)

$$\ddot{\theta}(x,t) = -\omega^2 \sin\theta - \mu\dot{\theta} + \delta\partial_{xx}\theta, \tag{2.7}$$

where $\theta(x,t)$ is the angle formed by the pendulum and the vertical axis at position x and time t, and $\delta \equiv \kappa dx$. One advantage of considering this limit is that it allows one to perform various analytical calculations.

The model equation (2.7) can be applied to another relevant physical system, namely an extended Josephson [60]. Figure 2.5 displays Josephson junction.

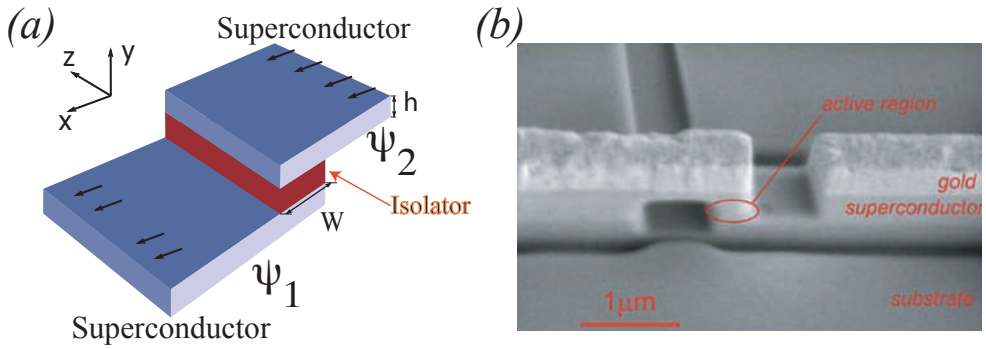

Figure 2.5: Josephson junctions. (a) Schematic representation of the Josephson junctions. ψ_1 and ψ_2 account for the amplitude probability of the superconductor state of the respective superconductor. (b) snapshots of the Josephson junction

To model these quantum elements, one can consider a quantum system consisting of two superconductors described by two wave functions ψ_1 and ψ_2 which is separated by an insulating film (see Fig. 2.5). When one applies a voltage difference, classically, one does not expect to observe electrical conduction, however, quantitatively, one observes

a current through the device, even without voltage. To describe this phenomenon, one can consider a two-state quantum system described by

$$i\hbar\partial_t\psi_1 = E_1\psi_1 + k\psi_2, \tag{2.8}$$

$$i\hbar\partial_t\psi_2 = E_2\psi_2 + k\psi_1, \tag{2.9}$$

where $\hbar$ is the Planck constant, E_1 and E_2 account for the energy of the superconductor, $E_2 - E_1 = -qV$, where V is the voltage between superconductors and q the electrical charge, and k accounts for the coupling between superconductors, which is determined by the properties and geometry of the insulating material. Introducing polar representation $\psi_l(t) \equiv \sqrt{\rho_l(t)}e^{i\phi_l(t)}$ $(l = \{1, 2\})$, where $\rho_l(t)$ accounts for the density of cooper pair, the set of equations read

$$\partial_t\rho_1 = \frac{k\sqrt{\rho_2\rho_1}}{\hbar}\sin(\phi_2 - \phi_1), \tag{2.10}$$

$$\partial_t\rho_2 = -\frac{k\sqrt{\rho_2\rho_1}}{\hbar}\sin(\phi_2 - \phi_1), \tag{2.11}$$

$$\partial_t\phi_1 = -\frac{E_1}{\hbar} - \frac{k}{\hbar}\sqrt{\frac{\rho_2}{\rho_1}}\cos(\phi_2 - \phi_1), \tag{2.12}$$

$$\partial_t\phi_2 = -\frac{E_2}{\hbar} - \frac{k}{\hbar}\sqrt{\frac{\rho_1}{\rho_2}}\cos(\phi_2 - \phi_1). \tag{2.13}$$

the current between superconductors is given by

$$J_s \equiv \partial_t\rho_1 = -\partial_t\rho_1 = \frac{k\sqrt{\rho_2\rho_1}}{\hbar}\sin(\phi_2 - \phi_1). \tag{2.14}$$

Hence, there is a current if there is a phase difference $\phi \equiv \phi_2 - \phi_1$ between the superconductors. This phase difference satisfies

$$\partial_t\phi = \frac{qV}{\hbar} - \frac{k}{\hbar}\cos(\phi)\left[\sqrt{\frac{\rho_2}{\rho_1}} - \sqrt{\frac{\rho_1}{\rho_2}}\right]. \tag{2.15}$$

Considering that both states have the same density $\rho_0 \equiv \rho_1 = \rho_2$, one finds Josephson's relationships

$$J_s = \frac{k\rho_0}{\hbar}\sin(\phi), \tag{2.16}$$

$$\partial_t\phi = \frac{qV}{\hbar}. \tag{2.17}$$

Note that even without voltage ($V = 0$), with a phase difference, one can see a quantum current (*Josephson effect*). On the other hand, the current and the voltage are connected using Maxwell equations, particularly by

$$\left(\frac{\partial_{tt}}{c^2} - \nabla^2\right)\vec{E} = \mu_0 \partial_t \vec{J}, \tag{2.18}$$

where $\vec{E}$ and $\vec{J}$ are the electric field and current between the superconductor, respectively. If the insulator is a thin film then $\vec{E} \approx -V/d\ \hat{y}$ with d the thickness of the insulator, and the current is composed of a normal and a superconductor current, $\vec{J} = (J_s + J_n)\hat{y}$. The normal current satisfies the Ohm law $J_n = -V/\eta d$ with η as the resistivity. Using the Maxwell equation, Josephson relations, the previous approximation, and assuming that phase difference depends of the transversal coordinate $\phi(x,t)$, one gets

$$\partial_{tt}\phi = -\frac{c^2 k \rho_0 d \mu_0}{\hbar^2 q}\sin\phi - \frac{c^2\mu_0}{\eta}\partial_t\phi + c^2\partial_{xx}. \tag{2.19}$$

Hence, the Josephson junctions are described by the sine-Gordon equation, where the natural frequency depends on the density of cooper pairs, electric charge, the constant coupled between the superconductor, and the thickness of the insulator.

2.2.2 Linear stability of uniform state

Notice that the equilibria of the small constituent systems also are solutions of the extended system. For example, for the chain of coupled pendulums, the upright and inverted pendulum solutions are also solutions ($\theta(x,t) = \{0, \pi\}$). To study the stability of these equilibria, we can consider the ansatz $\theta = 0 + u(x,t)$ with $u(x,t)$ a small auxiliary field ($u \ll 1$). Introducing this ansatz in Eq. (2.7) and linearizing in u, one obtains

$$\ddot{u}(x,t) = -\omega^2 u - \mu\dot{u} + \delta\partial_{xx}u. \tag{2.20}$$

Using Fourier modal decomposition, $u = u_0 e^{\lambda t + ikx}$ where u_0 is an arbitrary constant, one gets the growth rate relation,

$$\lambda^2 = -\omega^2 - \mu\lambda + -k^2. \tag{2.21}$$

or

$$\lambda(k) = \frac{-\mu \pm \sqrt{\mu^2 - 4(\omega^2 + k^2)}}{2}. \tag{2.22}$$

Figure 2.6 shows the growth rate as a function of wavenumber k. Note that all eigen-

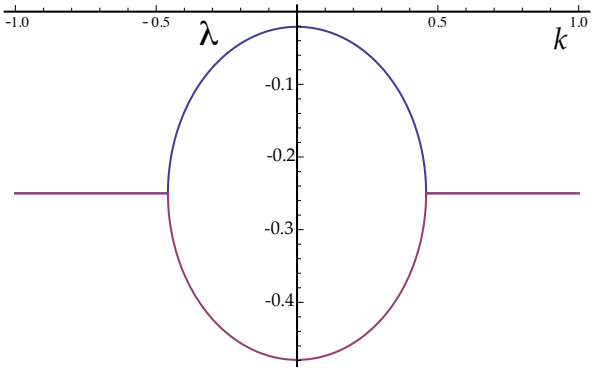

Figure 2.6: Spectrum of the upright state, $\theta = 0$, of the dissipative chain of pendulums, formula (2.21).

values have a negative part; that is, all modes are stable. Hence, the upright state of the dissipative chain of pendulums is stable. Note that for small and large wave numbers, respectively, the eigenvalues are purely real or complex numbers with no null imaginary part. Likewise, one could make a similar study for the state that corresponds to inverted pendulums $\theta(x,t) = \pi$. In this case, simply by symmetry, it corresponds to consider equation (2.21) changing ω by $i\omega$, that is, the stability is described by

$$\lambda^2 = \omega^2 - \mu\lambda + -k^2. \tag{2.23}$$

In this case, the solution is unstable. Notice that the above analysis is a linear stability study that implies nonlinear stability.

2.2.3 Weak nonlinear analysis

To illustrate this property, one can consider the first non-linear correlations, then the system is written

$$\begin{aligned} \dot{u}(x,t) &= W \\ \dot{W}(x,t) &= -\omega^2 u + \frac{\omega^2}{6}u^3 - \mu W + \delta\partial_{xx}u + O(u^5). \end{aligned} \tag{2.24}$$

Introducing the asymptotic change of variable

$$\begin{pmatrix} u \\ W \end{pmatrix} = \varepsilon \begin{pmatrix} p \\ q \end{pmatrix} + \varepsilon^3 \left|\Phi^{[3]}\right\rangle + \varepsilon^5 \left|\Phi^{[5]}\right\rangle + \cdots \tag{2.25}$$

where ε is a small arbitrary parameter ($\varepsilon \ll 1$), $\{q(x,t), p(x,t)\}$ are the new fields and $\left|\Phi^{[n]}\right\rangle$ are unknown vector function of $\{q,p\}$, we obtain an hierarchy of equations to different order in ϵ. In order ε, one gets

$$\begin{aligned} \dot{q}(x,t) &= p \\ \dot{p}(x,t) &= -\omega^2 q - \mu p + \delta \partial_{xx} q. \end{aligned} \tag{2.26}$$

at order ε^3, Eq. (2.24) reads

$$p\partial_q \left|\Phi^{[3]}\right\rangle + \dot{p}\partial_p \left|\Phi^{[3]}\right\rangle + \begin{bmatrix} 0 & 1 \\ -\mu & -\omega^2 + \partial_{xx} \end{bmatrix} \left|\Phi^{[3]}\right\rangle + \begin{pmatrix} 0 \\ \frac{\omega^2}{6} q^3 \end{pmatrix} = 0, \tag{2.27}$$

considering a general cubic solution for $\left|\Phi^{[3]}\right\rangle$, replacing the previous expression, neglecting the spatial variation, and after straightforward calculations, we get

$$\left|\Phi^{[3]}\right\rangle = \begin{pmatrix} a_1 q^3 + a_2 q^2 p + a_3 q p^2 + a_4 p3 \\ b_1 q^3 + b_2 q^2 p + b_3 q p^2 + b_4 p3 \end{pmatrix}. \tag{2.28}$$

where

$$a_1 = \frac{w^2\left(12\mu^2(1+\mu)+w^2\mu\left(-37-29\mu+8\mu^2\right)+w^4\left(2-\mu+8\mu^2\right)\right)}{12(4w^6(-1+4\mu)+3\mu^3(-2-\mu+3\mu^2)+w^4(9-41\mu+7\mu^2)+w^2\mu(-9+2\mu-18\mu^2+6\mu^3))},$$
$$a_2 = \frac{w^2\left(w^4(1-8\mu)-4w^2\mu(1+2\mu)+3\mu^2(1+3\mu)\right)}{6(4w^6(-1+4\mu)+3\mu^3(-2-\mu+3\mu^2)+w^4(9-41\mu+7\mu^2)+w^2\mu(-9+2\mu-18\mu^2+6\mu^3))},$$
$$a_3 = \frac{w^2\left(2w^4+3\mu^2(5+3\mu)-w^2\mu(40+3\mu)\right)}{12(4w^6(-1+4\mu)+3\mu^3(-2-\mu+3\mu^2)+w^4(9-41\mu+7\mu^2)+w^2\mu(-9+2\mu-18\mu^2+6\mu^3))},$$
$$a_4 = \frac{w^2\left(w^2(1-10\mu)+\mu\left(-1+2\mu+3\mu^2\right)\right)}{6(4w^6(-1+4\mu)+3\mu^3(-2-\mu+3\mu^2)+w^4(9-41\mu+7\mu^2)+w^2\mu(-9+2\mu-18\mu^2+6\mu^3))},$$
$$b_1 = \frac{w^4\left(4w^2\mu(1+2\mu)-3\mu^2(1+3\mu)+w^4(-1+8\mu)\right)}{6(4w^6(-1+4\mu)+3\mu^3(-2-\mu+3\mu^2)+w^4(9-41\mu+7\mu^2)+w^2\mu(-9+2\mu-18\mu^2+6\mu^3))},$$
$$b_2 = \frac{w^2\left(6\mu^2\left(2+\mu-3\mu^2\right)+w^2\mu\left(-37-21\mu+24\mu^2\right)+w^4\left(2-3\mu+24\mu^2\right)\right)}{12(4w^6(-1+4\mu)+3\mu^3(-2-\mu+3\mu^2)+w^4(9-41\mu+7\mu^2)+w^2\mu(-9+2\mu-18\mu^2+6\mu^3))},$$
$$b_3 = \frac{w^2\left(w^4(-1+12\mu)+w^2\mu\left(-5+18\mu-6\mu^2\right)+3\mu^2\left(2+\mu-3\mu^2\right)\right)}{6(4w^6(-1+4\mu)+3\mu^3(-2-\mu+3\mu^2)+w^4(9-41\mu+7\mu^2)+w^2\mu(-9+2\mu-18\mu^2+6\mu^3))}$$
$$b_4 = \frac{w^2\left(2w^4+3\mu\left(2+\mu-3\mu^2\right)+w^2\left(-6+20\mu-3\mu^2\right)\right)}{12(4w^6(-1+4\mu)+3\mu^3(-2-\mu+3\mu^2)+w^4(9-41\mu+7\mu^2)+w^2\mu(-9+2\mu-18\mu^2+6\mu^3))}.$$

Note that one can calculate order by order variable changes since the previous the linear operator is invertible. Thus, considering the change of variable (2.25) in nonlinear

equation (2.24) becomes a linear equation (2.26). This allows us to show that the linear analysis also accounts for the nonlinear stability. In order to illustrate the procedure of previous analysis, we consider the following scalar equation

$$\partial_t u = -\epsilon u - u^3 + \partial_{xx} u, \tag{2.29}$$

with $\epsilon > 0$. The trivial equilibrium of this model is $u(x,t) = u_c \equiv 0$, and the growth rate relation has the form $\lambda(k) = -\epsilon - k^2$. It is important to note that all modes have eigenvalues with negative real parts. Hence, u_c is a linearly stable state. To show that this state is nonlinearly stable, consider the following asymptotic change of variable

$$u = v + w^{[3]}(v) + w^{[5]}(v) + \cdots, \tag{2.30}$$

where $w^{[n]}(v)$ is a monomial of order n in v. Introducing the above ansatz in Eq. (2.29) at linear order, we get

$$\partial_t v = -\epsilon v + \partial_{xx} v, \tag{2.31}$$

to cubic order and using chain derivative

$$\partial_t u^{[3]} = (-\epsilon v + \partial_{xx} v)\partial_v w^{[3]} = (-\epsilon + \partial_{xx}) w^{[3]} - v^3, \tag{2.32}$$

or equivalently

$$\left[(-\epsilon v + \partial_{xx} v)\partial_v + \epsilon - \partial_{xx}\right] w^{[3]} = -v^3. \tag{2.33}$$

The operator $\mathcal{F} = \left[(-\epsilon v + \partial_{xx} v)\partial_v + \epsilon - \partial_{xx}\right]$ is called homological operator [91]. As we have mentioned the linear operator $(-\epsilon + \partial_{xx})$ has all eigenvalues with negative real parts, then it is invertible, thus

$$w^{[3]} = -\left[\frac{1}{(-\epsilon v + \partial_{xx} v)\partial_v + \epsilon - \partial_{xx}}\right] v^3, \tag{2.34}$$

Assuming v varies slowly in space, one gets

$$w^{[3]} \approx -\left(1 + \frac{\partial_{xx}}{\epsilon} + \frac{\partial_{xxxx}}{\epsilon^2} + v\partial_v - \frac{\partial_{xx} v}{\epsilon}\partial_v + \cdots\right)\frac{v^3}{\epsilon}. \tag{2.35}$$

To $O(v^{[5]})$, one can proceed in the same manner and gets

$$w^{[5]} = \left[\frac{1}{(-\epsilon v + \partial_{xx} v)\partial_v + \epsilon - \partial_{xx}}\right] 2v^2 \left[\frac{1}{(-\epsilon v + \partial_{xx} v)\partial_v + \epsilon - \partial_{xx}}\right] v^3. \tag{2.36}$$

Therefore, considering the Eq. (2.29) and using the change of variable

$$\begin{aligned} u &= v - \left[\frac{1}{(-\epsilon v + \partial_{xx} v)\partial_v + \epsilon - \partial_{xx}}\right] v^3 + \\ &\left[\frac{1}{(-\epsilon v + \partial_{xx} v)\partial_v + \epsilon - \partial_{xx}}\right] 2v^2 \left[\frac{1}{(-\epsilon v + \partial_{xx} v)\partial_v + \epsilon - \partial_{xx}}\right] v^3 + \cdots \end{aligned} \tag{2.37}$$

the variable v satisfied the linear equation (2.31). The analysis presented above allows us to justify a linear stability analysis involves nonlinear stability. We note that the above study is valid except dynamic with terms without polynomial series.

2.2.4 Alternative method: based on normal forms theory

To show that the zero solution $u = 0$ is stable in equation (2.29), we will separate the field $u(x,t)$ into a polynomial change of variable close to the identity and into a gradient expansion, that is,

$$u(x,t) = v(x,t) + U^{[2]}(v) + U^{[3]} + \cdots + U^{[2,1]}(v) + U^{[2,2]} + \cdots = v + \sum_{n,m} U^{[n,m]}, \tag{2.38}$$

where $U^{[n,m]}$ is a monomial of v of order n with a spatial derivative of order m. Namely, $U^{[n]} \equiv U^{[n,m]}$ is the nonlinear change of variable part. *Linear order* $O^{[1]}$: Considering the previous ansatz (2.38) and the equation for v at linear order

$$\begin{aligned} u(x,t) &= v(x,t), \\ \partial_t v &= f^{[1]}, \end{aligned} \tag{2.39}$$

where $f^{[1]}$ is a unknown function. Introducing the previous ansatz in Eq. (2.29), one get $f^{[1]} = -\epsilon v$. *At order two* $O^{[2]}$, we consider the ansatz

$$\begin{aligned} u(x,t) &= v(x,t) + a_2 v^2, \\ \partial_t v &= -\epsilon v + f^{[2]}, \end{aligned} \tag{2.40}$$

where a_2 and $f^{[2]}$ are unknown parameter and function, respectively. Introducing the previous ansatz in Eq. (2.29), one get

$$\begin{aligned}(\partial_t u)^{[2]} &= (-\epsilon u - u^3)^{[2]},\\ (\partial_t u)^{[2]} = \partial_t v^{[2]} + 2a_2 v \partial_t v^{[1]} &= f^{[2]} - 2a_2\epsilon v^2,\\ (-\epsilon u - u^3)^{[2]} &= -\epsilon a_2 v^2.\end{aligned} \tag{2.41}$$

Using the previous expressions

$$f^{[2]} - 3a_2\epsilon v^2 = 0. \tag{2.42}$$

Then, the minimum solution of this system, in the sense of considering the simplest change of variable and equation for v, is $f^{[2]} = 0$ and $a_2 = 0$.

At order three $O^{[3]}$, we consider the ansatz

$$\begin{aligned}u(x,t) &= v(x,t) + a_3 v^3,\\ \partial_t v &= -\epsilon v + f^{[3]},\end{aligned} \tag{2.43}$$

where a_3 and $f^{[3]}$ are unknown parameter and function, respectively. Introducing the previous ansatz in Eq. (2.29), one get

$$\begin{aligned}(\partial_t u)^{[3]} &= (-\epsilon u - u^3)^{[3]},\\ (\partial_t u)^{[3]} = \partial_t v^{[3]} + 3a_3 v^2 \partial_t v^{[1]} &= f^{[3]} - 3a_3\epsilon v^3,\\ (-\epsilon u - u^3)^{[3]} &= -\epsilon a_3 v^2 - v^3.\end{aligned} \tag{2.44}$$

Using the previous expressions

$$f^{[3]} - 4a_3\epsilon v^3 = -v^3. \tag{2.45}$$

Then, the minimum solution of this system, in the sense of considering the simplest change of variable and equation for v, is $f^{[3]} = 0$ and $a_3 = 1/4\epsilon$. Hence, the change of variable and v equation until this order is

$$\begin{aligned}u(x,t) &= v(x,t) + \frac{v^3}{4\epsilon},\\ \partial_t v &= -\epsilon v.\end{aligned} \tag{2.46}$$

The previous procedure can continue up to an arbitrary polynomial order. To illustrate this, consider the following order. *At order three* $O^{[4]}$, we consider the ansatz

$$\begin{aligned} u(x,t) &= v(x,t) + \frac{v^3}{4\epsilon} + a_4 v^4, \\ \partial_t v &= -\epsilon v + f^{[4]}, \end{aligned} \tag{2.47}$$

where a_4 and $f^{[4]}$ are unknown parameter and function, respectively. Introducing the previous ansatz in Eq. (2.29), one get

$$\begin{aligned} (\partial_t u)^{[4]} &= (-\epsilon u - u^3)^{[4]}, \\ (\partial_t u)^{[4]} = \partial_t v^{[4]} + 4a_4 v^3 \partial_t v^{[1]} &= f^{[4]} - 4a_4 \epsilon v^4, \\ (-\epsilon u - u^3)^{[3]} &= -\epsilon a_4 v^4. \end{aligned} \tag{2.48}$$

Using the previous expressions

$$f^{[4]} - 5a_4 \epsilon v^4 = 0. \tag{2.49}$$

Then, the minimum solution of this system, in the sense of considering the simplest change of variable and equation for v, is $f^{[4]} = 0$ and $a_4 = 0$. Note that all even-term coefficients in v are null due to the reflection symmetry of $u(x,t)$ for Eq. (2.29).

At order three $O^{[5]}$, we consider the ansatz

$$\begin{aligned} u(x,t) &= v(x,t) + \frac{v^3}{4\epsilon} + a_5 v^5, \\ \partial_t v &= -\epsilon v + f^{[5]}, \end{aligned} \tag{2.50}$$

where a_5 and $f^{[5]}$ are unknown parameter and function, respectively. Introducing the previous ansatz in Eq. (2.29), one get

$$\begin{aligned} (\partial_t u)^{[5]} &= (-\epsilon u - u^3)^{[5]}, \\ (\partial_t u)^{[3]} = \partial_t v^{[5]} + 5a_5 v^4 \partial_t v^{[1]} &= f^{[5]} - 5a_5 \epsilon v^5, \\ (-\epsilon u - u^3)^{[5]} &= -\epsilon a_5 v^5 - \frac{3}{4\epsilon} v^5. \end{aligned} \tag{2.51}$$

Using the previous expressions

$$f^{[5]} - 6a_5 \epsilon v^5 = -\frac{3}{4\epsilon} v^5. \tag{2.52}$$

Then, the minimum solution of this system, in the sense of considering the simplest change of variable and equation for v, is $f^{[5]} = 0$ and $a_5 = 1/8\epsilon^2$. Hence, the change of variable and v equation until this order is

$$\begin{aligned} u(x,t) &= v(x,t) + \frac{v^3}{4\epsilon} + \frac{v^5}{8\epsilon^2}, \\ \partial_t v &= -\epsilon v. \end{aligned} \tag{2.53}$$

We consider the spatial dependence in the variable change to account for spatial variations. *At order* $O^{[1,2]}$, we consider the ansatz

$$\begin{aligned} u(x,t) &= v(x,t) + \frac{v^3}{4\epsilon} + \frac{v^5}{8\epsilon^2} + b_2\partial_{xx}v, \\ \partial_t v &= -\epsilon v + f^{[1,2]}, \end{aligned} \tag{2.54}$$

where b_2 and $f^{[1,2]}$ are unknown parameter and function, respectively. Introducing the previous ansatz in Eq. (2.29), one get

$$\begin{aligned} (\partial_t u)^{[1,2]} &= (-\epsilon u - u^3 + \partial_{x,x}v)^{[1,2]}, \\ (\partial_t u)^{[1,2]} &= \partial_t v^{[1,2]} = f^{[1,2]}, \\ (-\epsilon u - u^3 + \partial_{x,x}v)^{[5]} &= \partial_{x,x}v. \end{aligned} \tag{2.55}$$

Using the previous expressions

$$f^{[1,2]} = \partial_{x,x}v. \tag{2.56}$$

Hence, the change of variable and v equation until this order is

$$\begin{aligned} u(x,t) &= v(x,t) + \frac{v^3}{4\epsilon} + \frac{v^5}{8\epsilon^2} + O(\epsilon^{-3}), \\ \partial_t v &= -\epsilon v + \partial_{xx}v. \end{aligned} \tag{2.57}$$

Therefore, employing a change of variable close to the identity, we show that the system can be transformed into a linear problem. Thus, the nonlinear system is stable since the linear system is stable. Likewise, it is important to note that when ϵ tends to zero (marginal case), the previous variable change does not converge, and the problem cannot be transformed into a linear equation.

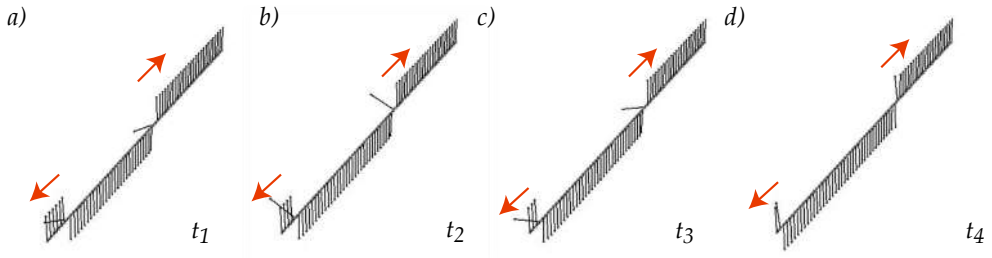

Figure 2.7: Front propagation into unstable state in the dissipative chain of pendulums. Increasing time sequence of images from left to right.

2.2.5 Nonlinear wave in a chain of pendula

Because the upright state is stable, pendulum disturbances around this state are characterized by relaxation and propagation toward equilibrium. On the other hand, equilibrium disturbances corresponding to the upside-down pendulums are characterized by the emergence of propagative solutions that connect the unstable with stable equilibrium. Figures 2.4 and 2.7 illustrate this phenomenon. This propagation corresponds to a nonlinear wave combining two unstable states, which is usually known in the literature as a Fisher-Kolmogorov-Petrosky-Piskunov front [159]. Figures 2.4c depicts the front speed for different coupling parameters.

In one spatial dimension from the point of view of dynamical systems theory, a front is a nonlinear solution that is identified in the co-moving frame system as a heteroclinic orbit linking two steady states [160, 55]. The evolution of front solutions can be regarded as a particle-type one, i.e., they can be characterized by a set of continuous parameters such as position, core width and so forth.

Chapter 3

Front propagation into unstable state

As we have mentioned in the previous chapter, numerical simulations of a chain of pendulums show the presence of propagative solutions between the stable and unstable states. This type of solution has been fundamental for the spread of diseases and populations and combustion [71, 97, 124, 125]. The first context where these fronts are observed was waves in the burning of candles [68] and chemical reactions [110]. Particularly in the context of burning candles, Michel Faraday played a relevant role in understanding the combustion process. The following sentence summarizes the relevance of the phenomenon: *There is no better; there is no more open door by which you can enter into the study of natural philosophy than by considering the physical phenomena of a candle* [68]. For simplicity, we consider a simple context, *the population dynamics*, where this type of front is investigated.

3.1 Populations dynamics

3.1.1 Logistic Model

Let us consider a single species, where $N(t)$ accounts for the population of the species at a time t. Then N is a physical quantity that can only be positive. In 1202, Leonardo of Pisa, known as Fibonacci, developed a model for the reproduction of rabbits, which

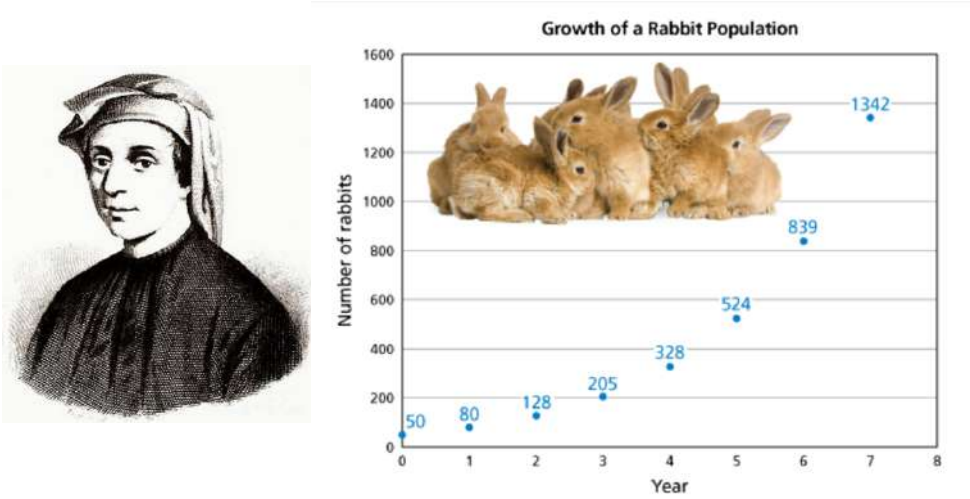

Figure 3.1: Leonardo of Pisa and temporal evolution of rabbit population.

exhibit accelerated or explosive dynamical growth (exponential). The simplest model is based on the rate of variation of population, given by two processes, the rate of birth and death, that is

$$\frac{dN}{dt} = birth - death, \tag{3.1}$$

Fibonacci assumes that the process of creation and death is proportional to the total population, then

$$\frac{dN}{dt} = \alpha N - \beta N, \tag{3.2}$$

where $\{\alpha, \beta\}$ are positive constants. Then the population evolves with the law $N(t) = N_0 e^{(\alpha-\beta)t}$. Then, depending on which process is more efficient, the population increases or decreases exponentially.

Verhulst published in 1838 [161], a manuscript where he opposes the indefinite exponential growth of populations, proposing a process of self limitation. Verhulst proposes the model

$$\frac{dN}{dt} = rN\left(1 - \frac{N}{K}\right), \tag{3.3}$$

where r is the intrinsic growth rate and K is the carrying capacity or the maximum number of individuals that the environment can support. The above model is well know as *logistic equation* or Bernoulli equation. The Verhulst equation was published after

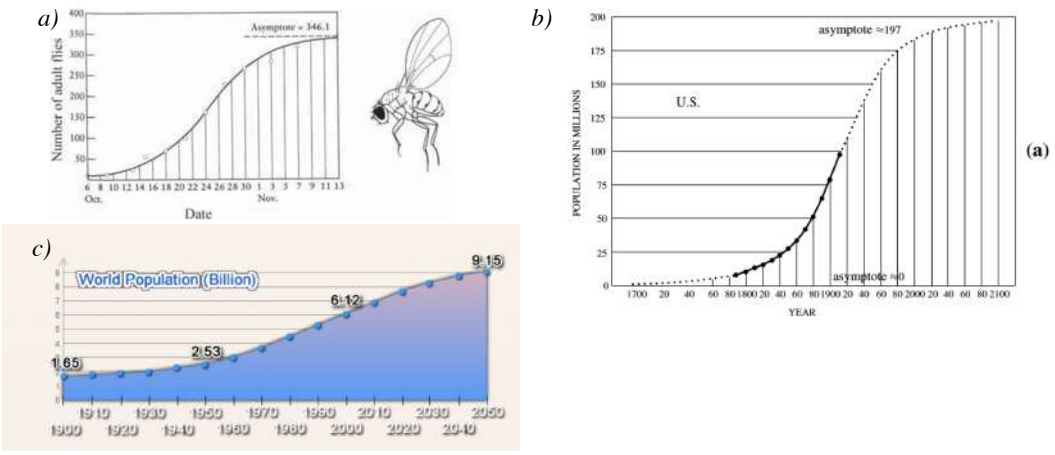

Figure 3.2: Temporal evolution of population of flies (a), humans in United States (b), and Earth.

Verhulst had read Thomas Malthus *An Essay on the Principle of Population* [113]. The logistic equation can be integrated exactly, and has solution

$$N = \frac{K}{1 + cKe^{-rt}}, \tag{3.4}$$

where c is an arbitrary parameter that sets the initial conditions. Figure 3.2 shows the temporal evolution of different species and emphasizes a quite good agreement with the logistic model and the explicit temporal evolution, formula (3.4). The low population dynamics is characterized by an exponential growth law described by Leonardo of Pisa. As the population increases saturates in a population equilibrium $N = K$ (cf. Fig. 3.2). The logistic model also has a counterpart in the context of chemical reactions. The following generic chemical reaction was proposed by Schlögl [144]

$$\mathrm{A} + \mathrm{U} \xrightarrow{\mathrm{k1}} 2\,\mathrm{U}, \tag{3.5}$$

$$2\,\mathrm{U} \xrightarrow{\mathrm{k2}} \mathrm{U} + \mathrm{A}, \tag{3.6}$$

$$\mathrm{B} + \mathrm{U} \xrightarrow{\mathrm{k3}} \mathrm{C}, \tag{3.7}$$

$k1$, $k2$, and $k3$ are the rate constants, which involve the collision cross section of the required molecules times the probability for the reaction. Indeed, these positive constants depend on temperature. The concentration of products A and B, ρ_a and ρ_b, are

kept constant employing thermostats. Product C is removed instantaneously. The rate equation for the concentration of the substance $U(t)$, ρ, is given by [158]

$$\frac{d\rho}{dt} = (k_1\rho_a - k_3\rho_b)\rho - k_2\rho^2. \tag{3.8}$$

Redefining the parameters, one can obtain the logistic model Eq. (3.3). Therefore the logistic model is a model that is observed in different contexts.

3.1.2 Fisher equation

As a matter of fact, when one looks at the evolution of populations in large areas, these exhibits large differences between one region and another. Figure 3.3 illustrates the distribution population of the human of the earth. Which is a natural consequence of the homogeneous distribution of sources that are necessary for development of the human species. Hence, one expects an interaction between different regions. In order to understand the dynamic phenomena that can emerge in these conditions, we consider a model of the population distributed along a straight line (see Fig. 3.4). This line will be partitioned in equivalent regions, which are labeled by the parameter i. The i-th

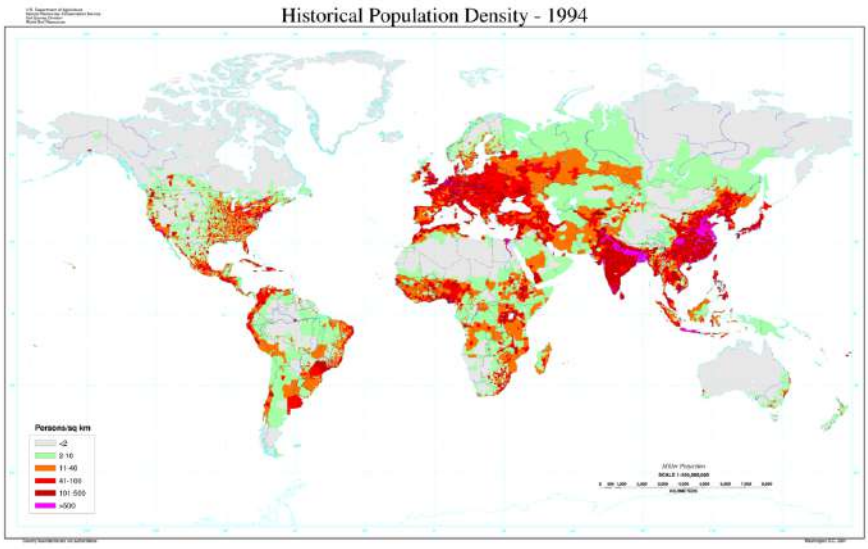

Figure 3.3: Human population distribution density (1994).

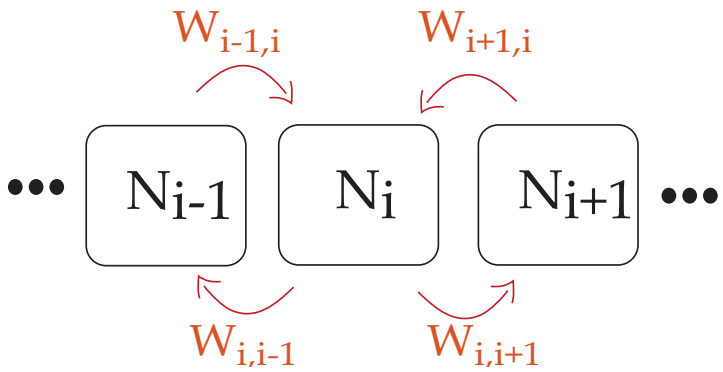

Figure 3.4: Schematic representation of a model of population distributed along a straight line. $N_i(t)$ stands for the population in i-th region. $W_{j,i}$ accounts for the population flux from j-th to i-th region.

region has a population $N_i(t)$ that is governs by a logistic dynamics. Likewise, the local population dynamics satisfies an equation that contains the process of birth, death, and migration, that is,

$$\frac{dN_i}{dt} = birth - death + migration, \tag{3.9}$$

For simplicity, we assume that each regions is only coupled to its neighboring regions (nearest neighbors), then the dynamics of populations reads

$$\partial_t N_i = rN_i\left(1 - \frac{N_i}{k}\right) + W_{i+1,i} + W_{i+1,i} - W_{i,i+1} - W_{i,i-1}, \tag{3.10}$$

where $W_{j,i}$ accounts for the population flux from j-th to i-th region. Assuming that the population flux is proportional to the population, $W_{j,i} = \alpha N_j$ with α a dimension constant parameter. The above model takes the form (the discrete Fisher equation [169])

$$\partial_t N_i = rN_i\left(1 - \frac{N_i}{k}\right) + \alpha(N_{i+1} - 2N_i + N_{i-1}). \tag{3.11}$$

Considering that regions are small compared to the entire system under study, one can consider the continuous limit as an appropriate description. Let us introduce dx as the size of regions. Hence, in the limit $dx \to 0$, we can promote the population density to a scalar field, that is, $N_i(t) \to N(x,t)$, which is a scalar that accounts for the population

at position x in time t. In the continuous limit the population equation reads

$$\partial_t N = rN\left(1 - \frac{N}{K}\right) + D\partial_{xx}N, \tag{3.12}$$

where the diffusion coefficient $D \equiv \alpha dx^2$. For the sake of simplicity from now on we can fix $D = 1$. The above is because one can always set the spatial scale in units that the diffusion coefficient is 1. This model Eq. (3.12) is known as the Fisher equation or also known as Kolmogorov-Petrovsky-Piscounov equation, KPP equation or Fisher-KPP equation or FKPP equation. In 1937, simultaneously Fisher [71] and Kolmogorov, Petrovsky, and Piscounov [97] propose this model. The statistician and biologist Ronald Fisher introduces model (3.12) in the context of spread of advantage gene. Kolmogorov et al. consider model (3.12) in the context of modified nonlinear diffusion equation with applications to populations dynamics. Figure 3.5 shows Portrait of Fisher, Kolmogorov, and Petrovsky,

Model (3.12) has two trivial equilibria the populated ($N = K$) and the unpopulated ($N = 0$) state. Performing a linear stability analysis, one infers that unpopulated and populated are unstable and stable, respectively. Analogous to what one observes in the chain of coupled pendulums (cf. Fig. 2.7), a disturbance of unpopulated state is characterized by the emergence of a two counter propagative solutions that connect the

Figure 3.5: Portrait of Fisher (1890 –1962), Kolmogorov (1903–1987), and Petrovsky (1901–1973), pioneers in the development of the understanding of fronts.

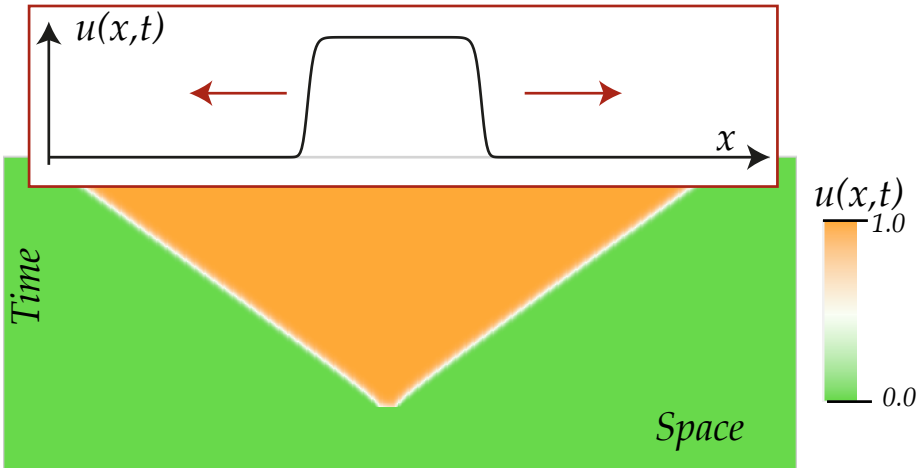

Figure 3.6: Front propagations into unstable state. Spatiotemporal diagram obtained from numerical simulation of model (3.12). Inset: population profile at given time.

unstable with stable equilibrium state. Figure 3.6 shows the spatiotemporal evolution of a localized perturbation from the unpopulated state. Hence, the FKPP model (3.12) predicts that population state invades the whole space through a nonlinear waves with a well-define speed and a characteristic profile as shown in Fig. 3.6. Note that independent on the initial condition, if it is bounded in the space, after a transient the system spreads with a well-defined speed and profile.

To determine the front speed, we consider wave solution—follow the propagative ansatz of Kolmogorov et al.—$N(x,t) = N(x - vt)$. Introducing this ansatz in Eq. (3.12), one obtains a Newtonian type equation

$$D\partial_{zz}N = -\frac{dU}{dN} - v\partial_z N = -rN\left(1 - \frac{N}{K}\right) - v\partial_z N, \tag{3.13}$$

where $z \equiv x - vt$ is a co-mobile coordinate, $U \equiv rN^2/2 - N^3/3K$ is an effective mechanical potential, and the front speed v is a damping coefficient. This potential is characterized by having two extremes, the populated and the unpopulated state. The populated and the unpopulated state correspond to a minimum and a maximum of the potential U, respectively. Figure 3.7 shows the effective potential and the phase portrait associate to Eq. (3.13). The front solution corresponds to the heteroclinic solution that

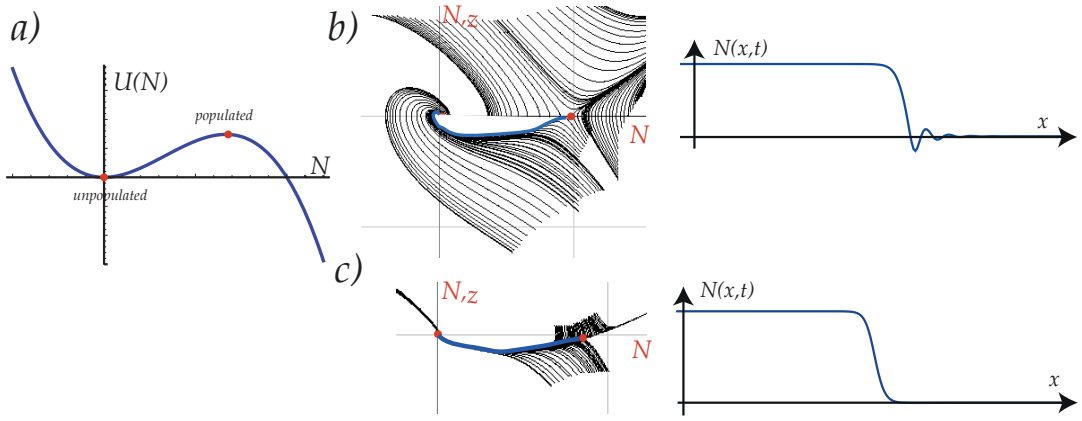

Figure 3.7: Effective mechanical potential and phase portrait of equation (3.13). a) Effective potential $U(N)$, b) and c) phase portraits of equation (3.13) with small and large damping and representation of their respective heteroclinic curve solutions.

connects the equilibria [160]. Figure 3.7 depicts this line in blue color. It is important to note that this dynamic system always has heteroclinic solutions in the presence of damping, that is, there are always fronts solution with difference speed. The different fronts are obtained with different initial conditions. However, for small damping v (front speed), this trajectory is characterized by to present damped oscillations near unpopulated state (cf. Fig. 3.7b). Conversely, for large damping, the heteroclinic curve does not exhibit damped oscillations as it is shown in Fig. 3.7c. From the standpoint of population dynamics front solutions with oscillations around unpopulated state is unacceptable and from a mathematical point of view these solutions are unstable stationary solutions. Note that these solutions from an ecological point of view are also unacceptable ($N > 0$). Therefore, only heteroclinic curves without oscillations around unpopulated state are observable. Then this establishes the existence of a minimum speed for the fronts, v_{min}.

3.1.3 Determination of v_{min}: linear analysis

As mentioned in previous section, front solutions with monotonous spatially profile are consequence of the damped to overdamped transition of unpopulated state. This transition can be characterized by a simple linear analysis around the unpopulated state [97, 71].

Linear criterium

Let us consider the dynamics around of unpopulated state in co-mobile dynamical system

$$\partial_{zz}N = -rN - v\partial_z N. \tag{3.14}$$

To study the stability of unpopulated state, we consider a solution of the form $N(z) = N_0 e^{\lambda z}$ and introducing this solution in above equation, one obtain the relation $\lambda^2 N + r + v\lambda = 0$. The damped to overdamping transition is characterized by the quadratic equation has a degenerate solution, i.e., discriminate equals to zero, $v^2 - 4r = 0$. Hence, the minimum speed is

$$v_{min} = 2\sqrt{r}. \tag{3.15}$$

Numerical simulations of the FKPP model (3.12) show that indeed this is the minimum speed of propagation of fronts. The first context where this minimal speed was predicted is in the context of chemical reactions waves [110]. However, the original derivation of this f ormula is not clear. Indeed, it was not obtained employing a linear analysis but possibly utilizing a simple dimension analysis and parameter adjustment.

Asymptotic criterium

As we have mention for different initial conditions, the front solution will strongly depend of the asymptotic behavior of $N(x, 0)$ for $x \to \pm\infty$. Considering an initial conditions of the form $N(x, 0) \sim N_0 e^{-kx}$ for $x \to \infty$ where $\{k, N_0\}$ are positive constants. The front propagates as a wave of the form $N(x, t) = N\left(k(x - vt)\right)$. Linearizing Eq.(3.12) and considering $N(x, t) \sim N_0 e^{-k(x-vt)}$ for $x \to \infty$ where k accounts for the

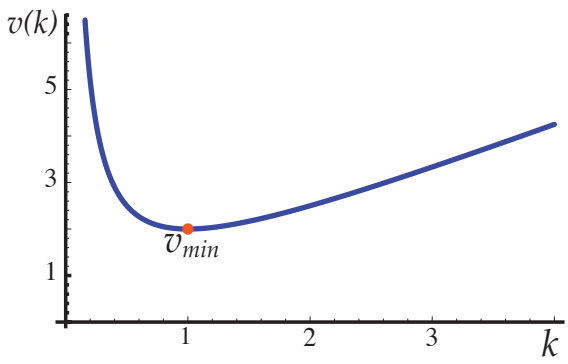

Figure 3.8: Front speed as function of the spatial decay length of the tail of the front, steepness k. The red dot shows the minimum speed

spatial decay length of the tail of the front (*steepness*), after straightforward calculations one can obtain the following relation [122],

$$v(k) = \frac{r}{k} + k. \tag{3.16}$$

Figure 3.8 shows the front speed as function of the spatial decay length of the tail of the front, k. Thus, v as function of k is a convex function. Minimizing the previous curve with respect to k, we obtain the critical steepness $k \equiv k_c = \sqrt{r}$, for which we obtain the minimal speed $v(k_c) \equiv v_{min} = 2\sqrt{r}$. This method is the *asymptotic process* [122], since it only considers the asymptotic behavior of the front. Namely, the nonlinear terms do not determine the front speed in the model under consideration. For any other value of the steepness k the front propagates with a speed larger than v_{min} ($v(k) \leq v_{min}$).

3.1.4 Analytical profile front solution

Despite the simplicity of model Eq. (3.12), the analytical solution of the nonlinear wave is unknown. To determine the profile of the front solution, we can introduce the following change of variable $z = v\zeta$ in Eq. (3.13), which reads

$$\epsilon \partial_{\zeta\zeta} N = -rN\left(1 - \frac{N}{K}\right) - \partial_\zeta N, \tag{3.17}$$

where $\epsilon \equiv D/v^2$. Considering $\epsilon \ll 1$ due to $v_{min} \geq 2\sqrt{r}$. Hence, we can use the following ansatz for the front solution (regular perturbation expansion)

$$N(z) = N_0(z) + \epsilon N_1 + \epsilon^2 N_2 + \cdots , \tag{3.18}$$

Introducing this ansatz in Eq. (3.17), one obtains a hierarchy of equations in ϵ

$$\begin{aligned} \partial_\zeta N_0 &= -rN_0\left(1 - \frac{N_0}{K}\right), \\ \partial_\zeta N_1 + N_1 r\left(1 - 2\frac{N_0}{K}\right) &= -\partial_{\zeta\zeta} N_0, \\ \partial_\zeta N_2 + N_2 r\left(1 - 2\frac{N_0}{K}\right) &= -\partial_{\zeta\zeta} N_1 + \frac{r}{K} N_1^2, \\ &\cdots \end{aligned} \tag{3.19}$$

Note that only the first equation of this set of equations is not linear and the others are linear with the same linear operator. The nonlinear equation for N_0 is a logistic equation with negative linear term (see Eq. 3.3), so the solution is

$$N_0(z) = \frac{K}{1 + cKe^{rz/v}}. \tag{3.20}$$

Thus, the profile of $N_0(z)$ is similar to those show in Fig. (3.7)c. Notice that dominate solution satisfies the boundary conditions $\{z \to -\infty, N_0(z) \to -K\}$ and $\{z \to \infty, N_0(z) \to 0\}$. We can choose $c = 1$, in order to fix the front position at the origin of z coordinate. The front position is defined as that position where the front exhibits greater spatial variation. To solve the equation for $N_1(z)$, we use the relation

$$\partial_{\zeta\zeta} N_0 = -r\left(1 - 2\frac{N_0}{K}\right)\partial_\zeta N_0, \tag{3.21}$$

and replacing this expression in N_1 equation, we get

$$\partial_\zeta N_1 - N_1 \frac{\partial_{\zeta\zeta} N_0}{\partial_\zeta N_0} = -\partial_{\zeta\zeta} N_0, \tag{3.22}$$

using the integration factor $1/\partial_\zeta N_0$ the above equation takes the form

$$\partial_\zeta\left(\frac{N_1}{\partial_\zeta N_0}\right) = -\frac{\partial_{\zeta\zeta} N_0}{\partial_\zeta N_0} = -\frac{d\ln(\partial_\zeta N_0)}{d\zeta}. \tag{3.23}$$

Finally,

$$N_1 = -\partial_\zeta N_0 \ln(\partial_\zeta N_0). \tag{3.24}$$

Using the same procedure, one can calculate the following corrections. Therefore, the solution has the form [123]

$$N(z) = \frac{K}{1+Ke^{rz/v}} - \frac{D}{v^2}\frac{rK^2e^{rz/v}}{(1+Ke^{rz/v})^2}\ln\left[\frac{rK^2e^{rz/v}}{(1+Ke^{rz/v})^2}\right] + \mathcal{O}\left(\frac{D^2}{v^4}\right) \tag{3.25}$$

where $v \geq v_{min}$. Therefore, the above solution is not only valid for the solution that propagates with the minimum speed but for all the front solutions of the FPKK equation.

3.1.5 Stability of front solution

Note that numerically the front solutions are observed, then one expects that these solutions are stable. To study their stability, one can consider a perturbation around this solution of the form $N(x,t) = N_{FKPP}(z = x - vt) + h(z,t)$, where $N_{FKPP}(z)$ is the front solution and $h(z,t)$ is a perturbation function. Introducing this ansatz in Eq. (3.12) and linearizing in h, we get

$$\partial_t h = rh - \frac{2rN_{FKPP}(z)}{K}h + v\partial_z h + \partial_{zz}h, \tag{3.26}$$

using the transformation $h(z,t) = g(z)e^{-\lambda t}$, it reads

$$\partial_{zz}g + v\partial_z g + r\left[1 - \frac{2N_{FKPP}(z)}{K} - \lambda\right]g = 0. \tag{3.27}$$

Which corresponds a Sturm-Liouville equation [168]. This type of linear equations are characterized by having a spectrum of sorted eigenvalues and eigenfunctions. The ground state has not zero, the first excited state has one, and so forth. Due to N_{FKPP} satisfies Eq. (3.13), thus $\partial_z N_{FKPP}$ satisfies the above equation with $\lambda = 0$. This solution has the shape of a bell. Indeed, It is the ground state. This zero eigenvalue is a consequence of the translation invariance of Eq. (3.12). In field theory this type of eigenfunction is denominated *Godlstone mode* [133]. The spectrum of the above equation has the form depicted in Fig. 3.9. Therefore, we conclude that the front solutions are stable solution of model Eq. (3.12).

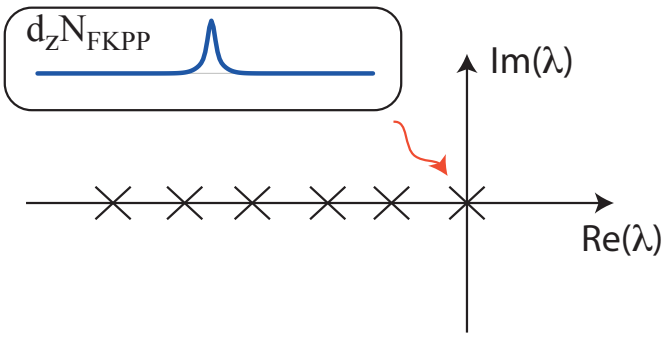

Figure 3.9: Typical spectrum of Strum Liouville with a Goldstone mode.

3.1.6 Transient dynamics towards the stationary front

In the previous section, we have presented a systematic way of obtaining a solution of the stationary front. In this section, we characterize how the system converges to this solution. As we have mentioned before, the dynamic of the front is entirely determined by linear theory. Then, the dynamics of relaxation to the stationary solution can also be determined by the linear theory [65, 159]. A systematic strategy to study a linear problem is to use Fourier transforms [32], that it,

$$N(k,t) = \int_{-\infty}^{\infty} dx e^{-ikx} N(x,t), \tag{3.28}$$

To study the fronts it is more appropriate to consider a base of propagative modes; then we introduce the decomposition $N(k,t) = \tilde{N}(k)e^{-i\omega(k)t}$. Therefore, the inverse Fourier transform reads [32]

$$N(x,t) = \frac{1}{2\pi}\int_{-\infty}^{\infty} dk \tilde{N}(k) e^{i(kx-\omega(k)t)}, \tag{3.29}$$

where the real part $[Re(\omega)]$ and the imaginary part $[Im(\omega)]$ of the of omega, respectively, account for the dispersion relation and the growth rate of the modes with wave number k. To describe this transformation in the co-mobile system ($z = x - vt$), we consider the transformation

$$N(z,t) = \frac{1}{2\pi}\int_{-\infty}^{\infty} dk \tilde{N}(k) e^{i[kz-(\omega(k)-kv)t]}. \tag{3.30}$$

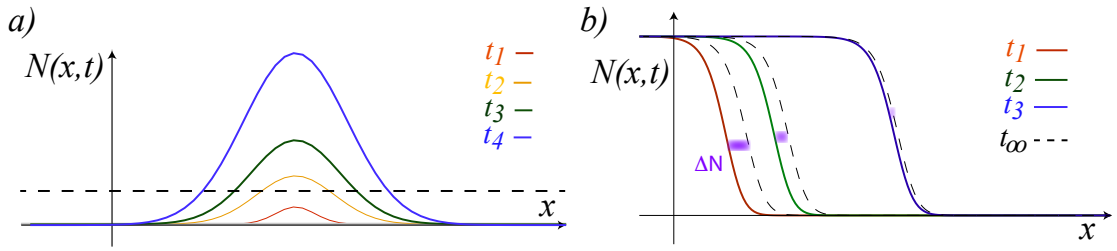

Figure 3.10: Linear evolution of the FKPP equation (3.12). a) Sequence of profiles for the FKPP equation with $t_1 < t_2 < t_3 < t_4$ from a localized perturbation. This evolution is consistent with the Gaussian type evolution given by the formula (3.34). b) Temporal sequence of the evolution of the front and comparison with the asymptotic solution, $t_1 < t_2 < t_3$. The right and left flank of the front connects the stable and the unstable state, respectively. The dashed curve accounts for the asymptotic front solution $N_{FKPP}(z) = \lim_{t\to\infty} N(z,t)$ with $z = x - vt$.

For the system reaches the equilibrium it is required that the extreme mode with k_c ($\partial Im(\omega)/\partial k|_{k_c} = 0$) that govern the relaxation dynamics. Note that this critical mode must be the mode that decays slowest, that is, it must be a minimum of the growth rate ($mim\{Im(\omega(k))\}$ see Fig. 3.8). The speed associated to this mode satisfies [32, 159] $Im(\omega - vk)|_{k_c} = 0$ or equivalent

$$v* = \frac{Im(\omega)}{Im(k)}|_{k_c}. \tag{3.31}$$

To understand the dynamics around the critical mode one can consider $k \approx k_c + \Delta k$ and the population for large z is describe by

$$\begin{aligned} N(z,t) &\approx |\tilde{N}(k_c)|\frac{1}{2\pi}\int_{-\infty}^{\infty} d\Delta k e^{i\left[k_c z + \Delta k z - \left(\omega(k_c) + \frac{\omega''(k_c)(\Delta k)^2}{2}\right)t\right]}, \\ &\approx \frac{|\tilde{N}(k_c)|e^{ik_c z}e^{-i\omega_r(k_c)t}}{2\pi}\int_{-\infty}^{\infty} d\Delta k e^{i[\Delta k z - (\frac{\omega''(k_c)(\Delta k)^2}{2})t]}. \end{aligned} \tag{3.32}$$

Introducing the notation $D = i\omega''(k_c)/2$, then

$$\begin{aligned} N(z,t) &\approx \frac{|\tilde{N}(k_c)|e^{ik_c z}e^{-i\omega_r(k_c)t}}{2\pi}\int_{-\infty}^{\infty} d\Delta k e^{[i\Delta k z - Dt(\Delta k)^2]} \\ &\approx \frac{|\tilde{N}(k_c)|e^{ik_c z}e^{-i\omega_r(k_c)t}e^{-\frac{z^2}{4Dt}}}{2\pi}\int_{-\infty}^{\infty} d\Delta k e^{-Dt\left[\Delta k - i\frac{z}{2\sqrt{Dt}}\right]^2} \end{aligned} \tag{3.33}$$

Integrating the Gaussian, one gets

$$N(z,t) \approx |\tilde{N}(k_c)| e^{i\kappa z - i\omega_r(k_c)t} \frac{e^{-\lambda z} e^{-\frac{z^2}{4Dt}}}{2\pi\sqrt{Dt}}, \tag{3.34}$$

with $\lambda \equiv Re(k_c)$ and $\kappa \equiv Im(k_c)$. The above formula accounts for the evolution of a disturbance given by a linear equation. It is important to note that this solution plays two crucial roles. One is the description of the initial perturbations, and another describes the asymptotic evolution of the profile, which determines the dynamic development of the front. Figure 3.10a shows a sequence of profiles for the FKPP equation (3.12) from a localized perturbation. In effect, the solution grows exponentially and similarly, it expands Gaussianly. Subsequently, the system enters the nonlinear regime that gives rise to the front solutions. It is this regime; again the previous solution becomes relevant since it describes the flank of the front around the unstable state. Indeed, the above solution (3.34) describes the system on the flank of the unstable side. Hence, as time evolves, the front decays to the asymptotic solution which tends to exponentially zero. Namely, the differences decay with a Gaussian tendency

$$\Delta N \equiv |N(z,t) - N_{FKPP}(z)| \approx e^{-ln\sqrt{Dt} - \frac{z^2}{4Dt}}, \tag{3.35}$$

where $N_{FKPP}(z) = \lim_{t\to\infty} N(z,t)$ is the stationary front solution. Figure 3.10b depicts the evolution ΔN.

In the case of FKPP equation (3.12), the linear relationship is

$$\omega(k) = ir\left(1 - k^2\right), \tag{3.36}$$

Thus $Re[\omega(k)] = 0$, $Im[\omega(k)] = r(1-k^2)$, $k_c = 1$, $D = 1$, and the front around the flank of the unstable solution

$$N(z,t) \approx |\tilde{N}(k_c)| \frac{e^{-z - \ln\sqrt{t} - \frac{z^2}{4t}}}{2\pi}. \tag{3.37}$$

when z is large, the solution tends to

$$N(z, t\to\infty) \approx |\tilde{N}(k_c)| e^{-z-\ln\sqrt{t}}/2\pi = N\left((x - vt) + \ln\sqrt{t}\right). \tag{3.38}$$

Universal asymptotic front speed

To estimate the expression of the front speed, one can take the temporal derivative of the argument of the solution $N\left((x-vt)+\ln\sqrt{t}\right)$

$$v^*(t) \approx v - \frac{1}{2t}. \tag{3.39}$$

Therefore as the system evolves, the front speed tends to asymptotic speed decaying with a power law. This result is consistent with the fact that the front solution has a Goldstone mode; Accordingly, it can only decay with power laws.

A rigorous calculation and demonstration to determine the front speed considering the FKPP equation (3.12) was done by M.D. Bramson [33] who obtained

$$v^*(t) = v - \frac{3}{2t} + \frac{3\sqrt{\pi}}{2t^{3/2}} + \cdots . \tag{3.40}$$

This result is based on the linear equation of FKPP Eq. (3.12), then based on a general linear equation of the form $\partial_t u = f'(u)|_{u=0} + \partial_{xx} u$ around the equilibrium $u = 0$, Ebert and Van Saarloos show [65, 160] that the previous result is universal.

3.1.7 Particle-type behavior and interaction of fronts

Numerically, making a disturbance of unpopulated state one observes the emergences of two counter propagative waves that after a transient converges to the two fronts propagating in opposite directions (see Fig. 3.6). Note that the characterization of

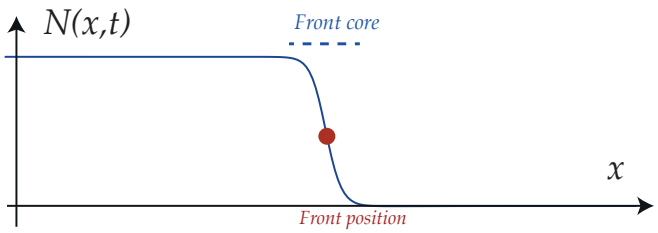

Figure 3.11: Front solution: the front position accounts for the spatial location that has maximum spatial variation and its core is given by the spatial size around of front position.

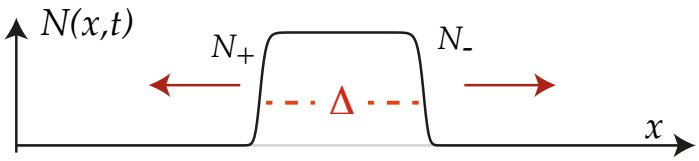

Figure 3.12: Front interaction. Schematic representation of two counter propagative fronts. $\{N_+, N_-\}$ are front solutions spreads leftward and rightward, respectively. Δ accounts for the distance between fronts.

the front solutions—despite being a spatial extended solution—is simply given by two quantities its *position* and *core*. The front position is given by the position of the space that has maximum spatial variation and its core is given by the spatial size around of front position. Let P be the front position. The front position can be characterized mathematically by the expression

$$P(t) \equiv \frac{\int_{-L/2}^{L/2} x \partial_x N(x,t) dx}{\int_{-L/2}^{L/2} \partial_x N(x,t) dx}. \tag{3.41}$$

This formula is based on considering that the spatial derivative of the front around the front position is symmetric. The front core is a characteristic length that accounts for the region of greater variation of the front. Figure 3.11 illustrates these two quantities that characterize the front solution. Using the previous formula for the front position for FKPP fronts, one gets

$$\dot{P} = v, \tag{3.42}$$

where v is the speed of the front.

Due to the FKPP model (3.12) is a nonlinear equation, the front solution is a solution. However, the addition of two propagative counter fronts is not a solution. To figure out the dynamics of large separated two counter propagative fronts, we consider the ansatz

$$N(x,t) = \frac{N_+\left(z_+ \equiv x + vt + \frac{\Delta(t)}{2}\right) N_-\left(z_- \equiv x - vt - \frac{\Delta}{2}\right)}{K} + w(x,t,P), \tag{3.43}$$

where $\{N_+, N_-\}$ are front solutions spreads leftward and rightward, respectively, Δ accounts for the distance between fronts, and $w(x,t,P)$ is a small correction function.

The previous ansatz is schematically represented in Fig. 3.12. As result of the spatial translation invariance the front position can locate in any position in space. That is, the front solution is parameterized by a continuous parameter, the front position. The position of the left (right) front is $-\Delta/2$ ($\Delta/2$). When the two counter fronts spread far enough away from each other, the dynamics of the system is given by the Goldstone mode. This is based on the fact that the slower modes govern, the slower dynamics of a system, the former is known as *the central manifold* [81]. Then, we promote the parameter Δ a temporal variable to describe this dynamics [$\Delta(t)$]. Introducing the ansatz (3.43) in equation (3.12), and linearizing in w, after straightforward calculations, one obtains

$$\begin{aligned}\partial_t N &= \left(v+\frac{\dot{\Delta}}{2}\right) N_-\partial_{z_+}N_+ - \left(v+\frac{\dot{\Delta}}{2}\right) N_+\partial_{z_-}N_- \\ &\quad +\mathcal{L}w + rN_-N_+(1-\frac{N_-N_+}{K}) + N_-\partial_{z_+z_+}N_+ + N_+\partial_{z_-z_-}N_-, \end{aligned} \tag{3.44}$$

with the linear operator

$$\mathcal{L} \equiv \left[r - \frac{2N_-N_+}{K} - v\partial_{z_-} + v\partial_{z_+} + \partial_{z_+z_+} + \partial_{z_-z_-}\right], \tag{3.45}$$

and $z_\pm \equiv x \pm vt \pm \Delta/2$ are coordinates in the respectively co-mobile system. The above linear equation can rewrite as

$$\begin{aligned}\mathcal{L}w &= -\left(v+\frac{\dot{\Delta}}{2}\right) N_-\partial_{z_+}N_+ + \left(v+\frac{\dot{\Delta}}{2}\right) N_+\partial_{z_-}N_- \\ &\quad +rN_-N_+(1-\frac{N_-N_+}{K}) + \partial_{z_+z_+}N_+ + \partial_{z_-z_-}N_-. \end{aligned} \tag{3.46}$$

To solve the above linear equation, we introduce the inner product

$$\langle f|g\rangle = \frac{1}{L}\int_{-L/2}^{L/2} fg dz. \tag{3.47}$$

Thus the adjoint operator associated to $\mathcal{L}$ is

$$\mathcal{L}^\dagger \equiv \left[r - 2\frac{cN_-N_+}{K} + v\partial_{z_-} - v\partial_{z_+} + \partial_{z_+z_+} + \partial_{z_-z_-}\right]. \tag{3.48}$$

Notice this operator is not self-adjoint. Let Φ an element of $\ker(\mathcal{L}^\dagger)$, i.e. $\mathcal{L}^\dagger\Phi = 0$. Φ is an unknown function, however its asymptotic behavior is known by simple linear analysis,

$$\Phi = \begin{cases} \Phi_0 e^{\left(v-\sqrt{v^2+4r}\right)z_-}, & z_- \to -\infty, \\ \Phi_0 e^{\left(v+\sqrt{v^2-4r}\right)z_-}, & z_- \to \infty, \\ \Phi_0 e^{\left(-v-\sqrt{v^2-4r}\right)z_+}, & z_+ \to -\infty, \\ \Phi_0 e^{\left(-v-\sqrt{v^2+4r}\right)z_+}, & z_+ \to \infty. \end{cases} \tag{3.49}$$

To solve the linear Eq. (3.50) we impose the solvability conditions (Fredholm alternative [138]), that is, we impose that right side of the linear equation is orthogonal to the elements of the kernel of $\mathcal{L}^\dagger$. Thus we obtain

$$\begin{aligned} 0 \;=\; & \langle\Phi| - \left(v + \frac{\dot{\Delta}}{2}\right) N_-\partial_{z_+}N_+ + \left(v + \frac{\dot{\Delta}}{2}\right) N_+\partial_{z_-}N_-\rangle \\ & \langle\Phi| + rN_-N_+(1 - N_-N_+) + \partial_{z_+z_+}N_+ + \partial_{z_-z_-}N_-\rangle. \end{aligned} \tag{3.50}$$

Because the spatial variations of the front solution are only relevant around front core. The above integral can only evaluated around of each front position. Using the fact that each front behaves with respect to other

$$N_+ \;\to\; K - K^2 e^{-\left(v+\sqrt{v^2+4r}\right)(z-\Delta)}, \qquad z \to \frac{\Delta}{2}, \tag{3.51}$$

$$N_- \;\to\; K - K^2 e^{\left(v+\sqrt{v^2+4r}\right)(z-\Delta)}, \qquad z \to -\frac{\Delta}{2}. \tag{3.52}$$

Using this asymptotic behavior, equations $-v\partial_{z_-}N_- = rN_-(1 - N_-/K) + \partial_{z_-z_-}N_-$, $v\partial_{z_+}N_+ = rN_+(1 - N_+/K) + \partial_{z_+z_+}N_+$ and relation $\langle\phi|\partial_{z_+}N_+\rangle = -\langle\phi|\partial_{z_-}N_-\rangle$, after straightforward calculations

$$\dot{\Delta} = -ae^{-\left(v+\sqrt{v^2+4r}\right)\Delta}. \tag{3.53}$$

with $a \equiv 2\langle\Phi|rK^2e^{\left(v+\sqrt{v^2+4r}\right)z}N_+(1 - 2N_+)\rangle/\langle\Phi|\partial_{z_+}N_+\rangle$. Hence, the interaction between front is attractive and exponentially small with the distance between them. In brief this force is irrelevant in the front dynamics. Since the main dynamics is given by the propagation.

3.1.8 Front propagation into unstable state in a liquid crystal light valve experiment

In this section, we will analyze a front which can be studied in the laboratory. The system is composed by a Liquid crystal light valve (LCLV) with an optical feedback loop is an optical experiment that exhibits a transition of molecular reorientation of subcritical type [52]. In other words, when a liquid crystal with a planar anchor is subjected to a voltage that depends on its own molecular orientation, it presents a reorientation transition of the first order. The experimental setup is schematically represented in Fig. 3.13. The LCLV is composed of a thin nematic liquid crystal film between a glass and a photoconductive plate over which a dielectric mirror is deposed. The liquid crystal film has planar alignment with thickness $d = 15$ [μm]. The liquid crystal used is a nematic LC-654 (NIOPIK). It is a mixture of cyano-biphenyls, with a positive dielectric anisotropy $\varepsilon_a = 10.7$ and large optical birefringence $\Delta n = 0.2$. The photoconductor behaves like a variable resistance, which decreases for increasing illumination. Liquid crystal light valve with optical feedback has been studied extensively in the literature (see review article [140] and references therein).

Transparent electrodes over the glass plates allow the application of voltage V_0 to induce an electric field. The LCLV is illuminated by a He-Ne laser beam ($\lambda = 632.8$ nm) with intensity $I_{in} = 35$ mW. The laser beam passes through a Holoeye LC 2002 Transmissive Spatial Light Modulator (SLM), which allows manipulation of the spatial profile of the intensity, controlling the front dynamics and imposing a quasi-one-dimensional configuration. The optical path is schematically represented in Fig. 3.13(a). Over a critical voltage, *i.e.* Fréedericksz voltage V_{FT}, the molecules tend to align along the direction of the applied electric field. The molecular orientation changes locally and dynamically following the spatial illumination distribution present in the photoconductor wall of the cell. The light-driven feedback is obtained by sending back onto the photoconductor, I_w, the light that has passed through the liquid crystal layer and has been reflected by the dielectric mirror. The light beam experiences a phase shift that

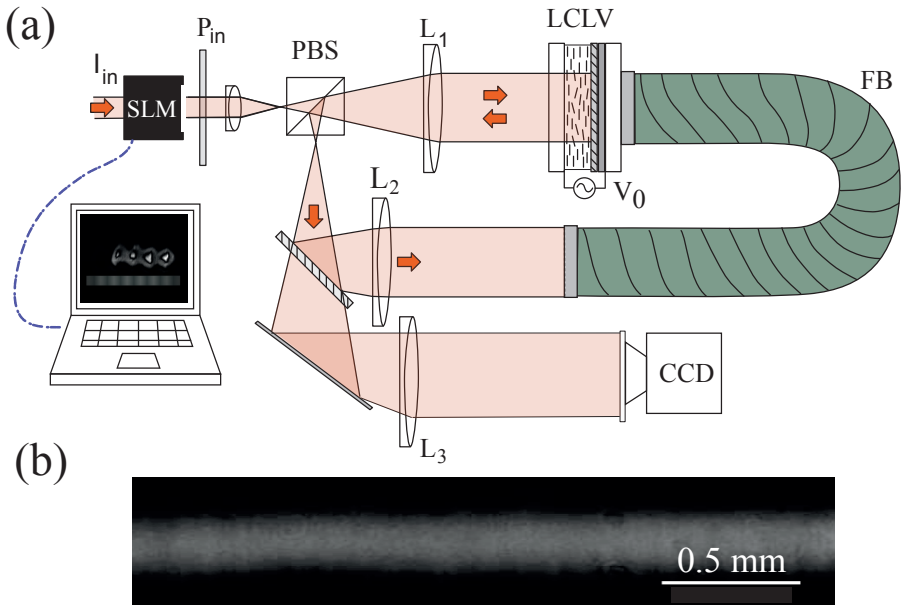

Figure 3.13: Liquid crystal light valve (LCLV) setup. (a) Schematic representation of the liquid crystal light valve with optical feedback. I_{in} input light intensity, P_{in} is a polarizer, PBS is the polarized beam splitter, L_1, L_2, and L_3 are lenses, V_0 is the external voltage applied, FB is the fiber bundle, and CCD is the camera that captures the images. (b) Snapshots of the LCLV without optical feedback with the unforced [7].

depends on the liquid-crystal orientation [see [140] and references therein]. By inserting a polarized beam splitter, phase shifts are converted into intensity variations, modulating the illumination onto the photoconductor and, hence, the effective voltage applied to the liquid crystal layer. Finally, the laser beam is directed to a charge-coupled device (CCD) camera, where the images of the LCLV are taken.

Using the SLM, one can illuminate a channel in the LCLV of 3.5 mm long and 0.25 mm wide (see the rectangles of the left panels of Fig. 3.20). Indeed, the nature of the system is almost one-dimensional. For low external voltages, no change is observed. The illuminated area remains dark, which is a manifestation of no molecular reorientation [see bottom inset in Fig. 3.15]. Above a critical value V_{FT}, the region begins to change color to gray [see the panels in Figs. 3.13 and 3.15]. The experimental bifurcation di-

agram of this transition is illustrated in Fig. 3.15(a) [7]. The intensity change of the illuminated area is abrupt, which is consistent with a subcritical molecular reorientation transition [43]. Characterization of this instability using the total intensity is consistent with the subcritical Fréedericksz transition [see Fig. 3.15]. Namely, increasing the voltage ($V > V_{FT}$), the gray state changes slightly. Similarly, decreasing the voltage, the gray state is maintained until a critical value $V_b < V_{FT}$. Hence, the system exhibits a hysteresis or bistable region [7]. Note that the Fréedericksz transition from black to gray region is characterized by the emergence of a gray spot that begins invading the system. Indeed, this phenomenon corresponds to a FKPP front propagation between the unstable (black region) to the stable state (gray region). Figure 3.20 shows this phenomenon observed at $V_0 = 3.69$ [V_{rms}]. Note that as a consequence of the inevitable imperfections of the experiment, as the front propagates, the speed slightly

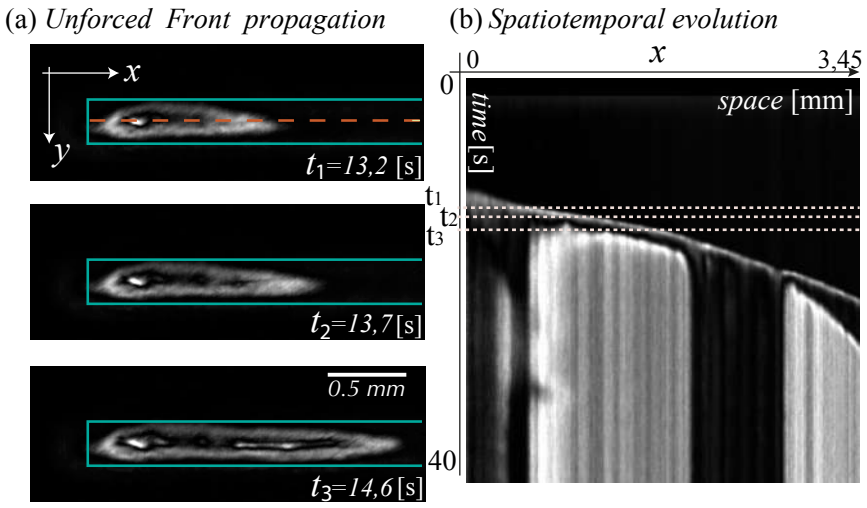

Figure 3.14: Experimental front propagation of liquid crystal light valve with optical feedback, snapshots (a) and respective spatiotemporal diagrams (b) at $V_0 = 3.69$ [V_{rms}]. The left panels account for a temporal sequence of snapshots. The rectangle accounts for the illuminated area with optical feedback, and the dashed curve is the extracted region to obtain the spatiotemporal diagrams. The right panel stands for the spatiotemporal evolution of the fronts. The horizontal dashed lines account for the moments where the top snapshots are extracted [7].

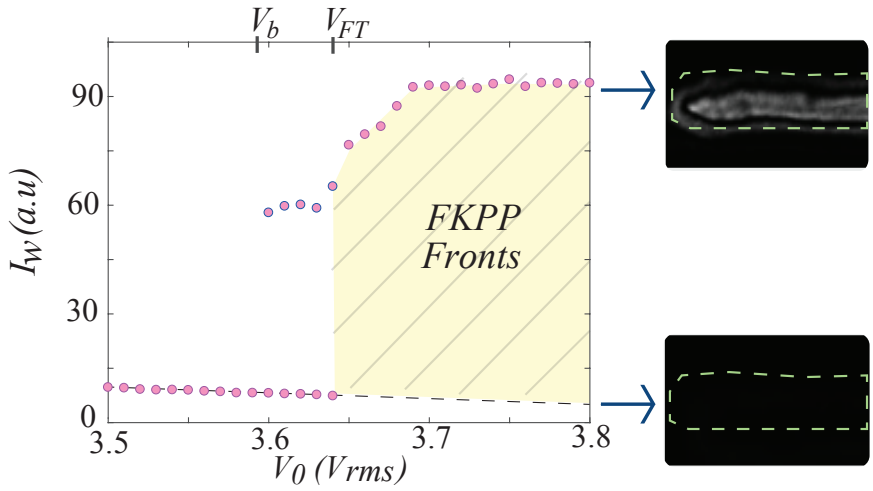

Figure 3.15: Experimental bifurcation diagram performed in a liquid crystal light valve with optical feedback, intensity I_w as a function of the applied voltage V_0. The points correspond to values of total light intensity I_w at the LCLV. The dashed line is a schematic representation of the aligned molecular state induced by the anchoring of the walls. The painted area accounts for the region of coexistence between stable and unstable states, where FKPP fronts are observed. The insets are the snapshot of the typically observed states. Bifurcation diagram retrieved from [7].

changes. The average speed of propagation is 3.3 mm/s. In most of the observed cases, the fronts are triggered from the edges of the illuminated region (see left panels of Fig. 3.20). Therefore this experimental system exhibits fronts into an unstable state that give an account when a molecular configuration becomes unstable compared with a new one that invades the system. Note that the spatiotemporal diagram in Fig.3.15 shows that the front speed as it propagates accelerates. This behavior is due to the inherent inhomogeneity of the physical system.

3.1.9 Front propagation in inhomogeneous media

It is a fact that many populations develop in certain privileged physical places due to the facilitation of sources that allow their development. Later when population spreads these conditions change and make their propagation affected by the spatial change of the parameters. To illustrate this behavior, Figure 3.16 shows the spread of dengue

patients in Cambodia during 2002 and 2004. Clearly the patient population is spread by certain privileged areas which are mainly connected by urban roads (see green lines). To figure out how fronts spread in an inhomogeneous medium, let us consider the following inhomogeneous FKPP-equation.

$$\partial_t N = rN\,(1-N) + D\partial_{xx}N + \epsilon\rho(x)\partial_{xx}N, \tag{3.54}$$

where ϵ is a small parameter ($\epsilon \ll 1$) and $\rho(x)$ an arbitrary function. Then this model describes the evolution of a population with an inhomogeneous transport coefficients. Notice that this model does not modified the unpopulated stated ($N(x,t) = 1$). Using the following ansatz

$$N(x,t) = N_{FKPP}(z = x - vt - P(t)) + \epsilon W(z, P(t)), \tag{3.55}$$

in Eq. (3.66) and linearizing in W, one obtains

$$\mathcal{L}W = \dot{P}\partial_z N_{FKPP}(z) + \epsilon\rho(x)\partial_{xx}N_{FKPP}, \tag{3.56}$$

where the linear operator is defined $\mathcal{L} \equiv (r - 2N_{FKPP} + \partial_{zz} + v\partial_z)$. Using inner product (3.47), one can introduce the self-adjoint operator $\mathcal{L}^\dagger \equiv (r - 2N_{FKPP}(z) + \partial_{zz} - v\partial_z)$. Let $\Phi(z)$ is an element of the kernel of $\mathcal{L}^\dagger$, i.e. $\mathcal{L}^\dagger\Phi(z) = 0$. Figure 3.19b depicts the numerical kernel function $\Phi(z)$. To solve the above equation, one must impose the right side of the above equation is orthogonal to the kernel elements $\mathcal{L}^\dagger$ (solvability condition or Fredholm alternative [138]).

$$0 = \dot{P}\langle\Phi(z)|\partial_z N_{FKPP}\rangle + \epsilon\langle\Phi(z)|\rho(x = z + vt + P)\partial_{zz}N_{FKPP}\rangle. \tag{3.57}$$

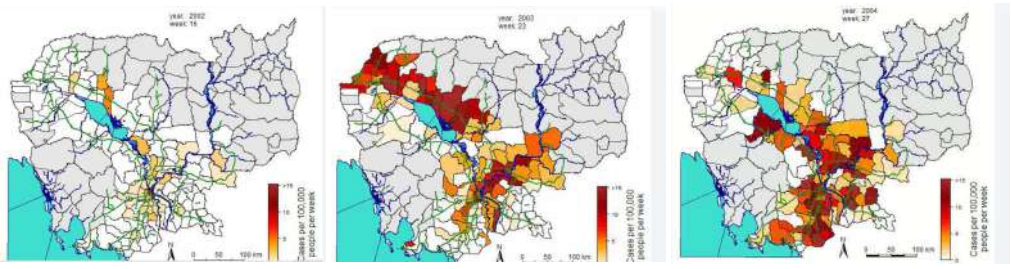

Figure 3.16: Spread of dengue patients in Cambodia during 2002 and 2004.

For simplicity we consider a periodic force $\rho(x) = \mu\cos(\omega x)$, thus the above equation reads

$$\dot{P} = \epsilon\mu\frac{\langle\Phi(z)|cos(\omega(z+vt+P))\partial_{zz}N_{FKPP}\rangle}{\langle\Phi(z)|\partial_z N_{FKPP}\rangle}. \tag{3.58}$$

Using trigonometric relation $\cos(\omega(z+vt+P)) = \cos(\omega z)\cos(\omega(vt+P)) - \sin(\omega z)\sin(\omega(vt+P))$, one get

$$\dot{P} = \epsilon\mu\left[K_1\cos(\omega(vt+P)) + K_2\sin(\omega(vt+P))\right]. \tag{3.59}$$

where,

$$K_1 = \frac{\langle\Phi(z)|\cos(\omega z)\partial_{zz}N_{FKPP}\rangle}{\langle\Phi(z)|\partial_z N_{FKPP}\rangle}, \qquad K_2 = -\frac{\langle\Phi(z)|\sin(\omega z)\partial_{zz}N_{FKPP}\rangle}{\langle\Phi(z)|\partial_z N_{FKPP}\rangle}. \tag{3.60}$$

It is important to note that all these integrals are well-defined. Hence, the front position satisfied an equation

$$\dot{P} = \Gamma\cos(\omega(vt+P)+\varphi), \tag{3.61}$$

with $\tan(\varphi) \equiv K_2/K_1$ and $\Gamma \equiv \epsilon\mu\sqrt{K_1^2+K_2^2}$. To integrate above equation, we introduce the change of variable $u = vt + P + \varphi$ and integrating

$$\int\frac{du}{v+\Gamma\cos(\omega u)} = (t-t_0). \tag{3.62}$$

The solution of this integral is

$$(t-t_0) = -\frac{2}{\sqrt{-v^2+\Gamma^2}\omega}arctanh\left[\frac{(v-\Gamma)\tan\left[\frac{u\omega}{2}\right]}{\sqrt{-v^2+\Gamma^2}}\right]. \tag{3.63}$$

rewriting the above expression

$$P(t) = -vt+\varphi-\frac{2}{\omega}\arctan\left(\frac{\sqrt{-v^2+\Gamma^2}}{v-\Gamma}\tanh\left[\frac{(t-t_0)\sqrt{-v^2+\Gamma^2}\omega}{2}\right]\right). \tag{3.64}$$

Thus, the front propagates with a periodical motion as consequences of the periodical inhomogeneity. Comparison of the above formula and direct numerical simulations of

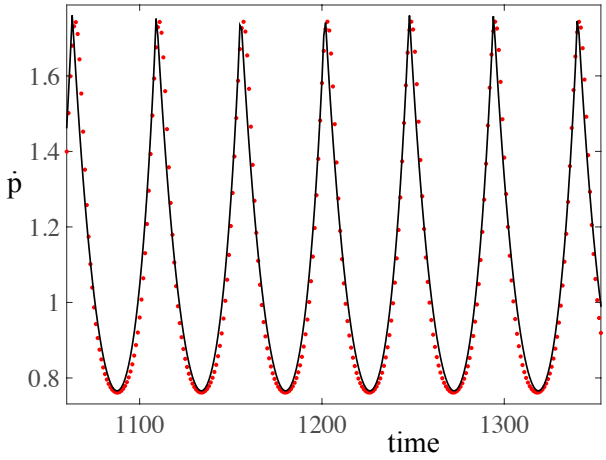

Figure 3.17: Comparison of the front speed from formula (3.64) and direct numerical simulations of Eq. (3.66) with a periodic inhomogeneity ($\rho(x) = \mu\cos(\omega x)$).

Eq. (3.66) with a periodic inhomogeneity ($\rho(x) = \mu\cos(\omega x)$) show quite good agreement (see Fig. 3.17).

Let us introduce the front position $x_0 \equiv vt + P(t)$, using Eq. (3.61) one gets

$$\dot{X}_0 = v + \Gamma\cos(\omega X_0 + \varphi) = -\frac{\partial U}{\partial x_0}. \tag{3.65}$$

This equation is known as Adler's equation and was proposed for the synchronization of

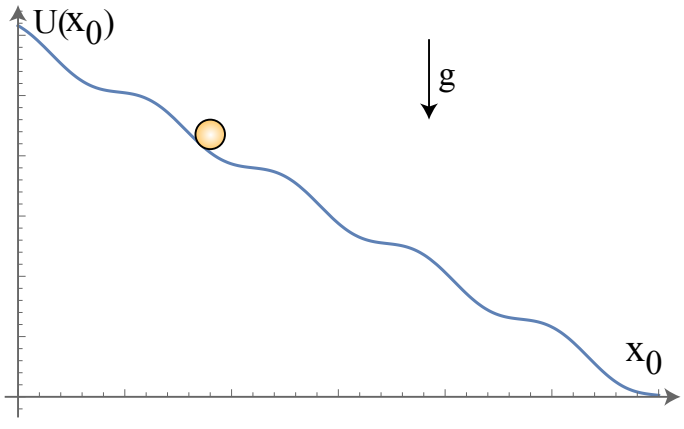

Figure 3.18: A mechanical interpretation of equation (3.65). Punctual particle in washboard potential.

electrical oscillators [2]. Note that this equation can be interpreted as an overdamped particle in a washboard potential $U(x_0)$, which is quite inclined ($v \gg \Gamma$). Figure 3.18 shows a schematic representation of punctual particles in washboard potential. Hence, when the particle propagates, it exhibits oscillatory behavior.

Liquid crystal light valve experiment

As we have mentioned before (section 3.1.8), the propagation of fronts in an optical valve with optical feedback exhibits a front speed that as it advances accelerates (cf. Fig. 3.20). The above phenomenon can be model close to the reorientation instability by

$$\partial_t \theta(x,t) = \epsilon\theta - \theta^3 + D\partial_{xx}\theta + \rho(x)\theta = -\frac{\partial U(\theta)}{\partial \theta} + D\partial_{xx}\theta + \rho(x)\theta, \tag{3.66}$$

where $\theta(x,t)$ accounts for the average angle of molecular orientation of the liquid crystal, ϵ is the bifurcation parameter which is proportional to the voltage minus the critical one and the geometry of the cell (see for more details Sec. 4.4), D accounts for the elastic coupling, $\rho(x)$ describes the inhomogeneities in the cell, and $U(\theta)$ is the potential (cf. Fig. 3.19). This model when ϵ is negative has a single stable equilibrium that corresponds to the molecules aligned with the walls ($\theta = 0$). Conversely, when ϵ is positive, the system exhibits two stable symmetric ($\theta = \pm\sqrt{\epsilon}$) and one unstable equilibrium cor-

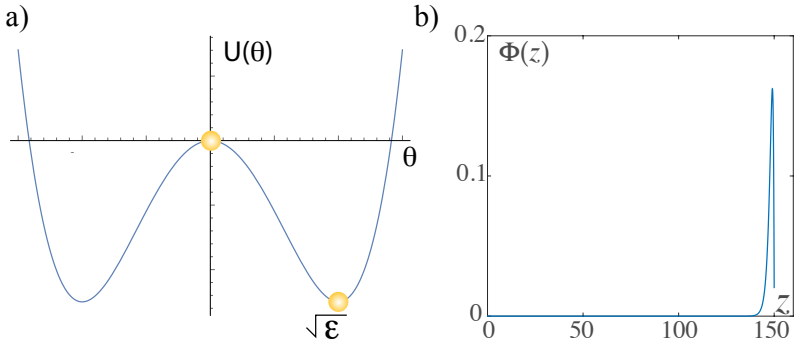

Figure 3.19: Liquid crystal model. (a) Effective potential close to reorientation instability. (b) Numerical kernel element of $\mathcal{L}^\dagger \equiv \epsilon - 2\theta_F^2 + \partial_{zz} + v\partial_z$, i.e. $\mathcal{L}^\dagger\Phi(z) = 0$.

responding to the reorientation and non-oriented of molecules, respectively. Figure 3.19 depicts the potential for positive ϵ. Likewise, for positive ϵ and $\rho(x) = 0$, the system presents fronts into an unstable state, between the oriented and non-oriented state, $\theta_F(x - vt)$. These fronts are characterized by being a family of solutions parameterized by the front speed $v \geq v_{min} \equiv 2\sqrt{\epsilon}$.

To understand the effect of the inhomogeneous term, one considers that this is of perturbative nature. Using the same methodology presented in the previous section one finds after straightforward calculations

$$\dot{P} = v + \frac{\langle \Phi(z)|\rho(z+p)\theta_F(z)\rangle}{\langle \Phi(z)|\partial_z\theta_F\rangle}, \tag{3.67}$$

where $\Phi(z)$ is an element of the kernel of $\mathcal{L}^\dagger \equiv \epsilon - 2\theta_F^2 + \partial_{zz} + v\partial_z$, i.e. $\mathcal{L}^\dagger\Phi(z) = 0$. Note that this eigenfunction diverges and converges, respectively, on the flank of the unstable and stable state (see Fig. 3.20b). In the case that $\rho(z)$ is a linear function, i.e. $\rho(z) = \beta z + \gamma$ ($\beta \sim \gamma \ll 1$), one gets

$$\dot{P} = v + \gamma' + \beta' P, \tag{3.68}$$

where $\beta' \equiv \beta\langle \Phi(z)|z\theta_F(z)\rangle / \langle \Phi(z)|\partial_z\theta_F\rangle$ and $\gamma' \equiv \gamma\langle \Phi(z)|\theta_F(z)\rangle / \langle \Phi(z)|\partial_z\theta_F\rangle$. The previous integrals are well defined since when $\Phi(z)$ diverges the front solution θ_F converges to zero with the same exponential rate. Furthermore, when $\Phi(z)$ solution tends to zero, the front solution θ_F is constant. Hence, these integrals depend on the size of the system. However, since the dynamics of the front position relies on the quotient of these integrals, one concludes that the result is independent of the size of the system. From this expression, one concludes that γ' renormalizes the front speed and that as the front moves the speed increases linearly with distance. The acceleration of the front speed is $\beta' v$. Indeed, experimentally the speed increases as the front propagate (cf. Fig. 3.20). Thanks to the use of a spatial light modulator (SLM, see Fig. 3.13), one can control the type of perturbations in the liquid crystal light valve with optical feedback. In the case of considering a periodical modulated one-dimensional mask, the dynamic of the front is characterized by a periodic movement, such as that of an overdamped particle

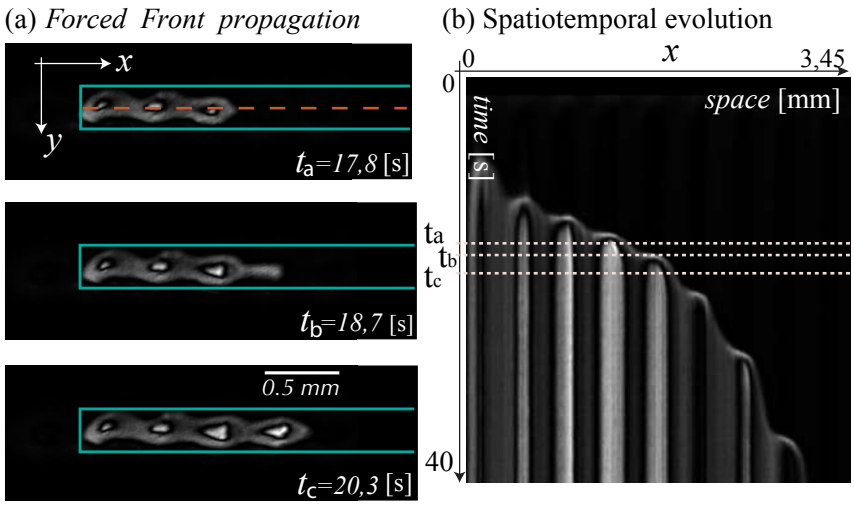

Figure 3.20: Experimental front propagation of liquid crystal light valve with optical feedback and periodic spatial forcing induced by spatial light modulator. Snapshots (a) and respective spatiotemporal diagrams (b) at $V_0 = 3.69$ $[V_{rms}]$. The left panels account for a temporal sequence of snapshots. The rectangle accounts for the illuminated area with optical feedback, and the dashed curve is the extracted region to obtain the spatiotemporal diagrams. The right panel stands for the spatiotemporal evolution of the fronts. The horizontal dashed lines account for the moments where the top snapshots are extracted [7].

in a washboard potential (cf. equation 3.65). Due to the presence of oscillatory force, the front propagates slower than in the unforced case.

3.1.10 Stochastic Populations dynamics

As mentioned macroscopic systems must be described by stochastic differential equations. This is usually accomplished by incorporating stochastic terms in the dynamics equation of the system understand, which are usually referred to as *Lagevine equation* [103, 75, 158, 89]. An additive stochastic term in the dynamical equation, it is usually called *additive* or *internal noise* and if the dependent on variables of the system under study is called *multiplicative* or *external noise*. Let us consider a population dynamics

with a logistic growth and an additive noise

$$\partial_t N = rN\,(1-N) + D\partial_{xx}N + \sqrt{\eta}\zeta(x,t), \tag{3.69}$$

where $\zeta(x,t)$ is a Gaussian white noise defined at each point x, with zero mean value $\langle\zeta(x,t)\rangle = 0$ and correlation $\langle\zeta(x,t)\zeta(x',t')\rangle = \delta(x-x')\delta(t-t')$, and η accounts for the level of intensity of noise [74]. This noise is called white because it is completely flat on its Fourier power transform. Figure 3.22 illustrates the mean features of Gaussian white noise. Likewise, one concludes that the stochastic term exhibits a complex spatiotemporal behavior. Numerical simulations of above population equations show this equation is unacceptable because it generates negative local population densities. Hence, additive white noise is unacceptable description for population dynamics.

Let us consider a population dynamics with logistic growth and simple linear multi-

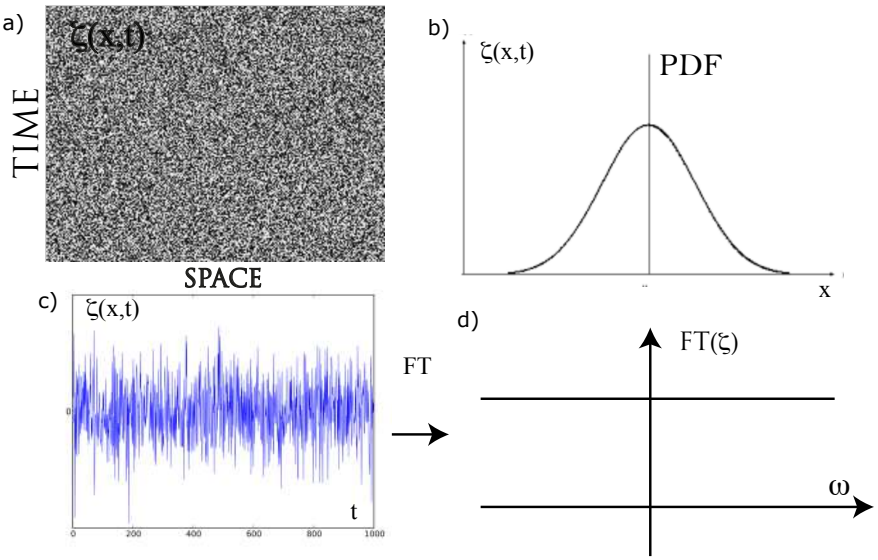

Figure 3.21: Gaussian white Noise. a) spatiotemporal evolution of the white noise $\zeta(x,t)$ with zero mean value $\langle\zeta(x,t)\rangle = 0$ and correlation $\langle\zeta(x,t)\zeta(x',t')\rangle = \delta(x-x')\delta(t-t')$. b) Probability density distribution (PDF) of $\zeta(x,t)$ at given time t. This PDF correspond to a Gaussian distribution. c) temporal signal of $\zeta(x,t)$ at given position. d) Schematic Fourier transform (FT) of the temporal signal.

plicative noise

$$\partial_t N = rN\left(1-N\right) + D\partial_{xx}N + N(x,t)\sqrt{\eta}\zeta(x,t), \tag{3.70}$$

then unpopulated state, $N = 0$, can not display fluctuations. It is important to note that if the initial population is positive this remains positive. This is simple to understand using the argument that if one linearized Eq. (3.78) around unpopulated state and neglected the inhomogeneties, the dynamics becomes linear

$$\partial_t N = \left[r + \sqrt{\eta}\zeta(t)\right] N. \tag{3.71}$$

Integrating this equation, one gets

$$N(t) = N_0 e^{rt + \int_0^t \zeta(t)dt} \tag{3.72}$$

Hence, independent, if the pre-factor is positive or negative initial condition increases or decreases exponentially, thus maintaining the property of being semi definite positive ($N_0 \geq 0$). To understand the front dynamics let us consider small intensity of noise ($\eta \ll 1$) and the ansatz

$$N(x,t) = N_{FKPP}(x - vt - P(t)) + w(x - vt, P), \tag{3.73}$$

in the stochastic FKPP equation (3.78) and performing a similar process of the previous section, after straightforward calculations, one obtains the solvability condition

$$\dot{P} = \sqrt{\eta}\frac{\langle\Phi(z)|\zeta(z,t)N_{FKKP}\rangle}{\langle\Phi(z)|\partial_z N_{FKKP}\rangle}. \tag{3.74}$$

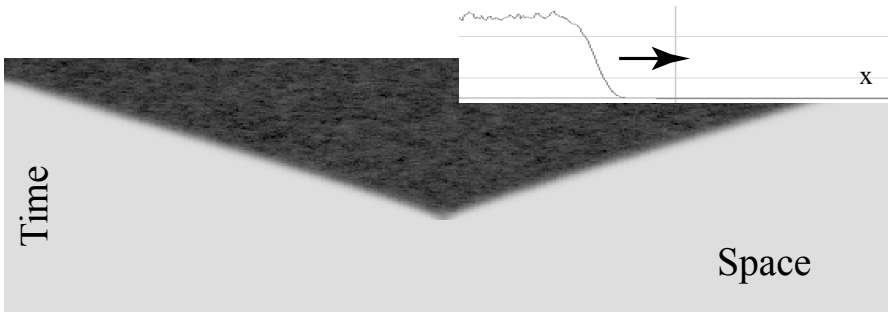

Figure 3.22: Stochastic FKPP front propagation using model (3.78). Inset accounts for the front profile in a given fixed time.

Using the central limit theorem, one can introduce an effective noise,

$$\xi(t) = \frac{\langle \Phi(z)|\zeta(z,t)N_{FKKP}\rangle}{\langle \Phi(z)|\partial_z N_{FKKP}\rangle}, \tag{3.75}$$

then the front position satisfies a Brownian dynamics, described by

$$\dot{P} = \sqrt{\eta}\xi(t). \tag{3.76}$$

where $\xi(t)$ is a white noise with zero mean value and correlation

$$\langle \xi(t)\xi(t')\rangle = \left|\left| \frac{\langle \Phi(z)|N_{FKKP}\rangle}{\langle \Phi(z)|\partial_z N_{FKKP}\rangle} \right|\right|^2 \delta(t-t'). \tag{3.77}$$

From the extended discrete system, model (3.10), using transition probability between the various constituents, one can obtain a suitable master equation for probability. From this master equation one can obtain the respective Lagevine equation [118]

$$\partial_t N = rN\left(1-N\right) + D\partial_{xx}N + N(x,t)\sqrt{r}\zeta(x,t), \tag{3.78}$$

Notice this model satisfies fluctuations dissipation theorem [158]. Hence, the above model is rigorous and consistence with the microscopic description.

3.2 Front solution in reactions dynamical systems

FKPP-fronts have been observed in pioneering work in auto-catalytic chemical reaction [110], Taylor-Couette instability [5], Rayleigh-Benard experiments [70], pearling and pinching on the propagating Rayleigh instability [136], spinodal decomposition in polymer mixtures [102], liquid crystal light valves with optical feedback [51, 7] and population dynamics [124, 125]. All these reports emphasize that this is a universal phenomenon that the only ingredients that need to be observed is the coexistence of a stable state, and one unstable [159].

3.2.1 Pushed and pulled fronts

A natural question that arises is, *why the speed of the fronts is determined by a linear analysis if fronts are intrinsically nonlinear phenomena?* To answer this question, we

consider FKPP Eq. (3.12) with an initially localized disturbance during an initial time and then impose the coefficient $D = 0$, that is; initially, populations are coupled and are subsequently isolated. Figure 3.23 clearly shows that the front continued spreading at an increasingly slower speed. This we can understand as follows: the Laplacian is responsible for an initial condition that penetrates all space by a Gaussian and then spreads from stable to unstable state. The above behavior leads us to conclude that the diffusive dynamic controls front propagation. The fronts whose minimum propagation speed is determined by this criterion are called *pulled fronts*. On the contrary, if the nonlinearity is large (strong nonlinearity), one expects that the minimum speed is no longer determined by the linear approach. The fronts whose minimum propagation speed is not determined by the linear or marginal criterion are called *pushed fronts* [159]. Figure 3.24 shows a schematic representation of a pulled and pushed front.
Let us consider the reaction-diffusion model

$$\partial_t u = f(u) + \partial_{xx} u, \tag{3.79}$$

where $u(x,t)$ is a scalar field and $f(u)$ is a smooth function. We assume that the system without loss of generality has two equilibria, one stable and another unstable in $u = 1$, and $u = 0$, respectively. Consequently, $f(0) = f(1) = 0$ and $f'(0) > 0$ and $f'(1) < 0$. Considering that the system is weakly nonlinear, that is, the most important

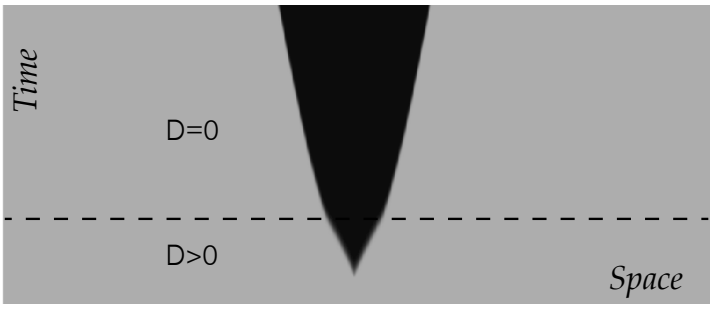

Figure 3.23: Front propagations of FKPP Eq. (3.12) with an initial localized disturbance during an initial time and then impose the coefficient $D = 0$. Dashed straight line accounts for the moment when there is interrupted coupling.

growth rate is given by the linearization around the unstable state, then $f'(0)u \geq f(u)$. Figure 3.25 shows a typical weakly nonlinear reaction term. Therefore, to use the linear criterion for the front speed, we need to impose the condition $f'(0)u \geq f(u)$, which had beed stablished by Kolmogorov and co-workers [97]. By simple dimension analysis the minimum front speed, v_{min}, satisfies [27]

$$2\sqrt{f'(0)} \leq v_{min} \leq 2\sqrt{\frac{f(u)}{u}}. \tag{3.80}$$

Hence, for dynamical system with weak nonlinearity one has $2\sqrt{f'(0)} \geq 2\sqrt{f(u)/u}$ and minimum front speed is $v_{min} = 2\sqrt{f'(0)}$. A natural example of weak nonlinearity is the coupled chain of pendulums, Eq. (2.7), where the fronts connecting the upright and upside-down position of pendulums are FKPP fronts with marginal criterion (cf. Fig. 2.7).

To figure out the transition from pulled to pushed front, let us consider the following nonlinear reaction-diffusion equation with cubic nonlinearity (bistable model) [82]

$$\partial_t N = N(1-N)(1+aN) + \partial_{xx} N. \tag{3.81}$$

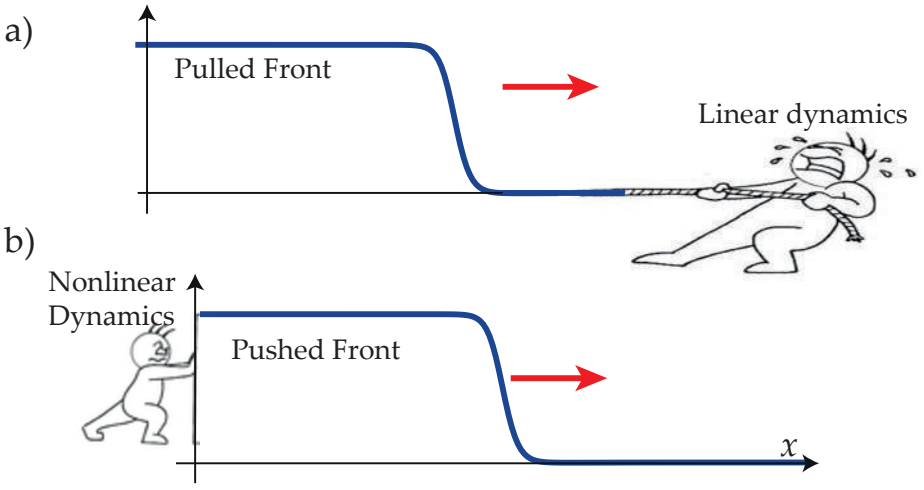

Figure 3.24: Schematic representation of a pulled and pushed front. The minimum speed of pulled (pushed) fronts is (not) determined by the linear marginal criterium.

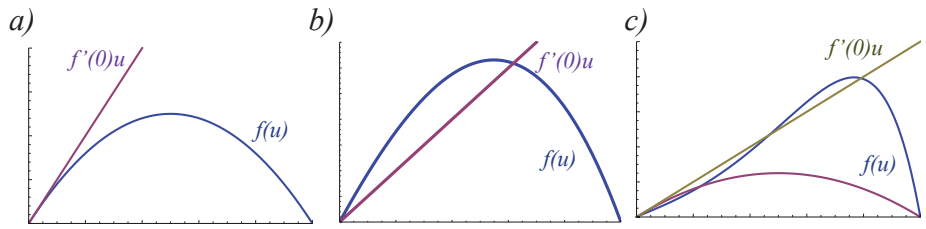

Figure 3.25: Different reaction terms. a) weak nonlinearity, b) and c) strong nonlinearity.

Note that for $a < 0$, the above model accounts for the Nagumo model [124], which describes several biological systems. The uniform solutions of this model are $N = \{0, 1, -1/a\}$. The two first solutions correspond to populated and unpopulated states. $N = -1/a$ makes no sense from the viewpoint of density populations. The population and unpopulated state are stable and unstable, respectively. For $a \leq a_{\equiv}1$, the dynamical behavior of this model is characterized by being ruled by weak dynamics. That is, the minimal front speed between unpopulated and populated states is regulated by linear marginal criteria. The front speed has the form

$$v = \begin{cases} 2, & -1 \leq a \leq 2, \\ \frac{a+2}{\sqrt{2a}}, & a > 2. \end{cases} \tag{3.82}$$

This result was obtained by explicitly find the front solution [82]. In order to derive this speed and the front profile, we consider the solution in the mobile system $N(x,t) = N(z \equiv x - vt)$, thus, the above equation (3.81) reads

$$-v\partial_z N = N(1-N)(1+aN) + \partial_{zz}N, \tag{3.83}$$

where $z = x - t$ is the co-moving coordinate. The front solution satisfies $N(z \to -\infty) = 1$ and $N(z \to \infty) = 0$, introducing the auxiliary function $G[N(z)] = \partial_z N$, the equation takes the form

$$G\frac{\partial G}{\partial N} + vG + N(1-N)(1+aN) = 0. \tag{3.84}$$

This auxiliary function fulfills $G[0] = G[1] = 0$. In addition, if one considers that the solutions decay exponentially $N(z) \sim e^{-\beta z}$ ($G \sim e^{-\beta z}$). Hence, introducing the

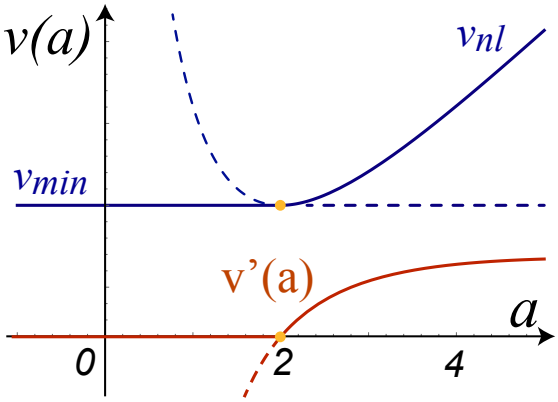

Figure 3.26: Pulled-pushed front transition of model Eq. (3.81). The horizontal blue curves account for the speed using the linear criterion (v_{min}), The continuous curve accounts for the front with minimum speed. The dashed curve accounts for a front that is spread with a speed greater than the minimum speed. $v'(a) = \partial_a v$ accounts for the variation of front speed as a function of parameter a.

algebraic ansatz $G = \beta N(N-1)$ in Eq. (3.84), one obtain for the different power of N

$$\begin{aligned} 2\beta^2 - a &= 0, \\ -3\beta^2 + v\beta + (a-1) &= 0, \\ \beta^2 - v\beta + 1 &= 0. \end{aligned}$$

From the first relation one obtains $\beta = \sqrt{a/2}$ and for the other relations $v = v_{Nl} \equiv (a+2)/\sqrt{2a}$. Likewise, the front profile satisfies (the Riccati equation [142] or logistic equation [161])

$$\frac{\partial N}{\partial z} = \beta N(N-1), \tag{3.85}$$

which has a solution of the form

$$N(x,t) = \frac{1}{1+e^{\beta z}} = \frac{1}{1+e^{\beta(x-v_{NL}t)}}. \tag{3.86}$$

Figure 3.26 shows the front speed as a function of the parameter a. Note that for parameter a lower (greater) than 2, the system exhibits pulled (pushed) fronts. Indeed, the system exhibits a pulled-pushed front transition for $a = a_T = 2$. To characterize the nature of this transition, one can consider the front speed as an order parameter.

We note that when the fronts are pulled (pushed), this order parameter is null (varies). From the previous graphs, one infers that the transition is supercritical (continuous). In addition, this transition corresponds to a collision between stable and unstable front solutions that exchange stability. This type of bifurcations are denominated in the theory of transitions as transcritical bifurcations [150]. In the next section, we shall study a physical example that has pulled and pushed fronts.

3.2.2 Nematic-isotropic transition: pushed front

The nematic-isotropic transition is a classic problem of the theory of liquid crystals, in which the nematic phase is characterized by the rod like molecules are oriented locally in one direction, unlike the isotropic liquid phase which is characterized by the molecules are locally disordered [163, 41, 62]. Figure 3.27 shows a typical structure of liquid crystal molecules containing several coupled cycles benzenes. The interaction between molecules (electric and magnetic) and temperature allow the formation of different phases, such as: *crystalline solid, liquid crystal* and *isotropic liquid*. Figure 3.27b schematically illustrates these phases. Therefore, as a function of temperature T one

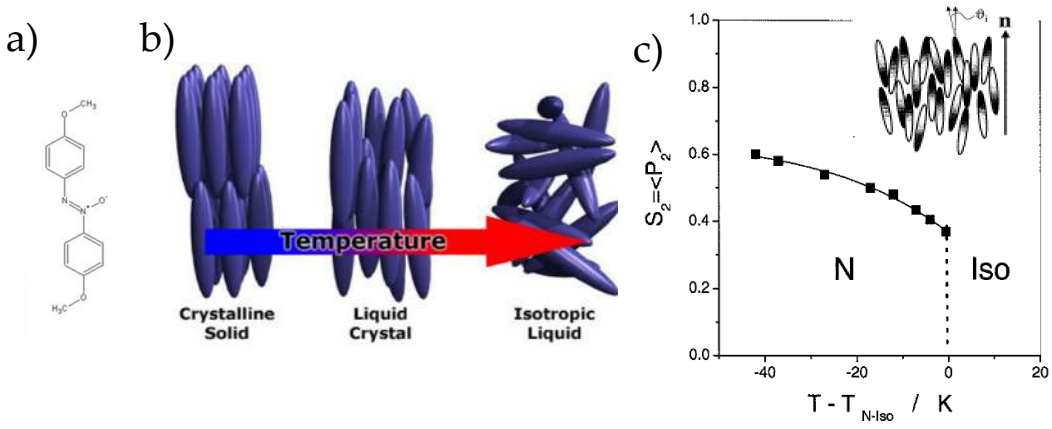

Figure 3.27: Liquid Crystals state of matter. a) Typical molecule of liquid crystal with rod-like structures. b) Schematic representation of different phases of rod-like molecules as a function of temperature. c) Bifurcation diagram of a liquid crystal [?].

expects to observe this transition, that is, there is a critical temperature T_c at which one observes the emergence of a phase on the other. T_c typically ranges from a few to hundreds celsius. Due to the molecules have a preferred direction but not a sense, this transition is characterized by a second rank tensor [163, 41, 62]. This tensor is a symmetric matrix with zero trace, characterized by a single scalar parameter

$$S(\vec{r},t) = \frac{3}{2}\langle \cos^2(\theta)\rangle - \frac{1}{2}, \tag{3.87}$$

which is an order parameter[1] that accounts for the alignment of the molecules and θ is an angle with respect to a direction must be oriented the molecules (cf. Fig. 3.27). Then, when S is small (order one) accounts for the isotropic liquid (nematic) phase.

The dynamic of the order parameter is characterized by the free energy (Landau-de Gennes theory) [163, 41, 62]

$$\mathcal{F}[\mathcal{S},\nabla\mathcal{S}] = \frac{A}{2}S^2 - \frac{B}{2}S^3 + \frac{1}{2}S^4 + \frac{(\nabla S)^2}{2}, \tag{3.88}$$

where $\{A, B\}$ are phenomenological positive parameters. It is worthy to note that due to S accounts for an orientation, the free energy $\mathcal{F}$ does not depend linearly in S [62]. Usually A parameter is proportional to difference of the temperature with the critical one ($A \propto T - T_c$) [163, 41, 62], this is the bifurcation parameter.

The temporal evolution of S is characterized by the minimization of the free energy, that is

$$\frac{\partial S}{\partial t} = -\frac{\delta \mathcal{F}}{\delta S} = -AS + BS^2 - S^3 + \nabla^2 S. \tag{3.89}$$

From the standpoint of dynamic system, this model describes an extended transcritical bifurcation [59]. This model has the steady states $S = S_I = 0$ and $S \equiv S_M = (B \pm \sqrt{B^2 - 4A})/2$ that accounts, respectively, for the isotropic liquid and nematic phase. For large values of the bifurcation parameter ($A \gg 1$), the only supported state is the isotropic liquid phase, S_I. When the bifurcation parameter is diminished to zero ($A = 0$), the isotropic state becomes unstable by a discontinuous bifurcation (first order transition or subcritical bifurcation [150]), that is, this bifurcation generates

[1] An order parameter is the simplest variable characterizing the dynamics of a bifurcation[100].

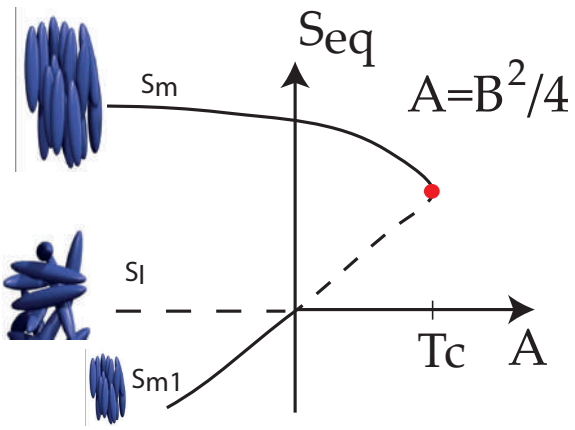

Figure 3.28: Bifurcation diagram of nematic isotropic transition described by model (3.89). The A parameter accounts for temperature. T_c is the critical temperature from which the system exhibits coexistence between the nematic (S_m and S_{m1}) and isotropic liquid phase (S_I).

an abrupt change of equilibria. This bifurcation generates the emergence of nematic phase, S_M. This phase has a region of hysteresis (coexistence) with isotropic state between $A = 0$ to $A = B^2/4$. For negative A the stable state are nematic phases (S_m and S_{m1}). Moreover, for $A < 0$ the isotropic liquid phase is unstable. Figure 3.28 shows a bifurcation diagram of isotropic nematic transition described by model (3.89). Hence, in this region of parameter one can observe FKPP front between the nematic and isotropic liquid phase. Figure 3.29 displays the typical front propagation for $A < 0$ and experimental observation of nematic isotropic transition induced by light [130].

Front propagation in nematic isotropic transition

For the sake of simplicity, we consider a one-dimensional liquid crystal medium described by (Landau-De Gennes Model)

$$\frac{\partial S(x,t)}{\partial t} = -AS + BS^2 - S^3 + \partial_{xx}S. \tag{3.90}$$

Let us consider a nonlinear traveling wave solution for the other parameter $S(x,t) = S(z = x - vt)$, which satisfies

$$-v\partial_z S = -AS + BS^2 - S^3 + \partial_{xx}S. \tag{3.91}$$

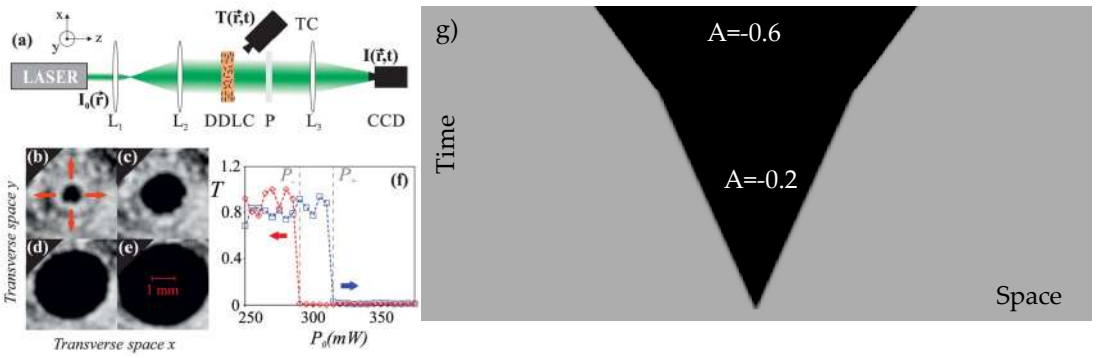

Figure 3.29: Isotropic nematic front propagation. a) Schematic sketch of the experimental setup. L1 and L2 are plano-convex lenses; DDLC corresponds to a dye-doped liquid crystal cell; P is a polarizer along x-axis; L3 is an imaging lens; TC accounts for an infrared thermal camera; CCD is a charge-coupled device camera. (b)-(e) Experimental smoothed snapshots for P0 350 mW and w 3.4 mm (I0 1.93W/cm2) at 55, 65, 125, and 500 s, respectively. (f) Sample transmissivity T as a function of the input power. Panels retrieved from Ref. [130]. g) Spatiotemporal diagram of numerical simulation of nematic isotropic model (3.89) for two differ values of A=-0.2,-0,6 and $B = 1.0$.

Introducing the ansatz

$$S = \frac{\alpha}{2}\left[1 + \tanh(\beta z)\right], \tag{3.92}$$

in the above equation one gets

$$\begin{aligned} 0 &= -\frac{1}{8}\alpha\left(1+\tanh[z\beta]\right)\left\{4A - 2B\alpha + \alpha^2 - 4v\beta + \right. \\ &\left. 2\left(-B\alpha + \alpha^2 + 2\beta(v+2\beta)\right)\tanh[z\beta] + \left(\alpha^2 - 8\beta^2\right)\tanh[z\beta]^2\right\} \end{aligned} \tag{3.93}$$

or equivalently

$$0 = 4A - 2B\alpha + \alpha^2 - 4v\beta + 2\left(-B\alpha + \alpha^2 + 2\beta(v+2\beta)\right)\tanh[z\beta] + \left(\alpha^2 - 8\beta^2\right)\tanh[z\beta]^2 \tag{3.94}$$

from the term proportional to $\tanh^2(\beta z)$, one obtains $\beta = \alpha/2\sqrt{2}$. Using this property in term proportional to $\tanh(\beta z)$, one gets

$$-2\beta v = -B\alpha + \alpha^2 + 4\beta^2 \tag{3.95}$$

$$0 = 4A - 2B\alpha + \alpha^2 - 4v\beta \tag{3.96}$$

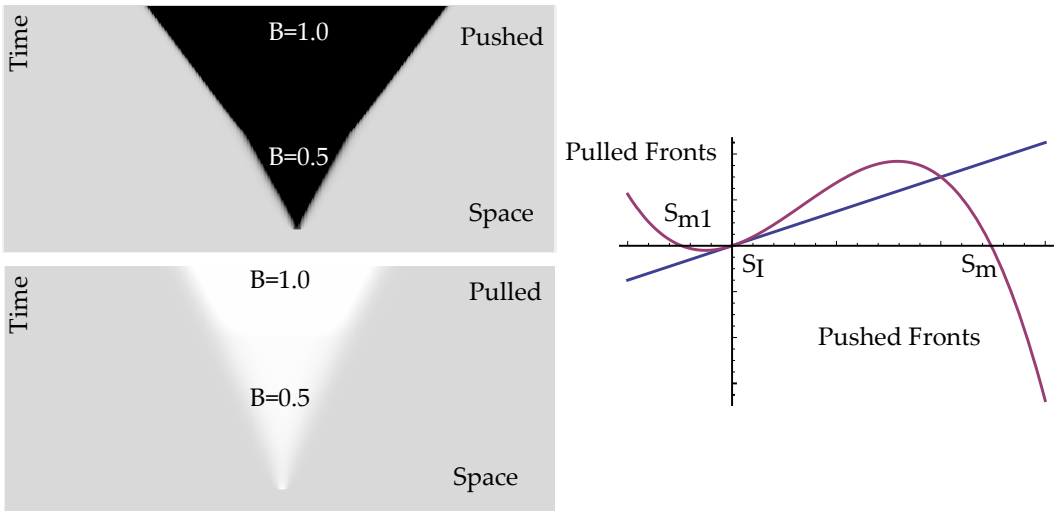

Figure 3.30: Front propagation of model (3.90). For negative A, the model has three equilibria: two stable (S_m and S_{m1}) and one unstable (S_I). The top left panel shows a pushed front between S_m and S_I, when B parameter is modified. The bottom left panel shows a pulled front between S_{m1} and S_I, when B parameter is modified. The right panel characterizes the dynamics of the model (3.90).

Using Eq. 3.95 in 3.96, one gets $A - B\alpha + \alpha^2 = 0$ and then $\alpha = (B + \sqrt{B^2 - 4A})/2$ and the front speed

$$v = \frac{A - 4\beta}{2\beta} \tag{3.97}$$

with $\beta = B + \sqrt{B^2 - 4A}/4\sqrt{2}$.

We must use the criterion to characterize whether fronts between nematic to isotropic liquid transition are pulled or pushed (3.80). Thus, we have to compare the functions $f(S) = -AS + BS^2 - S^3$ with $f'(0)S = AS$ in the interval $[0, (B + \sqrt{B^2 - 4A})/2]$. Imposing these two functions are equal, one finds the point of interception $S^* = B$, which is inside the interval of interest. Hence, fronts exhibited by the nematic isotropic transition between phase S_I and S_m are of a pushed nature. Likewise, the above analysis is valid for the nematic state S_{m1} and isotropic liquid S_I, then, applying the Kolmogorov criterion, one finds that these fronts are marginal type.

Note that the speed (3.97) is a function of the parameters A and B. By setting B, one

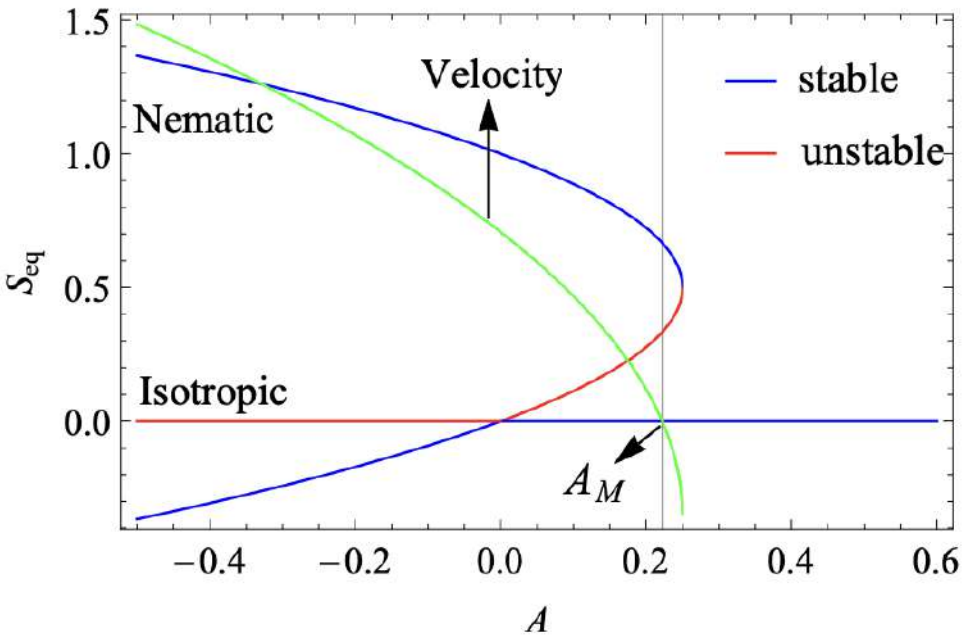

Figure 3.31: Front speed v, formula (3.97), as a function of the bifurcation parameter A (green curve).

can plot the speed $v(A, B)$ as a function of the bifurcation parameter and can compare it with the bifurcation diagram. Figure 3.31 shows the speed as a function of the bifurcation parameter. For $A < 0$, the front accounts for a nonlinear wave that connects a stable and unstable state, continuously connecting with the region of bistable fronts. The previous behavior manifests that pushed-type fronts can continuously connect with bistable fronts.

3.3 Variational characterization of front speed

As we have already noted, dynamical systems with strong nonlinearities exhibit fronts between stable and unstable states, for which the determination of front speed is a complex task. One method that has been proposed to determine the speed is based on the principle of variations [27]. To understand how one gets this method, let us consider

Eq. (3.6) for front speed

$$-v\partial_z u = f(u) + \partial_{zz} u, \tag{3.98}$$

where $f(0) = f(1) = 0$ and $f'(0) > 0$ and $f'(1) < 0$. Introducing the variable $P(u) = -\partial_z u$ that corresponds to a momentum type variable. Thus, the above equation reads

$$0 = f(u) - vP + P\frac{\partial P}{\partial u}. \tag{3.99}$$

Considering a positive define function $g(u) > 0$ and $-g'(u) > 0$ in interval $[0, 1]$, multiplying by g/P and integrating between the equilibria, one obtains

$$v = \frac{\int_0^1 \frac{f(u)g(u)}{P} - g'(u)Pdz}{\int_0^1 g(u)dz}. \tag{3.100}$$

One considers positive definite functions so that the divisor is well-defined. Furthermore, using

$$\frac{f(u)g(u)}{P} - g'(u)P \leq 2\sqrt{-fgg'}, \tag{3.101}$$

one obtains the front speed [27]

$$v = 2Sup\left(\frac{\int_0^1 \sqrt{-fgg'}dz}{\int_0^1 g(u)dz}\right). \tag{3.102}$$

Hence, using a function test $g(u)$, one can obtain adequate speed [27].

3.4 Experimental observation of pulled pushed front transitions

The analysis and study presented in this section are based on article [15].

As we have mentioned, the FKPP front solutions are peculiar to connecting a stable state with an unstable one. The propagation speed of these fronts depends on the initial conditions. When the disturbance of the unstable state is bounded, the fronts always propagate with a minimal speed [159]. In liquid crystals, these fronts have been the

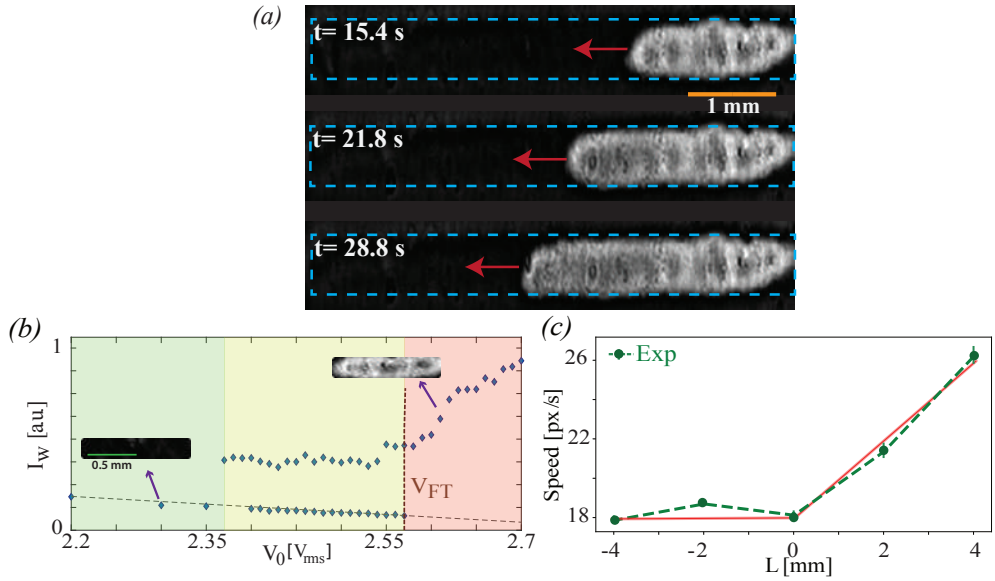

Figure 3.32: Experimental characterization of the bifurcation diagram and the front propagation transition. (a) Temporal snapshot sequence of the front propagation showed in the LCLV. Dark and light areas account for different molecular orientations, respectively. The dashed rectangles mark the illuminated region. (b) A bifurcation diagram was observed in the LCLV with optical feedback. The points account for the intensity of the reflected light by the LCLV as a function of the applied voltage V_0. The system exhibits three regions, two monostable and one bistable between the planar and reorienting state. V_{FT} accounts for the critical value of the reorientation instability, *the Fréedericksz transition*. The insets stand for respective snapshots obtained in the indicated voltages. (c) Front speed as a function of diffraction length L at $V_0 = 2.62V_{rms}$. The points account for the front speed measured in pixels per second. The dashed line is the union between consecutive experimental points. The continuous curve stands for the trend line of the experimental points.

subject of intense research [13, 52, 51, 87, 88, 141, 140], since they play a fundamental role in understanding and applying molecular reorientations through light.

Theoretically, the interface dynamical behaviors are well understood by variational systems. In contrast, nonvariational systems do not pursue a minimization of free energy. Indeed, front propagation into an unstable state does not follow a minimization principle, and its dynamics are less explored. However, front propagation between two stable states in nonvariational systems has been analyzed in [13] (see Section 4.7). The

non-variationality is a generic characteristic of nonequilibrium systems [129, 84].
To understand the effect of non-variational terms, we consider the effect of diffraction in the front propagation between two domains of molecular orientations in a liquid crystal light valve with optical feedback (see Section 3.1.8). The diffraction produced by the free propagation length L governs the nonvariational effects. Depending on diffraction, front speed exhibits a supercritical transition between pulled and pushed fronts.

Experimental characterization of front propagation into an unstable state

Thanks to the use of the spatial light modulator, a bi-dimensional channel is illuminated on the liquid crystal light valve of dimensions 6 mm long by 0.9 mm wide (cf. Fig. 3.32(a)). By changing the voltage V_0 applied to the liquid crystal film and monitoring the evolution of light intensity that goes through the LCLV employing a CCD camera (the camera measures the I_w intensity), one can characterize the bifurcation diagram of the molecular reorientation transition. Figure 3.32(a) shows the bifurcation diagram obtained. For small voltage $V_0 < V_{FT}$, when the molecules are not reoriented, a little light is transmitted in the optical feedback, which corresponds to the channel being dark [see inset in Fig. 3.32(a)]. The critical voltage from which the molecules begin to reorient is designated by V_{FT}. On the contrary, when the molecules are reoriented, the transmitted light increases, and then the channel turns light gray. Note that the transition of molecular reorientation of the LCLV with optical feedback is of the first order type [52, 51]. Indeed, the transition exhibits an abrupt color change. Besides, a hysteresis loop is observed between the molecular configurations when the voltage varies. The hysteresis region is between the two monostable regions.
We follow the strategy to study the front propagation into an unstable state: initially applied voltage is small ($V_0 \ll V_{FT}$). Hence, the initial configuration is planar, and it is stable. Subsequently, the applied voltage is increased above a critical value of reorientation bifurcation ($V_0 = 2.62V_{rms} > V_{FT}$ and $V_0 \approx V_{FT}$). Then, the planar state becomes unstable (dark state), and the reoriented alignment becomes stable (gray state). The reoriented state starts to invade the planar alignment from the edges or imperfections

of the channel. Figure 3.32(a) shows a sequence of snapshots of the observed front propagation. From the recording of the front propagation, its speed is determined. Subsequently, by changing the position of the optical fibers bundle, we can change the value of the free propagation length L, which is the distance where light diffraction occurs in the experimental setup. Figure 3.32(c) shows the front speed as a function of the free propagation length L at fixed applied voltage V_0. Unexpectedly, it is observed that the front speed is modified slightly for small and negative L (pulled fronts), but for L positive, this speed increases and is significantly modified (pushed fronts). Therefore, experimentally, it is observed that the front speed transitions between a plateau and a growing regime correspond to a *pushed-pulled transition*. It is worth noting that L does not change the relative stability between the molecular configurations but instead changes the coupling between the molecular average arrangements. The origin of the front propagation transition will be elucidated in the next section.

3.4.1 Theoretical model of pulled-pushed fronts in the LCLV with optical feedback

Based on the elastic theory, dielectric effects, and optical feedback, close to the Fréedericksz transition V_{FT}, the molecular reorientation is given by the dimensionless model [52, 51, 13]

$$\partial_t u = \mu u + \beta u^2 + u^3 - u^5 + \partial_{xx} u + bu\partial_{xx} u + c(\partial_x u)^2, \tag{3.103}$$

where x and t account for the spatial transverse coordinate and time. The order parameter $u(x,t)$ is the amplitude of the critical mode of the molecular reorientation. μ is the bifurcation parameter that accounts for the competition between the electric and elastic force, which is proportional to $(V_0 - V_{FT})/V_{FT}$. β is a phenomenological parameter that accounts for the pretilt induced by the anchoring in the walls of the liquid crystal layer. The cubic and quintic terms represent the competition between elastic and electrical forces induced by optical feedback [51]. The diffusion term $\partial_{xx} u$ describes the transverse elastic coupling. The coefficients b and c account for the nonlinear dif-

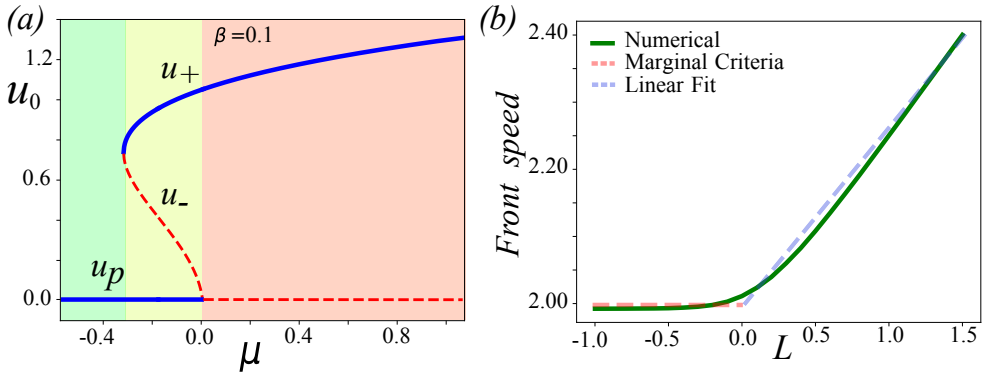

Figure 3.33: (After [15]) Characterization of bifurcation diagram and front speed of model Eq. (3.103). (a) Bifurcation diagram of Eq. (3.103). Equilibrium amplitude u_o as a function of the parameter μ for fixed β. The continuous and dashed curves account for stable and unstable equilibrium, respectively. These curves were obtained by solving the algebraic equation $0 = \mu u_0 + \beta u_0^2 + u_0^3 - u_0^5$; u_p, u_-, and u_p account for the upper, middle, and lower equilibrium branches, respectively. The system exhibits three regions, two monostable and one bistable. (b) Front speed as a function of free propagation length L. The continuous curve shows the front speed of model Eq. (3.103) obtained numerically with $\mu = 1.0$, $\beta = 0.1$, and $b = c = L$. The dashed horizontal curve accounts for the minimal front speed using the marginal criterion $v_{min} = 2\sqrt{\mu}$.

fusion and advection. These two terms are proportional to the free propagation length L and have the same sign. Indeed, when $L = 0$, $b = c = 0$, the previous model (3.103) satisfies an equation that is governed by the minimization of free energy $\mathcal{F}[u, \partial_x u]$, that is,

$$\partial_t u = -\frac{\partial \mathcal{F}}{\partial u}, \tag{3.104}$$

where $\mathcal{F} = \int dx[-\mu u^2/2 - \beta u^3/3 - u^4/4 + u^6/6 + (\partial_x u)^2/2]$. The diffraction effect generates that diffusion and the nonlinear advection allow the emergence of permanent dynamics, such as spatiotemporal chaos [46] or oscillatory behaviors [47]. This type of behavior is incompatible with a dynamic governed by a minimization principle. The methodology of how to derive the parameters $\{\mu, \beta, b, c\}$ and the relation with the physical parameters are given in Refs. [51, 13].

The term proportional to β breaks the reflection symmetry of the amplitude u. This

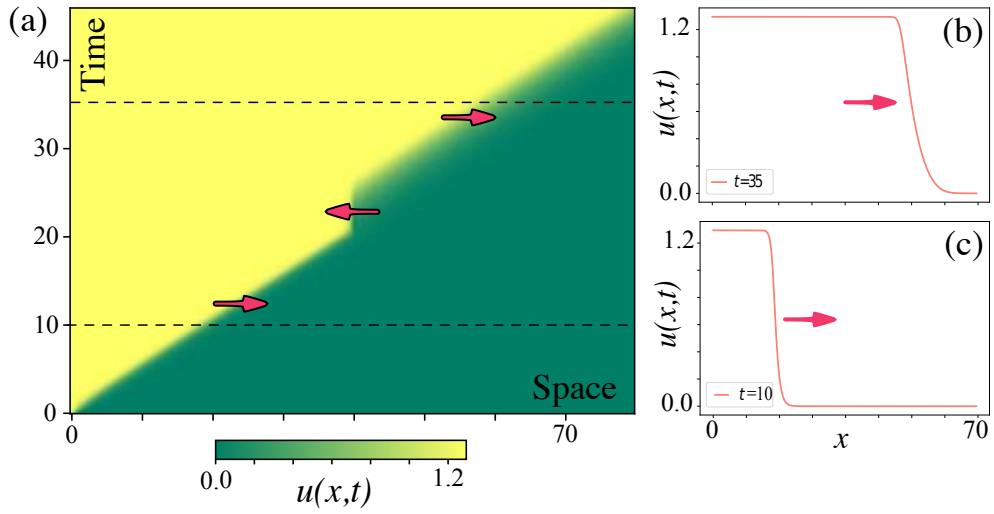

Figure 3.34: (After [15]) Front propagation into an unstable state of model Eq. (3.103). (a) Spatiotemporal evolution of amplitude of critical model $u(x,t)$ of model Eq. (3.103) by $\mu = 1.0$, $\beta = 0.1$, and $b = 0$. Temporal evolution of the front propagation after ($c = 0$, $t < 20$) and before ($c = -30$, $t > 20$) consider the nonvariational advection term. The arrows show the direction of front propagation in the respective periods.

effect always renders the reorientation transition into a discontinuous instability with a small hysteresis. Note that positive and negative equilibria exist for $\beta, \mu > 0$. Besides, the negative values of the amplitude $u(x,t)$ have no physical sense because it is not detectable experimentally. Figure 3.33 shows the bifurcation diagram of model Eq. (3.103). This model is characterized by exhibiting a first-order bifurcation when $\mu = 0$. Then, the system presents a hysteresis region between two monostable regions. Note that this bifurcation diagram is qualitatively similar to that observed experimentally (cf. Fig. 3.32(a)).

An ideal region to study fronts into an unstable state is $\mu > 0$. The model equation presents the FKPP front between $u \equiv u_p = 0$ and u_+, Namely, in this region of parameter space, there are fronts between the planar unstable u_p and stable reoriented state u_+. Figure 3.34 shows the front propagation for $\mu > 0$. To study the effects of nonvariational terms, we consider a front solution initially with $b = c = 0$, and at a

given time ($t = 20$), we activate the nonvariational effects ($b = 0$ and $c = -30$). In the variational regime, the minimal front speed v_{min} is determined by the linear terms, *marginal criterion* [159], which has the explicit expression $v_{min} = 2\sqrt{\mu}$. Indeed, if the values of the nonlinear parameters are changed, the front speed does not change. From Fig. 3.34, one can infer that the front profile is modified when the nonvariational terms are included. The front solution exhibited a readjusting of the spatial profile where the front suffered a backpropagation. After this readjust, the front solution acquires a form with which it spreads with the marginal speed. Figure 3.34 depicts the front profiles without and with the influence of non-variational terms. Unexpectedly, although the front profile is markedly modified, the front speed remains constant.

To analyze how the front speed is modified as a function of the non-variational terms, we have numerically measured the front speed as a function of $b = c = L$. This is consistent with the functional dependence of the parameters as a function of the free propagation length L. Figure 3.33(b) summarizes the front speed as a function of the free propagation length L. We observe that the front speed is constant for free negative propagation lengths. As it increases the numerical precision, it tends to the front speed predicted by the marginal criterion (see Fig. 3.33(b)). It is well-known that numerical discretization effects modify this speed [10]. For free positive propagation lengths, we observed that the speed of the front grows linearly with L. Hence, we observe that the front speed presents a transition between a plateau and a growing regime, which is consistent with experimental observations (cf. Figs. 3.32(b) and 3.33(b)). Indeed, the system exhibits a transition between fronts where its speed is determined by the marginal criterion (pulled front [159]) to fronts where the nonlinear terms determine the speed, nonlinear criterion (pushed front [159]). A pulled-pushed transition of fronts, with a speed transition diagram similar to that shown in Fig. 3.33(b), is well-known in a cubic reaction-diffusion model when the nonlinear terms are modified [82]. A perturbative analysis can be performed to determine how the presence of the nonvariational terms modifies the front speed.

3.4.2 Analytical and Numerical analysis of the front speed

Due to the transition between pulled-pushed fronts occurring at free propagation length $L = 0$, we can consider the nonlinear diffusion and advection terms as perturbative ones ($b, c \ll 1$). Let us consider $u_f(x - v_0 t)$ as the front solution for the unperturbed problem of Eq. (3.103) with $b = c = 0$, where $v_0 = 2\sqrt{\mu}$ is the front speed. To calculate the front speed for the perturbed problem, we consider the following ansatz,

$$u(x,t) = u_f\left(z \equiv x - v_0 t - \dot{P}(t)\right) + w(x - v_0 t - p(t)), \tag{3.105}$$

where z is the coordinate in the co-moving system, $\dot{P}$ and w account for the correction of the front speed and the profile function, respectively. Moreover, $\dot{P}$ and w are of order of $b \sim c \sim \epsilon$, where $\epsilon \ll 1$ is a small control parameter. Introducing the ansatz (3.105) in Eq. (3.103) and leaving only the terms up to ϵ order, after straightforward calculations, we get the linear equation

$$\mathcal{L}w = -\dot{p}(t)\partial_z u_f - b u_f \partial_{zz} u_f - c(\partial_z u_f)^2, \tag{3.106}$$

where the linear operator has the form $\mathcal{L} \equiv [\mu + 2\beta u_f + 3u_f^2 - 5u_f^4 + v\partial_z + \partial_{zz}]$. To solve this linear equation, we use the Fredholm alternative or solvability condition [73] and obtain

$$\dot{p}(t) = v_{nv} \equiv -b\frac{\langle\phi|u_f\partial_{zz}u_f\rangle}{\langle\phi|\partial_z u_f\rangle} - c\frac{\langle\phi|(\partial_z u_f)^2\rangle}{\langle\phi|\partial_z u_f\rangle}, \tag{3.107}$$

where the symbol $\langle f|g\rangle \equiv \int_{-\infty}^{\infty} f(z)g(z)dz$ and the function $\phi(z)$ belong to the kernel of the adjoint operator of $\mathcal{L}$, which is independent of diffraction effect. The ϕ function is only accessible numerically. As a matter of fact, the correction of the front speed of nonvariational origin is proportional to the free propagation length L. When $L > 0$ (L<0), the previous integrals are negative (positive), and then v_{nv} is positive (negative). Hence, the front speed has two contributions, one of variational origin given by the linear criterion and another nonlinear one given by the nonvariational effects , i.e.,

$$v = v_0 + v_{nv}. \tag{3.108}$$

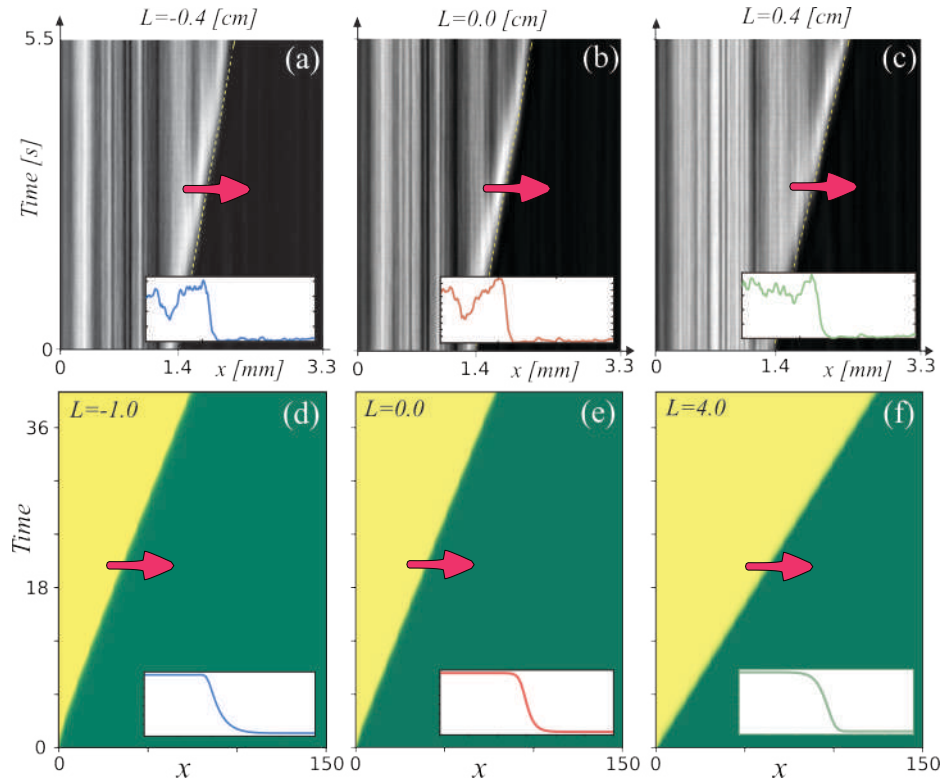

Figure 3.35: (After [15]) Spatiotemporal propagation of front solution into an unstable state for different diffraction lengths. Top panels account for front propagation in the experiment by $L = -0.4$ cm (a), $L = 0.0$ cm (b), and $L = 0.4$ cm (c), respectively. Bottom panels stand for the front propagation of model Eq. (3.103) by $\mu = 1.0$, $\beta = 0.1$, and free propagation length $L = -1.0$ (d), $L = 0$ (e), and $L = 4.0$ (f). The insets account for the front profile experimentally and numerically at a given instant.

Therefore, from this perturbative analysis, it is expected that the front speed increases or decreases with the free propagation length L. However, numerically, only for positive diffraction, the front speed increases linearly with the free propagation length (cf. Fig. 3.33(b)). Figure 3.35 shows how the front speed and profile are modified when the free propagation length L is changed. Despite the above calculation, for $L < 0$, the speed of the front remains at the minimum speed in contradiction with Eq. (3.108). This behavior can be understood in the following way: the front modifies its asymptotic profile (cf. Figs. 3.34 and 3.35), which increases its propagation speed given by the linear criterion [122, 159], so that it cancels the decrease in the speed induced by

the nonvariational effects. Then, the previous perturbative analysis cannot be valid because the base solution is modified and it is not a minor correction. This mechanism explains the origin of the pull-pushed transition of fronts when the disturbance tries to decrease the front speed, it adapts its shape to maintain the minimum speed. Also, when the disturbance increases the propagation speed, the system responds by increasing the speed. Therefore, the system exhibits a pull-pushed transition of fronts when the disturbance begins to increase the minimum speed.

3.5 Extended stable equilibrium invaded by an unstable state

3.5.1 One-dimensional front propagation from unstable state

Let us consider an one-dimensional scalar field $u(x,t)$, which satisfies a dimensionless reaction-diffusion equation

$$\partial_t u = -\frac{\partial V}{\partial u} + \partial_{xx} u, \tag{3.109}$$

where $V(u)$ is a potential that characterizes the dynamical evolution of u. Considering the potential for coexistence between a stable and an unstable state, Figure 3.36a illustrates the typical potential. The unstable and stable equilibriums are represented by symbols A and B, respectively. Stable and unstable equilibria are characterized by being a local minimum and maximum/saddle of the potential. Hence, the stable state always has less energy than the unstable equilibrium. The model, Eq. (4.6), has a front solution that connects the equilibrium states that propagates at a constant speed in order to minimize the energy (cf. Fig. 3.36a) [159, 125]. Let us consider a multistable system, which has two stable states, an unstable and a half-stable equilibrium. A half-stable equilibrium is a state in which one side is attractive while the other side is repulsive [150]. Namely, the half-stable equilibrium corresponds to a nonlinear unstable saddle point. Note that this equilibrium is non-generic because requires imposing a saddle fixed point. Figure 3.36b depicts an associated potential. Stable equilibria

are represented by the symbols C and B, and the unstable and half-stable states by the symbols D and A, respectively. Depending on the initial condition, this system can present different nonlinear waves between equilibrium states. In this scenario, an intriguing and unexpected front connects the stable state B and the saddle equilibrium A. Counterintuitively, the unstable stable state A invades the stable equilibrium B. Figure 3.36b illustrates this front propagation. The unstable state A invades the stable state B because it is more favorable energetically. Considering additive noise, we observe that the front between the A and B states propagates; however, at a later time, an extra front appears between the stable state C and saddle state A. Finally, the state C invades state A and then state B. Indeed, the propagation of a front from an unstable to a stable state is a transient phenomenon because the physical system must tend to its global equilibrium.

Let us consider an one-dimensional scalar field $u(x,t)$, which satisfies a dimensionless reaction-diffusion equation

$$\partial_t u = -\frac{\partial V}{\partial u} + \partial_{xx} u, \tag{3.110}$$

where $V(u)$ is a potential that characterizes the dynamical evolution of u. Considering a potential that has coexistence between a stable and an unstable state. Figure 3.36a illustrates the typical potential.

The unstable and stable equilibriums are represented by symbols A and B, respectively. Stable and unstable equilibria are characterized by being a local minimum and maximum/saddle of the potential. Hence, the stable state always has less energy than the unstable equilibrium. The model, Eq. (4.6), has a front solution that connects the equilibrium states that propagates at a constant speed in order to minimize the energy (cf. Fig. 3.36a) [159, 125]. Let us consider a multi-stable system, which has two stable states, an unstable and a half-stable equilibrium. A half-stable equilibrium is a state in which one side is attractive while the other side is repulsive [150]. Namely, the half-stable equilibrium corresponds to a nonlinear unstable saddle point. Note that this equilibrium is non-generic because requires imposing a saddle fixed point. Figure 3.36b

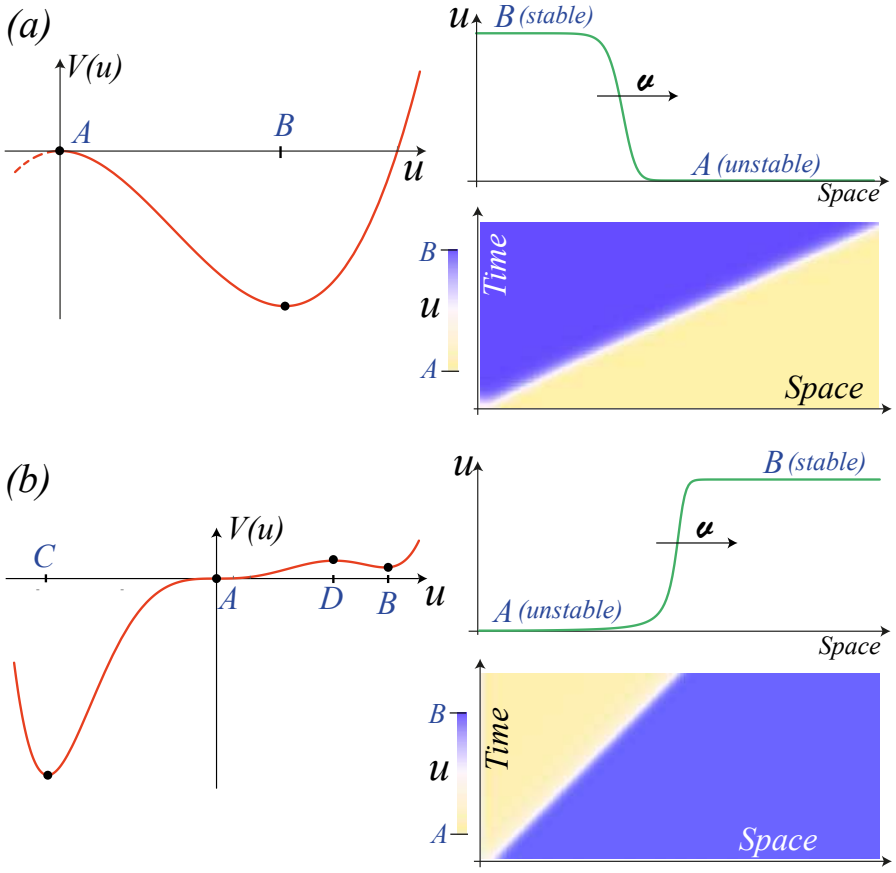

Figure 3.36: Front propagation between a stable and an unstable state. (a) Front propagation into unstable state, $V(u) = -u^2/2 + u^3/3$, $A = 0$ and $B = 1$ are unstable and stable states, respectively. The speed of propagation $v = 2$. (b) Front propagation from unstable state, $V(u) = u^6/6 - 0.7u^5/5 - u^4/4 + 0.7u^3/3$, $A = 0$, $B = 1$, $C = -1$, and $D = 0.7$, where B and C are stable state, D is an unstable state and A is a half stable equilibrium [150]. The left panels account for the respective potential. The right panels stand for the spatiotemporal evolution and profile of the fronts. Figure retrieved from Ref. [40].

depicts an associated potential. Stable equilibria are represented by the symbols C and B, and the unstable and half-stable states by the symbols D and A, respectively. Depending on the initial condition, this system can present different nonlinear waves between equilibrium states. In this scenario, an intriguing and unexpected front connects the stable state B and the saddle equilibrium A. Counterintuitively, the unstable stable state A invades the stable equilibrium B. Figure 3.36b illustrates this front prop-

agation. The unstable state A invades the stable state B because it is more favorable energetically. Considering additive noise, we observe that the front between the A and B states propagates; however, later, an extra front appears between the stable state C and saddle state A. Finally, the state C invades state A and then state B. Indeed, the propagation of a front from an unstable to a stable state is a transient phenomenon because the physical system must tend to its global equilibrium.

Including inherent fluctuations (noise) in differential equations offers a more realistic description of macroscopic systems. The fluctuations are responsible for causing the blow-up of unstable equilibria, giving rise to front propagation. Indeed, the fluctuations generate the emergence of fronts in different spatial places [10]. The typical time of the emergence of fronts is proportional to the logarithmic of the noise level [10]. Hence, the front will be observed without interference from the fluctuations while the observation time is lower than this characteristic time. Figure 3.37 shows the front propagation into an unstable state obtained from the numerical simulation of model Eq. (4.6) with $V(u) = u^6/6 - 0.7u^5/5 - u^4/4 + 0.7u^3/3$ and additive Gaussian white noise. Initially, the system is prepared in the stable state $u = 1$; then, a perturbation is introduced at one end of the spatial domain that induces a front between the unstable (A) and the stable (B) state. Subsequently, after the characteristic time of the fluctuations in state A, the fluctuations induce a front between the states A and C, which coexists with the front between the stable and unstable state. Later, a front between the states B and C is generated (cf. Fig. 3.37). Multistable systems are characterized by a rich variety of fronts and dynamics, among them [26, 135, 155].

To observe these intriguing fronts, the system under study needs a half-stable equilibrium. Hence, the system requires that at least one parameter must be set to the given value. Namely, this makes observing these fronts between homogeneous states less generic. As we shall show in the case of pattern formation, these fronts are generic.

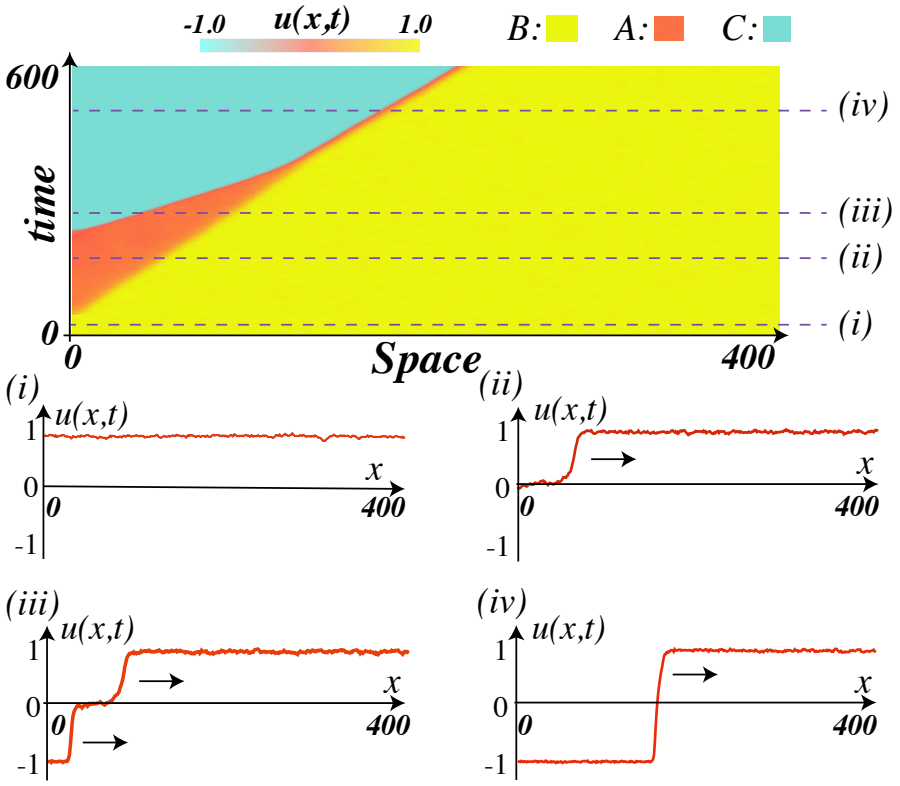

Figure 3.37: Front propagation of model Eq. (4.6), $V(u) = u^6/6 - 0.7u^5/5 - u^4/4 + 0.7u^3/3$, with additive Gaussian white noise and noise level intensity 0.1 and $D = 0.85$. $B = 1$, $C = -1$, and $A = 0$ are the stable and saddle equilibrium. The upper panel shows the spatiotemporal diagram from the initial condition homogeneous solution u = 1. The lower panels account for the profile of the field $u(x,t)$ at the instant represented by the (i), (ii), (iii), and (iv). Figure retrieved from Ref. [40]

3.5.2 Two-dimensional front propagation from unstable state

Non-equilibrium processes often lead in nature to the formation of spatial structures developed from a homogeneous state through a spontaneous breaking of symmetries present in the system [129, 133, 58]. The observed patterns correspond to spatial modes that become linearly unstable, which are stabilized by the nonlinear effects. The observed wavelength can be determined by the system's physical dimensions or geometrical constraints [58]. However, this wavelength can be also intrinsic, which is determined by the competition of different dynamic transport mechanisms. The origin of these patterns is often called Turing instability [156]. Several physical systems that

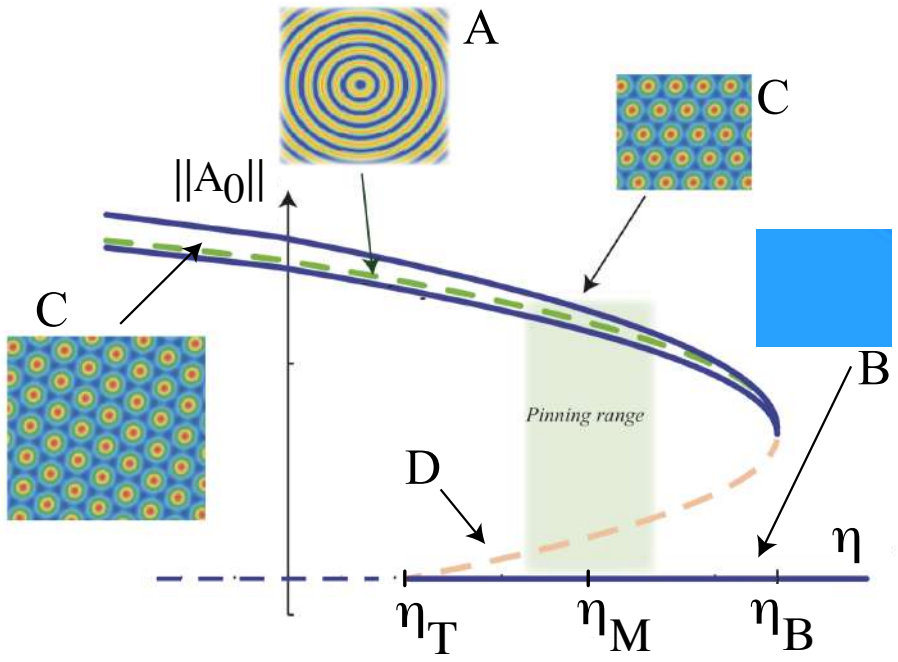

Figure 3.38: Schematic representation of the bifurcation diagram of the generalized Swift-Hohenberg model, Eq. (3.111) as function of η parameter for $\nu < 0$ and $\mu < 0$. The vertical axis accounts for the amplitude $||A_0||$ of the spatial oscillation of the pattern. η_T, η_B, and η_M account for the critical value or the transition, the nascent of bistability, and the Maxwell point, respectively. The shaded area accounts for the pinning region. Insets stand for the different equilibria, where B, A, C, and D account for the uniform stable, saddle type, hexagonal pattern, and unstable state. Figure retrieved from Ref. [40].

undergo a symmetry-breaking instability close to a second-order critical point can be described by real-order parameter equations in the form of Swift-Hohenberg type of models. These models have been derived in various fields of nonlinear science, such as hydrodynamics [151], chemistry [119], plant ecology [104], nonlinear optics [153, 47], and elastic materials [149]. Hence, this model is the paradigmatic equation that describes the pattern formation. Let us consider a generalized Swift-Hohenberg model for the real scalar field $u = u(x, y, t)$, which reads [153]

$$\partial_t u = \eta + \mu u - u^3 + \nu \nabla^2 u - \nabla^4 u. \tag{3.111}$$

Depending on the context in which this equation has been derived, the physical meaning of the field variable could be the electric field, deviation of molecular orientations, phytomass density, or chemical concentration. The control parameter μ measures the input field amplitude, the aridity parameter, or the chemical concentration. The parameter η accounts for the asymmetry between the homogeneous states. The parameter ν stands for the diffusion coefficient; when this parameter is negative, it induces an anti-diffusion process. This process is responsible for the emergence of patterns.

For $\nu < 0$ and $\mu < 0$, the system only exhibits a single homogenous state. When $|\eta|$ is large, the system is monostable. By decreasing $\eta < \eta_T$, the system exhibits a first-order spatial instability, giving rise to the appearance of hexagonal patterns. Hence, there is a coexistence region between the pattern and homogeneous states ($\eta_T < \eta < \eta_B$). Figure 3.38 depicts the bifurcation diagram of Eq. (3.111) as function of the parameter η (for details of the bifurcation diagram see Refs. [119, 153, 31]). The vertical axis accounts for the amplitude $||A||$ of the pattern. When the hexagons appear, they can be oriented in different directions due to the isotropy of the system (cf. Fig. 3.38). Another obvious spatial solution of the system corresponds to the superposition of concentric rings (see Fig. 3.38). However, this solution is unstable and is a saddle-type solution, because the interaction of spatial modes gives rise to the hexagonal patterns [58]. Likewise, numerically, it has been demonstrated that the concentric ring pattern is unstable [108]. Note that localized concentric ring solutions with a small number of rings have been studied in Refs. [109, 117]. A saddle equilibrium is characterized by being linearly marginal, nonlinear unstable, and having at least an unstable direction. Based on the mode dynamics, the states formed by many equivalent modes, which is the case of concentric rings, are generally saddle-type [58].

In the coexistence region, one envisages to observe fronts between the states. Depending on the value of η, one state is more favorable than the other one. Both states are energetically equivalent at Maxwell point (η_M). However, the system has a region of the parameter space where the front between these states is motionless, the *pinning range* [135], although one state is more stable than the other one. The shaded region in

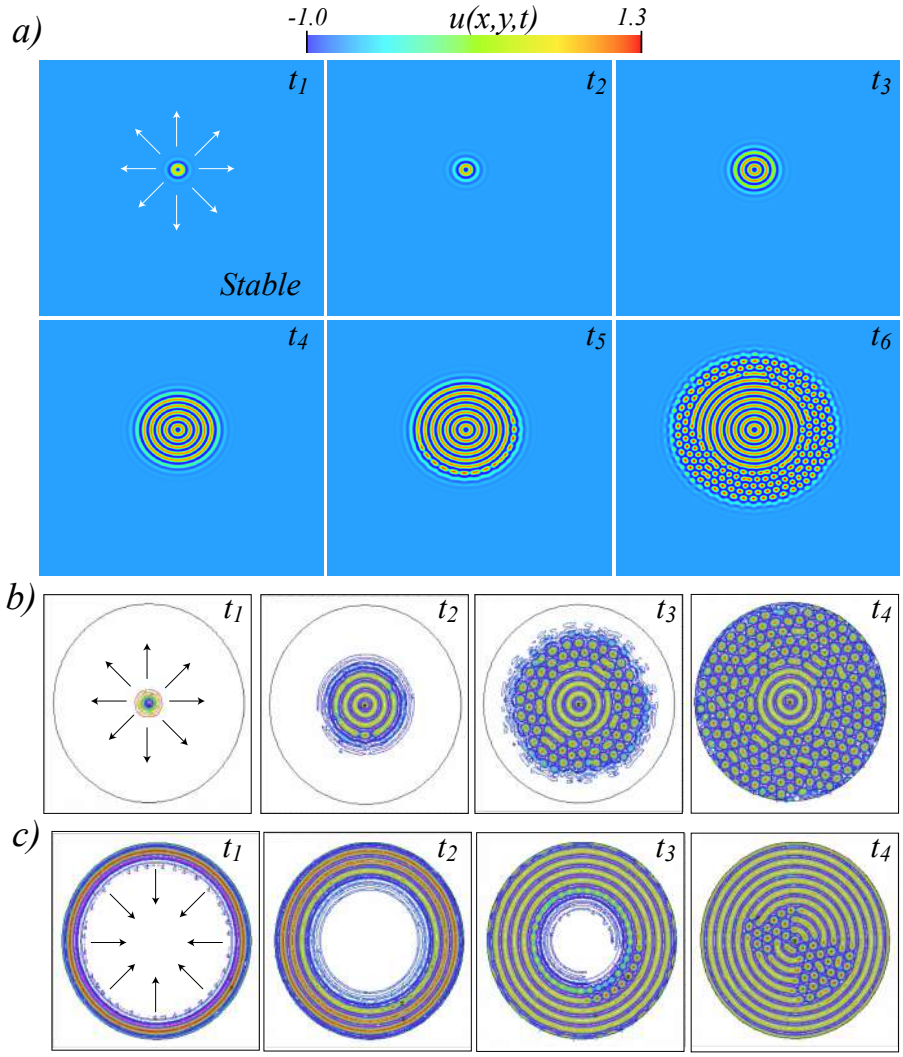

Figure 3.39: Unstable concentric ring pattern invades stable homogeneous state. Temporal sequence of numerical simulation of model Eq. (3.111) with $\eta = -0.216$, $\mu = 0.025$, $\nu = -2.0$, periodic (a) and Neumann boundary conditions (b) and (c) $[t_1 < t_2 < t_3 < t_4 < t_5 < t_6]$. Figure retrieved from Ref. [40].

Figure 2 illustrates the pinning region. Outside this region, the most favorable equilibrium spreads on the other one. When η approaches η_T ($\eta > \eta_T$), the homogeneous state is stable but close to becoming unstable. Then, in this region of the parameter space, the unstable concentric ring pattern fulfills all the conditions required to invade the stable homogeneous state. Namely, the concentric ring patterns and the homogeneous state schematically correspond, respectively, to the equilibria A and B of the potential

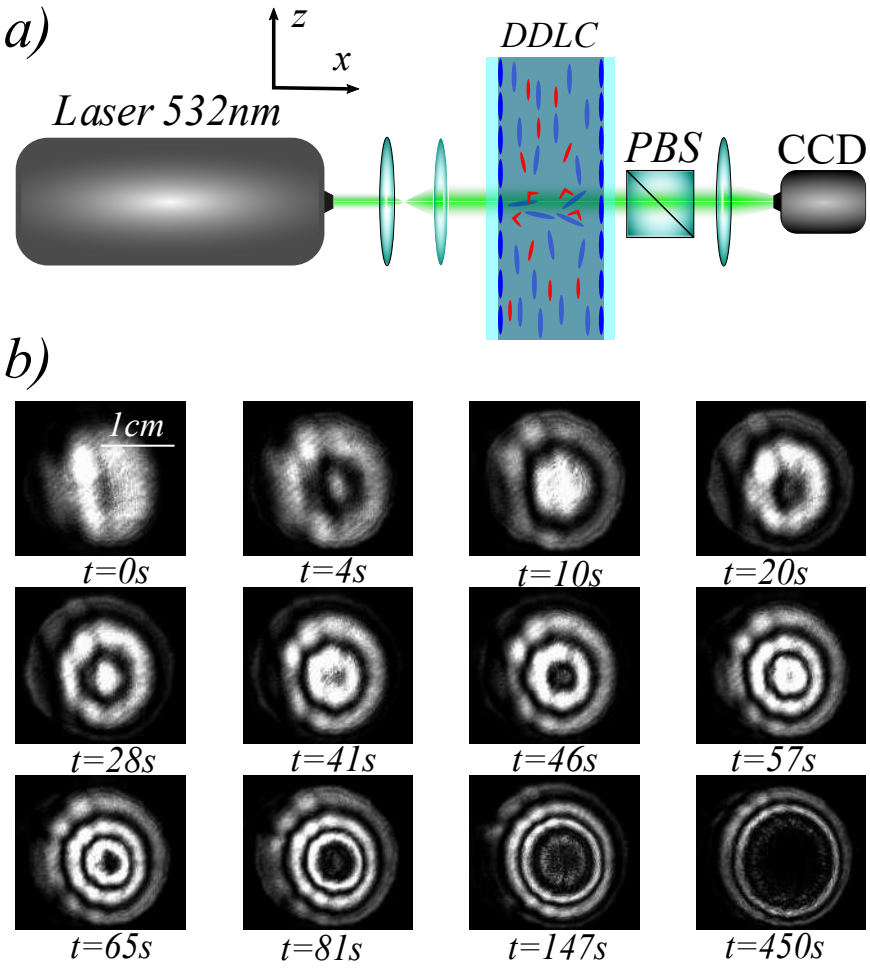

Figure 3.40: Concentric ring pattern propagation in photo-isomerization process in a dye-doped nematic liquid crystal layer illuminated by a laser beam with a Gaussian profile. (a) Schematic representation of experimental setup, DDLC: dye-doped nematic liquid crystal cell, PBS: polariser beam-splitter, and CCD: charge-coupled camera device. (b) Temporal sequence of concentric ring pattern propagation. Figure retrieved from Ref. [40].

of Fig. 3.36b. Figure 3.39 illustrates the spread of the unstable concentric ring pattern over the stable homogeneous state. Figure 3.39a shows this propagation considering periodic boundary conditions and, as an initial condition, a spot disturbance with small stochastic perturbations. Note that the spot disturbance must exceed a critical size because if it is too small, the system relaxes the uniform state. Due to the initial perturbations and the boundary conditions, the front is destabilized from a given temporal

moment ($t_4 < t < t_5$). Generating the emergence of hexagonal patterns that propagate over the unstable state. Finally, the hexagonal pattern invades the homogeneous state [86], however, the concentric ring pattern is pinned by the defects that are induced between both patterns (see the textbook [133] and reference therein). Note that pinning defects generate the richness of textures observed in spatial patterns. A similar phenomenon is observed when one considers a circular domain disturbed at the center with the Neumann boundary condition (cf. Fig. 3.39b). Likewise, we have considered a ring-shaped disturbance at the edge of the domain to analyze how the front penetrates into the inside of the domain (see Fig. 3.39c). Therefore, an unstable pattern invades a stable extended state. Note that the difference between the dynamics observed in one and two spatial dimensions is that the secondary front that connects the two stable states invades the entire system (one dimension) and partially (two dimensions) due to the existence of defects.

3.5.3 Experimental front propagation from unstable state in photo-isomerization process in a dye-doped nematic liquid crystal layer

To experimentally observe front propagation from an unstable state, we consider the photo-isomerization process in a dye-doped nematic liquid crystal layer illuminated by a laser beam with a Gaussian profile. For high enough input power, a phase transition from the nematic to the isotropic state takes place in the illuminated area, and then the two phases are spatially connected via a front propagating outward from the center of the beam [130]. For lower input power, photo-isomerization can induce patterns that correspond to the spatial modulation of the molecular order. Figure 3.40 depicts the experimental setup under study. Theoretically was demonstrated recently that an equivalent model to Eq. (3.111) describes the photo-isomerization process in a dye-doped nematic liquid crystal layer, where u stands for the Landau-DeGennes molecular scalar order parameter (see the details in [17] and the equivalence of the models in

supplementary material).

The cell consists of two glass plates coated with Poly-Vinyl-Alcohol and rubbed to favor the planar alignment of the liquid crystal molecules, with a separation of $25\,\mu m$. The gap is filled with an E7 nematic liquid crystal doped with the azo-dye Methyl-Red at a concentration of 0.75% by weight. To induce the fronts, the cell is irradiated with a frequency-doubled Nd^{+3}:YVO_4 laser, polarized in the vertical direction with wavelength $\lambda_0 = 532\,nm$ in the absorption band of the dopants. A polarizer beam-splitter is placed in between the liquid crystal sample and the CCD camera to distinguish the molecular orientation in the sample. Two planoconvex lenses increase the laser beam diameter to $2cm$. The cell was subjected to input powers between $P = 300$ and $P = 700$ mW.

Applying a light beam on the sample creates the gradual emergence of concentric rings that propagate from the center of the beam to the outside. Figure 3.40b displays a temporal sequence of the unstable concentric ring propagation. Near the boundary of the illuminated region, the rings begin to deform with a similar morphology that was observed in the numerical simulations. However, hexagonal patterns are not observed since the phase that finally invades the system is the isotropic liquid state that corresponds to the black zone within the illuminated domain. This region is black since light can not cross an isotropic medium between crossed polarizers. Since this stable state is homogeneous, no trace of the concentric rings remains. In the event that the final state is a pattern, there will always be a trace of the front between the stable and the unstable state (cf. Fig. 3.39). Some rings are observed in experimental [22] or in nature [98], which is the *footprint* that there was an unstable state that invaded a stable one.

3.6 Front propagation in discrete media

Let us consider a simple discrete version of the Fisher-Kolmogorov-Petrosvky-Piskunov model, Eq. (3.11) [169]

$$\dot{u}_i = u_i(1 - u_i) + \frac{u_{i+1} - 2u_i + u_{i-1}}{dx^2}, \tag{3.112}$$

where $u_i(t)$ stands for the population in i-th position. Note that the dynamics of the discrete FKPP model can be rewritten in the following form

$$\partial_t u_i = -\frac{\partial \mathcal{F}(u_i)}{\partial u_i} \tag{3.113}$$

where the Lyapunov function is defined as

$$\mathcal{F} = \sum_i \left(-\frac{u_i^2}{2} + \frac{u_i^3}{3} + \frac{(u_{i+1} - u_i)^2}{2\,dx^2} \right) = \sum_i V_i + \frac{(u_{i+1} - u_i)^2}{2\,dx^2}, \tag{3.114}$$

where V_i is the potential. Hence, the dynamics of Eq. (3.112) is characterized by the minimization of functional F. Indeed, using Eq. (3.112), one obtains

$$\frac{d\mathcal{F}}{dt} = \sum_i \frac{\partial \mathcal{F}}{\partial u_i} \frac{\partial u_i}{\partial t} = -\sum_i \left(\frac{\partial \mathcal{F}}{\partial u_i} \right)^2. \tag{3.115}$$

The discrete Fisher-Kolmogorov-Petrosvky-Piskunov Eq. (3.112) exhibits front propagation into an unstable state. In Ref.[169], it has been established the existence of these solutions. However, numerical simulation of this model show oscillatory propagation [9]. Figure 3.41 shows a schematic representation of potential V_i, the front solution, the front position and minimum speed for different values of discreteness obtained from numerical simulations of model Eq. (3.112). From this figure, one trivially deduces the energy source of the front propagation.

Defining the front position as the spatial position that interpolate the maximum spatial gradient, $u(x_0) = 1/2$ (cf. Fig. 3.41b), one can study the front propagation. Indeed, front propagates with an oscillatory speed with a given mean speed [9]. When coupling parameter dx increases, the mean speed, amplitude and frequency of oscillations increases. Moreover, the oscillations exhibited by the speed are non-harmonic type. Figure 3.42a shows the mean speed as a function of the coupling parameter. For large dx the speed increases linearly.

From a numerical solution of FKPP model Eq. (3.112), we have computed the Lyapunov functional (3.114). Figure 3.42b shows evolution of Lyapunov functional as a function of the front position. Inset of figure 3.42b shows the Lyapunov functional in the comobile system. As we can see, Lyapunov functional decreases with time in a oscillatory manner.

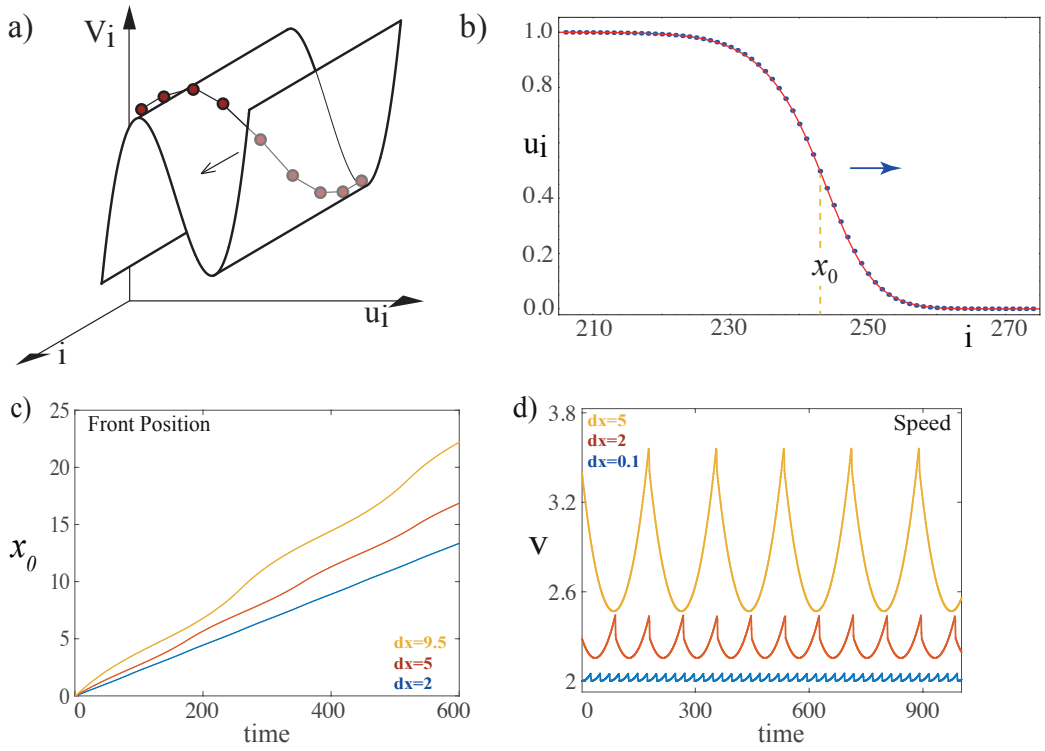

Figure 3.41: Front solution of discrete FKKP model Eq. (3.112). a) Schematic representation of potential V_i. b) Front solution obtained numerically from Eq. (3.112) (blue dots) and the asymptotic solution Eq.(3.25) (solid line); x_0 accounts for the front position. c) Temporal evolution of front position $x_0(t)$. The upper (yellow), middle (orange) and lower (blue) lines correspond to $dx = 9.5$, $dx = 5$, and $dx = 2$, respectively. d) Temporal evolution of front speed $\dot{x}_0(t)$. The upper (yellow), middle (orange) and lower (blue) lines correspond to $dx = 5$, $dx = 2$, and $dx = 0.1$, respectively [9].

Usually, the study of the front dynamics is reduced to the front position, i.e., the dynamical tracking of point x_0, where $u(x_0) = 1/2$ is the maximum of the spatial gradient. This is based on the assumption that the front behaves as a point-like particle. Thus, point x_0 will gives us enough information about the whole structure dynamics. Surprisingly, the FKPP front exhibits an extended object behavior: each point of the front shows an oscillation dynamics with the same frequency but different amplitude. Figure 3.43a shows the spatiotemporal diagram of the front. From this figure, is easy to infer that the front propagates as an extended object. Moreover, the oscillation with respect to front position x_0 are in anti-phase (see Fig. 3.43b). That is, the maximum

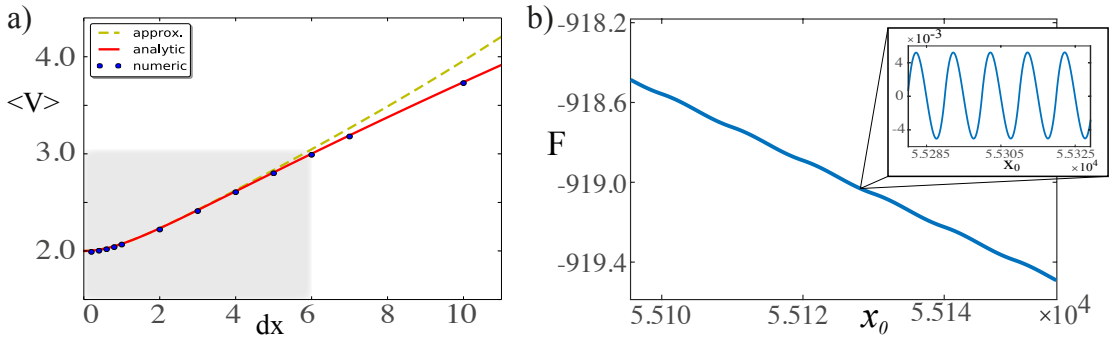

Figure 3.42: (color online) Front propagation into an unstable state in FKPP model, equation (3.112). a) Minimum mean speed as a function of the discreteness dx. Dots (blue) correspond to numerical simulations of model (3.112). The solid (red) and dashed (yellow) lines are the exact and approximative curve obtained form expressions (3.123) and (3.126), respectively. b) Lyapunov functional as a function of front position obtained from numerical simulations of Eq. (3.112) with $dx = 10$. Inset: Lyapunov functional computed in the co-mobile system.

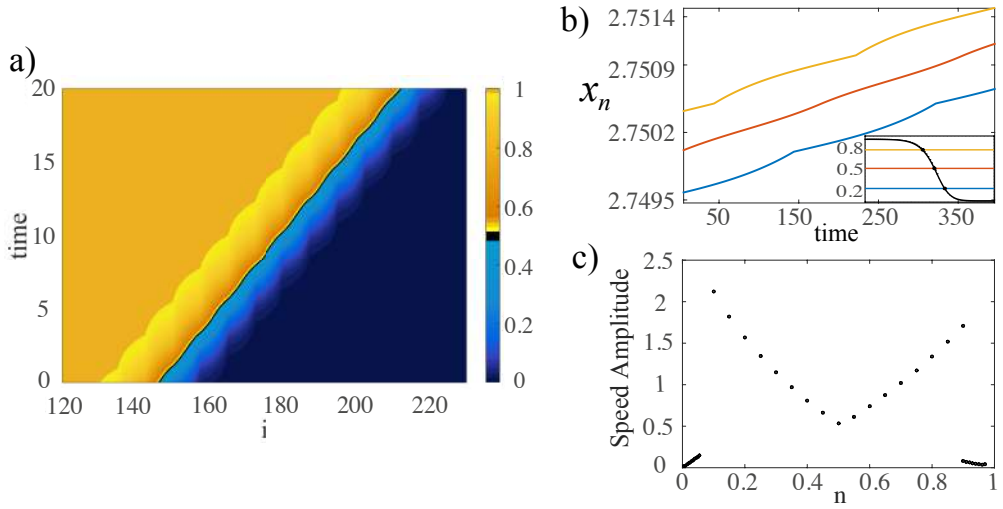

Figure 3.43: Front propagation into an unstable state in discrete FKPP model (3.112). a) Spatiotemporal evolution of the front propagation into an unstable state in discrete FKPP model (3.112) with $dx = 7.5$. b) Trajectory of three different points or cuts: Above (upper yellow line), in (middle red line), and below (lower blue line) the front position. Inset illustrates different cuts under consideration. c) Oscillation amplitude of the front speed in different points.

oscillation of a point to the left of the front position coincides with the minimum oscillation of a point to the right. To explore the structure of the potential over which

the front propagates, we have followed different points or "cuts" along the front profile, studying each one separately. Figure 3.43c displays the amplitude of oscillation of the front speed for different cuts. From this figure, we conclude that this amplitude is minimal at the front position, increases as one moves away from the front position and decays to zero abruptly in the front tails.

3.6.1 Theoretical description of the mean speed for the discrete FKPP model

For discrete media, the *FKPP procedure*[2] is unsuitable to determine the minimum speed. Due to there is not a continuos dynamical system associated to the co-mobile system inferred for traveling wave solutions. To compute the minimal front speed, we generalize the asymptotic procedure ansatz for the front tail [122],

$$u_i(t) = e^{(\alpha t - 2i\beta)} \left[1 + f^{\omega}_{dx;i}(t)\right], \qquad i \gg 1, \tag{3.116}$$

with $\alpha \equiv k\langle v\rangle$ and $\beta \equiv k\,dx/2$ are parameters. The index $i \geq 0$ is a positive and large integer number, dx is the discretization parameter, $\langle v\rangle$ is the mean speed of the front, and $f^{\omega}_{dx,i}(t)$ is a time periodic function with period $T \equiv 2\pi/\omega$, i.e., $f^{\omega}_{dx;i}(t) = f^{\omega}_{dx;i}(t+T)$, which accounts for the oscillation of the front speed at the i-th position (cf. Fig. 3.43). In addition, $f^{\omega}_{dx;i}(t) \to 0$ when $i \to \infty$. Hence, function $f^{\omega}_{dx,i}(t)$ takes into account the periodicity introduced by the discreteness. Linearizing discrete FKKP model (3.112) and replacing ansatz (3.116), we get

$$\dot{u}_i = \dot{f}^{\omega}_{dx;i} + \alpha\left[1 + f^{\omega}_{dx;i}\right] = \left[1 + f^{\omega}_{dx;i}\right] + \frac{k^2}{\beta^2}\left[\left(\sinh^2(\beta)\right) + \left(\sinh^2(\beta)\right) f^{\omega}_{dx;i}\right]. \tag{3.117}$$

Integrating this expression in a normalized period T

$$\langle \dot{f}^{\omega}_{dx;i} + \alpha\left[1 + f^{\omega}_{dx;i}\right]\rangle = \langle\left[1 + f^{\omega}_{dx;i}\right] + \frac{k^2}{\beta^2}\left[\left(\sinh^2\beta\right) + \left(\sinh^2\beta\right) f^{\omega}_{dx;i}\right]\rangle, \tag{3.118}$$

[2]Based in study the stationary dynamical system and determine the critical front speed for which there is a transition of damped and overdamped of unpopulated state

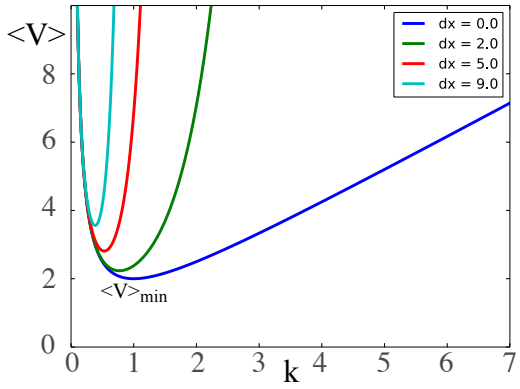

Figure 3.44: Mean speed $\langle v \rangle$ as a function of the steepness parameter k for different values of the discretization parameter dx, formula (3.120). From the lower to upper curve we consider $dx = 0, 2, 5$ and 9, respectively.

where

$$\langle g(t) \rangle \equiv \frac{1}{T} \int_0^T g(t) dt, \tag{3.119}$$

we obtain an expression for the mean speed $\langle v \rangle$

$$\langle v \rangle = \frac{1}{k} + k \left(\frac{\sinh \beta}{\beta} \right)^2 . \tag{3.120}$$

with $\langle f^{\omega}_{dx;i} \rangle = \langle \dot{f}^{\omega}_{dx;i} \rangle = 0$, due to $f^{\omega}_{dx;i}(t)$ periodicity. This expression accounts for the mean speed as a function of steepness and discreteness parameters. Note that $\langle v \rangle$ tends to expression (3.16) when $dx \to 0$ ($\beta \to 0$), which corresponds to the continuous limit. Figure 3.44 shows the mean speed as a function of the parameter k for different values of the discretization parameter dx. For different values of discretization parameter dx, $\langle v \rangle$ is a concave function. We can observe, that the minimum speed $\langle v \rangle_{min}$ increases as the discretization parameter dx grows. Meanwhile, the critical steepness k_c decreases. By differentiating the mean speed relation (3.120) and equating to zero, we obtain an expression for the discretization parameter,

$$dx^2 = 4 \sinh \beta_c (2\beta_c \cosh \beta - \sinh \beta_c), \tag{3.121}$$

where $\beta_c = k_c dx/2$ and k_c is the critical steepness to obtain the minimum speed. Replacing the definition of β_c in above expression, we get

$$dx^2 = 4\sinh\left(\frac{k_c dx}{2}\right)\left[k_c dx\cosh\left(\frac{k_c dx}{2}\right) - \sinh\left(\frac{k_c dx}{2}\right)\right]. \tag{3.122}$$

One can not explicitly determine the critical steepness as fa unction of discretization parameter dx, $k_c(dx)$. Hence, minimum speed as a function of dx is a implicit formula

$$\langle v\rangle_{mim} = \frac{1}{k_c(dx)} + k_c(dx)\left(\frac{\sinh\beta(dx)}{\beta(dx)}\right)^2. \tag{3.123}$$

The continuos curve in Fig. 3.42a is the minimal mean speed as a function of the discretization, expression (3.123). Numerical simulations show quite good agreement with this expression (cf. Fig. 3.42a).

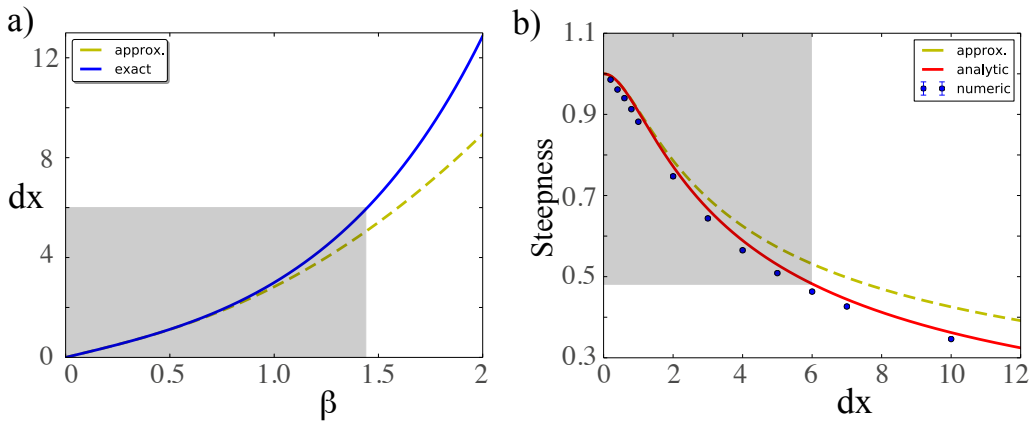

Figure 3.45: (color online) Parameter as function of discretization. a) Discretization as a function of β parameter. Solid (blue) and dashed (yellow) lines are the exact and approximative analytic curves (3.122) and (3.124), respectively. b) Steepness k as a function of the discretization parameter, dx. Solid and dashed lines are the exact and approximative analytic curves (3.122) and (3.125), respectively. Dots (blue) are obtained by numerical simulations.

To have an explicit analytical expression we consider the limit $\beta \to 0$, thus expression (3.124) can be simplified to

$$dx \approx 2\beta_c\sqrt{1+\beta_c^2}. \tag{3.124}$$

From here, we can write the parameter β_c

$$\beta_c \approx \frac{dx}{\sqrt{2\left(1+\sqrt{1+dx^2}\right)}}$$

and the critical steepness

$$k_c \approx \sqrt{\frac{2}{1+\sqrt{1+dx^2}}} \tag{3.125}$$

as a function of the discretization parameter dx. Figure 3.45 shows the discretization parameter dx as a function of β (Eq. (3.124)). The shadow area illustrates the limit where the approximation $\beta \to 0$ is valid. Likewise, figure (3.45) shows the steepness k as a function of the parameter dx. From both, we can infer that expressions (3.124) and (3.125) are valid in a wide range of the parameter dx. Therefore, in a good approximation the mean speed $\langle v \rangle$ can take the form,

$$v \approx \sqrt{\frac{1+\sqrt{1+dx^2}}{2}} \left[1 + \frac{4}{dx^2} \sinh^2 \left(\frac{dx}{\sqrt{2\left(1+\sqrt{1+dx^2}\right)}} \right) \right]. \tag{3.126}$$

Figure 3.42 shows the mean speed as a function of the discretization parameter dx. Up to a value of $dx = 6.0$, expression (3.126) is an adequate approximation. We observe a good accordance between the analytic expression and the mean speed obtained by numerical simulations.

In brief, *the asymptotic procedure* allows an adequate characterization of the average features of front propagation into unstable states in discrete media. In the next section, we shall apply this procedure to characterize the mean properties of front propagation into unstable state in a chain of dissipative coupled pendula.

3.6.2 Theoretical description of the mean speed for the Chain of dissipative coupled pendula

For the chain of dissipative coupled pendula, Eq. (2.3), the unstable state correspond to $\theta_i = \pi/2$. Considering the asymptotic ansatz for the front tail around this state, we get,

$$\theta_i(t) = \frac{\pi}{2} + A_0 e^{(\alpha t - 2i\beta)} \left[1 + f^{\omega}_{dx;i}(t) \right], \tag{3.127}$$

where A_0 is a constant that characterizes the shape of the front tail, $\alpha \equiv k\langle v \rangle$ and $\beta \equiv k\, dx/2$ are parameters. $f^{\omega}_{dx;i}(t)$ is a periodic function of frequency ω in i-th position

of the chain that describes the oscillatory behavior of the speed. Introducing the above ansatz in Eq. (2.3) and taking into account only the linear leading terms, we obtain,

$$\begin{aligned}\ddot{\theta}_i &= \alpha^2\left[1+f^{\omega}_{dx;i}(t)\right]+2\alpha\dot{f}^{\omega}_{dx;i}(t)+\ddot{f}^{\omega}_{dx;i}(t), \\ &= \omega^2\left[1+f^{\omega}_{dx;i}(t)\right]-\mu\left[\alpha\left[1+f^{\omega}_{dx;i}(t)\right]+\dot{f}^{\omega}_{dx;i}(t)\right]+\frac{4}{dx^2}\sinh^2(\beta)\left[1+f^{\omega}_{dx;i}(t)\right].\end{aligned} \tag{3.128}$$

Integrating this expression in a normalized period $T=2\pi/\omega$, and considering $\langle f^{\omega}_{dx;i}(t)\rangle = \langle \dot{f}^{\omega}_{dx;i}(t)\rangle = \langle \ddot{f}^{\omega}_{dx;i}(t)\rangle = 0$, after straightforward calculations, we obtain

$$\alpha^2 = \omega^2 - \mu\alpha + \frac{4}{dx^2}\sinh^2(\beta). \tag{3.129}$$

Substituting the definition of α, the mean speed reads

$$\langle v\rangle = -\frac{\mu}{k}+\frac{1}{k}\sqrt{\mu^2+\omega^2+\frac{k^2}{\beta^2}\sinh^2(\beta)}, \tag{3.130}$$

and replacing $k=2\beta/dx$,

$$\langle v\rangle = -\frac{\mu}{2\beta}dx+\frac{1}{2\beta}\sqrt{dx^2\left(\mu^2+\omega^2\right)+4\sinh^2(\beta)} \tag{3.131}$$

The above expression accounts for front speed as a function of the steepness. In order to deduce the minimal front speed, we differentiate the above speed with respect to β

$$\begin{aligned}&\omega^2\left(\mu^2+\omega^2\right)dx^4+4\left[\left(\mu^2+2\omega^2\right)\sinh^2(\beta)-2\left(\mu^2+\omega^2\right)\beta\sinh(\beta)\cosh(\beta)\right]dx^2 \\ +\;&16\sinh^2(\beta)\left[\sinh(\beta)-\beta\cosh(\beta)\right]^2=0.\end{aligned} \tag{3.132}$$

This expression gives us a relation between the critical steepness k_c and the coupling parameter dx. An explicit expression $k_c(dx)$ cannot be derived. Using expression (3.132) in formula (3.131), we obtain the minimal front speed for the chain of dissipative coupled pendula, Eq (2.3). Note that this analytical results has quite fair agreement with the numerical simulations as it is shown in Fig. 3.46a. Therefore, the asymptotic procedure is a suitable method to characterize the mean properties of front propagation.

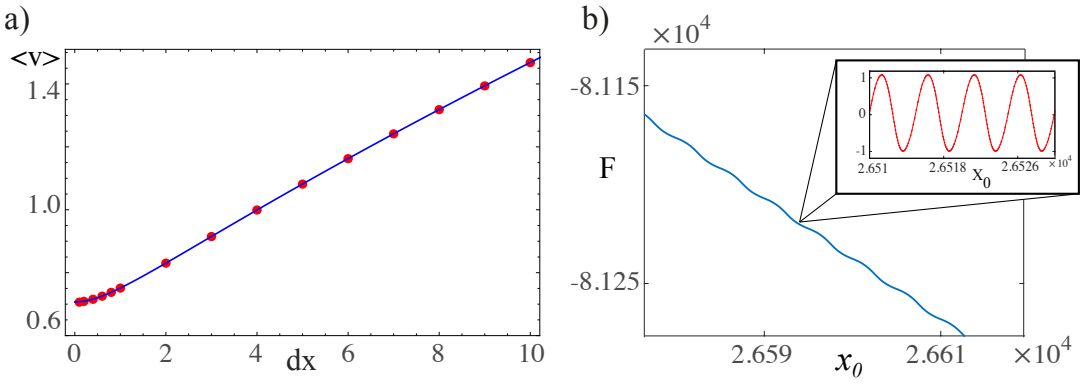

Figure 3.46: Front propagation into an unstable state in discrete chain of dissipative coupled pendula. a) Mean front speed as a function of the coupling parameter. Dots (red) are obtained by means of numerical simulations of Eq. (2.3) with $\omega = 1.0$, $dx = 5.0$ and $\mu = 2.0$. The solid line is obtained by using the formulas (3.131) and (3.132). b) Lyapunov functional as function of front position obtained by numerical simulations of Eq. (2.3) for the same parameters. Inset: Lyapunov functional computed in the co-mobile system.

3.7 Effective continuous model: oscillatory properties of front propagation

Due to the complexity of discrete dissipative systems, to obtain analytical results is a daunting task. In order to figure out the oscillatory behavior of the front, we shall consider a similar strategy to that used in Ref. [45], which is based on considering an effective continuous equation that accounts for the dynamics of the discrete system. The benefit of this approach is that analytical calculations are accessible.

3.7.1 Generalized Peierls-Nabarro potential

Let us consider the continuos order parameter $u(x,t)$, which satisfies

$$\partial_t u = -\frac{\delta \mathcal{F}}{\delta u}, \tag{3.133}$$

where the Lyapunov functional has the form

$$\mathcal{F} = \int \left(-\frac{u^2}{2} + \frac{u^3}{3} + \frac{(\partial_x u)^2}{2} + \frac{(\partial_x u)^2 \Gamma_{dx}(x)}{2} \right) dx, \tag{3.134}$$

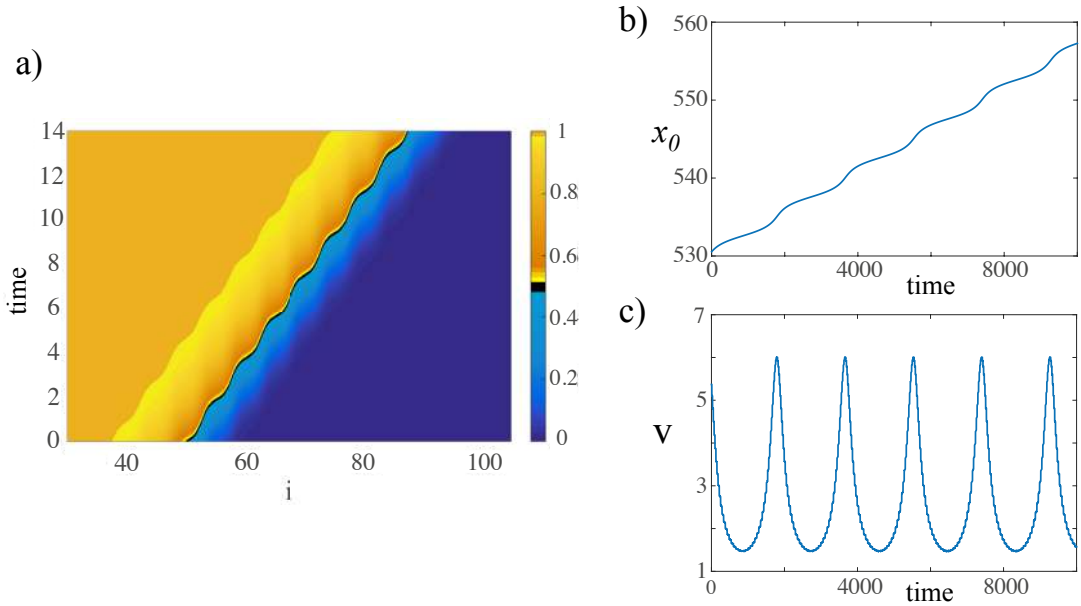

Figure 3.47: (color online) Front propagation into an unstable state in FKPP Eq. (3.135) with a harmonic generalized Peierls-Nabarro potential, $\Gamma_{dx}(x) = A\cos(2\pi x/dx)$ with $A = 0.06$, and $dx = 5.0$. The numerical discretization parameter of the finite differences method is 0.1. a) Spatiotemporal evolution of the front propagation into unstable state. b) Temporal evolution of the front position and c) minimum speed.

$\Gamma_{dx}(x)$ is a spatial periodic function with dx period, $\Gamma_{dx}(x + dx) = \Gamma_{dx}(x)$. This function accounts for the discreteness of the system. The last term of the free energy is a generalization of the Peierls-Nabarro potential. An effective potential has been used to explain the dynamics of defects position such as dislocations in condensed matter physics or dynamics of the position of kink or fronts (see [36, 35] and reference therein). Here, we consider an effective equation for the entire field $u(x,t)$, which reads

$$\partial_t u = u(1-u) + D\partial_{xx}u + \Gamma_{dx}(x)\partial_{xx}u + \Gamma'_{dx}(x)\partial_x u. \tag{3.135}$$

This equation is a populations dynamical model with linear growth, nonlinear saturation, inhomogeneous diffusion and drift force. Numerical simulations with a harmonic potential $\Gamma_{dx}(x)$ exhibit front solutions. It is important to note that for these numerical simulations, we have discretized the Laplacian and gradient of u to first neighbors considering a small dx. For which the discreteness effects are negligible. Figura 3.47 shows

the spatiotemporal diagram of the front into an unstable state of the effective FKPP, Eq. (3.135), with a harmonic generalized Peierls-Nabarro potential. Its trajectory and speed are also illustrated. We can observe that the numerical simulations of the effective FKPP, Eq. (3.135), and discrete FKPP, Eq. (3.112), have similar qualitative dynamical behaviors.

To understand better the generalized Peierls-Nabarro potential, Figure 3.48a shows the effective force for the harmonic case and the amplitude speed for the effective FKPP Eq. (3.135). From this figure, we infer that the effective force, $f \equiv \Gamma_{dx}(x)\partial_{xx}u + \Gamma'_{dx}(x)\partial_x u$, has an oscillatory structure concentrated in the region where the front displays larger spatial variations. Moreover, we observe that the structure of the amplitude of the speed is similar to that observed in the discrete case (cf. Figs. 3.48b and 3.43c).

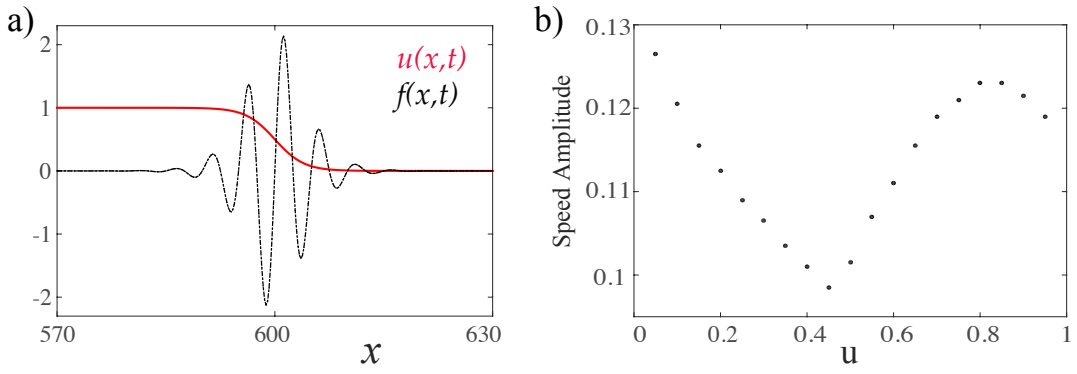

Figure 3.48: The generalized Peierls-Nabarro force for a harmonic case, $\Gamma_{dx}(x) = A\cos(2\pi x/dx)$. a) Front solution and effective force $f \equiv 2\Gamma_{dx}(x)\partial_{xx}u + 2\Gamma'_{dx}(x)\partial_x u$. b) Amplitude of the speed for the effective FKPP Eq. (3.135) with $D = 1.97$, $A = 0.03$, and $dx = 5.0$. The numerical discretization parameter of the finite differences method is 0.1.

Dynamics of front position

The equilibria are not affected by the presence of the periodical extra terms, effective force. In the continuous limit, $dx \to 0$ and $\Gamma_{dx}(x) \to 0$ one recovers the Fisher-Kolmogorov-Petrosvky-Piskunov model Eq. (3.12). Then for $dx \ll 1$, the last two terms of Eq. (3.135) are of perturbative nature. We shall analyze this region of parameters,

where we can obtain analytical results.

The Fisher-Kolmogorov-Petrosvky-Piskunov model Eq. (3.12) has front solutions of the form $u_{FKPP}(x-vt-p)$, where p is a constant that accounts for the front position and v the front speed. Analytical expressions of this solution are unknown, however solutions in the form of perturbative series are available [123]. Considering the following ansatz for small discreteness ($dx \ll 1$)

$$u(x,t) = u_{FKPP}\left(x - vt - p(t)\right) + w(x - vt - p(t), p(t)), \tag{3.136}$$

where front position is promoted to a temporal function, $p(t)$ and w is a corrective function on the order of the perturbative force. Introducing the above ansatz in Eq. (3.135) and linearizing in w, after straightforward calculations, we obtain

$$\mathcal{L}w = -\dot{p}(t)\partial_\xi u_{FKPP} - 2\Gamma_{dx}(x)\partial_{\xi\xi}u_{FKPP} - 2\Gamma'_{dx}(x)\partial_\xi u_{FKPP}, \tag{3.137}$$

where $\mathcal{L} \equiv \partial_{\xi\xi} + v\partial_\xi + 1 - 2u_{FKPP}(\xi)$ is a linear operator and $\xi = x - vt - p$ is the coordinate in the co-mobile system. Considering the inner product

$$\langle f|g\rangle = \int_{-L}^{L} f(\xi)g(\xi)d\xi, \tag{3.138}$$

where $2L$ is the system size. In order to solve the linear Eq. (3.137), we apply the Fredholm alternative or solvability condition, and obtain

$$\dot{p}(t) = -2\frac{\langle\Gamma_{dx}(\xi + vt + p)\partial_{\xi\xi}u_{FKPP}|\psi\rangle}{\langle\partial_\xi u_{FKPP}|\psi\rangle} - 2\frac{\langle\Gamma'_{dx}(\xi + vt + p)\partial_\xi u_{FKPP}|\psi\rangle}{\langle\partial_\xi u_{FKPP}|\psi\rangle}, \tag{3.139}$$

where $\psi(\xi)$ is an element of kernel of adjoint of $\mathcal{L}$, $\mathcal{L}^\dagger \equiv \partial_{\xi\xi} - v\partial_\xi + 1 - 2u_{FKPP}(\xi)$, that is $\mathcal{L}^\dagger\psi = 0$. The ψ function is unknown analytically, however the asymptotic behavior of this function are characterized to diverges exponentially with the the same exponent that u_{FKPP} converges to their equilibria. Therefore the above integrals diverge proportional to L, however the ratio is well-defined.

To understand the dynamics described by the above equation for simplicity we shall consider the generalized Peierls-Nabarro potential for a harmonic case, that is,

$$\Gamma_{dx}(x) = \gamma(x) \equiv A\cos\left(\frac{2\pi x}{dx}\right), \tag{3.140}$$

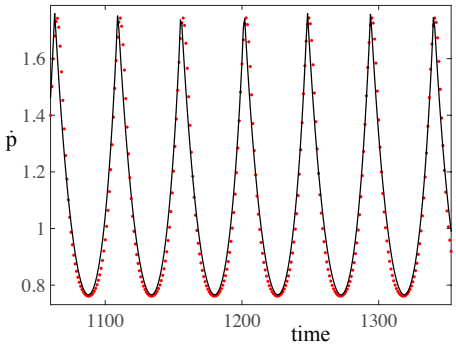

Figure 3.49: Fitting curve for $\dot{p}$ given by the expression $\dot{p} = \frac{a\sec^2(bx+c)}{1+(d\tan(bx+c)-e)^2} + f$ with $a = 0.57$, $b = 0.0682$, $c = 0.6157$, $d = 1$, $e = 0.8$, and $f = 0.5$

Replacing this expression in Eq. (3.139), after straightforward calculations, we obtain

$$\dot{p}(t) = \sqrt{K_1^2 + K_2^2}\cos\left(\frac{2\pi}{dx}(p - vt) + \phi_0\right), \tag{3.141}$$

with

$$\begin{aligned} K_1 &= A\frac{\left\langle \cos\left(\frac{2\pi\xi}{dx}\right)\partial_{\xi\xi}u_{FKPP}(\xi) - \frac{2\pi\xi}{dx}\sin\left(\frac{2\pi\xi}{dx}\right)\partial_\xi u_{FKPP}|\psi(\xi)\right\rangle}{\langle\partial_\xi u_{FKPP}|\psi(\xi)\rangle}, \\ K_2 &= -A\frac{\left\langle \sin\left(\frac{2\pi\xi}{dx}\right)\partial_{\xi\xi}u_{FKPP}(\xi) + \frac{2\pi\xi}{dx}\cos\left(\frac{2\pi\xi}{dx}\right)\partial_\xi u_{FKPP}|\psi(\xi)\right\rangle}{\langle\partial_\xi u_{FKPP}|\psi(\xi)\rangle}, \\ \tan(\phi_0) &= \frac{K_1}{K_2}. \end{aligned} \tag{3.142}$$

Therefore, the front position propagates in a oscillatory manner. Notice that the Peierls-Nabarro potential propagates together with the front. Figure 3.48 shows fitting curve for $\dot{p}$ using solution of (3.141) if $\Gamma_{dx}(x)$ is given by (3.140). We can see that the analytical result is in good agreement with the observed dynamics.

In this section, we have studied the effect of discretization on systems that have pulled fronts. In the case of considering pushed fronts, one expects to get the same results presented in this section. In short, the effect of discretization is to generate a periodic potential in the effective continuous description.

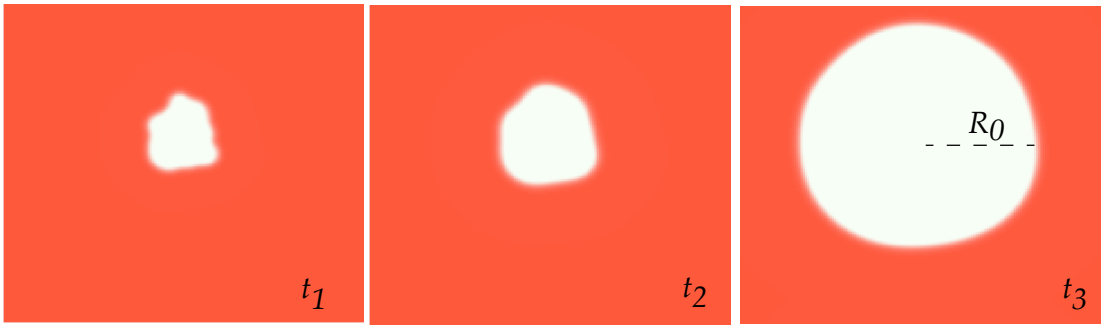

Figure 3.50: Temporal sequence of umerical simulation of extended logistic model in two dimensions, Eq. 3.143 ($t_1 < t_2 < t_3$).

3.8 Front propagation in two dimensions

In our daily life many populations spread in two dimensions, not one. In this section we will consider the propagation of fronts in two spatial dimensions. Let us consider a extended logistic model in two dimensions (two-dimensional FKPP equation)

$$\partial_t N(\vec{r}, t) = rN\,(1 - N) + \nabla^2 N, \tag{3.143}$$

where $N(\vec{r}, t)$ is the density of population at given position $\vec{r}$ and time t. Figure 3.50 shows a sequence of numerical simulations of temporal images of above model from a localized perturbation at time t_1. As the system evolves, we can see that the front or

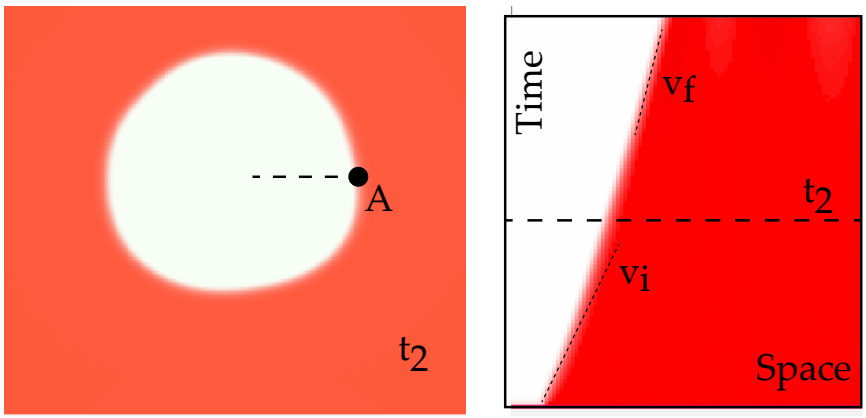

Figure 3.51: Spatiotemporal evolution of a point in te interface. This point is illustartes by A in the left panel. $\{v_i, v_f\}$ account for initial and asymptotic speed.

interface tends to exhibit a circular front that propagates asymptotically at constant speed front (cf. Fig. 3.50). Hence, the propagation speed is affected by the curvature of the interface. Figure 3.51 depicts the spatiotemporal evolution of a point in the interface. From the images of Figs. 3.50 and 3.51, ones concludes that the front speed v indecreases with curvature (see Fig. 3.51), that is, $v = v_\infty + \alpha\kappa$ with v_∞ asymptotic front speed of a flat interface, κ curvature and α appropriate dimensionless constant. It follows from these images that the interface tends to become smooth. The above result is known as velocity-curvature or Gibbs-Thomson effect [133, 83].

3.8.1 Gibbs-Thomson effect

This effect corresponds to variation in pressure or chemical potential across a curved surface between two coexistence substances or states. To figure out this effect, let us imagine a flat interface between to states A and B as is illustrated in Fig. 3.52b. The physical quantity that accounts for these interface in thermodynamic equilibrium is the Gibbs free energy $\mathcal{G}(T, P, N)$ where $\{T, P, N\}$ account for temperature, pressure and number of particles, respectively. The variation of this quantity satisfies

$$\Delta\mathcal{G} = -S\Delta T + V\Delta p + \mu\Delta N. \tag{3.144}$$

Considering both states have same temperature and there is not interchange of particle. The pressure difference between both states is $\Delta p = \Delta\mathcal{G}/V$. Introducing the density of free energy $\Delta\epsilon \equiv \Delta\mathcal{G}/V$ and assuming the system is viscous, then the interface speed v is proportional to the pressure difference and reads

$$v = -\frac{\Delta\epsilon}{M}, \tag{3.145}$$

where M is the mobility. Therefore the interface propagates from more stable state to lower one. Indeed, a motionless interface is only admissible if both state have the same pressure ($P_1 = P_2$), that is when a mechanical equilibrium is established. However the above scenario changes completely when one considers a circular interface (cf. Fig. 3.52).

One must consider an extra term in the free energy associated with surface energy (Laplace law [25]), that is,

$$\Delta\mathcal{G} = -S\Delta T + V\Delta p + \mu\Delta N - \gamma A. \tag{3.146}$$

where γ is the surface tension. Analogously to the above considerations, one gets

$$\Delta p = \Delta\epsilon + \gamma\frac{A}{V}. \tag{3.147}$$

Consider a circular drop of radius R, we have $A = 2\pi R$ and $V = \pi R^2$, then

$$\Delta p = \Delta\epsilon + 2\gamma\kappa, \tag{3.148}$$

with $\kappa \equiv 1/R$ is the curvature of the drop. Hence, the drop speed is (the Gibbs-Thomson effect)

$$v = \frac{\Delta\epsilon}{M} + \Gamma\kappa, \tag{3.149}$$

with $\Gamma \equiv 2\gamma/M$. Therefore, the drops can have a difference of pressure as result of curvature (see Fig. 3.52) and the interface can propagate by to mechanism: i) difference of energy of the states and ii) curvature of the interface. We note that in the population dynamics simulations in two spatial dimensions we observe the same phenomenon.

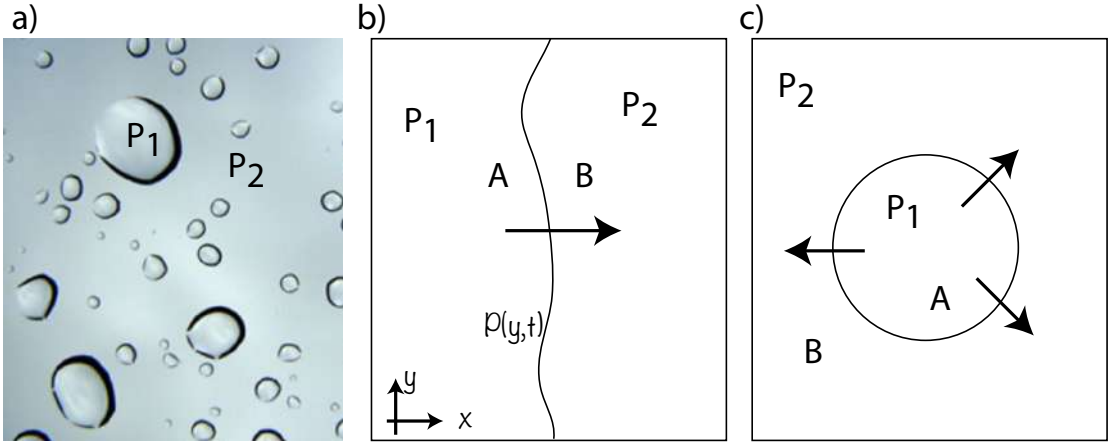

Figure 3.52: Coexistence drop of water and water vapor. a) Snapshot of water drop. Schematic representation of a flat (b) and circular interface between two states (c), represented by A and B. P_1 and P_2 are the respectively pressures. $P(y,t)$ parametrizes the interface.

Another physical context where it is known that the speed depends on the curvature is in crystal growth [37].

3.8.2 Analytical explanation of velocity-curvature effect

Let us consider a circular front $N(r-vt)$ of model (3.143), where $\{r,\theta\}$ are the radial and angular coordinate, that satisfies

$$-v\partial_r N(r,t) = rN\left(1-N\right) + \partial_{rr}N + \frac{1}{r}\partial_r N. \tag{3.150}$$

Introducing local coordinate $r = R_0 + x$ and $y = R_0\theta$ with R_0 the radius of the front position in the above equation, one gets

$$-v\partial_x N(x,t) = rN\left(1-N\right) + \partial_{xx}N + \frac{1}{R_0+x}\partial_x N. \tag{3.151}$$

Assuming the a large circular front in compare with the front width, $1/(R_0+x) \approx 1/R_0$. Thus the front equation satisfies

$$rN\left(1-N\right) + \partial_{xx}N + \left(v + \frac{1}{R_0}\right)\partial_x N = 0, \tag{3.152}$$

which corresponds to a one-dimensional FKPP equation with a equivalent speed $v' = v + 1/R_0$. Hence, the front profile for large radius is given by formula (3.25).

3.8.3 Dynamics around a flat interface

To model the transverse dynamics of a propagative front of population in a two-dimensional system, we consider a flat or slightly disturbing interface, as illustrated in Fig. 3.52b. Note that FKPP equation (3.143) has a flat front solution that corresponds to the one dimension FKPP solution (3.25) extended in the transversal, that is

$$N(x,y,t) = N_{FKPP}(x - vt - P), \tag{3.153}$$

where $N_{FKPP}(x-vt)$ is a solution of Eq. (3.12) and P stands for the front position or interface. To account the slightly perturbation of the flat interface, we consider the

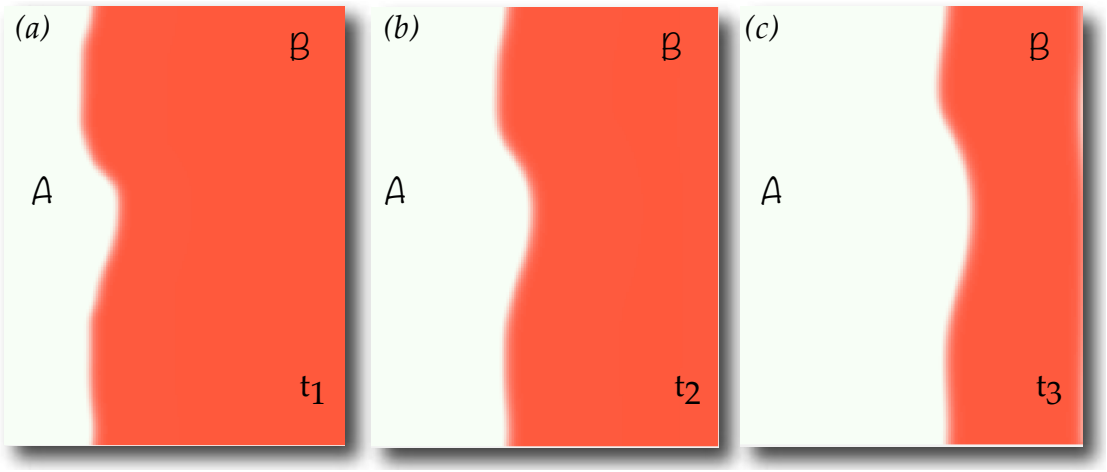

Figure 3.53: Sequence of temporal evolution of a perturbative flat interface between two state $\{A, B\}$ $(t_1 < t_2 < t_3)$.

ansatz

$$N(x, y, t) = N_{FKPP}[x - vt - P(y, t)] + w(z \equiv x - vt - P, P), \tag{3.154}$$

where the front interface $P(y, t)$ as promoted to a scalar temporal field, that is, $P(y, t)$ parametrizes the interface (cf. Fig. 3.52b); w accounts for the profile settings when the interface is deformed. Introducing the former ansatz in Eq. (3.143) and linearized in w, one gets at dominant order

$$\begin{aligned} \partial_t N &= -(v + \partial_t P)\partial_z N_{FKPP} - v\partial_z w = rN_{FKPP}(1 - N_{FKPP}) + \partial_{zz} N_{FKPP} \\ &+ (r - 2N_{FKPP} + \partial_{zz})w + \partial_{zz} N_{FKPP}(\partial_y P)^2 - \partial_z N_{FKPP}\partial_{yy} P. \end{aligned} \tag{3.155}$$

Rewriting the above expression and using that N_{FKPP} is solution of Eq. (3.12), one gets

$$-\left(r - 2N_{FKPP} + v\partial_z + \partial_{zz}\right) w = \partial_t P \partial_z N_{FKPP} + \partial_{zz} N_{FKPP}(\partial_y P)^2 - \partial_z N_{FKPP}\partial_{yy} P. \tag{3.156}$$

To solve the above equation, we impose the Fredholm alternative or solvability condition[3] and it reads

$$\partial_t P = \frac{\langle \Phi(z) | \partial_z N_{FKPP} \rangle}{\langle \Phi(z) | \partial_z N_{FKPP} \rangle} \partial_{yy} P + \frac{\langle \Phi(z) | \partial_{zz} N_{FKPP} \rangle}{\langle \Phi(z) | \partial_z N_{FKPP} \rangle} (\partial_y P)^2. \tag{3.157}$$

[3]Similar method was used in Section 3.1.9.

This equation with additive noise corresponds to a nonlinear diffusion equation known as the Kardar-Parisi-Zhang (KPZ) equation [94]. The dynamics of the previous equation are characterized by diffusive dynamics plus a nonlinear advection term that tends to cancel out the local protuberances.

Then, the interface in the co-mobile system satisfies a diffusion equation, that is, the perturbation of the flat interface diffuses and disappears. Therefore, the propagative flat interface is stable. Figure 3.53 shows the temporal evolution of a perturbative flat interface, which is consistent with a diffusive equation.

Given a curve $P(y,t)$ parametrized in the space by y, assuming that this curve is not multi evaluated, the curvature is defined by

$$\kappa = \sqrt{\left(\frac{\partial_{yy}P}{\sqrt{1+(\partial_y P)^2}} - \frac{(\partial_y P)^2\partial_{yy}P}{[1+(\partial_y P)^2]^{3/2}}\right)^2 + \left(\frac{(\partial_y P)^2\partial_{yy}P}{[1+(\partial_y P)^2]^{3/2}}\right)^2}, \tag{3.158}$$

Considering the flat interface is smooth enough ($\partial_y P \ll \partial_{yy}P \ll 1$) at dominate order, we obtain that $\kappa \approx \partial_{yy}P$. Thus, Eq. (3.157) can write as $\partial_t P = \alpha\kappa(P)$. Hence, in general we expect that the interface satisfies an equation of the form

$$\partial_t P = \alpha\partial_{yy}P + \beta(\partial_y P)^2\partial_{yy}P, \tag{3.159}$$

which correspond to a nonlinear diffusion equation. Figure 3.54 illustrates a numerical simulation of the above model. One clearly notes that the interface tends to soften and subsequent dynamic is controlled by the linear diffusion equation. Hence, the interface propagates and ends in a stable flat interface. The above equation can rewrite as

$$\partial_t P = \partial_y J \equiv \partial_y\left(\alpha\partial_y P + \beta\frac{(\partial_y P)^3}{3}\right), \tag{3.160}$$

where J is a flux of the interface P. Indeed, the interface satisfies a continuity equation, that is, in the co-mobile reference system the area of the interface, $\int P(y,t)dy$, is conserve. Furthermore, equation (3.159) is a variational model becuse

$$\partial_t P = -\frac{\delta F}{\delta P}, \tag{3.161}$$

with

$$F[P_y] = \int \left(\alpha \frac{P_y^2}{2} + \beta \frac{P_y^4}{12} \right) dy. \tag{3.162}$$

Therefore, the dynamical evolution of model (3.159) is characterized to minimize the functional F. Taking the spatial derivative and introducing the variable $\Lambda = \partial_y P$, the above equation reads

$$\partial_t \Lambda = \partial_{yy} \frac{\delta \mathcal{F}}{\partial \Lambda} = \partial_{yy} \left(\alpha \Lambda + \beta \frac{\Lambda^3}{3} \right), \tag{3.163}$$

where

$$\mathcal{F}[\Lambda] = \int \left(\alpha \frac{\Lambda^2}{2} + \beta \frac{\Lambda^4}{12} \right) dy. \tag{3.164}$$

This model it is know as the Cahn-Hilliard equation [38, 39, 19]. Let us consider

$$\frac{d\mathcal{F}}{dt} = \int dy \frac{\delta \mathcal{F}}{\partial \Lambda} \partial_t \Lambda = \int dy \frac{\delta \mathcal{F}}{\partial \Lambda} \partial_{yy} \frac{\delta \mathcal{F}}{\partial \Lambda} = - \int dy \left(\partial_y \frac{\delta \mathcal{F}}{\partial \Lambda} \right)^2 \leq 0. \tag{3.165}$$

Hence, the dynamics of this model (3.163) is characterized by the minimization of $\mathcal{F}$, that is, this equation is relaxation type.

The Cahn-Hilliard equation has been derived to describe the phase separation dynamics in a conservative system, such as binary alloys [66], binary liquids [145], glasses [80],

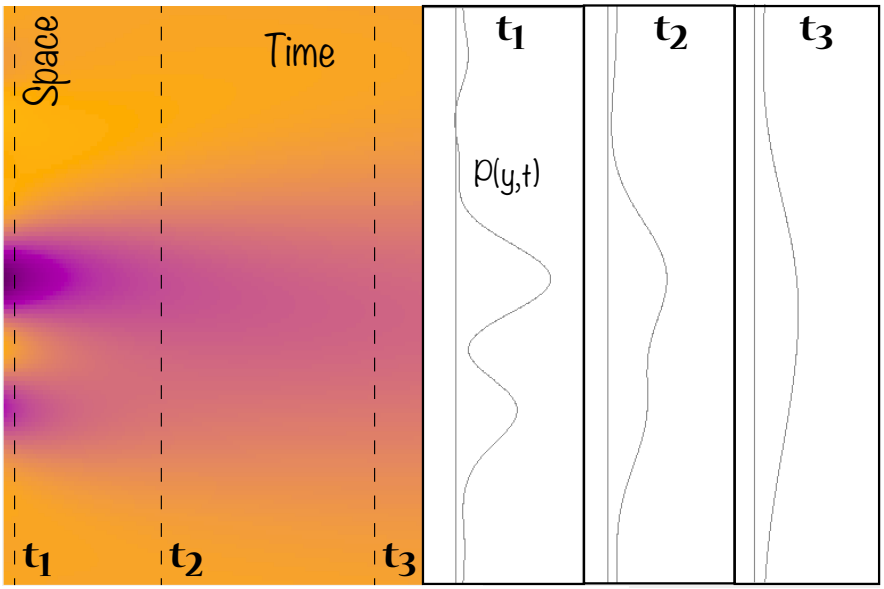

Figure 3.54: Spatiotemporal evolution of the nonlinear diffusion equation (3.159). The right panels correspond to the profile of the interface given three times $\{t_1, t_2, t_3\}$, respectively.

and polymer solutions [147] to mention a few.

3.9 Front propagation in Nonreciprocal Coupling

The analysis and study presented in this section are based on article [132].

The dynamics of coupled oscillators have attracted the attention of physics since its dawn. Phenomena like synchronization [131], energy transfers from one oscillator to another [63], or wave propagation [69] are paradigmatic dynamical behaviors of coupled oscillators. In all the above examples, the oscillators are usually coupled with reciprocal elastic media. Namely, the elastic media are characterized by applying a force of equal magnitude and opposite direction to each coupled oscillator; such dynamical behavior is known as Maxwell-Betti reciprocity [116, 29]. Namely, if the oscillators are swapped, the force or propagation of the energy is indistinguishable. Non-reciprocal behavior has been studied in diverse physical fields due to asymmetrical, nonlinear, and/or time non-reversal features. In optics, non-reciprocal responses have been observed in birefringent prisms [6], optomechanical resonators [121], and asymmetric cavities [167]. In acoustics, an emitter and a receiver can exhibit non-reciprocal behaviors in a resonant ring cavity biased by a circulating fluid [72]. A similar phenomenon is achieved for electrically driven non-reciprocity on a silicon chip [107]. Non-reciprocal behaviors for the propagation of electromagnetic waves have been accomplished through the application of magnetic fields [166, 85], angular momentum [148], nonlinear coupling [105], and moving photonic crystal [165]. In active matter, non-reciprocal couplings are a rule rather than an exception [128, 77]. Recently, through the use of mechanical metamaterials [54, 93], non-reciprocal coupling elements have been built up.

To study the non-reciprocal coupling effect on nonlinear waves, based on a prototype model of a nonlinear chain, the dissipative Frenkel-Kontorova model [35] with non-reciprocal coupling to nearest neighbors, a convective instability between unstable and stable equilibrium is observed. Let us consider a dimensionless chain of $N+1$ dissipative coupled pendulums (the dissipative Frenkel-Kontorova model with non-reciprocal

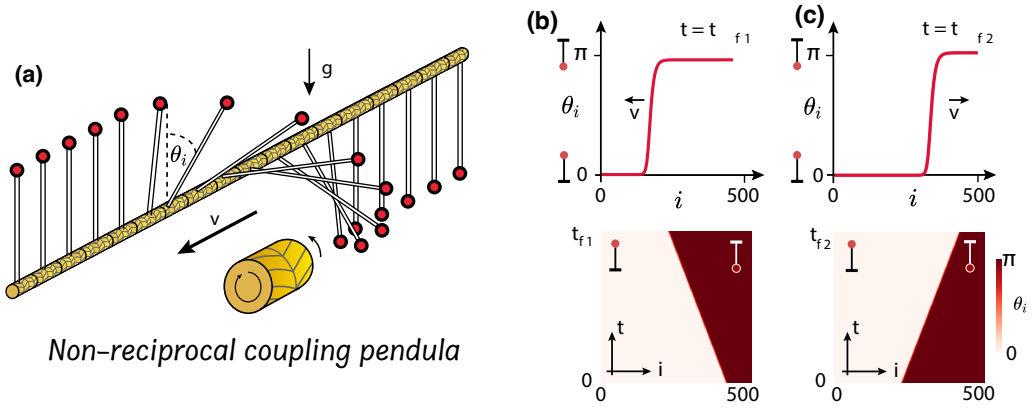

Figure 3.55: Non-reciprocal coupled pendula chain and front propagation. (a) Schematic representation of a chain of pendulums coupled with a non-reciprocal material. $\theta_i(t)$ is the angle formed by the pendulum and the vertical axis in the i-position at time t. Yellow cylinder accounts for a non-reciprocal metamaterial. Instantaneous profile and spatiotemporal evolution of π-kink obtained for Eq. (3.170) with $\omega = 1$, $D = 4$, $\alpha = 1$ (b), and $\alpha = 2.5$ (c). This figure is a modification of a figure of article [132].

coupling [132])

$$\ddot{\theta}_i = \omega^2 \sin\theta_i - \mu\dot{\theta}_i + (D-\alpha)\,(\theta_{i+1} - \theta_i) - (D+\alpha)(\theta_i - \theta_{i-1}), \tag{3.166}$$

where $\theta_i(t)$ is the angle formed by the pendulum and the vertical axis in the i-position at time t (cf. Fig. 3.55a). ω and μ are the natural frequency and the damping coefficient of pendulums. D and α account for coupling elements that have different left-to-right and right-to-left linear responses. α accounts for the non-reciprocal coupling; when $\alpha = 0$, the chain has a reciprocal coupling. D stands for the linear deformation of an elastic material. α could account for the linear deformations of a rubber non-reciprocal torsion metamaterial [54] or a non-reciprocal robotic coupling [34]. Figure 3.55 shows a schematic representation of a chain of dissipative coupled pendulums. Note that $\theta_i = 0$ and $\theta_i = \pi$ describe the upside-down and upright pendulum, respectively. Equation (3.166) is of Lagrangian nature, which has the form [132]

$$\mathcal{L} = \sum_i \left[\frac{\dot{\theta}_i^2}{2} - \omega^2 \cos\theta_i - \frac{D-\alpha}{2}(\theta_{i+1} - \theta_i)^2 \right] e^{\mu t} \Lambda^i,$$

where $\Lambda \equiv (D-\alpha)/(D+\alpha)$ is an auxiliary parameter. Using the principle of least action, the Euler-Lagrange equation reads

$$\frac{d}{dt}\left(\frac{\partial L}{\partial \dot{\theta}_k}\right) - \frac{\partial L}{\partial \theta_k} = 0. \tag{3.167}$$

To obtain this equation, one must determine

$$\frac{\partial L}{\partial \theta_k} = \left(\omega^2 \sin\theta_k + (D-\alpha)(\theta_{k+1}-\theta_k)\left(\frac{D-\alpha}{D+\alpha}\right)^k - (D-\alpha)(\theta_k-\theta_{k-1})\left(\frac{D-\alpha}{D+\alpha}\right)^{k-1}\right) e^{\mu t}, \tag{3.168}$$

and

$$\frac{d}{dt}\left(\frac{\partial L}{\partial \dot{\theta}_k}\right) = \left(\ddot{\theta}_k + \mu\dot{\theta}_k\right)\left(\frac{D-\alpha}{D+\alpha}\right)^k e^{\mu t}. \tag{3.169}$$

Equating both terms, factoring $e^{\mu t}$ and $\left(\frac{D-\alpha}{D+\alpha}\right)^k$, one obtains Eq. (3.170). Thereby, the dynamics of Eq. (3.166) is steered by a principle of least Action. To figure out that the non-reciprocal chain dynamics have more straightforward calculations and analytical expressions, we consider the overdamped limit of the dissipative Frenkel-Kontorova model ($\mu \to \infty$). Then equation (3.166) can be approximated by

$$\dot{\theta}_i = \omega^2 \sin\theta_i + (D-\alpha)(\theta_{i+1}-\theta_i) - (D+\alpha)(\theta_i-\theta_{i-1}). \tag{3.170}$$

A similar model was proposed to study coupled Josephson junctions [154]. Two evident extended steady states correspond to the uniform upside-down and upright pendulums. To study the dynamics of nonlinear waves between these two states, we consider the boundary conditions being Dirichlet ($\theta_0(t) = 0$) and Neumann ($\theta_N(t) = \theta_{N-1}(t)$) on the left and right flank of the chain, respectively.

In the reciprocal limit, $\alpha = 0$, considering all upside-down pendulums as an initial condition, disturbing a pendulum is observed in the emergence of a nonlinear wave that propagates from the upright to the upside-down pendulums with a well-defined speed. This nonlinear wave is known as π-kink [10]. The front speed is characterized by exhibiting a weakly oscillatory behavior [10]. π-kinks are persistent in the presence of non-reciprocal coupling. Figure 3.55 shows the profile of a π-kink wave and its

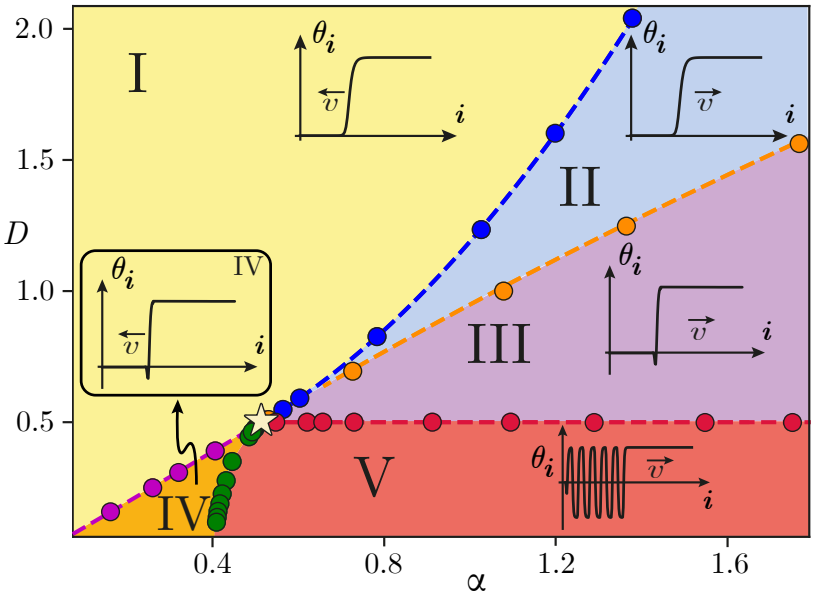

Figure 3.56: Phase diagram of the overdamped Frenkel-Kontorova equation (3.170) with $\omega = 1$. In zone I, the upright pendulums invade the upside-down ones. This process is reversed in zone II. The blue curve, formula (3.174), is the analytical absolute convective instability between the upright and upside-down pendula. The purple ($D = \alpha$) and orange curves account for the monotonous to non-monotonous front transition, using the formula (3.172). The star symbol ($\star$) accounts for the critical point ($\alpha = 1/2, D = 1/2$) where the critical curves converge. Red and green curves separate the localized structures' self-assembly region. The red curve was obtained using the formula $D = 1/2$. The green curve is achieved through the divergence of the self-assembly wavelength. All circles are obtained employing numerical simulations. This bifurcation diagram is reported in Ref. [132].

respective spatiotemporal diagram. These diagrams were obtained employing numerical simulations.

As a result of non-reciprocal coupling, the speed of the π-kink decreases when α is increased. π-kinks that invade the upside-down pendulums are observed in zone I of Fig. 3.56. The previous dynamical behaviors change when considering large enough α, through an absolute convective instability [106], the upside-down pendulums invade upright ones, see Fig. 3.55c. These fronts are observed in zone II on the bifurcation diagram in Fig 3.56.

To characterize the absolute convective instability, we use the same strategy presented

in Ref. [11]. Let us introduce the ansatz $\theta_i(t) = Ae^{k(i+\langle v\rangle t)}$ for the tail of the front, to determine the average front speed $\langle v\rangle$, where k accounts for the front steepness. Most precisely, let us consider the following ansatz for the asymptotic left tail of the front

$$\theta(i,t) \sim e^{k(i+vt)}(1+f^T_{k,i}),$$

where $f^T_{k,i}(t)$ is a small oscillatory function, $f^T_{k,i}(t) \ll 1$, with period T and zero mean value. Inserting this ansatz in Eq. (3.170), we get

$$\begin{aligned} kv(1+f^T_{k,i}) + \dot{f^T_{k,i}} = (\omega^2 - 2D + 2D\cosh k - 2\alpha\sinh k)(1+f^T_{k,i}) \\ +D(f^T_{k,i+1} - 2f^T_{k,i} + f^T_{k,i-1}) - \alpha(f^T_{k,i+1} - f^T_{k,i-1}). \end{aligned} \tag{3.171}$$

Averaging over the period T, $\langle v\rangle \equiv \int_t^{t+T} v(t')dt'/T$, we get the average front speed $\langle v\rangle$ satisfies

$$\langle v(k)\rangle = \frac{\omega^2 - 2D}{k} + 2\left(\frac{D\cosh(k) - \alpha\sinh(k)}{k}\right). \tag{3.172}$$

Note that this is equivalent to proposing the following ansatz for the asymptotic left tail of the front $\theta(i,t) \sim e^{k(i+\langle v\rangle t)}$. Therefore, the system exhibits a continuous family of nonlinear waves, fronts, parameterized by their respective steepness k and front speed $\langle v(k)\rangle$. Bounded disturbances induce front propagation into the unstable state with the minimum front speed v_{min} as a function of the steepness, i.e., $v_{min} = \langle v(k = k_c)\rangle$, where the critical k_c satisfies $\partial_k\langle v(k = k_c)\rangle = 0$ and $\partial_{kk}\langle v(k = k_c)\rangle > 0$ [159].

3.9.1 Absolute convective instability of the FKPP front

The absolute convective instability corresponds when the minimum speed is zero $\langle v(k = k_c)\rangle = 0$ [106]. Then, around this region of parameters, the propagation of the front may change the direction of propagation. In Figure 3.56, the curve that separates zone I from II corresponds to absolute convective instability. Hence, one can impose that $\langle v(k = k_c)\rangle = 0$ at this bifurcation. Using the relation

$$\partial_k(kv) = v + k\partial_k v = 2\partial_k g(k),$$

where $g(k) \equiv D\cosh k - \alpha \sinh k$ and imposing the conditions $\partial_k v = v = 0$, we get

$$\partial_k g(k)|_{k_c} = 0.$$

From this expression, it is obtained $k_c = arctanh(\alpha/D)$. Replacing k_c in formula (3.172), we obtain

$$0 = \omega^2 - 2D + 2g\left(arctanh\frac{\alpha}{D}\right).$$

Using $\cosh(arctanhx) = 1/\sqrt{1-x^2}$ and $\sinh(arctanhx) = x/\sqrt{1-x^2}$, the following expression describes the absolute-convective instability in the (D, α) plane

$$0 = \omega^2 - 2D + \frac{2D}{\sqrt{1-\left(\frac{\alpha}{D}\right)^2}} - \frac{2\alpha^2/D}{\sqrt{1-\left(\frac{\alpha}{D}\right)^2}} = \omega^2 - 2D + \frac{2D}{\sqrt{1-\left(\frac{\alpha}{D}\right)^2}}\left(1 - \left(\frac{\alpha}{D}\right)^2\right). \tag{3.173}$$

Simplifying this expression

$$\omega^2(\omega^2 - 4D) = -4\alpha^2,$$

and finally solving for D, it reduces to

$$D = \frac{\alpha^2}{\omega^2} + \frac{\omega^2}{4}. \tag{3.174}$$

Figure 3.56 shows the bifurcation diagram of the overdamped Frenkel-Kontorova model, Eq. (3.170). The dashed blue curve accounts for the previous expression (absolute convective instability). Notice that for large D coupling, the system is adequately described by the continuous limit, the dissipative sine-Gordon equation with advection, where the dynamic behaviors described above are expected.

3.9.2 Phase diagram of the overdamped Frenkel-Kontorova equation

Surprisingly, as α increases further, the fronts exhibit a transition from monotonous to non-monotonous fronts. Figure 3.57 shows the typical non-monotonous front observed and its propagation. These fronts are observed in zones III and IV of the phase diagram shown in Fig. 3.56. In zone III (IV), the upside-down (upright) state propagates into

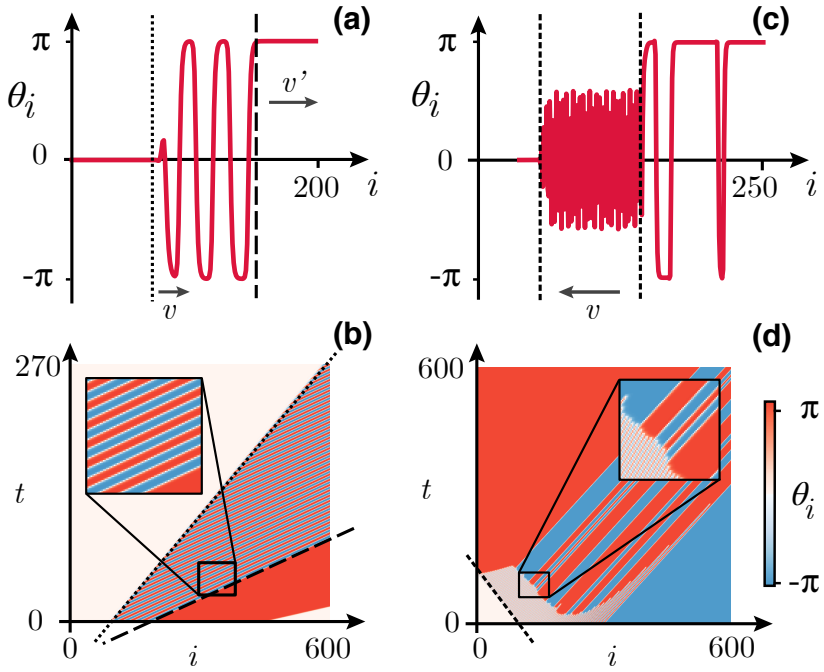

Figure 3.57: Non-monotonous fronts of the overdamped Frenkel-Kontorova equation (3.170) with $\omega = 1$. Profile (a) and spatiotemporal evolution (b) of a non-monotonous front propagates from upside-down pendulums into upright ones for $D = 1$ and $\alpha = 1.25$. v and v' account for speeds of different fronts. Profile (c) and spatiotemporal evolution (d) of a non-monotonous front propagates from upright pendulums into upside-down for $D = 0.25$, and $\alpha = 0.325$. This figure is reported in Ref. [132].

the upright (upside-down) one. The transition from monotonous to non-monotonous front is characterized by the fact that the speed curve $\langle v(k)\rangle$, formula (3.172), ceases to have a minimum, which becomes an inflection point. Indeed, the minimum is now in the complex plane of k, where the imaginary part corresponds to the spatial oscillations observed in the front profile (cf. Fig. 3.57). By imposing that $\langle v(k = k_c)\rangle$ stops having a minimum, we obtain

$$\frac{2D - \omega^2}{\operatorname{arctanh}\left(\frac{D}{\alpha}\right)} = 2\alpha\sqrt{1 - \left(\frac{D}{\alpha}\right)^2}. \tag{3.175}$$

For $D < \omega^2/2$, an explicit solution of the above transcendent equation is $D = \alpha$. Notice that this relationship corresponds to the fact that each oscillator is only coupled towards the left flank. Furthermore, when $D < \alpha$, springs towards the right side are not of restoring behavior; that is, their elastic constant is negative. The above is

Figure 3.58: Self-assembly of localized structures and the wavelength surface map for the overdamped Frenkel-Kontorova Eq. (3.170) with $D = 0.4$, $\alpha = 0.5$, and $\omega = 1$. (a) Spatiotemporal evolution and respective profiles in two instants of time, $t_1 = 120$ and $t_2 = 395$. v accounts for the traveling wave velocity. (b) Wavelength surface map for the D and α parameter space.

unacceptable for mechanical springs. However, this type of coupling can be achieved using non-reciprocal robotic metamaterials [34]. For $D > \omega^2/2$, an explicit analytic expression is not accessible. Note that the curve obtained parametrically, formula (3.175), is slightly below the straight line $D = \alpha$. Figure 3.56 illustrates these curves through the purple and orange dashed line, respectively. $D = \alpha = \omega^2/2$ is a critical point where the different transition curves converge, which is represented by a star in the phase diagram of Fig. 3.58. From non-monotonous fronts where the upside-down pendulum state invades upright ones, unexpectedly, as D decreases, the emergence of a traveling wave is observed; see Fig. 3.58. Note that these patterns are characterized by connecting the vertical pendulum to itself. These propagative waves are observed in zone V on the phase diagram of Fig. 3.58.

3.10 Convective instabilities and front propagation

In population dynamics, one can imagine non-reciprocal coupling, for example, as a consequence of fluid movement. This is the case, for example, with fish populations, where one imagines that the population dynamics can be described by the model

$$\partial_t N = \mu N(1 - N) + \partial_{xx} N - v\partial_x N, \tag{3.176}$$

where N accounts for the fish populations, μ growth rate of populations with a logistic saturation, diffusive transport, and v account for the nonreciprocal coupling as consequence of drag force of the fluid. Figure 3.59a illustrates weighing in a turbulent fluid. Considering that there is no non-reciprocal effect $v = 0$, a local perturbation of the non-populated state induces two fronts that enter the system as shown in Fig. 3.59b.

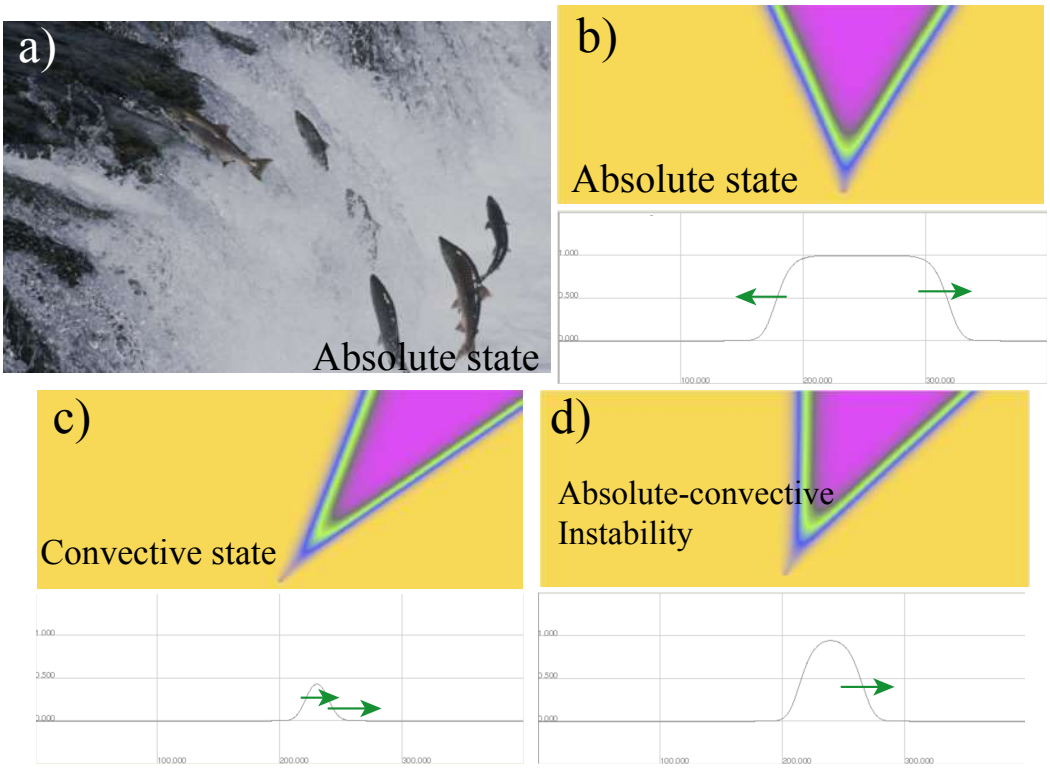

Figure 3.59: Systems with advection. a) Snapshot of fish in an environment of large force of drag by means of a fluid. Spatiotemporal diagram and profile of the population at a given instant: b) Absolute regime of the logistic model with advection, $v < v_{cia}$. A small disturbance invades the system. c) convective regime, where a small perturbation is completely advected into the system ($v > v_{cia}$), i.e. the perturbation is pulled out of the system so that the system returns to its population state. d) Convective-absolute instability, in which the disturbances cannot enter the system $v = v_{cai}$, but neither can they be advected out of the system.

If we consider a reciprocal coupling effect that is large enough $v \neq 0$, we observe that when a similar perturbation is performed, the perturbations are advected as shown in Fig.$v_{min} + v$. Namely, the disturbance generates two fronts that connect the non-population state with the population state. In this case, both fronts propagate in the same direction determined by the non-reciprocal term. Notice that the front on the right propagates faster than the front on the left (see Fig. 3.59c). A simple way to understand the previous phenomenon is to change the co-mobile reference system. Let

us introduce the coordinates $y = x - vt$ and $t = \tau$; then, Eq. (3.178) takes the form

$$\partial_\tau N = \mu N(1 - N) + \partial_{yy} N, \tag{3.177}$$

which corresponds to the FKPP model used for the propagation of fronts into a stable state, see for more details on the Chapter 3. For local perturbation, the previous equation has front solutions $N_{FKPP}(y - v_{min}\tau)$ that connect the population ($N = 1$) and non-population ($N = 0$) state that propagate with a minimum speed $v_{min} = \sqrt{u}$. Hence, the system exhibits two from $N_{FKPP}(x - (v_{min} \pm v)t)$. When $v > v_{min}$, the system has two fronts that spread towards the right flank with different speeds, the forward one $v_{min} + v$ and the rear one $v_{min} + v$, see Fig. 3.59c). Therefore, in this parameter regime, *advective regime*, the state of the population is stabilized because any disturbance is advective outside the system. On the other hand, when $v < v_{min}$ and $v > 0$, the population state invades the system with a velocity towards the right flack with $v_{min} + v$ and to the left flack with $v_{min} - v$. This regime corresponds to the *absolute regime*, the population state invading the system.

From the previous analysis, one can see that there is a critical value of velocity v_{cai}, where the system presents a transition between the absolute advective regime. This transition is achieved when the drag speed is equal to the speed of the front $v = v_{cai} = v_{min} = 2\sqrt{\mu}$. Figure 3.59d illustrates the point of absolute and convective instability. In this transition, the right front advances to the left flank, but the left front is motionless.

3.10.1 Linear analysis of absolute convective instability

Let us consider the linearized model (3.178)

$$\partial_t n = \mu n + \partial_{xx} n - v\partial_x n, \tag{3.178}$$

where $N \approx 0 + n(x, t)$ and n is a small scalar field ($n \ll 1$). Let us consider a leftward propagative perturbation in Fourier space which takes the form $n = n_0 e^{\kappa(x+v_0 t)} e^{i(kx+\omega t)}$, where κ is the steepness of the front, v_0 speed of the front, k and ω the wavenumber

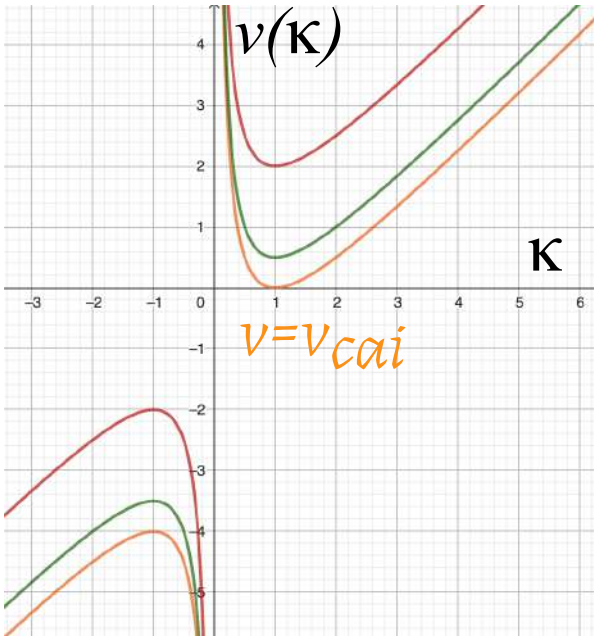

Figure 3.60: Front speed $v_0(\kappa)$ as a function of the steepness κ given a speed of the non-reciprocal term v. The curves with different colors correspond to front speed curves for different intensities of non-reciprocal coupling. The red, green and orange curves correspond to $v = \{0, 1.5\sqrt{\mu}, v_{cai} = 2\sqrt{\mu}\}$.

and frequency of the mode. Introducing this ansatz in the previous equation, one gets

$$\begin{aligned} v_o(\kappa, k) &= \frac{\mu}{\kappa} + \kappa - k^2 - v, \\ \omega(\kappa, k) &= 2k\kappa - kv, \end{aligned} \tag{3.179}$$

Figure 3.60 shows the typical form of the front speed $v_0(\kappa)$ as a function of the steepness κ given a speed of the non-reciprocal term v. Notice that the speed of the front has a minimum. To compute this minimum, we compute the derivate of V_0 as function of κ and k

$$\begin{aligned} \frac{\partial v_0}{\partial k} &= 0 = -2k, \\ \frac{\partial v_0}{\partial \kappa} &= 0 = -\frac{\mu}{\kappa^2} + 1, \end{aligned}$$

Thus the critical value $k^* = 0$ and $\kappa^* = \sqrt{\mu}$, the speed takes the form

$$v_0(\kappa^*, k^*, \{\mu, v\}) = 2\sqrt{\mu} - v, \tag{3.180}$$

$$\omega(\kappa^*, k^*) = 0, \tag{3.181}$$

Then, the speed of the front $v_0(\kappa)$ is cero for a critical velocity of the drag $v \equiv v_{cia} = 2\sqrt{\mu}$. Hence, for this drag speed v_{cia}, the left front of the propagation is motionless as illustrated in Fig. 3.60d). For speeds lower than this critical, $v < v_{cia}$, the population state invades the system, absolute regime.

3.10.2 Noise sustain structures

Chapter 4

Front propagation between stable state: bistable fronts

4.1 Motivation

Let us consider the model of nematic-isotropic transition, Eq. (3.90), with noise

$$\frac{\partial S(x,t)}{\partial t} = -AS + BS^2 - S^3 + \partial_{xx}S + \sqrt{\eta}\zeta(x,t), \tag{4.1}$$

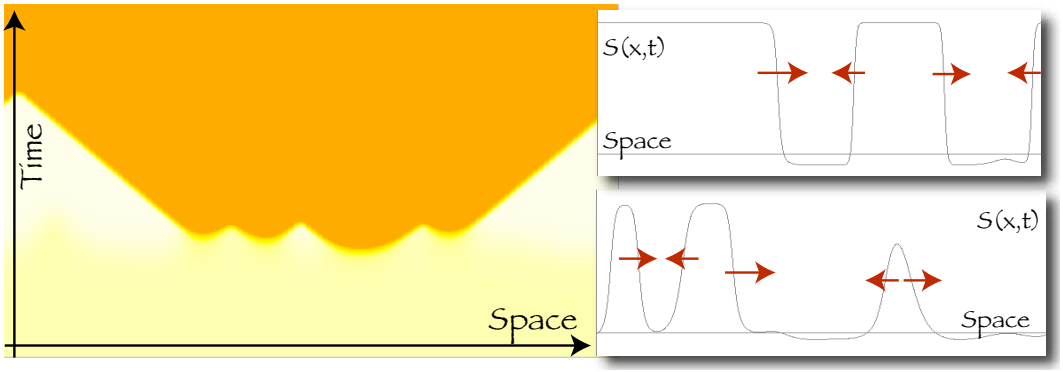

Figure 4.1: Spatiotemporal evolution of the order parameter $S(x,t)$ from the unstable state using model Eq. (4.1) with $A = 0.05$, $B = 1$, and $\eta = 10^{-5}$. The right panels illustrate the profile of S in two given consecutive instants.

where $\zeta(x,t)$ is a gaussian noise with zero mean value and correlation $\langle\zeta(x,t)\zeta(x',t')\rangle = \delta(x-x')\delta(t-t')$. For negative A, this model has two stable $\{S_m, S_{m1}\}$ and unstable state (S_I) as illustrated in the bifurcation diagram (cf. Fig. 3.28). Numerical simulations of this model from the unstable state as initial condition is characterized by the emergence of FKPP fronts between the different nematic states. Subsequently, these fronts collide, generating nonlinear wave between these two stable equilibria. Figure 4.1 depicts this front dynamics process. From this figure, one can see that the waves between the stable state propagating with a well defined speed. Throughout this chapter will be devoted to the understanding of these nonlinear waves, which we call *normal fronts* [141].

4.2 Simple model of Ferromagnetic transition

Ferromagnetic materials are characterized by exhibiting a permanent magnetic (magnets). Typical materials that exhibit this property are cobalt, iron and nickel. However, when one increases the temperature these materials lose this magnetic property. When one decreases the temperature becomes another magnetic exactly at the same critical temperature, which is referred to as the Curie temperature, T_C [96]. From a microscopic

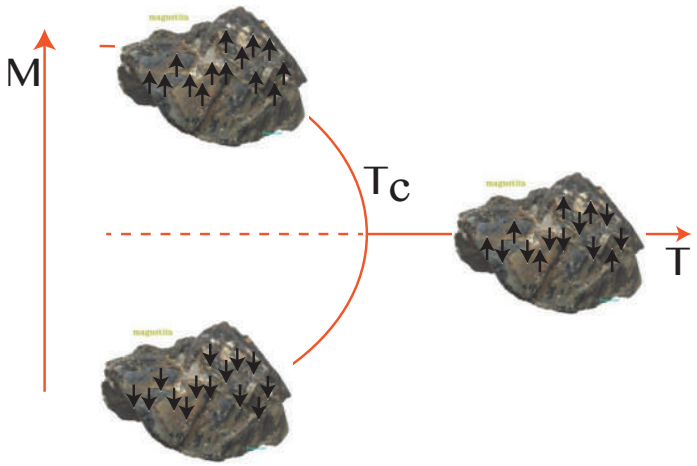

Figure 4.2: Schematic representation of ferromagnetic transition. T and M account for the temperature and magnetization, respectively.

point of view to sufficiently high temperatures the magnetic spins of the material are disordered. Figure 4.2 illustrates the ferromagnetic materials as function of temperature. For temperatures lower than the Curie temperature, the magnetic spins are arranged in one or another direction.

Following the spirit of Landau to describe this transition [152, 101], let us consider as an order parameter the magnetization $M(\vec{r},t)$, which accounts for the density of magnetic spins or moments. When the magnetization is zero the system does not exhibit magnetism. Assuming the ferromagnetic transition is smooth and there is magnetic exchange with the first neighbors. The free energy that characterize the ferromagnetic transition is

$$F = \int \left(\epsilon \frac{M^2}{2} + \frac{M^4}{4} + \cdots + \frac{[\partial_x M]^2}{2} \right) dx, \tag{4.2}$$

where ϵ is the bifurcation parameter that is proportional to $T - T_c$. The dynamics of magnetization is given by (dissipative ϕ^4-model)

$$\partial_t M = -\frac{\delta F}{\delta M} = \epsilon M - M^3 + \partial_{xx} M. \tag{4.3}$$

For positive ϵ there is only one states ($M = 0$) and for ϵ negative, the system has three equilibria one unstable and two stables. Figure 4.2 shows the bifurcation diagram of

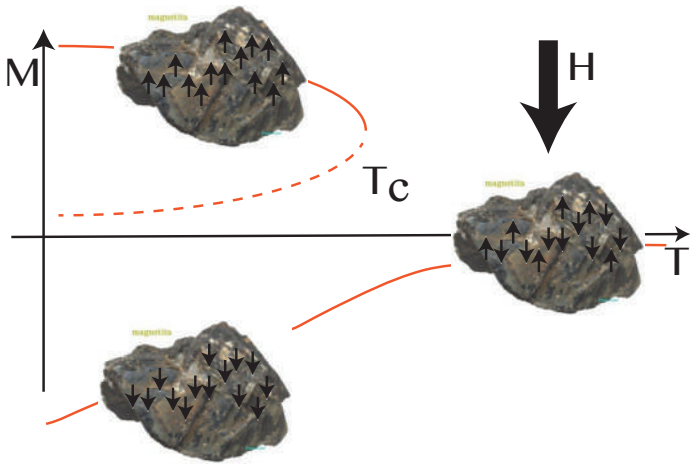

Figure 4.3: Schematic representation of ferromagnetic transition under the influence of an external magnetic field H.

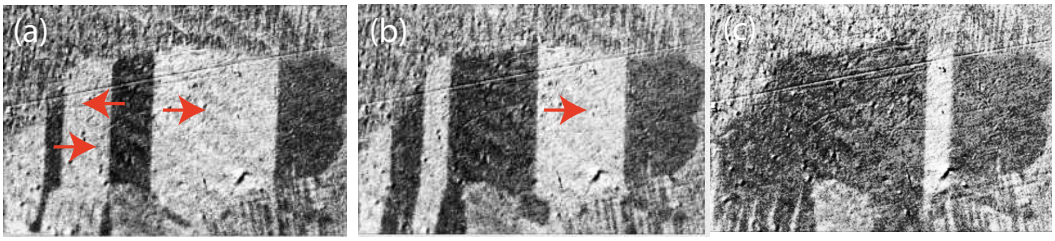

Figure 4.4: Temporal sequence of snapshot of a magnetic material under the influence of an external magnetic field.

this model, where the equilibria are $M = \{0, \pm\sqrt{\epsilon}\}$. In presence of external magnetic field the above scenario changes, the ferromagnetic transition becomes an imperfect transition as it is illustrated in Fig. 4.3. Indeed, the forced magnetic material is a magnet even over the curie temperature (cf. Fig. 4.3). The external magnetic field favors a magnetization on the other. Hence, the external magnetic field broke the symmetry between both magnetic equilibria. A simple term that broke this symmetry in the free energy is

$$F = \int \left(HM + \epsilon \frac{M^2}{2} + \frac{M^4}{4} + \cdots + \frac{[\partial_x M]^2}{2} \right) dx, \tag{4.4}$$

likewise the dynamics of the magnetization reads

$$\partial_t M = H - \epsilon M - M^3 + \partial_{xx} M. \tag{4.5}$$

The bifurcation diagram of this model is depicted in Fig. 4.3. Due to this transition has coexistence between two stable domain, one expect to observe front propagation between this two asymmetric states. Figure 4.4 shows a temporal evolution of a magnetic material under the influence of an external magnetic field.

4.3 Analytical characterization of front speed

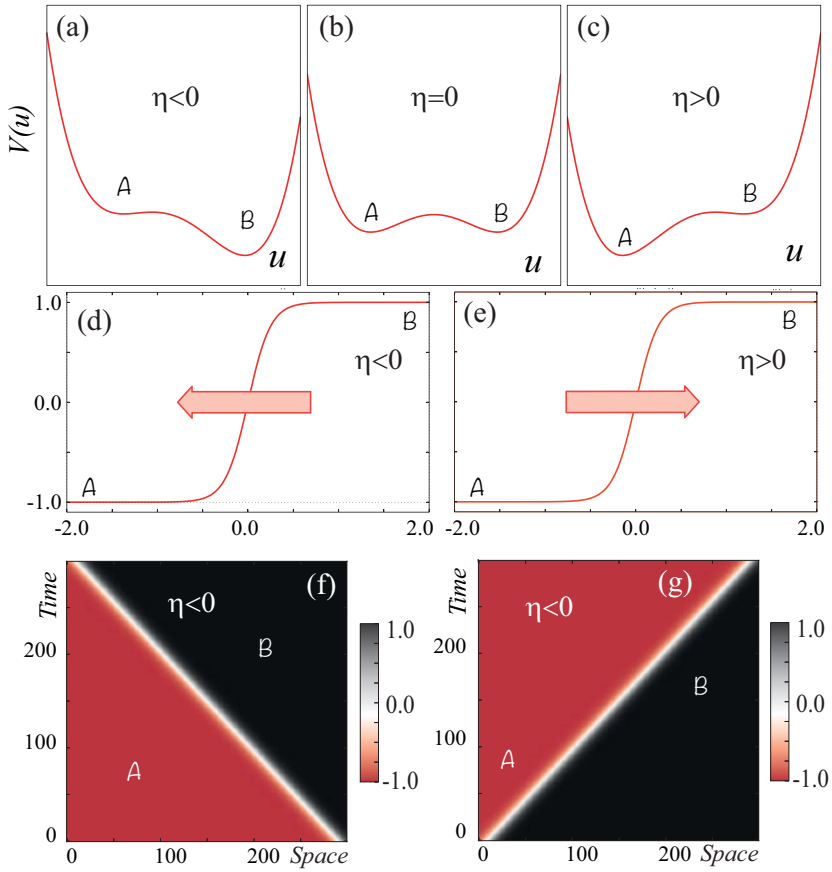

Figure 4.5: Front propagation in bistable variational model Eq. (4.9) with positive ϵ. The upper panels represent the potential, $V(u)$, for different values of η. The middle and lower panels illustrate the front profile and their respective spatiotemporal evolution [14].

4.3.1 Variational systems

Let us consider a simple one dimensional reaction diffusion model of the form

$$\partial_t u = -\frac{\partial V}{\partial u} + \partial_{xx} u = -\frac{\delta F}{\delta u}, \tag{4.6}$$

with a bistable potential and

$$F = \int \left(V(u) + \frac{[\partial_x u]^2}{2} \right) dx. \tag{4.7}$$

To fix ideas we can consider a potential

$$V(u) = -\eta u - \epsilon u^2/2 + u^4/4. \tag{4.8}$$

In the upper panels of Fig. 4.5 is represented the potential for different value of η and positive ϵ. This system have two trivial equilibria represented by $\{\mathcal{A}, \mathcal{B}\}$, that is, in this region of parameters the system exhibits bistability. For small η, the equilibria has the form $\mathcal{A} = \sqrt{\epsilon} + O(\eta)$ and $\mathcal{B} = -\sqrt{\epsilon} + O(\eta)$.

Thus, the reaction diffusion equation reads

$$\partial_t u = \eta + \epsilon u - u^3 + \partial_{xx} u. \tag{4.9}$$

This model correspond to a simplified model of ferromagnetic transition. From the dynamical point of view this model correspond to an extended pitchfork bifurcation [59], where ϵ and η are the bifurcation parameter and parameter that controls the relative stability between equilibria. This bifurcation accounts for the nascent of bistability [153]. In the context of catastrophe theory the previous model corresponds to an extended cusp catastrophe [20, 76].

Numerical simulations of the above model by small η and positive ϵ show front propagation between the equilibria. Figure 4.5 shows the profile and spatiotemporal evolution of front solutions of simple bistable model (4.9). Considering a propagative solution $u(x - vt)$, we have the following Newton type equation

$$-v\partial_z u = -\frac{\partial V}{\partial u} + \partial_{zz} u, \tag{4.10}$$

where $z = x - vt$ is the co-mobile coordinate. Thus the above equation can rewrite as

$$\partial_{zz} u = \frac{\partial V}{\partial u} - v\partial_z u = -\frac{\partial W}{\partial u} - v\partial_z u, \tag{4.11}$$

This equation correspond to a Newton type equation with a potential $W(u) = -V(u)$, that is, the potential is inverted. Figura 4.6 depicts the respective potentials V and W. Hence for this Newton type equation, the front solution corresponds to a heteroclinic curve between the equilibria. Then, starting from $\mathcal{B}$ state, there is an only one damping coefficient v_c, for which the system presented an heteroclinic. For larger speeds ($v > v_c$) the trajectory from $\mathcal{B}$ ends at the unstable equilibrium, which corresponds to a local minimum of effective potential W. Figure 4.6 shows this equilibrium that is represented

by $\mathcal{C}$. Contrary to lower speeds ($v < v_c$), the trajectory diverges to infinity. Therefore, normal fronts only have a single speed of propagation ($v = v_c$). Which it is a completely different features in compare to FKPP fronts.

In the case of considering a front connecting $\mathcal{A}$ with $\mathcal{B}$, it is important to note that the state $\mathcal{A}$ corresponds to a local minimum, then the speed is negative to generate this trajectory, i.e., this term is now an injection energy ($v < 0$). From Newton type equation, one can infer that when two states have the same energy, the front solution is motionless. The possibility of parameter space having a motionless front is known in the literature as Maxwell point [79]. Thus the mechanism of propagation of fronts between stable states for variational systems is the energy difference between these states. That is, when the front spreads the free energy F decreases.

To determine analytically the front speed, one can multiply Eq. (4.10) by $\partial_z u$ and integrated in the entire domain, one gets

$$\begin{aligned} -v\int dz(\partial_z u)^2 &= -\int dz\frac{\partial V}{\partial u}\partial_z u + \int dz\partial_{zz}u\partial_z u, \\ &= -\int dz\frac{\partial V}{\partial z} + \int dz\partial_z\left(\frac{[\partial_z u]^2}{2}\right), \\ &= -\Delta V + \frac{[\partial_z u]^2}{2}|_{-\infty}^{\infty}, \end{aligned} \tag{4.12}$$

where $\Delta V = V(z=-\infty) - V(z=\infty) = V(\mathcal{A}) - V(\mathcal{B})$. Using the fact that the front in infinity converges to the steady state, thus $\partial_z u|_{\pm\infty} = 0$. Finally, one obtains the

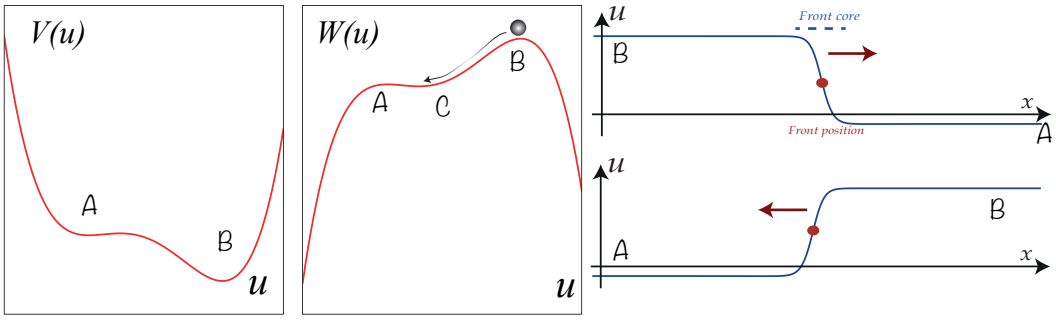

Figure 4.6: Bistable potential. Left and central panel correspond to original and effective potential in the Newton type equation. Right panels account for the normal front solutions.

following expression for the front speed [135]

$$v = \frac{\Delta V}{\int dz(\partial_z u)^2}. \tag{4.13}$$

From the above formula, one can conclude that the front speed is proportional to the energy difference. However, the above expression is not an explicit formula for the front speed since the $u(z)$ profile depends on v. Note that the above result is valid for any variational system of the form (4.6).

Front propagation close to Maxwell's point

Let us consider $\eta = 0$, Maxwell's point, the bistable model (4.9) has a motionless front solution of the form

$$u(x,t) = \sqrt{\epsilon}\tanh\left(\frac{\sqrt{\epsilon}(x-x_0)}{2}\right), \tag{4.14}$$

where x_0 stands for the front position. Considered the term proportional to η as a perturbative one, we can consider the following ansatz

$$u(x,t) = \sqrt{\epsilon}\tanh\left(\frac{\sqrt{\epsilon}(x-x_0(t))}{2}\right) + w(x,x_0), \tag{4.15}$$

where the front position is promoted to a temporal function and w is a small correction function. We assume that the temporal variation of front position and w are the orden of perturbation ($\dot{x}_0 \sim w \sim \eta$). Introducing the above ansatz in Eq. (4.9), linearizing in w, and after straightforward calculations we obtain the following solvability condition

$$\dot{x}_0 = \frac{\eta \int dz \partial_z u}{\int dz(\partial_z u)^2} = \frac{3\sqrt{2}}{2\epsilon}\eta. \tag{4.16}$$

Then the front speed is proportional to η.

4.4 Front propagation at the Freedericksz transition

As we have already mentioned in Chapter 3.2.2, the liquid crystals are characterized by having a locally orientational order. This soft material must be sustained in a container. The container walls interact with the liquid crystal molecules in the walls inducing

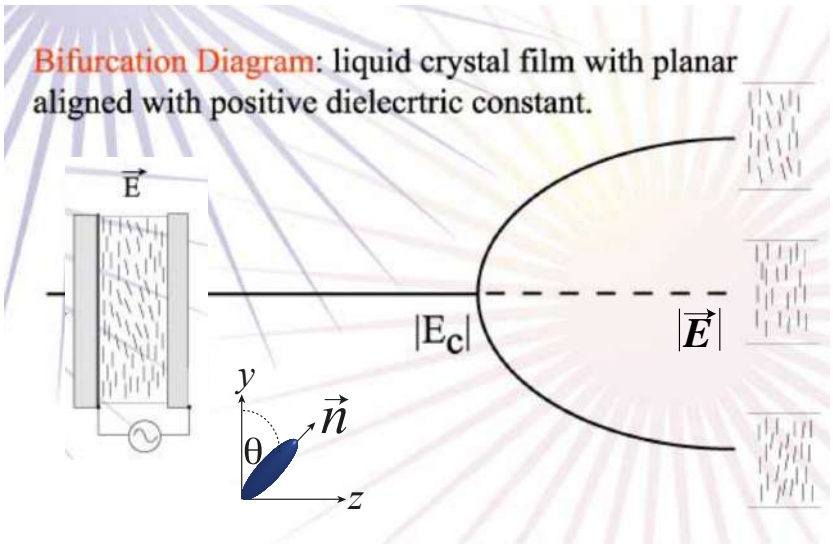

Figure 4.7: Schematic representation of the Freedericksz transition for a nematic liquid crystal with planar anchoring.

certain orientations. If molecules are oriented parallel or orthogonal to the walls is referred to as planar or homeotropic anchoring [41, 62]. Figure 4.7 shows a nematic liquid crystal sample with planar anchoring. As a result of anchoring all molecules are oriented in the same direction, because anchoring molecules apply a torque over the other molecules. Through the application of an external field one can induce an extra torque [41, 62]. In particular, if the molecules have positive dielectric constant, the application of a voltage orthogonal to the walls can induce a torque such that molecules like to be parallel to electric field. Competition between the torque induced by the anchored molecules (elasticity) and the torque induced by the external field can induce an instability for the molecular orientational order. This instability is well-know as *the Freedericksz transition* [41, 62]. Indeed, there is a critical value of the intensity of the electric field, $|\vec{E}_c|$, for which the molecules stars to rotate. Figure 4.7 depicts the the Freedericksz transition.

Experimental observations of Freedericksz transition to nematic liquid crystal samples show that this instability is supercritical [62]. To describe the dynamics of a nematic liquid crystal thin film must be introduced as order parameter average angle molecules

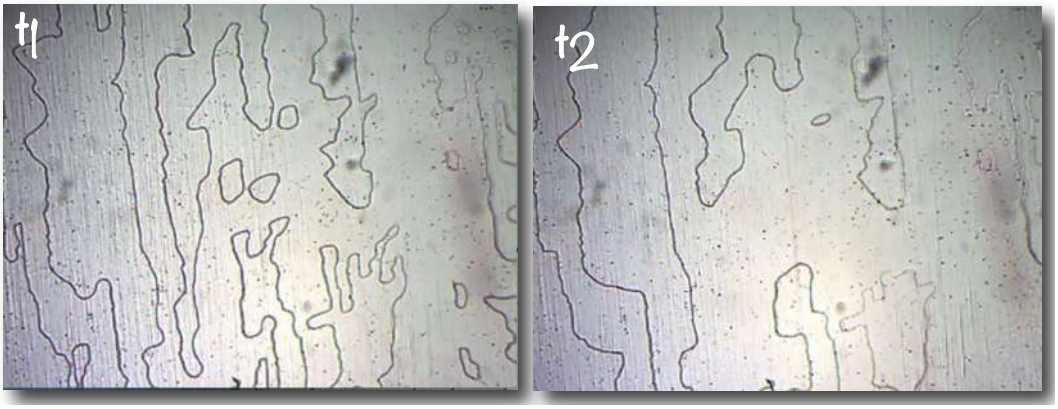

Figure 4.8: Domain walls above the Freedericksz transition for successive instant ($t_1 > t_2$), courtesy LAFER.

$\theta(r_\perp, t)$ in the thickness direction. In the inset of Fig. 4.7 this angle is illustrated. Based on the theory of bifurcations close to the Freedericksz transition, we can introduce the following model describing this transition

$$\dot{\theta} = \alpha(|\vec{E}|^2 - K_3)\theta - \beta\theta^3 + \kappa\nabla_\perp^2\theta, \tag{4.17}$$

where $\{\alpha, \beta\}$ are adequate dimensional parameters, κ accounts for diffusion length, and $\nabla_\perp^2$ accounts for the Laplacian in transversal coordinates. Below the transition point ($|\vec{E}|^2 < K_3$)), the only stable equilibrium corresponds to the molecules parallel to the walls, $\theta = 0$. Above the transition point ($|\vec{E}|^2 \geq K_3$), the system exhibits two homogeneous configurations as equilibrium, $\theta = \pm\sqrt{|\vec{E}|^2 - K_3}$. Energetically these two configurations are equivalent. That is, this transition corresponds to a spontaneous breaking of the reflection symmetry. For an arbitrary initial condition this system exhibits different domains separated by defects. This front solution are denominated Ising wall because connect symmetric states. Moreover, this solution due to connect energetically equivalent states are denominated *kink solutions* [115, 157]. Figure 4.8 shows the interface dynamics close to Freedericksz transition. To understand the rich dynamics of Ising walls, in the next section we will study the interaction of walls.

4.5 Kink interaction

To figure out the rich dynamics of interface between Ising nematic wall. Let us consider the kink dynamics in one-dimension described by

$$\partial_t u = \epsilon u - u^3 + \partial_{xx} u, \tag{4.18}$$

where $u(x,t) \equiv \sqrt{\beta}\theta(x,t)$ and $x = r_\perp/\sqrt{\kappa}$ are the normalized order parameter and spatial coordinate. $\epsilon \equiv \alpha(|\vec{E}|^2 - K_3)$ is the bifurcation parameter. As we have mention this model has kink and anti-kink solutions (cf. formula 4.14). In the next session, based on the pioneering work of Kawasaki and Ohta [95], we will characterize the kinks interaction.

4.5.1 Kinematic law of a pair kinks

Let $\{u_-, u_+\}$ kink and anti-kink solutions of model Eq. (4.18), respectively. The kink solutions are characterized by a continuos parameter the kink position[1] and fixed parameter the front width. Note that the translation invariance generates a Lie group with respect to the translation parameter [143]. Figure 4.9a displays the front position and width. Consider a pair of kinks sufficiently separated as shown in Figure 4.9b. To describe this solution we consider the ansatz

$$u(x,t) = u_k[x - x_-(t)] + u_{Ak}[x - x_+(t)] - \sqrt{\epsilon} + w(x, x_-, x_+), \tag{4.19}$$

where $\{x_-, x_+\}$ are the kink positions that are promoted temporal function and w is a small correction function. The third term of the above expression is necessary for that the kink-antikink solution in infinite tends to $-\sqrt{\epsilon}$. Introducing the above ansatz in Eq. (4.18), and linearized in w after straightforward calculations we obtain

[1] This position corresponds to the spatial location of the front that presents maximum spatial variation. In the particular case of kink solutions of Eq. (4.18), this position corresponds to the root of the kink.

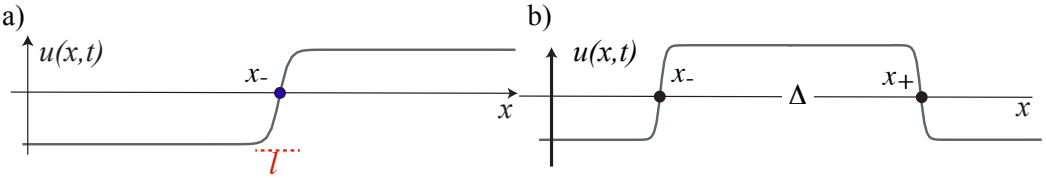

Figure 4.9: Schematic representation of kink solutions. a) Kink solution obtained from numerical solutions of Eq. (4.18). x_- and l stand for the kink position and width. b) kink and anti-kink solution, $\{x_-, x_+\}$ are the kink positions and Δ is the distance between kinks.

$$\begin{aligned}\partial_t u &= -\dot{x}_-\partial_z u_k(z \equiv x - x_-) - \dot{x}_+\partial_z u_{Ak}(z \equiv x - x_+) \\ &= \left(\epsilon - (u_k + u_{Ak} - \sqrt{\epsilon})^2 + \partial_{xx}\right) w + \epsilon(u_k + u_{Ak} - \sqrt{\epsilon}) \\ &- (u_k + u_{Ak} - \sqrt{\epsilon})^3 + \partial_{xx}u_k + \partial_{xx}u_{Ak}, \end{aligned} \tag{4.20}$$

rewriting the above expression using the fact that $\epsilon u_k - u_k^3 + \partial_{xx}u_k = 0$ and $\epsilon u_{Ak} - u_{Ak}^3 + \partial_{xx}u_{Ak} = 0$, one obtains

$$\begin{aligned}\mathcal{L}w &\equiv -\left(\epsilon - 3(u_k + u_{Ak} - \sqrt{\epsilon})^2 + \partial_{xx}\right) w = \dot{x}_-\partial_z u_k + \dot{x}_+\partial_z u_{Ak} \\ &- 3u_k^2(u_{Ak} - \sqrt{\epsilon}) - 3u_k(u_{Ak} - \sqrt{\epsilon})^2 + 3u_{Ak}\sqrt{\epsilon}(u_{Ak} - \sqrt{\epsilon}). \end{aligned} \tag{4.21}$$

To solve the above linear equation, we must to introduce the inner product

$$\langle f|g\rangle = \int_{-\infty}^{\infty} f(x)g(x)dx, \tag{4.22}$$

then $\mathcal{L}$ is a self adjoint operator, $\mathcal{L}^\dagger = -(\epsilon - 3(u_k + u_{Ak} - \sqrt{\epsilon})^2 + \partial_{xx})$. Notice that this operator is Hamiltonian type, i.e., $\mathcal{L}^\dagger = -\partial_{xx} + V(x)$, where the associated potential is defined by $V(x) \equiv -\epsilon + 3\left[u_k(x) + u_{Ak}(x) - \sqrt{\epsilon}\right]^2$, which corresponds a bistable potential. Figure 4.10 shows the bistable potential of the kink interaction. This potential has a fundamental mode related to translations of the kinks. In the case that the distance between the kinks is large enough ($\Delta \ll \sqrt{\epsilon}$), the fundamental mode as results of translation invariance can be approach by

$$|\chi_T\rangle = \partial_x u_k + \partial_x u_{Ak} + O(e^{-\sqrt{2\epsilon}\Delta}), \tag{4.23}$$

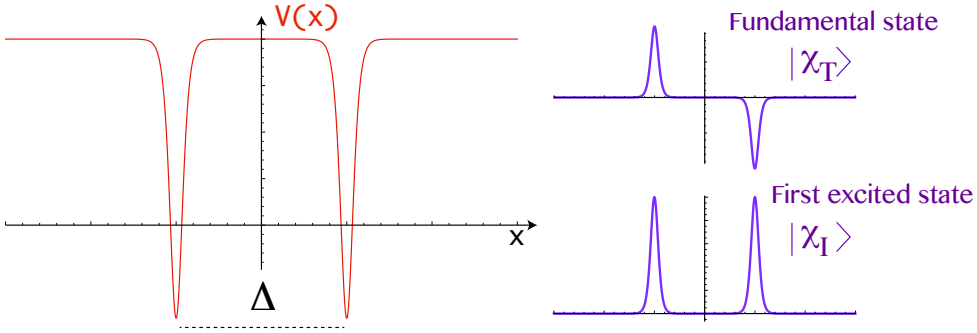

Figure 4.10: Effective bistable potential of kink interaction. Δ accounts for the distance between the minima. Insets account for the fundamental and first excited states.

This mode is an element of kernel of $\mathcal{L}^\dagger$, i.e. $\mathcal{L}^\dagger|\chi_T\rangle = 0$. Moreover, $\mathcal{L}^\dagger\left[\partial_x u_k + \partial_x u_{Ak}\right] = O(e^{-\sqrt{2\epsilon}\Delta})$. Another important mode is the first excited state $|\chi_I\rangle$, which is this related to the mode of interaction of kinks. This mode can be write

$$|\chi_I\rangle = \partial_x u_k - \partial_x u_{Ak} + O(e^{-\sqrt{2\epsilon}\Delta}), \tag{4.24}$$

Note that

$$\mathcal{L}^\dagger|\chi_I\rangle = O(e^{-\sqrt{2\epsilon}\Delta}). \tag{4.25}$$

Therefore, for long separated kinks, $\Delta \ll \sqrt{\epsilon}$, the functions $\{\partial_x u_k + \partial_x u_{Ak}, \partial_x u_k - \partial_x u_{Ak}\}$ are pseudo eigenfunctions of $\mathcal{L}^\dagger$, that is, these eigenfunctions have eigenvalues with exponential small values. In a similar manner of two-body problem, we introduce a change of variables to the central position $\delta(t)$[2] and the distance between kinks $\Delta(t)$. Introducing the change of variable

$$\begin{aligned} \delta(t) &\equiv \frac{x_-(t) + x_+(t)}{2}, \\ \Delta(t) &\equiv x_-(t) - x_+(t). \end{aligned} \tag{4.26}$$

Analogously one obtains

$$\begin{aligned} x_-(t) &= \delta - \frac{\Delta}{2}, \\ x_+(t) &= \delta + \frac{\Delta}{2}. \end{aligned} \tag{4.27}$$

[2]Which corresponds to the equivalent mass center.

Introducing this change of variable in Eq. (4.21), this reads

$$\begin{aligned}\mathcal{L}w &= \dot{\delta}\left(\partial_z u_k + \partial_z u_{Ak}\right) - \dot{\Delta}\left(\partial_z u_k - \partial_z u_{Ak}\right) \\ &- 3u_k^2(u_{Ak}-\sqrt{\epsilon}) - 3u_k(u_{Ak}-\sqrt{\epsilon})^2 + 3u_{Ak}\sqrt{\epsilon}(u_{Ak}-\sqrt{\epsilon}). \end{aligned} \tag{4.28}$$

To solve the above linear equation we must to impose the solvability condition, that is, the right hand side of above equation is orthogonal to the pseudo eigenfunctions $\{|\chi_T\rangle, |\chi_I\rangle\}$. Imposing the solvability conditions with respect to translation mode, we obtain

$$\dot{\delta}\langle\chi_T|\left(\partial_z u_k + \partial_z u_{Ak}\right)\rangle = \langle\chi_T|3u_k^2(u_{Ak}-\sqrt{\epsilon}) - 3u_k(u_{Ak}-\sqrt{\epsilon})^2 + 3u_{Ak}\sqrt{\epsilon}(u_{Ak}-\sqrt{\epsilon})\rangle. \tag{4.29}$$

The above equations can rewrite

$$\begin{aligned}\dot{\delta}||\chi_T||^2 &= \langle\partial_z u_k|3u_k^2(u_{Ak}-\sqrt{\epsilon}) - 3u_k(u_{Ak}-\sqrt{\epsilon})^2 + 3u_{Ak}\sqrt{\epsilon}(u_{Ak}-\sqrt{\epsilon})\rangle \\ + \quad &\langle\partial_z u_{Ak}|3u_k^2(u_{Ak}-\sqrt{\epsilon}) - 3u_k(u_{Ak}-\sqrt{\epsilon})^2 + 3u_{Ak}\sqrt{\epsilon}(u_{Ak}-\sqrt{\epsilon})\rangle. \end{aligned} \tag{4.30}$$

By symmetry arguments

$$\begin{aligned}&3u_k^2(u_{Ak}-\sqrt{\epsilon}) - 3u_k(u_{Ak}-\sqrt{\epsilon})^2 + 3u_{Ak}\sqrt{\epsilon}(u_{Ak}-\sqrt{\epsilon}) = \\ &3u_{Ak}^2(u_k-\sqrt{\epsilon}) - 3u_{Ak}(u_k-\sqrt{\epsilon})^2 + 3u_k\sqrt{\epsilon}(u_k-\sqrt{\epsilon}). \end{aligned} \tag{4.31}$$

Hence, the dynamic of central position is

$$\begin{aligned}\dot{\delta}||\chi_T||^2 &= \langle\partial_z u_k|3u_k^2(u_{Ak}-\sqrt{\epsilon}) - 3u_k(u_{Ak}-\sqrt{\epsilon})^2 + 3u_{Ak}\sqrt{\epsilon}(u_{Ak}-\sqrt{\epsilon})\rangle \\ &+ \langle\partial_z u_{Ak}|3u_{Ak}^2(u_k-\sqrt{\epsilon}) - 3u_{Ak}(u_k-\sqrt{\epsilon})^2 + 3u_k\sqrt{\epsilon}(u_k-\sqrt{\epsilon})\rangle. \end{aligned} \tag{4.32}$$

The spatial variation of the kink solution u_k is characterized by being centered in the kink position, i.e. it is exponentially small almost everywhere except in the region close to the kink core. Figura 4.11 shows the function $\partial_x u_k$. Then the first term on the right side is an integral to be evaluated around x_-. The anti-kink solution around x_- minus $\sqrt{\epsilon}$ when both kinks are enough separated has the form

$$\left(u_{Ak}(x\to-\infty) - \sqrt{\epsilon}\right) \longrightarrow -2\sqrt{\epsilon}e^{-2\sqrt{\epsilon/2}(x-\delta-\Delta/2)}. \tag{4.33}$$

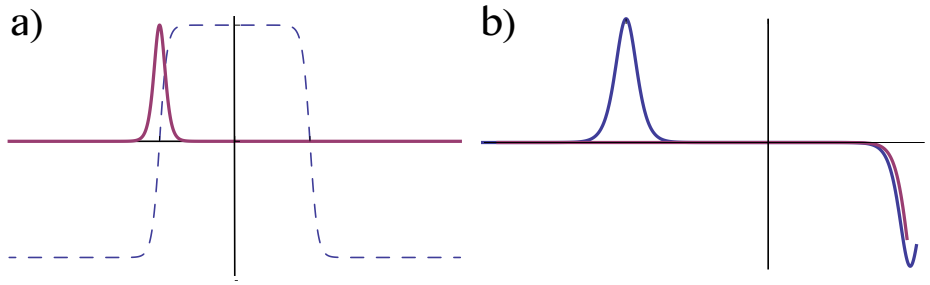

Figure 4.11: Kink solution. a) Spatial variation of the kink solution, $\partial_x u_k$. b) Asymptotic behavior of $u_{Ak} - \sqrt{\epsilon}$ around kink position.

This function around the kink position decays exponentially and $u_{Ak} \approx \sqrt{\epsilon} - 2e^{-2\sqrt{\epsilon/2}(x-\delta-\Delta/2)}$. Thus, the first term on the right side can be approximate by

$$\langle \partial_z u_k | u_k^2(u_{Ak} - \sqrt{\epsilon}) - u_k(u_{Ak} - \sqrt{\epsilon})^2 + u_{Ak}\sqrt{\epsilon}(u_{Ak} - \sqrt{\epsilon}) \rangle \approx \langle \partial_z u_k | u_{Ak}\sqrt{\epsilon}(u_{Ak} - \sqrt{\epsilon}) \rangle. \tag{4.34}$$

This last integral can be approximate

$$\langle \partial_z u_k | u_{Ak}\sqrt{\epsilon}(u_{Ak} - \sqrt{\epsilon}) \rangle \approx -2\epsilon \int_{-\infty}^{\infty} dx \partial_z u_k \left(x - \delta + \frac{\Delta}{2} \right) e^{-2\sqrt{\epsilon/2}(x-\delta-\Delta/2)} H\left(-x + \delta + \frac{\Delta}{2} \right), \tag{4.35}$$

where $H(x)$ is the Heaviside step function [28]. The introduction of the H function is to describe adequately the behavior of the function $u_{Ak}(x) - \sqrt{\epsilon}$ in infinite. Changing the variable of integration $z = x - \delta + \Delta/2$, this integral reads

$$\langle \partial_z u_k | u_{Ak}\sqrt{\epsilon}(u_{Ak} - \sqrt{\epsilon}) \rangle \approx -\frac{a}{2} e^{-2\sqrt{\epsilon/2}\Delta}, \tag{4.36}$$

where $a \equiv 4\epsilon \int \partial_z u_k(z) e^{-\sqrt{\epsilon}z} H(-z + \Delta)$. Hence, one obtains

$$\langle \partial_z u_k | u_k^2(u_{Ak} - \sqrt{\epsilon}) - u_k(u_{Ak} - \sqrt{\epsilon})^2 + u_{Ak}\sqrt{\epsilon}(u_{Ak} - \sqrt{\epsilon}) \rangle \approx -\frac{a}{2} e^{-2\sqrt{\epsilon/2}\Delta}. \tag{4.37}$$

Analogously to previous analysis for the second term on the right side of Eq. (4.32), one can perform the same type of approach[3] and gets

$$\langle \partial_z u_{Ak} | 3u_{Ak}^2(u_k - \sqrt{\epsilon}) - 3u_{Ak}(u_k - \sqrt{\epsilon})^2 + 3u_k\sqrt{\epsilon}(u_k - \sqrt{\epsilon}) \rangle \approx \frac{a}{2} e^{-2\sqrt{\epsilon/2}\Delta}. \tag{4.38}$$

[3]The difference that the spatial variation of the anti-kink compared with the kink is the opposite sign $\int \partial_z u_k(z) = -\int \partial_z u_{Ak}(z)$.

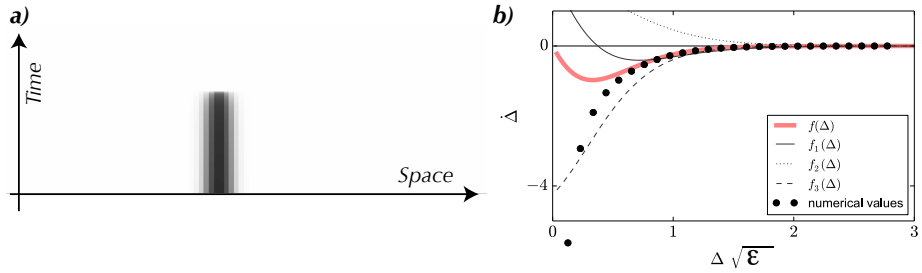

Figure 4.12: Kink interaction. a) Spatiotemporal evolution of a kinks pair. b) Numerical comparison of the kink interaction and numerical simulation. Points are obtained numerically by considering two close kink and anti-kink solution, then numerically the system evolves during a brief moment of time, and finally the temporal variation of the kink position is calculated, where curves are defined by $f(\Delta) \equiv \langle \chi_I | 3u_k^2(u_{Ak} - \sqrt{\epsilon}) + 3u_k(u_{Ak} - \sqrt{\epsilon})^2 + 3u_{Ak}\sqrt{\epsilon}(u_{Ak} - \sqrt{\epsilon}) \rangle$, $f_1(\Delta) \equiv \langle \chi_I | 3u_{Ak}\sqrt{\epsilon}(u_{Ak} - \sqrt{\epsilon}) \rangle$, $f_2(\Delta) \equiv \langle \chi_I | 3u_k^2(u_{Ak} - \sqrt{\epsilon}) \rangle$, $f_3(\Delta) \equiv \langle \chi_I | 3u_k(u_{Ak} - \sqrt{\epsilon})^2 \rangle$ [53].

Therefore, the dynamics of the central positions of the kinks is $\dot{\delta} = 0$. From this result we can infer that the kinks dynamics can be characterized by either attract or repel the kinks symmetrically. The above dynamic one also can be understood as a consequence of the reflection invariance of Eq. (4.18)

Imposing the solvability conditions with respect to interaction mode $|\chi_I\rangle$, after straightforward calculation we obtain

$$\begin{aligned} \dot{\Delta}||\chi_I||^2 &= \langle \partial_z u_k | 3u_k^2(u_{Ak} - \sqrt{\epsilon}) - 3u_k(u_{Ak} - \sqrt{\epsilon})^2 + 3u_{Ak}\sqrt{\epsilon}(u_{Ak} - \sqrt{\epsilon}) \rangle \\ &- \langle \partial_z u_{Ak} | 3u_{Ak}^2(u_k - \sqrt{\epsilon}) - 3u_{Ak}(u_k - \sqrt{\epsilon})^2 + 3u_k\sqrt{\epsilon}(u_k - \sqrt{\epsilon}) \rangle. \quad (4.39) \end{aligned}$$

Using the results obtained in formulas (4.37,4.38), the dynamics for the distance between kinks Δ satisfies (The kinematic law of kinks) [56]

$$\dot{\Delta} \approx -be^{-\sqrt{2\epsilon}\Delta}, \quad (4.40)$$

with $b \equiv a/||\chi_I||^2 = 3a/2\epsilon^{3/2} > 0$. Therefore, the kink interaction is characterized by being attractive and decreased exponentially with the distance between kinks. The system then seeks to find its overall energy minimum through the kink attract and reach the homogeneous state. Figure **??** shows the spatiotemporal evolution of a kinks

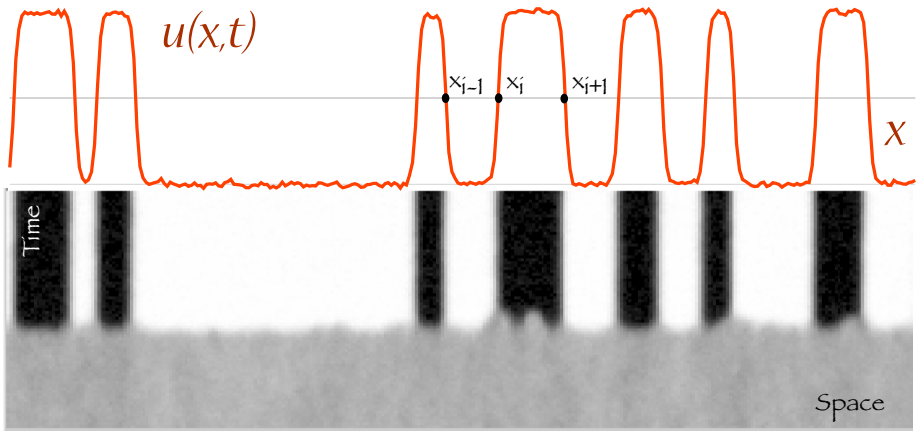

Figure 4.13: Spatiotemporal evolution of emergence of domains walls. Numerical simulation of model Eq. (4.18) with noise before and after transition. x_i accounts for the kink position.

pair and also the comparison of the different terms of the interaction with numerical simulations. These results show an appropriate agreement even for distances of the order of the kink core, where the other terms of the interaction have been take into account [53].

4.5.2 Interaction of a gas of kinks: coarsegraning

Numerical simulations of model Eq. (4.18) with noise before the transition exhibit fluctuations around the zero equilibrium. Crossing transition, the system presents the emergence of diverse walls. These domains are separated by several kinks that are interacting. Figure 4.13 illustrates the previous process. To account for these wall domains, we consider the following ansatz (multiple kinks solutions)

$$u(x,t) \approx \sum_n (-1)^n u_k(x - x_n(t)) - \sqrt{\epsilon}, \tag{4.41}$$

where x_n stands for the position n-kink. Using the pair interaction law, Eq. (4.40), between the kinks, we obtains (n-kink interaction law) [56]

$$\dot{x}_n = b\sum_{i<n}(-1)^i e^{-2\sqrt{\epsilon/2}|x_n - x_i|} - b\sum_{i>n}(-1)^i e^{-2\sqrt{\epsilon/2}|x_i - x_n|}. \tag{4.42}$$

Due to the n-kink interaction decays exponentially, we can approximate it by the interaction of first neighbors, that is,

$$\dot{x}_n \approx -be^{-2\sqrt{\epsilon/2}(x_{n+1}-x_n)} + be^{-2\sqrt{\epsilon/2}(x_n-x_{n-1})}. \tag{4.43}$$

Then the closest kinks attract the central kink with the aim of annihilating it. It is important to note that this type of force between kinks is weak and short-range, which makes it difficult to verify this type of interaction numerically.

An unexpected property of the interaction of a gas of kinks is that it is self-similar, that is, the interaction is simultaneously invariant to temporal and coordinate transformations [146, 23]. As a result of this type of symmetry one expects to find laws for the dynamics. A classic example of self-similarity is the Newton interaction that cause the Kepler's third law [146, 23]. Considering the transformation

$$\begin{aligned} (x_{n+1}-x_n) &\rightarrow (x_{n+1}-x_n+\lambda), \\ t &\rightarrow te^{\sqrt{2\epsilon}\lambda}, \end{aligned} \tag{4.44}$$

that corresponds to a temporal and spatial dilatation, the kink interaction Eq. (4.43) is invariant. This means that if one separates the distance between kinks in a λ distance is equivalent to delay time by a fact $e^2\sqrt{\epsilon/2}\lambda$.

A macroscopic parameter characterizing the dynamics of kinks is the average distance between kinks $\langle l\rangle$, defined by

$$\langle l(t)\rangle \equiv \sum_i \frac{x_{i+1}(t)-x_i(t)}{N(t)} = \frac{L}{N(t)}, \tag{4.45}$$

where $N(t)$ the number of kinks at time t. Indeed, this quantitive characterizes the number of kink inside the system. Since the kink interaction controls the dynamics of these defects, the above expression also must be controlled by this interaction. Thus, this also should be self-similar, i.e.

$$\begin{aligned} \langle l+\lambda\rangle &= \langle l(te^{\sqrt{2\epsilon}\lambda})\rangle, \\ \langle l+\lambda\rangle &= \langle l(t)\rangle + \lambda \end{aligned} \tag{4.46}$$

then

$$\langle l(te^{\sqrt{2\epsilon}\lambda})\rangle = \langle l(t)\rangle + \lambda. \tag{4.47}$$

The only function that satisfies the above property is

$$\langle l(t)\rangle = \frac{1}{\sqrt{2\epsilon}}\ln(t). \tag{4.48}$$

Therefore, one can infer that the number of kink decrease logarithmic in time, $N(t) = \sqrt{2\epsilon}/\ln(t)$. That is, from interaction laws of defects one can deduce macroscopic laws. This type of behavior is usually denominated as coarsening dynamics [139]. Figure 4.14 shows a set up of inhomogeneous electro-convection, which has interface between two convection rolls [126, 127]. This interface due to the anisotropic elastic constant is unstable generating a complex dynamic of kinks as illustrated in Fig. 4.14. A kink separates two regions with opposite slope. Experimentally it was studied the average distance of kinks as a function of time and found that satisfies a logarithmic law [126]. This confirms the results presented above.

4.5.3 Effect of discretization kink interaction

Numerical simulations of model Eq. (4.18) from an initial uniform solution $u = 0$ with noise and positive ϵ is characterized by the appearance of several domains (cf. Fig. 4.13). The interaction between nearest walls is characterized by annihilating, kinks interaction; however for sufficiently large time, the system is frozen. That is, domains are no longer changed in the course of time. This phenomenon can be understood by the combination of two factors: firstly the kink interaction which is very weak and on the other hand the discreteness of the system under simulation. As we have shown in Sec. 3.7.1, a discrete system can be described by an effective continuos equation of the

$$\partial_t u = \epsilon u - u^3 + \partial_{xx}u + \Gamma_{dx}(x)\partial_{xx}u + \Gamma'_{dx}(x)\partial_x u, \tag{4.49}$$

where $\Gamma_{dx}(x)$ is a small spatial periodic function with dx period, $\Gamma_{dx}(x+dx) = \Gamma_{dx}(x)$, and Γ'_{dx} accounts for derivative of Γ_{dx}. This function accounts for the discreteness of

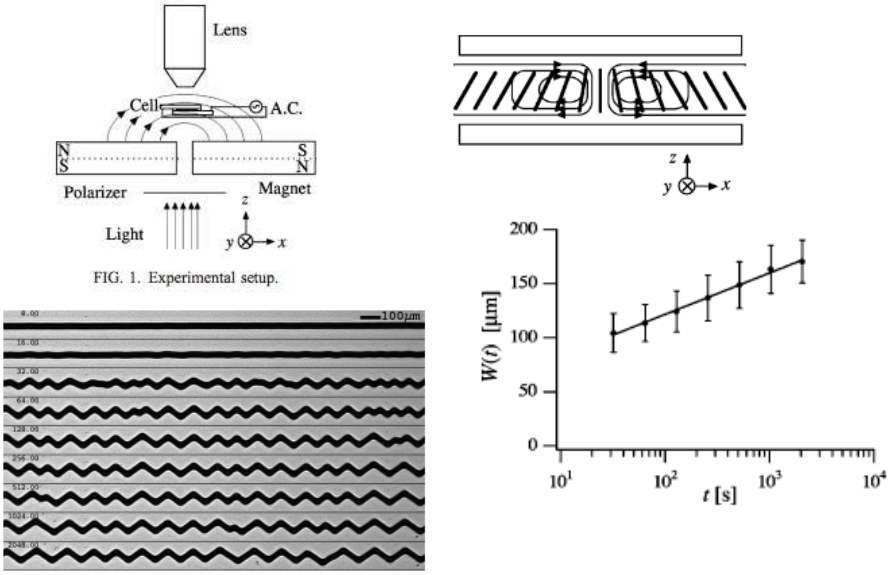

Figure 4.14: Kink dynamics in inhomogeneous electro-convection experiment. In top left panel is schematic repersented the setup, in top right panel panel is depicted the interface between two convection rolls, in bottom left panel is illustrated a sequence of temporal snapshot of the interface and in bottom right panel the temporal evolution of average length between kinks [126].

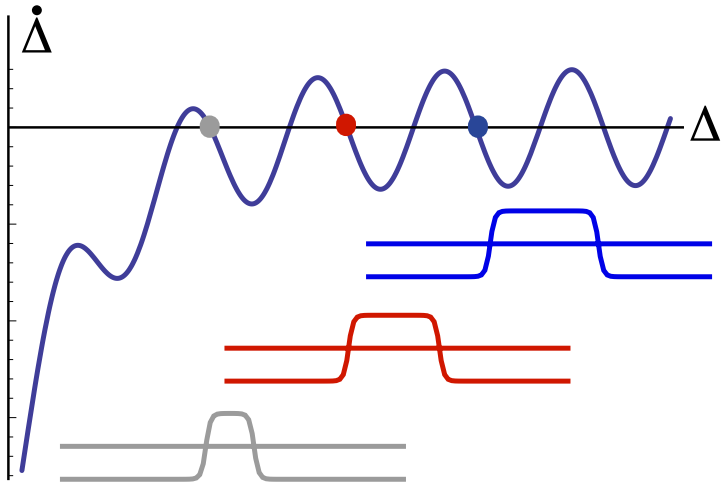

Figure 4.15: Kink interaction formula (4.50). the inset account for different localized states.

the system. Likewise, in Sec. 3.7.1, we have shown that the presence of periodic forcing modified the front dynamics by a periodic force (Peierls- Nabarro force). Similarly, the

kinematic law of kink Eq. (4.40), is modified by the presence of a periodic force, then this reads

$$\dot{\Delta} \approx -be^{-\sqrt{2\epsilon}\Delta} + \gamma_{dx}(\Delta), \tag{4.50}$$

where $\gamma_{dx}(\Delta)$ is a periodic function, $\gamma_{dx}(\Delta + dx) = \gamma_{dx}(\Delta)$. Figure 4.15 depict the typical kink force. For large enough distance between kinks ($\Delta \gg \sqrt{\epsilon}$), the system has several equilibrium positions as a result of discreteness, i.e. the interaction is completely neglected. These positions correspond to the kink takes a symmetrical distribution of the points that form it. Decreasing the distance between the kinks, the interaction between kinks becomes more relevant. The system exhibits a family of localized states with different widths. The localized structures width is of order of multiple of dx. It is important to note that these localized solutions are not solutions of Eq. (4.18), but are solutions of corresponding discrete model of Eq. (4.18)[4] or effective Eq. (4.49). Therefore from the discreteness we have visualized the possibility of localized states.

4.6 Localized states as result of kink interaction

During the last years, emerging macroscopic particle-type solutions or localized states or localized structure in macroscopic extended dissipative systems have been observed in different fields, such as: domains in magnetic materials, chiral bubbles in liquid crystals, current filaments in gas discharge, spots in chemical reactions, localized states in fluid surface waves, oscillons in granular media, isolated states in thermal convection, solitary waves in nonlinear optics, among others [64, 137, 1]. Hence, one can infer the universality of the localized states dynamics. Although these states are spatially extended, they exhibit properties typically associated with particles. Consequently one can characterized them with a family of continuous parameters such as position, amplitude and width. This is exactly the type of description used in more fundamental physical theories like Quantum Mechanics and Particle Physics. However, localized states emerging in extended dissipative systems are characterized by being made of a

[4] which is using for the numerical analysis.

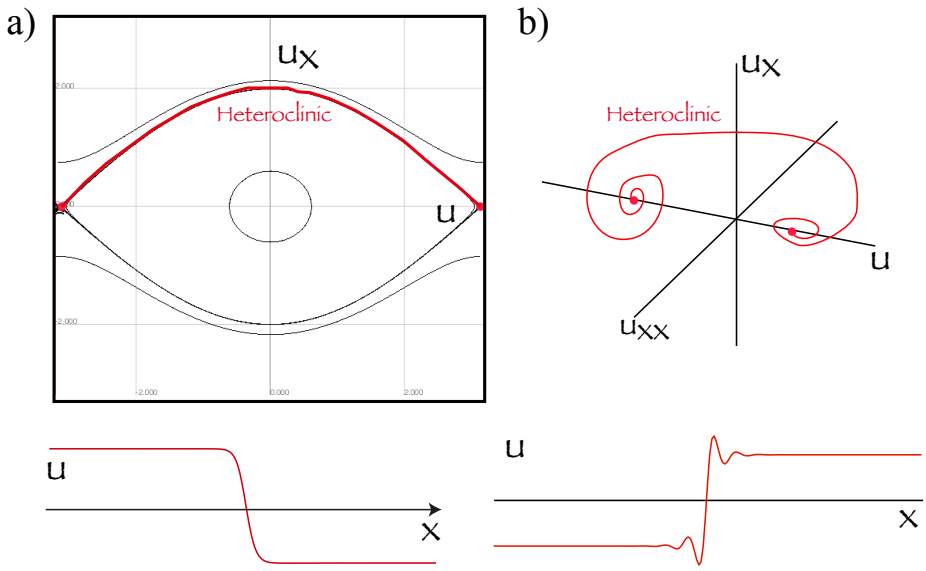

Figure 4.16: Schematic representation of heteroclinic curves for a spatial dynamical system of different dimensions. Top panels show the heteroclinic curves in their respective phase portrait. Bottom panels display the respective profile of heteroclinic curves.

large number of atoms or molecules (of the order of Avogadro's number) that behave coherently.

In this section we want to respond to the possibility of localized structure as a result of the kinks interaction. As we have seen in previous sections of kink interaction is determined by their asymptotic behavior. From the point of view of geometry in phase space, the Kinks corresponds to heteroclinic solutions. The heteroclinic curves are trajectories in phase portrait that connect hyperbolic points. In spatial dynamical systems of dimension two, the homoclinic curves does not exhibit spatial oscillations (cf. Fig. 4.16a). This property is a consequence of that two-dimensional dynamic system stable manifolds are one-dimensional. The above scenario changes when the associated spatial dynamical systems have high dimensions. The hyperbolic points are characterized to have complex eigenvalues, then the associated manifolds (attractive/repulsive) are characterized to exhibit oscillatory trajectories around the hyperbolic point range. Indeed,

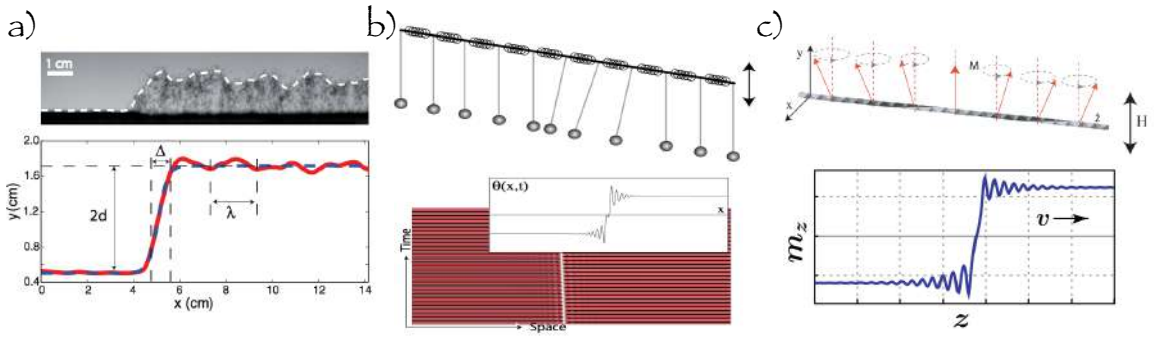

Figure 4.17: Kink solutions with damping spatial oscillations. a) fluidized granular media [111, 112], b) vertically driven chain of pendula [48, 49], and c) forcing magnetic wire with easy plane [44].

the heteroclinic curves shows spatial damping oscillations as it tends to equilibrium. Figure 4.16 shows the typical heteroclinic curves. Kinks with spatial damping oscillation have been observed in several contexts such as driven granular media [111, 112], population dynamics [48, 49], vertically driven chain of pendula [44], forcing magnetic wire [44], to mention a few. Figure 4.17 shows kinks solution with damping oscillation in several contexts.

4.6.1 Simple model: Turing-Swift-Hohenberg equation

In the previous sections, we have considered a simple model, Eq. (4.18), that displays spatially monotonic kinks. A natural generation of this equation, based on pioneering spirit of the work of Alan Turing [61], is considered higher gradients, that is (Turing-Swift-Hohenberg model)

$$\partial_t u = \epsilon u - u^3 + \nu \partial_{xx} u - \partial_{xxxx} u, \tag{4.51}$$

where $u = u(x, y, t)$ is a real scalar field, x and y are spatial coordinates and t is time. Depending on the context in which this equation has been derived, the physical meaning of the field variable $u(x, y, t)$ could be the electric field, deviation of molecular orientations, phytomass density, amplitude of velocity or temperature modes, or chemical concentration. The control or the bifurcation parameter ϵ measures the input field

amplitude, the aridity parameter, temperature difference or chemical concentration. The parameter ν stands for the diffusion coefficient, when this parameter is negative ($\nu > 0$), it induces an anti diffusion process. Thus the first two terms on the right hand side of Eq. (4.65) account for homogeneous or local nonlinear dynamics, the third and fourth term stand for the transport mechanisms or spatial coupling via diffusion and hyperdiffusion, respectively.

Eq. (4.65) is a prototype model which exhibits both localized and extended patterns. This is an isotropic nonlinear model deduced originally to describe the pattern formation of Benard convection [151]. Usually this model is denominated as Swift-Hohenberg. An important property of Eq. (4.65) is that it possess a gradient form, i.e.

$$\frac{\partial u}{\partial t} = -\frac{\delta F[u, \partial_x u, \partial_{xx} u]}{\delta u}, \tag{4.52}$$

with the functional

$$F \equiv \int \left(-\epsilon \frac{u^2}{2} + \frac{u^4}{4} + \nu \frac{(\partial_x u)^2}{2} + \frac{(\partial_{xx} u)^2}{2} \right) dx. \tag{4.53}$$

Note that using the solutions of Eq. (4.65), this functional satisfies

$$\frac{dF}{dt} = -\int dx \, (\partial_t u)^2 \leq 0. \tag{4.54}$$

Hence, F is a Lyapunov functional that can only decrease in the course of time. This functional guarantees that time evolution proceeds toward the state for which the functional has the smallest possible value which is compatible with the systems boundary conditions. Any initial distribution $u(x,t)$ evolves towards a homogeneous or inhomogeneous (periodic or localized) stationary state corresponding to a local or global minimum of F. The analysis of the functional F is provided in Ref. [164]. In the bistability region ($\epsilon > 0$), as result of hyperdiffusion the kink solutions exhibit spatial damping oscillations (cf. Fig. 4.16b).

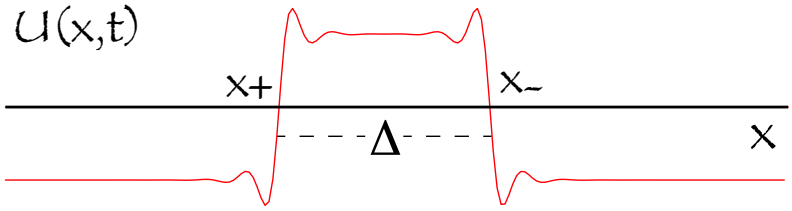

Figure 4.18: Schematic representation of a pair of kink solutions of model Eq. (**??**). Δ is the distance between kinks.

Kink interaction with damping oscillations

Analogously to section 4.5.1, to study the kink interaction we can consider the following solutions

$$u(x,t) = u_k[x - x_-(t)] + u_{Ak}[x - x_+(t)] - \sqrt{\epsilon} + w(x, x_-, x_+), \tag{4.55}$$

where $\{x_-, x_+\}$ are the kink positions that are promoted temporal function and w is a small correction function. The third term of the above expression is necessary for that the kink-antikink solution in infinite tends to $-\sqrt{\epsilon}$. The above solution is represented in Fig. 4.18. The analytical expression of the kink solution is unknown, nevertheless, its asymptotic behavior is simple to characterize by linear analysis around the equilibria. Thus,

$$u_k(x \to \pm\infty) \to \pm\sqrt{\epsilon}\left(1 - 2\gamma e^{\mp\alpha x}\cos(\beta x + \delta_0)\right), \tag{4.56}$$

where $\{\alpha, \beta\}$ correspond to the real and imaginary part of eigenvalue that characterize the manifold around the equilibria $\pm\sqrt{\epsilon}$.

Introducing the above ansatz in Eq. (**??**), and linearized in w after straightforward calculations we obtain

$$\begin{aligned} \mathcal{L}w \;\equiv\; & -\left(\epsilon - 3(u_k + u_{Ak} - \sqrt{\epsilon})^2 + \nu\partial_{xx} - \partial_{xxxx}\right) w = \dot{x}_-\partial_z u_k + \dot{x}_+\partial_z u_{Ak} \\ - \;\; & 3u_k^2(u_{Ak} - \sqrt{\epsilon}) - 3u_k(u_{Ak} - \sqrt{\epsilon})^2 + 3u_{Ak}\sqrt{\epsilon}(u_{Ak} - \sqrt{\epsilon}). \end{aligned} \tag{4.57}$$

Introducing the canonical inner product

$$\langle f|g\rangle = \int_{-\infty}^{\infty} f(x)g(x)dx, \tag{4.58}$$

then $\mathcal{L}$ is a self adjoint operator. Similarly, to what shown in Sec. 4.5.1, the linear operator $\mathcal{L}$ has two pseudo-eigenfunctions related to translation ($|\chi_T\rangle$) and interaction ($|\chi_I\rangle$) mode, which have the form

$$\begin{aligned} |\chi_T\rangle &= \partial_x u_k + \partial_x u_{Ak} + O(e^{-\sqrt{\alpha}\Delta}), \\ |\chi_I\rangle &= \partial_x u_k - \partial_x u_{Ak} + O(e^{-\sqrt{\alpha}\Delta}). \end{aligned} \tag{4.59}$$

Introducing the central position $\delta(t) = (x_-(t) + x_+(t))/2$ and the distance between kinks $\Delta(t) = x_-(t) - x_+(t)$, the linear Eq. (4.57) reads

$$\begin{aligned} \mathcal{L}w &= \dot{\delta}\left(\partial_z u_k + \partial_z u_{Ak}\right) - \dot{\Delta}\left(\partial_z u_k - \partial_z u_{Ak}\right) \\ &- 3u_k^2(u_{Ak} - \sqrt{\epsilon}) - 3u_k(u_{Ak} - \sqrt{\epsilon})^2 + 3u_{Ak}\sqrt{\epsilon}(u_{Ak} - \sqrt{\epsilon}). \end{aligned} \tag{4.60}$$

Imposing the solvability condition, one gets

$$\begin{aligned} \dot{\delta}||\chi_T||^2 &= \langle \partial_z u_k | 3u_k^2(u_{Ak} - \sqrt{\epsilon}) - 3u_k(u_{Ak} - \sqrt{\epsilon})^2 + 3u_{Ak}\sqrt{\epsilon}(u_{Ak} - \sqrt{\epsilon})\rangle \\ &+ \langle \partial_z u_{Ak} | 3u_{Ak}^2(u_k - \sqrt{\epsilon}) - 3u_{Ak}(u_k - \sqrt{\epsilon})^2 + 3u_k\sqrt{\epsilon}(u_k - \sqrt{\epsilon})\rangle, \\ \dot{\Delta}||\chi_I||^2 &= \langle \partial_z u_k | 3u_k^2(u_{Ak} - \sqrt{\epsilon}) - 3u_k(u_{Ak} - \sqrt{\epsilon})^2 + 3u_{Ak}\sqrt{\epsilon}(u_{Ak} - \sqrt{\epsilon})\rangle \\ &- \langle \partial_z u_{Ak} | 3u_{Ak}^2(u_k - \sqrt{\epsilon}) - 3u_{Ak}(u_k - \sqrt{\epsilon})^2 + 3u_k\sqrt{\epsilon}(u_k - \sqrt{\epsilon})\rangle. \end{aligned} \tag{4.61}$$

Using the asymptotic behaviors of kink and anti-kink solutions, symmetry arguments, and similar arguments using in Sec. 4.5.1, after straightforward calculations we obtain

$$\begin{aligned} \dot{\delta} &= 0, \\ \dot{\Delta} &= -b_1 e^{-\alpha\Delta}\cos(\beta\Delta + \delta_1), \end{aligned} \tag{4.62}$$

where $\{b_1, \delta_1\}$ are parameters determined numerically. The first equation tells us that the center position is not changed by the displacement of the kinks. The second equation tells us that the kink interaction alternates between being attractive and positive, and its intensity decays exponentially with the kink distance. Hence, the system exhibits a family of localized states with different widths, which are of the order of a multiple of

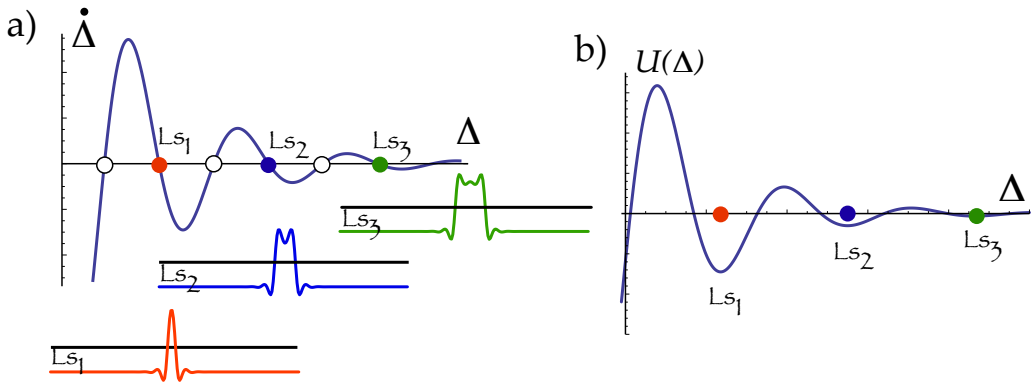

Figure 4.19: Schematic representation of the kink interaction. a) Interaction law, Δ accounts for the localized structure width. Ls_i stands for the i-localized structure. The insets account for the different localized structures. b) Potential of the interaction.

the wavelength of the kink spatial oscillation [56, 55]. Figure 4.19 shows the profile of the kink interaction and depicts the smallest localized structures. Notice that the kink interaction is a variational dynamics, i.e.

$$\dot{\Delta} = -\frac{\partial U}{\partial \Delta}, \tag{4.63}$$

where the potential

$$U(\Delta) = -b_1 \frac{e^{-\alpha\Delta}}{\beta^2 + \alpha^2} \left(\alpha \cos(\beta\Delta + \delta_1) - \beta \sin(\beta\Delta + \delta_1)\right). \tag{4.64}$$

From this potential, we can conclude that the smaller the localized structure are more stable. Likewise, the respective basins of attraction are bigger for smaller localized structures. Hence, in present of noise the smaller states are more stable.

4.6.2 Localized structures as result front interaction

A natural generalization of of Turing-Swift-Hohenberg Eq. (4.65) is consider a constant term in the dynamics, that is

$$\partial_t u = \eta + \epsilon u - u^3 + \nu \partial_{xx} u - \partial_{xxxx} u, \tag{4.65}$$

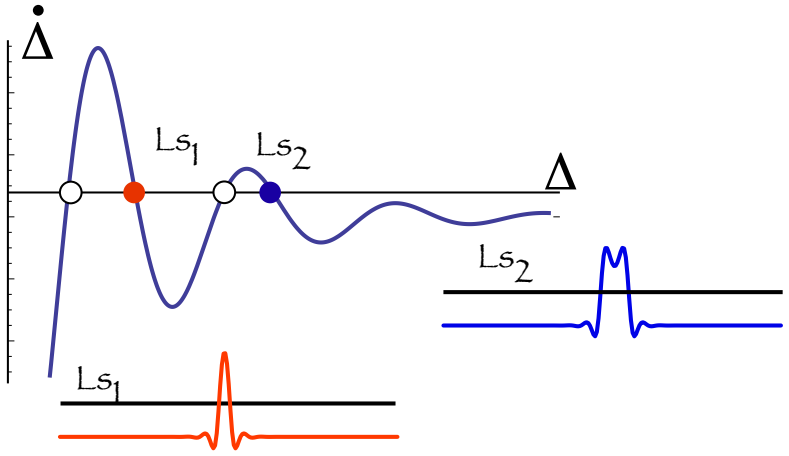

Figure 4.20: Schematic representation of the front interaction. Δ accounts for the localized structure width. Ls_i stands for the i-localized structure. The insets account for the different localized structures.

where η parameter breaks the reflection symmetry $u \to -u$, thus it accounts for the asymmetry between homogeneous states. This parameter becomes the pitchfork bifurcation in an imperfect one. This model was initially proposed to describe the dynamics of the envelope electric field inside a nonlinear cavity, which is forced with an external electric field at its resonant frequency [153, 114]. As we have shown in Sec. 4.3, this extra parameter is responsible of front propagation between the asymmetric states. That is, this term is responsible for a drift dynamic of fronts. In order to analyze how this term affects the kink dynamics, we consider that this term as perturbative one. It is a fact of matter that we can perform an analogous analysis to the previous section incorporated the effect η (cf. Sec. 4.3) the front dynamics reads

$$\begin{aligned} \dot{\delta} &= 0, \\ \dot{\Delta} &= -b_1 e^{-\alpha\Delta}\cos(\beta\Delta + \delta_1) + \frac{3\sqrt{2}}{\epsilon}\eta. \end{aligned} \tag{4.66}$$

Then the last term of the equation of interaction can be interpreted as a constant force on the dynamics of fronts. The presence of this extra force modified the size of localized structures.

4.6.3 Flaming 2-π kinks in parametrically driven systems

see article 106,121

4.7 Liftshitz normal form: nonvariational generalization of Turing-Swift-Hohenberg Equation

In the previous section, we considered a generalization of the Swift-Hohenberg equation (4.65) that considers a term that breaks the reflection symmetry of the order parameter. However, the relevant question that one must establish is the general model that describes the formation of the pattern in one-dimensional systems. As result of the spatial and temporal scales separation of the microscopic variables, the dynamics of macroscopic systems is described by a small number of variables (coarse-graining process), which generally satisfy non-variational or non-gradient equations [129, 133, 59, 58]. Indeed, the evolution of these dynamic systems is not characterized by the minimization of a free energy [30, 24]. Then, in this type of system, one expects to observe permanent behavior such as oscillations, chaos, temporal space chaos, and turbulence among others.

In this framework, walls connecting two equivalent vectorial fields through spontaneous symmetry breaking can spread according to a given chirality of the vector field [**?**]. This mechanism, the non-variational Ising–Bloch transition, is well known [**?**]. The deeper understanding of the front propagation in macroscopic systems out of equilibrium will open the possibilities for applications in non-equilibrium crystal growth, operation of non-equilibrium magnetic and optical memories, control of non-equilibrium chemical reactions, to mention a few.

The aim of this rapid comunication is to show that front solutions in scalar field models generically propagate based on two mechanism: i) the energy difference between states, and ii) non-variational effects. Considering a simple non–variational bistable model, we show analytically and numerically that the front propagation is leaded by

non-variational dynamics. A quasi one–dimensional liquid–crystal light valve (LCLV) experiment with optical feedback allow us to evidence non-variational front propagation between different molecular orientations. Free diffraction length allows us to control the variational or non-variational nature of this optical system. A phenomenological model for small free diffraction length is derived. Numerical simulations of this model have quite good agreement with experimental observations.

Simple bistable model.- Let us consider a bistable model

$$\begin{aligned} \partial_t u &= \eta + \mu u - u^3 + \partial_{xx} u + \epsilon \left[c(\partial_x u)^2 + b u \partial_{xx} u \right], \\ &= -\frac{\delta F}{\delta u} + \epsilon F_{NV}, \end{aligned} \tag{4.67}$$

where the scalar field $u(x,t)$ is an order parameter that accounts for an imperfect pitchfork bifurcation [58], μ is a bifurcation parameter, η stands for the asymmetry between the equilibria, ϵ is an small parameter, $\epsilon \ll 1$, that controls non-variational force $F_{NM} \equiv c(\partial_x u)^2 + b u \partial_{xx} u$, $\{c, b\}$ account for, respectively, nonlinear convective and diffusive terms, and the functional

$$F \equiv \int dx \left[V(u) + \frac{(\partial_x u)^2}{2} \right], \tag{4.68}$$

where $V(u) \equiv -\eta u - \mu u^2/2 + u^4/4$ is a potential. Notice the above model is invariant under spatial reflection symmetry ($x \to -x$). Moreover, model (4.67) is variational when $b = 2c$.

For $\epsilon = 0$, the above model (4.67) becomes a variational one. This model has two stable equilibria for η small and positive μ, $u = \pm\sqrt{\mu} + O(\eta)$, represented by $\{\mathcal{A}, \mathcal{B}\}$. Figure 4.21 depicts the potential $V(u)$ for different values of η. A nontrivial solution of this variational model is front waves, $u_F(x - vt) \approx \pm\sqrt{\mu}\tanh(\sqrt{\mu/2}(x - vt)) + O(\eta)$,

Figure 4.21: (color online) Front propagation in the bistable variational model Eq. (4.67) with $\epsilon = 0$. The upper panels represent the potential, $V(u)$, for different values of η, (a) $\eta = 0.2$, (b) $\eta = 0$, and (c) $\eta = -0.2$ with $\mu = 1.0$. The middle and lower panels illustrate the front profile and their respective spatiotemporal evolution for $\mu = 1.0$, $\eta = 0.3$ (d, f), and $\eta = -0.3$ (e, g).

Figure 4.22: (color online) Non-variational front propagation model, Eq. (4.67), at Maxwell's point ($\eta = 0$, $\epsilon = 1$, and $\mu = 1$). (a) potential $V(u)$. Front profiles at given instant for positive $c = 3$ (b), negative $c = -3$ (c) and $b = 0$. Middle panels represents spatiotemporal evolution of front solution with positive and negative parameter c and $b = 0$. (f) Front speed as function of parameter c. Points account for the numerical front speed obtained from Eq. (4.71) with $b = 0$, $\eta = 0$ and $\epsilon = 1$, solid straight line is obtained from analytical formula $v_{NV} \approx (2c - b)\epsilon\mu\sqrt{2}/5$, and soft line is obtained using formula (4.70) with a numerical front profile u_F.

that connects these two equilibria [?]. The middle and lower panels of Fig. 4.21 show the profile of the front solutions and their respective spatiotemporal evolution. Notice that fronts propagate at a constant speed. The location and the region of the space where the front has greater variation is known as front position and core, respectively. In the pioneering work of Pomeau [?], it is shown that front speed v is ($\eta \ll 1$)

$$v = v_V \equiv \frac{V(\mathcal{A}) - V(\mathcal{B})}{\int_{-\infty}^{\infty}(\partial_x u_F)^2 dx} \approx \frac{3\sqrt{2}}{2\mu}\eta. \tag{4.69}$$

Hence, the front speed is proportional to the energy difference between equilibria and the front core shape (denominator). Indeed, the most energetically favorable state invades the least favorable one (cf. Fig. 4.67). Likewise, when both states have the same energy, $\eta = 0$, the front is motionless, corresponding to Maxwell's point. Therefore, for variational systems, the mechanism of front propagation is the energy difference between the connected equilibria.

n the case of consider non-variational terms, $\epsilon \neq 0$, the above scenario changes drastically. To figure out this changes, we consider model Eq. (4.67) at Maxwell's point and non-variational terms as perturbative type, $\epsilon \ll 1$. Then, in this limit we can use the

Figure 4.23: (color online) Front propagation model Eq. (4.67) with $\eta = 0.3$ and $\mu = 1$. (a) the potential $V(u)$. (b) Front profiles for zero (dashed line) and positive (solid line) c and $b = 0$. Right panels (c,d) represent spatiotemporal evolution of front solution with zero and positive parameter c. (f) Front speed as function of parameter c. Points account for the numerical front speed and continuos curve $v = v_V + v_{NV}$.

following ansatz for the front solution $u(x,t) = u_F(x-vt) + w(x-vt,v)$, where w is a small adjustment function, which is of order of ϵ. Using this ansatz in Eq. (4.67), linearizing in w and imposing solvability conditions, we get

$$v_{NV} \equiv \epsilon \frac{c\int_{-\infty}^{+\infty}(\partial_x u_F)^3 dx + b\int_{-\infty}^{+\infty} u_F \partial_x u_F \partial_{xx} u_F dx}{\int_{-\infty}^{+\infty}(\partial_x u_F)^2 dx}. \tag{4.70}$$

Then, the front speed is proportional to the non-variational terms. Notice that a similar method to obtain the speed of propagative front was used to characterize Ising-Bloch transition [**?**].

From the above formula, we can conclude that the mechanism generating the spread of this front is only the front shape. Namely, the front core shape [$\partial_x u_F \sim O(1)$] determines the propagation speed and not the energy difference between equilibria. The above expression can be approximated by $v_{NV} \approx (2c-b)\epsilon\mu\sqrt{2}/5$. Figure 4.22 illustrates the non-variational front propagation observed from model [4.67] for different values of parameter c. For small c, the system exhibits a quite good agreement with the above approximation. For large c, we can use formula (4.70) with u_F obtained numerically. This semi-analytical approach has quite fair agreement (cf. Fig. 4.22). Notice that the nonlinear convection and diffusion are opposite effects for front speed. The front becomes motionless when the system is variational ($b = 2c$).

Consider the general case of asymmetry between equilibria ($\eta \neq 0$) and the presence of non-variational terms, front speed is determined by the two mechanisms discussed above, i.e., front speed is $v = v_V + v_{NV}$. Figure 4.23 depicts the front propagation in the generic case. Comparison between numerical simulations and theoretical results show a quite good agreement (cf. Fig. 4.23). Note that there is always a point in the parameter space where the front is motionless ($v_V = -v_{NV}$), but which does not correspond to equal energy between states.

Liquid–crystal light valve with optical feedback.- A simple physical system that exhibits non-variational behaviors and multistability is a LCLV with optical feedback [**?**, 140]. This setup contains a LCLV inserted in an optical feedback loop (see Fig. **??**). The LCLV is composed with a nematic liquid–crystal film sandwiched in between a glass and

a photoconductive plate over which a dielectric mirror is deposed (see Rev. [140] and references therein). The feedback loop is closed by an optical fiber bundle (FB) and is designed in such a way that diffraction and polarization interference are simultaneously present. The optical free propagation length is given by L.

The liquid–crystal film under consideration is planarly aligned (nematic director $\vec{n}$ parallel to the walls), with a thickness $d = 15\ \mu m$. The liquid–crystal filling the LCLV is a nematic LC-654, produced by NIOPIK. It is a mixture of cyano-biphenyls, with a positive dielectric anisotropy $\Delta\varepsilon = \varepsilon_{\|} - \varepsilon_{\perp} = 10.7$ and large optical birefringence, $\Delta n = n_{\|} - n_{\perp} = 0.2$, where $\varepsilon_{\|}$ and $\varepsilon_{\perp}$ are the dielectric permittivities $\|$ and $\perp$ to $\vec{n}$, respectively, and $n_{\|}$ and are $n_{\perp}$ are the extraordinary ($\|$ to $\vec{n}$) and ordinary ($\perp$ to $\vec{n}$) refractive index [**?**]. Transparent electrodes over the glass plates allow the application of an electrical voltage V_0 across the nematic layer. The photoconductor behaves like a variable resistance, which decreases for increasing illumination. The light which has passed through the liquid–crystal layer and has been reflected by the dielectric mirror experiences a phase shift which depends on the liquid–crystal molecular orientation and, on its turn, modulates the effective voltage that is locally applied to the liquid–crystal sample. Over a critical voltage, molecules tend to orient along the direction of the applied electric field, which changes local and dynamically following the illumination spatial distribution present in the photoconductor wall of the cell. When liquid–crystal molecules reorient, due to their birefringent nature, they induce a refractive index change. Thus, the LCLV acts as a manageable Kerr medium, causing a phase variation $\phi = \beta \cos^2\theta \equiv 2kd\Delta n \cos^2\theta$ in the reflected beam proportional to the intensity of the incoming beam I_w on the photoconductive side, where θ is the longitudinal average of molecular reorientation. Here, $k = 2\pi/\lambda$ is the optical wave number. The LCLV is illuminated by an expanded He-Ne laser beam, $\lambda = 633\ nm$, with 1 cm transverse diameter and power $I_{in} = 6.5\ mW/cm^2$, linearly polarized along the vertical y-axis. A spatial light modulator (SLM, controlled through an external computer) was placed in the input beam in order to carry out one-dimensional experiments. The system dynamics is controlled by adjusting the external voltage V_0 and free propagation

length L.

Theoretical description of the LCLV.- The light intensity I_w reaching the photoconductor is given by $I_w(\theta, L) = I_{in}|e^{-i\frac{L}{2k}\partial_{xx}}(1 + e^{-i\beta cos^2\theta})|^2/2$ [140], where x is the transverse direction of the liquid-crystal layer. As long as I_{in} is sufficiently small ($I_{in} \sim mW/cm^2$), the effective voltage, V_{eff}, applied to the liquid-crystal layer can be expressed as $V_{\text{eff}} = \Gamma V_0 + \alpha I_w$, $0 < \Gamma < 1$ is a transfer factor that depends on the electrical impedances of the photoconductor, dielectric mirror and liquid-crystal while α is a phenomenological dimensional parameter that describes the linear response of the photoconductor [140]. The dynamics of the average director tilt $\theta(x, t)$ is described by a nonlocal relaxation equation of the form [**?**]

$$\tau\partial_t\theta = l^2\partial_{xx}\theta - \theta + \frac{\pi}{2}\left(1 - \sqrt{\frac{\Gamma V_{FT}}{\Gamma V_0 + \alpha I_w(\theta, L)}}\right), \tag{4.71}$$

with $V_{FT} \approx 3.2\ V_{rms}$ the threshold for the Fréedericksz transition, $\tau = 30$ ms the liquid-crystal relaxation time, and $l = 30\ \mu$m the electric coherence length.

Let us consider zero free propagation length, $L = 0$, $I_w(\theta, L = 0) = I_{in}\{1+\cos(\beta\cos^2\theta)\}/2$. In this limit Eq. (4.71) is a gradient model. To derive a simple description of the above model, we study its dynamics around the emergence of bistability, i.e., when the system becomes multi-valued or exhibits a nascent of bistability [**?**]. Figure 4.24(a) depicts a nascent of bistability. We express the expression for equilibria $\theta(x, t) = \theta_0$ as follow $V_0(\theta_0) = V_{FT}/\Gamma\left(1 - 2\pi^{-1}\theta_0\right)^2 - \alpha\, I_{in}\left[1 + \cos(\beta\cos^2\theta_0)\right]/2\Gamma$, and from this relation we determine the values of parameters for the emergence of bistability. Indeed, in the parameter space, the above expression generates a folded surface from which one can geometrically infer the points of nascent of bistability (cf. Fig 4.24(a)). In fact, θ_0 becomes multi-valued when the function $V_0(\theta_0, I_{in})$ has a saddle point at $\theta_0 = \theta_c$.

Around the saddle point $V_0(\theta_c)$ creates two new extreme points that determine the width of the bistability region. To find the saddle points of $V_0(\theta_c, I_{in})$, we have to impose the conditions $dV_0/d\theta_c = 0$, $d^2V_0/d^2\theta_c = 0$ and, after straightforward algebraic calculations, we obtain the relations $I_{in} = \pi^2 V_{FT}/\alpha\beta\left(\pi/2 - \theta_c\right)^3\sin(2\theta_c)\sin\left(\beta\cos^2\theta_c\right)$, and $\left(\theta_c - \pi/2\right)\left[2\csc 2\theta_c + \beta\sin 2\theta_c\cot(\beta\cos^2\theta_c)\right] = 3$. The first expression gives the

Figure 4.24: (color online) Front propagation of numerical simulation of phenomenological model of LCLV with optical feedback Eq. (4.71). (a) Bifurcation diagram of molecular average orientations θ_0 as function of voltage V_0. V_0^c accounts for a critical value of voltage for which the system exhibits nascent of bistability at $\theta_0 = \theta_c$. (b) Front speeds as function of voltage V_0 for difference free propagation length.

critical value of I_{in} for which V_0 becomes multi-valued. The second expression is an algebraic equation that depends only on the parameter β and determines all the points of nascent of bistability. Notice that only half of them have physical significance because the other half correspond to negative values of the intensity. By taking into account the constraint that the intensity must be positive and considering that the cotangent function is π-periodic, we have that the actual number of points of nascent of bistability is equal to the next smallest integer of $\beta/2\pi$. For the values considered in our experiment β is about 54, then one expects to find 8 points of nascent of bistability in the entire (V_0, I_{in}) parameter space, a prediction that is confirmed by the experiment [**?**].

The dynamics around a nascent of bistability point can be described by a scalar field $u(x,t)$ governed by a cubic nonlinearity. Hence, close to this point, $I_{in} \equiv I_{in}^c$, $V_0 \equiv V_0^c$, and we can consider

$$\theta(x,t) \approx \theta_c + u(x,t)/u_0, \tag{4.72}$$

where $u_0^2 \equiv 2\beta \cos 2\theta_c \cot(\beta \cos^2\theta_c) + (4+\beta^2 \sin 2\theta_c)/3 - 2/\left(\pi/2-\theta_c\right)^2$ is a normalization constant.

Considering the above ansatz into Eq. (4.71) with zero free propagation length, $L = 0$, and developing in Taylor series by keeping the cubic terms, after straightforward algebraic calculations, we can reduce the full LCLV model to a simple bistable model

$$\tau \partial_t u = \eta + \mu u - u^3 + l^2 \partial_{xx} u, \tag{4.73}$$

where $\eta \equiv \alpha\left[1-\cos(\beta\cos^2\theta_c)\right]\left(\pi/2-\theta_c\right)^3 \left[I_{in} - I_c + \alpha(1-\cos(\beta\cos^2\theta_c)(V_0-V_c)/2\right]/\pi^2 V_{FT}$, and $\mu \equiv 12\Gamma[\left(\pi/2-\theta_c\right)^2 (V_0-V_c) + \left(\pi^2 V_{FT}/12 - \left(\pi/2-\theta_c\right)^2\right)(I_{in}-I_c)/I_c]/\pi^2 V_{FT}$.

For small free propagation length ($L \sim \epsilon \ll 1$), the light intensity I_w reached in the

photoconductor can be approximated by a local model characterized by

$$\begin{aligned} I_w(\theta, L) &\approx I_{in}\{1+\cos(\beta\cos^2\theta) \\ &\quad +L(1+\cos(\beta\cos^2\theta)\partial_{xx}\sin(\beta\cos^2\theta))/k \\ &\quad -L\sin(\beta\cos^2\theta)\partial_{xx}\cos(\beta\cos^2\theta)/k\}/2. \end{aligned}$$

Introducing this expression in Eq. (4.71), using ansatz (4.72), developing in Taylor series by keeping the cubic terms in u, considering that the order parameter is a slow variable in space ($\partial_{xx}u \ll \partial_x u \ll 1$), renormalizing space and after straightforward calculations we obtain Eq. (4.67), with

$$b = c \equiv -\frac{\pi\alpha\beta\cos(2\theta_c)I_c\left(\frac{V_{FT}}{2V_c+\alpha I_c(1+\cos(\beta\cos^2\theta_c))}\right)^{3/2}}{\sqrt{2}lu_0V_{FT}}.$$

Hence, close to the nascent of bistability, model Eq. (4.71) can be approximated by a simple non-variational model Eq. (4.67), which describes the complex dynamics observed around this critical point.

Numerical simulations of model (4.71) in the region of bistability for small free propagation length show that the system exhibits front solutions. The front speed is affected when the free propagation length is changed. Therefore, these fronts present a propagation mechanism of a non-variational nature.

Experimental non-variational fronts propagation.- Using the SLM, we have conducted quasi-one dimensional experiments in a LCLV with optical feedback. As voltage V_0 is varied as a control parameter, we identify the bistable region, where two different molecular orientation states coexist. In this bistability region, the SLM is not only used to create a one-dimensional channel, but also to create localized perturbations, which allow us to observe the emergence of fronts between two different molecular orientations. Hence, the light observed in the near field has different intensities, which are associated with the molecular orientations. Figure **??**b shows a temporal sequence of snapshots of front propagation. By recording with a CCD camera the interface evolution over the channel, we have measured the front speed, which is plotted in Fig. **??**c as a function of V_0 for different values of free propagation length L. For small

L experimental imperfections are relevant. We consider non-small L. Note that as free propagation length increases, the front speed increases, which is consistent with the theoretical prediction. Therefore the mechanism that generates the spread of these fronts is the energy difference and front core shape (non-variational effect).

In summary, we have characterized a mechanism of non-variational front propagation in one-dimension scalar fields, where the responsible process generating the spread of this front is the front shape and not the energy difference between equilibria. In higher dimensions we expect that the propagation is only corrected by curvature effects, e.g. Gibbs-Thomson effect [**?**].

4.8 The universal law of the front speed close to the disappearance of bistability

The bistable fronts exhibit a single propagation speed that does not depend on the initial conditions. Regarding one-dimensional variational or gradient systems, propagation speed depends on the energy difference between the two equilibria [135, 87]. Hence, the more stable state invades, the less stable one. Then, one expects a point in the parameter space where the relative energy between the two equilibria is equal, *the Maxwell point* [79], at which the front is motionless. In his pioneering work, Pomeau proposes a universal semi-implicit formula for the front speed (see formula (4.13)[135]), which accounts for the energy difference between states. Analytical results are only accessible close to the Maxwell point from this general expression. The front speed is linear around the Maxwell point. In one-dimensional bistable non-variational systems, fronts can be motionless at a point in the parameter space without the need for both equilibria to have equal energy [13]. This extends the Maxwell point concept for systems without free energy. Even walls connecting two equivalent vectorial fields through spontaneous symmetry breaking can spread according to a given chirality of the vector field [57, 44, 120]

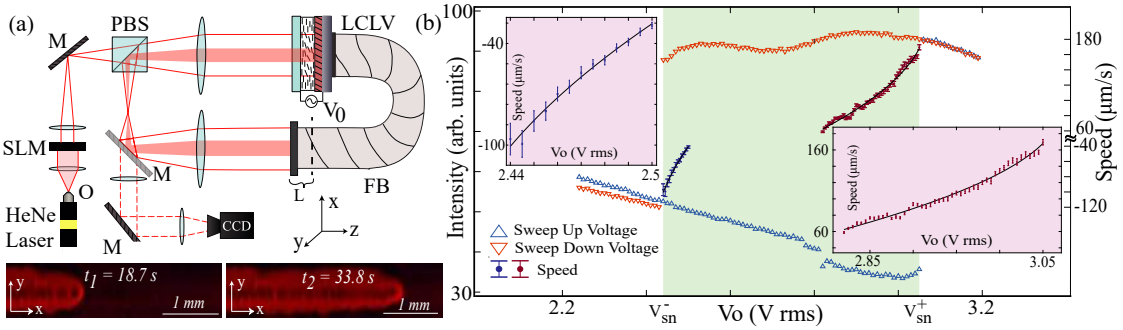

Figure 4.25: (Retrieved from [3]) Front propagation on a liquid crystal light valve (LCLV) with optical feedback close to the disappearance of bistability. (a) Schematic representation of LCLV with optical feedback setup. HeNe accounts for a Helium-Neon laser, SLM stands for spatial light modulator; this device selects a quasi-1D region under static and uniform illumination, M are mirrors, PBS is the polarized beam splitter, V_0 is the driven voltage applied to LCLV, O is an optical objective, FB is a fiber bundle, CCD is a Charge-Coupled Device to monitor the LCLV evolution, and L accounts for the free propagation length. Lower panels show temporal snapshots sequence of the front propagation exhibited in the LCLV close to the disappearance of bistability. (b) Bifurcation diagram of the total intensity and front speed of the LCLV with optical feedback as a function of the voltage applied V_0 by $L = 0.0\ cm$. The normal ($\triangle$) and inverted ($\triangledown$) triangles account for the total intensity of light measured by raising and lowering the voltage. The region of bistability is painted. V_{sn}^{+} accounts for the Fréedericksz voltage. The points with error bars account for the front speed between the different molecular orientations. Insets show a zoom of the front speed versus voltage V_0 near each bistability disappearance points. The continuous curves are the fits found for the front speeds, which have the form $v = v_0 + A\sqrt{|V_0 - V_{sn}^{\pm}|}$, where $\{v_0 = -183\ \mu m/s, A = 475.6\ V_{rms}^{-1/2}\mu m/s, V_{sn}^{-} = 2.41\ V_{rms}\}$, and $\{v_0 = 208.3\ \mu m/s, A = -292.3\ V_{rms}^{-1/2}\mu m/s, V_{sn}^{+} = 3.069\ V_{rms}\}$, for the left and right fit, respectively.

When a liquid crystal light valve is illuminated, the voltage applied to the cell V_0 is modified. Due to optical feedback, the system exhibits a subcritical bifurcation characterized by two different molecular orientation states [140, 52]. The Fréedericksz voltage characterizes the reorientation transition (see V_{sn}^{+} in Fig. 4.25b). Because these molecular orientations have different refractive indices, each equilibrium has a different intensity (see snapshots in Fig. 4.25a). Using the SLM, we can induce different domain walls and study the front propagation. Most precisely, fronts are usually triggered by the edges of the area under study, a quasi-1D channel induced by the SLM, or by local perturbations generated by the SLM that increase or decrease the illumination inside the channel. The bistability region is bounded by $\{V_{sn}^{-}, V_{sn}^{+}\}$, where $V_{sn}^{\pm}$ accounts for the disappearance of the bistability points. We have measured the front speed between two stable states close to the disappearance of bistability. Figure 4.25b) summarizes the results found. From this chart, we conclude that the front speed is close to the bistability disappearance exhibits a law of the form

$$v = v_0 + A\sqrt{|V_0 - V_{sn}^{\pm}|}, \tag{4.74}$$

where v_o is the front speed at the fold points. The main origin of the error bars and the initial propagation of the front are the inherent fluctuations of the system (noise) and the heterogeneities of the experimental setup. To illuminate the origin of this law, we will now consider different bistability models and analyze the front propagation.

4.8.1 Front propagation in prototype bistable models

A simple model that accounts for the transition from disordered to oriented molecules state (nematic-isotropic transition or clearance instability) was proposed by De Gennes [62], which has the dimensionless form [the **Landau-De Gennes model** Eq. (3.90)]

$$\partial_t u = \mu u + \alpha u^2 - u^3 + \partial_{xx} u, \tag{4.75}$$

where $u(x,t)$ is an order parameter, μ is the bifurcation parameter, α accounts for the nonlinear response. The last term accounts for elastic coupling, where ∂_{xx} is the

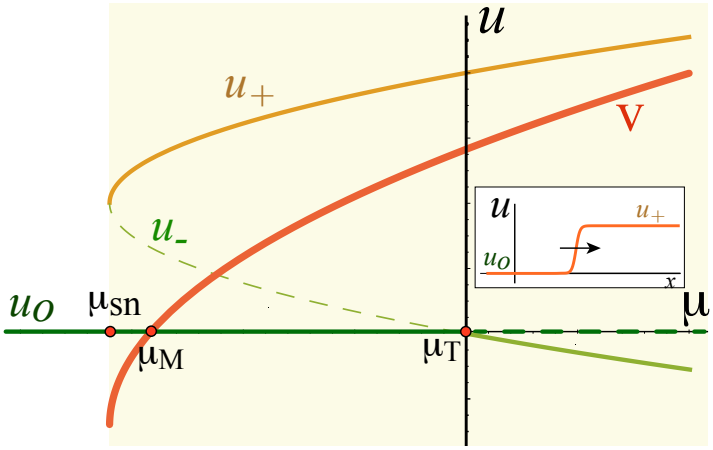

Figure 4.26: (Retrieved from [3]) Bifurcation diagram of Eq. (4.75) or (3.90). Equilibria u (u_0, u_-, and u_+) as a function of the bifurcation parameter μ. The hard and dashed curves account for stable and unstable states, respectively. The painted region stands for the bistable zone. The thick curve v stands for the front speed $v = \sqrt{2}(\alpha - 3\mu/u_+)/2$ between u_0 and u_+ state. μ_M accounts for the Maxwell point. The inset stands for a front profile.

Laplacian operator. The model Eq. (4.75) has also been used to describe hard colloidal rods [67], and anisotropic superfluid [16]. Equation (4.75) has three trivial equilibria $u = u_0 \equiv 0$ and $u = u_\pm \equiv (\alpha \pm \sqrt{\alpha^2 + 4\mu})/2$. Figure 4.26 shows the bifurcation diagram of Eq. (4.75). For $\mu < 0$, the u_0 state is stable, and for $\mu = \mu_T \equiv 0$, the system exhibits a transcritical instability, which generates that u_+ and u_- state are stable ones. The system is monostable when $\mu \leq \mu_{sn} \equiv -\alpha^2/4$, where the only stable equilibrium is u_0. The system is bistable for $\mu > \mu_{sn}$ (cf. Fig. 4.26). Namely, the system transitions from a bistable to a monostable region for $\mu = \mu_{sn}$ (disappearance of bistability). Then, the model presents a bistability region for $-\alpha^2/4 \leq \mu \leq 0$. Within this interval, the model Eq. (4.75) has fronts between u_0 and u_+ state, which has the form

$$u_F(x,t) = \frac{u_+}{2}\left[1 + \tanh\left(\frac{u_+(x - vt)}{2\sqrt{2}}\right)\right], \tag{4.76}$$

where $v = (\alpha - 3u_+/2)/\sqrt{2}$ (for more details see the Section 3.2.2). This is one of a few examples where the front speed is known in the entire parameter space. Close to disappearance of bistability, $\mu = -\alpha^2/4 + \Delta\mu$ where $\Delta\mu$ is a small parameter ($\Delta\mu \ll 1$)

and $u_+ \sim \alpha/2 + \sqrt{\Delta\mu}$, the front speed between stable states takes the form $v = v_0 + A\sqrt{\Delta\mu}$ with $v_0 \equiv \alpha/4\sqrt{2}$ and $A \equiv -3/2\sqrt{2}$.

4.8.2 Generic variational reaction-diffusion model

In one-dimension dynamical systems, a general description of a bistable system is given by the reaction-diffusion equation, which reads

$$\partial_t u = -\frac{\partial V}{\partial u} + \partial_{xx} u, \tag{4.77}$$

where $u(x,t)$ is a variable that describes the system under study and $V(u)$ is a bistable potential. In the case that the potential describes a symmetric system (Allen-Cahn Eq. [12]), the above model describes the domain wall dynamics. Assuming that the system has two equilibria, $\mathcal{A}$ and $\mathcal{B}$, that is, $\partial V(\mathcal{A})/\partial u = \partial V(\mathcal{B})/\partial u = 0$. One expects the system to exhibit propagative fronts between these two equilibria of the form $u(x,t) = u_F(x - vt)$. Introducing this ansatz into the diffusion-reaction Eq. (4.77), multiplying by $\partial_x u$ and integrating over the whole space, after straightforward calculations, one obtains the speed of bistable fronts [135]

$$v = \frac{V(\mathcal{B}) - V(\mathcal{A})}{\int (\partial_x u)^2 dx}. \tag{4.78}$$

As we have mentioned, in case both states have the same energy, $V(\mathcal{A}) = V(\mathcal{B})$, the speed is zero (Maxwell point).

Let us consider that equilibrium $\mathcal{B}$ is close to a saddle-node bifurcation (bistability disappearance), controlled by the bifurcation parameter Δ ($\Delta \ll 1$). Then $\mathcal{B} \approx \mathcal{B}_{sn} + \mathcal{B}_1\sqrt{\Delta}$ where $\mathcal{B}_{sn}$ is the equilibrium value at the bifurcation point. Since the front solution is proportional to the difference between equilibria, we can use $u(x,t) = (\mathcal{B} - \mathcal{A})H(x - vt)$. Using the above ansatz in formula (4.78), expanding in the Taylor series, one gets the universal law of front speed

$$v \approx \frac{V(\mathcal{B}_{sn}) - V(\mathcal{A})}{(\mathcal{B}_{sn} - \mathcal{A})^2 \int (\partial_x H_0)^2 dx} \left(1 - \frac{2\mathcal{B}_1\sqrt{\Delta}}{\mathcal{B}_{sn} - \mathcal{A}}\right), \tag{4.79}$$

$$\approx v_0 + A\sqrt{\Delta}, \tag{4.80}$$

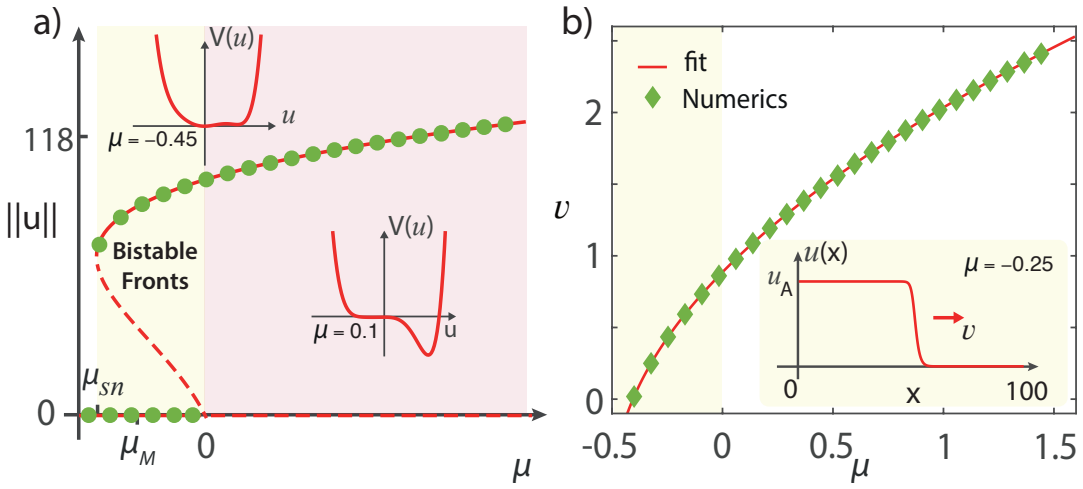

Figure 4.27: (Retrieved from [3]) Front propagation on the reaction-diffusion model (4.77) with cubic-quintic nonlinearity, $V(u) = -\mu u^2/2 - \beta u^3/3 - \delta u^4/4 + u^6/6$. (a) Bifurcation diagram, $||u|| = \sqrt{\int u^2 dx}$ as a function of the bifurcation parameter μ with $\beta = 0.5$ and $\delta = 0.8$. The solid and dashed red curves are the analytical curves obtained by multiplying the equilibria by the length of the system. The insets show the potential in different regions of parameter space. The points show the results obtained numerically. (b) Front speed as a function of the bifurcation parameter μ. The diamonds ($\diamond$) are the numerical results, and the continuous curve is the fit curve, formula (**??**), with $v_0 = -0.383$, $A = 1.971$, and $\mu_{sn} = 0.45$. The inset shows a typical profile of a front solution.

where v_0 is the front speed at the bistability disappearance point and $H_0 = H(x - v_0 t)$. Hence, any one-dimensional diffusion reaction-like system near the bistability disappearance will exhibit a square root-law front speed as a function of the bifurcation parameter. This is consistent with the experimental (see Fig. 4.25) and theoretical observations (cf. Fig. 4.26) discussed above.

To verify the validity of the universal formula (4.80), we consider the bistable cubic-quintic model with the potential $V(u) = -\mu u^2/2 - \beta u^3/3 - \delta u^4/4 + u^6/6$. This potential has been used to study the dynamics of molecular reorientation of optical valves with spatially modulated optical feedback [8]. Figure 4.27 shows the bifurcation diagram of this model with cubic-quintic nonlinearity and the front speed as a function of the bifurcation parameter. Note that this model has no analytical formula for the front speed. Unexpectedly, the universal formula (4.74) describes the front speed quite well,

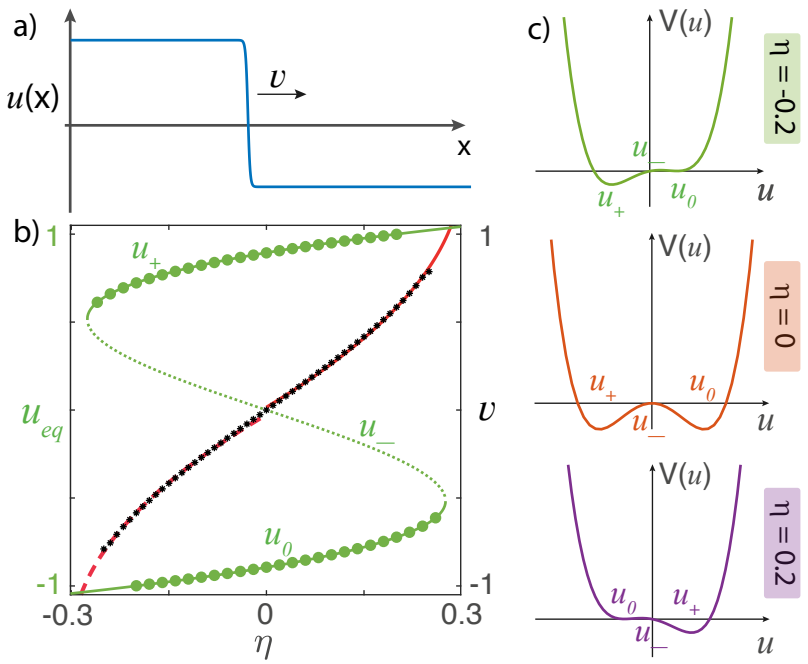

Figure 4.28: (Retrieved from [3]) Front propagation in the reaction-diffusion model (4.77) for a nascent bistability potential, $V(u) = -\eta u - \mu u^2 + u^4/4$. (a) Typical front profile. (b) Bifurcation diagram (green points and curves) and the front speed (black stars) as a function of the bifurcation parameter η with $\mu = 0.2$. The left and right vertical axes account for equilibria (u_{eq}) and the front speed, respectively. The solid and dashed curves are the stable (u_+, u_0) and unstable (u_-) states, respectively. The points show the results obtained numerically. The red solid ($v_0 = 1.358$, $A = -2.45$, and $\eta_{sn} = 0.3$) and dashed ($v_0 = -1.342$, $A = 2.401$, and $\eta_{sn} = 0.3$) curves are the fit curve formula (**??**). (c) The potential in different parameter space points with $\mu = 0.8$.

even far from its validity region.

Another relevant bistable model used to describe the nascent of bistability [153] or an imperfect pitchfork bifurcation, is the one governed by Eq. (4.77) with $V(u) = -\eta u - \mu u^2 + u^4/4$). This type of reaction-diffusion equation has been used to explain chemical reactions, biological models, and optical systems [99, 47]. Figure 4.28 shows the bifurcation diagram for this potential, its respective bistability zone, the shape of the potential for different values of the η parameter, the profile of the observed fronts, and the front speed as a function of the bifurcation parameter. In this case, the bistability region is bounded by two critical points (saddle-node bifurcations). We find

the universal law for the front speed (4.74) at each of these critical points.

4.8.3 Non-variational systems

The experimental and theoretical results presented above are valid for gradient or variational systems. Namely, the dynamics of these systems minimize a given free energy. However, one can consider nonvariational effects (such as nonlinear gradients or diffusions) and study how the front propagation is modified [13]. Let us consider the following prototype nonvariational bistable model [13, 15]

$$\begin{aligned} \partial_t u &= \eta + \mu u - u^3 + \partial_{xx} u + c(\partial_x u)^2 + bu\partial_{xx} u, \\ &= -\frac{\partial V}{\partial u} + \partial_{xx} u + c(\partial_x u)^2 + bu\partial_{xx} u, \end{aligned} \tag{4.81}$$

where the last two terms account for nonlinear drift and diffusion. A similar model with spatial instability (anti-diffusion) has been used to explain localized states with spatiotemporal chaos [162]. The model Eq. (4.81) describes the LCLV with free diffraction ($L \neq 0$) and spatiotemporal modulated forcing [4]. This experiment is achieved using the liquid crystal light valve with optical feedback shown in Fig. 4.25a, where the SLM now does a double role, selecting the one-dimensional region and spatiotemporally modulating the illumination in the optical liquid crystal light valve. Indeed, $c = b = 0$ when the experimental setup does not have free diffraction. Since the non-variational terms are proportional to the spatial derivatives, they do not modify the equilibria. Hence, the bifurcation diagram shown in Fig. 4.28 is still valid for the non-variational model (4.81). Considering the non-variational terms as perturbative terms ($c \sim b \ll 1$), using the strategy presented in [13], we can calculate how formula (4.79) is modified. Then, after straightforward calculations, we obtain the front speed between stable states close to the disappearance of bistability

$$\begin{aligned} v &\approx \frac{V(\mathcal{B}_{sn}) - V(\mathcal{A})}{(\mathcal{B}_{sn} - \mathcal{A})^2 \int (\partial_x H_0)^2 dx} \left(1 - \frac{2\mathcal{B}_1\sqrt{\Delta}}{\mathcal{B}_{sn} - \mathcal{A}}\right) + \\ &\quad (\mathcal{A} - \mathcal{B}_{sn}) \frac{c\int (\partial_x H_0)^3 dx + b\int (H_0 \partial_x H_0 \partial_{xx} H_0) dx}{\int (\partial_x H_0)^2 dx}. \end{aligned} \tag{4.82}$$

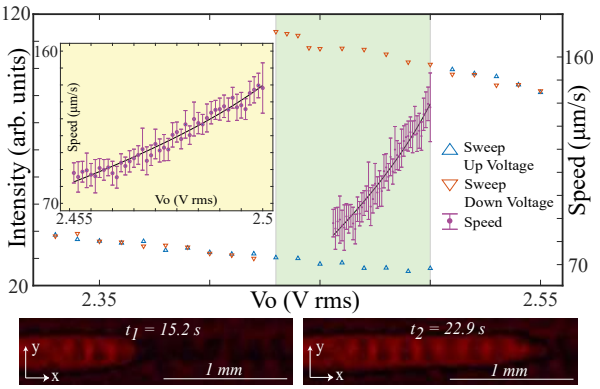

Figure 4.29: (Retrieved from [3]) Bifurcation diagram and front speed in an LCLV with free diffraction $L = -1.0\ cm$ and spatiotemporal optical feedback. This diagram is obtained using the same experimental setup as in Fig. 4.25a, where the SLM now fulfills a dual role, selecting the quasi-one-dimensional region and spatiotemporally modulating the illumination on the optical liquid crystal light valve. The diamonds and their respective error bars account for the front speed near the disappearance of bistability. The solid line is obtained using fit (4.74) with $v_0 = 203.5\ \mu$m/s, $A = -489.1\ V_{rms}^{-1/2} \mu m/s$, and $V_{sn} = 2.517\ V_{rms}$. Insets account for a magnification of the front speed as a function of V_0. Lower panels show temporal snapshots of the sequence of the front propagation.

Therefore, in the variational case, the front speed close to the bistability disappearance point also follows formula (4.74). To verify the validity of this result, experimentally, we introduce a standing wave type spatiotemporal forcing in the LCLV with optical feedback [4]. Figure 4.29 shows the bifurcation diagram and the front speed of the LCLV in the presence of free diffraction and spatiotemporal optical feedback. We observe a quite good agreement with the theoretical finding from this chart.

In brief, close to the transition between a bistable to a monostable region, we have shown that the front speed between stable states follows a square root law as a function of bifurcation parameters, independently the system is variational or not. The experimental findings show a fairly fair agreement with the theoretical results. In the case of other steady-state instabilities, the front speed may exhibit other critical exponents depending on the bifurcation parameters; for example, in a transcritical bifurcation, a linear law governs the front speed [27]. Because the fronts between bistable states are

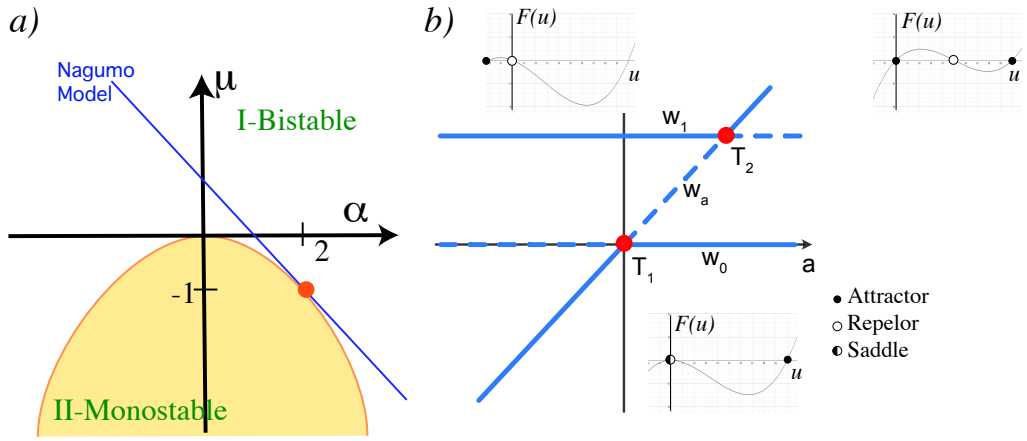

Figure 4.30: Landau-De Gennes and Nagumo model comparison. a) Phase diagram of the Landau-De Gennes model Eq. (4.75) in the parameter space. Zone I accounts for the bistable region. The painted region, II-monostable, corresponds to the monostable region, where the only solution is u_0. The red curve corresponds to the parabola $\mu = -\alpha^2/4$. The blue curve, $\alpha = 1 - \mu$, accounts for the parameter space the Nagumo model covers. b) Bifurcation diagram of the Nagumo model as a function of the a parameter. w_0, w_a, and w_1 account for the uniform equilibria. T_1 and T_2 stand for transcritical bifurcations. The insets give an account of the dynamics in the respective regions.

nonlinear, there are generally no analytical formulas for front speed. Then, studying critical points or bifurcations (such as the Maxwell point or point of disappearance of bistability) allows for universal behaviors for front speed.

4.8.4 Universal front speed behavior close to a transcritical bifurcation

Two prototypical bistability models are the Landau-De Gennes [62] and the Nagumo model [124], which have the form, respectively

$$\begin{aligned} \partial_t u &= \mu u + \alpha u^2 - u^3 + \partial_{xx} u, \quad \text{Landau-De Gennes} \\ \partial_t w &= w(w-a)(1-w) + \partial_{xx} w. \quad \text{Nagumo model} \end{aligned} \tag{4.83}$$

The Nagumo model is characterized by a single parameter a, where the system has solutions $w = w_0 \equiv 0$, $w = w_a \equiv a$, and $w = w_1 \equiv 1$ as equilibria. A similar

model Eq. (3.81) was studied in Section 3.2.1. Figure 4.30b shows the bifurcation diagram of the Nagumo model. This model presents two bifurcations, represented by red disks, where the stability is exchanged between equilibria, usually called a transcritical bifurcation [150]. The states that interchange stability grow linearly with the bifurcation parameter [150]. Then, the system has no monostable region. Hence, the model never exhibits a transition from a bistable to a monostable region, that is, the Nagumo model Eq. (4.83) does not exhibit the disappearance of bistability. To shed light on this property, we rewrite the Nagumo model as the Landau-De Gennes one, i.e.

$$\partial_t w = -aw + (a+1)w^2 - w^3 + \partial_{xx} w, \tag{4.84}$$

which corresponds to the particular choice of parameters of the Landau-De Gennes model (4.75) $\mu = -a$ and $\alpha = a+1$. Then, in the parameter space (μ, α) of the Landau-De Gennes model (cf. Fig. 4.30), the Nagumo model corresponds to the straight-line $\alpha = 1 - \mu$. The curve intersects the border of the bistable and monostable region but does not cross it (red disk), which corresponds to a transcritical bifurcation. Therefore, the Nagumo model never transits from the bistable to the monostable region.

In brief, Eq. (4.75) and (4.83) are not equivalent since it requires a renormalization parameter with complex values to cover the transitions between the bistable and monostable regions. Namely, the Nagumo model only covers the bistable region (cf. Fig. 4.30). However, the Nagumo model for $a = 0$ connects an unstable saddle solution with a stable state, and one expects to find a new universal behavior different from that found when bistability disappears. For an equivalent model of Nagumo model equation (3.81), one has

$$\partial_\tau N = N(1-N)(1+a'N) + \partial_{zz} N. \tag{4.85}$$

When $a' > 2$, the front speed c between a stable and unstable state is characterized by (cf. Formula 3.82)

$$c = \frac{2+a'}{\sqrt{2a'}}. \tag{4.86}$$

To transform the previous equation into the Nagumo equation, one can introduce the parameter $a = 1/a'$ and the scaling $\tau = t/a'$ and $z = x/\sqrt{a'}$. Thus, the front speed for

the Nagumo model reads

$$c = \frac{a}{\sqrt{a}} \frac{(2a+1)\sqrt{a}}{a\sqrt{2}} = \frac{(2a+1)}{\sqrt{2}}. \tag{4.87}$$

The Nagumo model Eq. (4.83) shows a transcritical bifurcation for $a = 0$, as illustrated in Fig. 4.30. Then, from the previous formula (4.88) for $a \approx \Delta \ll 1$, one can conclude that the front speed increases linearly with the bifurcation parameter a,

$$c(a = \Delta \ll 1) \approx \sqrt{2} + \sqrt{2}\Delta. \tag{4.88}$$

The previous result was obtained using the pushed fronts formula. We can then use variational methods to show these universal results. Let us consider the general front speed proposed by the in [27] (see Section 3.3)

$$c^2 = max\left(2\frac{\int_0^1 fgdq}{\int_0^1(-g^2/g')dq}\right), \tag{4.89}$$

where $f(u,\mu)$ is the drift or the reaction term of the system that has two equilibria $f(u=0) = f(u=1) = 0$, μ is a parameter that characterizes the system, and g is a trial function. Besides, let us consider the hypothesis that the system presents a transcritical bifurcation for $\mu = \mu_{TB}$. Close to the transcritical bifurcation $\mu = \mu_{TB} + \Delta\mu$, where $\Delta\mu$ is the bifurcation parameter, the reaction term can be written as

$$f(u,\mu) \approx f(u,\mu_{sd}) + \Delta\mu \frac{\partial f(u,\mu_{sd})}{\partial \mu}. \tag{4.90}$$

Introducing this expression in formula (4.89), one gets

$$\begin{aligned} c^2 &\approx max\left(\frac{2\int_0^1 f_0 g dq}{\int_0^1(-g^2/g')dq}\right) + max\left(\frac{2\int_0^1 f_1 g dq}{\int_0^1(-g^2/g')dq}\right)\Delta\mu, \\ &\approx c_0^2 + c_1^2\Delta\mu, \end{aligned} \tag{4.91}$$

where $f_0 \equiv f(u,\mu_{sd})$, $f_1 \equiv \partial f(u,\mu_{sd})/\partial\mu$, c_0 is the front speed at the transcritical bifurcation, and c_1 accounts for the first dominant correction of formula (4.89). Trial functions have no reason to be modified with the bifurcation parameter $\Delta\mu$. Applying

square root to formula (4.91) and keeping the dominant terms after straightforward calculations, one obtains

$$c \approx c_0 + \frac{c_1^2}{c_0}\Delta\mu. \tag{4.92}$$

Then, one infers that the front speed increases linearly with the bifurcation parameter in a transcritical bifurcation.

4.9 Non-variational Ising-Bloch transition

see article 188

4.10 Asymmetric counterpropagating fronts without flow

see article 90

4.11 Front propagation in inhomogeneous media

see article 76,79,107

4.12 Front propagation steered by a high-wavenumber modulation

see article 152

4.13 Alee effect in population dynamics: Nagumo Model

see article 49

Chapter 5

Front between patterns and homogeneous states

5.1 Prototype model of fronts between patterns and homogeneous states

see article 39,42,46, 70

5.2 Internal noise induces Front propagation

The analysis and study presented in this section are based on article [50].

see article 87

5.3 Pinning-depinning transition of fronts between standing wave

see article 64

Bibliography

[1] Thorsten Ackemann, WilliamJ Firth, and Gian-Luca Oppo. Fundamentals and applications of spatial dissipative solitons in photonic devices. *Advances in atomic, molecular, and optical physics*, 57:323–421, 2009.

[2] Robert Adler. A study of locking phenomena in oscillators. *Proceedings of the IRE*, 34(6):351–357, 1946.

[3] PJ Aguilera-Rojas, K Alfaro-Bittner, MG Clerc, G González-Cortés, and RG Rojas. The universal law of the front speed close to the disappearance of bistability. *Chaos, Solitons & Fractals*, 169:113241, 2023.

[4] PJ Aguilera-Rojas, MG Clerc, G Gonzalez-Cortes, and G Jara-Schulz. Localized standing waves induced by spatiotemporal forcing. *Physical Review E*, 104(4):044209, 2021.

[5] Guenter Ahlers and David S Cannell. Vortex-front propagation in rotating couette-taylor flow. *Physical Review Letters*, 50(20):1583, 1983.

[6] LV Alekseeva, IV Povkh, VI Stroganov, BI Kidyarov, and PG Pasko. A nonreciprocal optical element. *Journal of Optical Technology*, 70(7):525–526, 2003.

[7] K. Alfaro-Bittner, C. Castillo-Pinto, M. G. Clerc, G. González-Cortés, R. G. Rojas, and M. Wilson. Front propagation into an unstable state in a forced medium: Experiments and theory. *Phys. Rev. E*, 98:050201, Nov 2018.

[8] K Alfaro-Bittner, C Castillo-Pinto, MG Clerc, G González-Cortés, G Jara-Schulz, and RG Rojas. Front propagation steered by a high-wavenumber modulation: Theory and experiments. *Chaos: An Interdisciplinary Journal of Nonlinear Science*, 30(5), 2020.

[9] K. Alfaro-Bittner, M.G. Clerc, M. Garcia-Nustes, and R.G. Rojas. Front propagation into unstable states in discrete media. submited to Commun. Nonlinear. Sci. Numer. Simulat. (March 2016).

[10] K Alfaro-Bittner, MG Clerc, MA García-Ñustes, and RG Rojas. π-kink propagation in the damped frenkel-kontorova model. *EPL (Europhysics Letters)*, 119(4):40003, 2017.

[11] K Alfaro-Bittner, MG Clerc, RG Rojas, and MA García-Ñustes. Traveling wave into an unstable state in dissipative oscillator chains. *Nonlinear Dynamics*, 98:1391–1402, 2019.

[12] Samuel M Allen and John W Cahn. A microscopic theory for antiphase boundary motion and its application to antiphase domain coarsening. *Acta metallurgica*, 27(6):1085–1095, 1979.

[13] AJ Alvarez-Socorro, MG Clerc, G González-Cortés, and M Wilson. Nonvariational mechanism of front propagation: Theory and experiments. *Physical Review E*, 95(1):010202, 2017.

[14] AJ Alvarez-Socorro, MG Clerc, and M Tlidi. Spontaneous motion of localized structures induced by parity symmetry breaking transition. *Chaos: An Interdisciplinary Journal of Nonlinear Science*, 28(5):053119, 2018.

[15] Alejandro J Álvarez-Socorro, Camila Castillo-Pinto, Marcel G Clerc, Gregorio González-Cortes, and Mario Wilson. Front propagation transition induced by diffraction in a liquid crystal light valve. *Optics Express*, 27(9):12391–12398, 2019.

[16] V Ambegaokar, PG DeGennes, and D Rainer. Landau-ginsburg equations for an anisotropic superfluid. *Physical Review A*, 9(6):2676, 1974.

[17] Ignacio Andrade-Silva, Umberto Bortolozzo, Marcel G Clerc, Gregorio González-Cortés, Stefania Residori, and Mario Wilson. Spontaneous light-induced turing patterns in a dye-doped twisted nematic layer. *Scientific Reports*, 8(1):12867, 2018.

[18] Aleksandr Aleksandrovich Andronov, Aleksandr Adol'fovich Vitt, and Semen Emmanuilovich Khaikin. *Theory of Oscillators: Adiwes International Series in Physics*, volume 4. Elsevier, 2013.

[19] M Argentina, MG Clerc, R Rojas, and E Tirapegui. Coarsening dynamics of the one-dimensional cahn-hilliard model. *Physical Review E*, 71(4):046210, 2005.

[20] Vladimir I Arnol'd. *Catastrophe theory*. Springer Science & Business Media, 2003.

[21] Radu Balescu. Equilibrium and nonequilibrium statistical mechanics. *NASA STI/Recon Technical Report A*, 76, 1975.

[22] S Barbay, Y Ménesguen, X Hachair, L Leroy, I Sagnes, and R Kuszelewicz. Incoherent and coherent writing and erasure of cavity solitons in an optically pumped semiconductor amplifier. *Optics letters*, 31(10):1504–1506, 2006.

[23] Grigory Isaakovich Barenblatt. *Scaling, self-similarity, and intermediate asymptotics: dimensional analysis and intermediate asymptotics*, volume 14. Cambridge University Press, 1996.

[24] Felipe Barra, Orazio Descalzi, and Enrique Tirapegui. Nonvariational effects in nonequilibrium systems. *Physics Letters A*, 221(3-4):193–196, 1996.

[25] George Keith Batchelor. *An introduction to fluid dynamics*. Cambridge university press, 2000.

[26] John Bechhoefer, Hartmut Löwen, and Laurette S Tuckerman. Dynamical mechanism for the formation of metastable phases. *Physical review letters*, 67(10):1266, 1991.

[27] RD Benguria and MC Depassier. Variational characterization of the speed of propagation of fronts for the nonlinear diffusion equation. *Communications in mathematical physics*, 175(1):221–227, 1996.

[28] Ernst Julius Berg. *Heaviside's Operational Calculus as applied to Engineering and Physics*. McGraw-Hill book company, inc., 1936.

[29] Enrico Betti. Teoria della elasticita? *Il Nuovo Cimento (1869-1876)*, 7(1):69–97, 1872.

[30] Eberhard Bodenschatz, David S Cannell, John R de Bruyn, Robert Ecke, Yu-Chou Hu, Kristina Lerman, and Guenter Ahlers. Experiments on three systems with non-variational aspects. *Physica D: Nonlinear Phenomena*, 61(1-4):77–93, 1992.

[31] Ignacio Bordeu and Marcel G Clerc. Rodlike localized structure in isotropic pattern-forming systems. *Physical Review E*, 92(4):042915, 2015.

[32] Ronald Newbold Bracewell and Ronald N Bracewell. *The Fourier transform and its applications*, volume 31999. McGraw-Hill New York, 1986.

[33] Maury D Bramson. Maximal displacement of branching brownian motion. *Communications on Pure and Applied Mathematics*, 31(5):531–581, 1978.

[34] Martin Brandenbourger, Xander Locsin, Edan Lerner, and Corentin Coulais. Non-reciprocal robotic metamaterials. *Nature communications*, 10(1):4608, 2019.

[35] Oleg M Braun and Yuri Kivshar. *The Frenkel-Kontorova model: concepts, methods, and applications*. Springer Science & Business Media, 2013.

[36] Oleg M Braun and Yuri S Kivshar. Nonlinear dynamics of the frenkel–kontorova model. *Physics Reports*, 306(1):1–108, 1998.

[37] W-K Burton, N Cabrera, and FC Frank. The growth of crystals and the equilibrium structure of their surfaces. *Philosophical Transactions of the Royal Society of London A: Mathematical, Physical and Engineering Sciences*, 243(866):299–358, 1951.

[38] John W Cahn and John E Hilliard. Free energy of a nonuniform system. i. interfacial free energy. *The Journal of chemical physics*, 28(2):258–267, 1958.

[39] H Calisto, M Clerc, R Rojas, and Enrique Tirapegui. Bubbles interactions in the cahn-hilliard equation. *Physical review letters*, 85(18):3805, 2000.

[40] Camila Castillo-Pinto, Marcel G Clerc, and Gregorio González-Cortés. Extended stable equilibrium invaded by an unstable state. *Scientific Reports*, 9(1):15096, 2019.

[41] S. Chandrasekhar. *Liquid crystal*. Cambridge University Press, New York, 1992.

[42] M. Clerc, P. Coullet, and E. Tirapegui. Lorenz bifurcation: Instabilities in quasireversible systems. *Phys. Rev. Lett.*, 83:3820–3823, Nov 1999.

[43] M. G. Clerc, S. Residori, and C. S. Riera. First-order freedericksz transition in the presence of a light driven feedback. *Phys. Rev. E*, 63(060701), 2001.

[44] Marcel G Clerc, Saliya Coulibaly, and David Laroze. Nonvariational ising–bloch transition in parametrically driven systems. *International Journal of Bifurcation and Chaos*, 19(08):2717–2726, 2009.

[45] Marcel G Clerc, Ricardo G Elías, and René G Rojas. Continuous description of lattice discreteness effects in front propagation. *Philosophical Transactions of the Royal Society of London A: Mathematical, Physical and Engineering Sciences*, 369(1935):412–424, 2011.

[46] Marcel G Clerc, Gregorio González-Cortés, Vincent Odent, and Mario Wilson. Optical textures: characterizing spatiotemporal chaos. *Optics Express*, 24(14):15478–15485, 2016.

[47] Marcel G Clerc, Artem Petrossian, and Stefania Residori. Bouncing localized structures in a liquid-crystal light-valve experiment. *Physical Review E*, 71(1):015205, 2005.

[48] MG Clerc, D Escaff, and VM Kenkre. Patterns and localized structures in population dynamics. *Physical Review E*, 72(5):056217, 2005.

[49] MG Clerc, D Escaff, and VM Kenkre. Analytical studies of fronts, colonies, and patterns: combination of the allee effect and nonlocal competition interactions. *Physical Review E*, 82(3):036210, 2010.

[50] MG Clerc, C Falcon, and Enrique Tirapegui. Additive noise induces front propagation. *Physical review letters*, 94(14):148302, 2005.

[51] MG Clerc, Tomoyuki Nagaya, A Petrossian, Stefania Residori, and CS Riera. First-order fréedericksz transition and front propagation in a liquid crystal light valve with feedback. *The European Physical Journal D-Atomic, Molecular, Optical and Plasma Physics*, 28(3):435–445, 2004.

[52] MG Clerc, S Residori, and CS Riera. First-order fréedericksz transition in the presence of light-driven feedback in nematic liquid crystals. *Physical Review E*, 63(6):060701, 2001.

[53] Diego AC Contreras and Marcel G Clerc. Internal noise and system size effects induce nondiffusive kink dynamics. *Physical Review E*, 91(3):032922, 2015.

[54] Corentin Coulais, Dimitrios Sounas, and Andrea Alu. Static non-reciprocity in mechanical metamaterials. *Nature*, 542(7642):461–464, 2017.

[55] P Coullet. Localized patterns and fronts in nonequilibrium systems. *International Journal of Bifurcation and Chaos*, 12(11):2445–2457, 2002.

[56] P. Coullet, C. Elphick, and D. Repaux. Nature of spatial chaos. *Phys. Rev. Lett.*, 58:431–434, Feb 1987.

[57] P Coullet, J Lega, B Houchmandzadeh, and J Lajzerowicz. Breaking chirality in nonequilibrium systems. *Physical Review Letters*, 65(11):1352, 1990.

[58] M. Cross and H. Greenside. *Pattern Formation and Dynamics in Nonequilibrium Systems*. Cambridge University Press, New York, 2009.

[59] M. C. Cross and P. C. Hohenberg. Pattern formation outside of equilibrium. *Rev. Mod. Phys.*, 65(851), 1993.

[60] Jesús Cuevas-Maraver, Panayotis G Kevrekidis, and Floyd Williams. *The sine-Gordon model and its applications: From pendula and Josephson Junctions to Gravity and High-Energy Physics*, volume 10. Springer, 2014.

[61] Jonathan HP Dawes. After 1952: The later development of alan turing's ideas on the mathematics of pattern formation. *Historia Mathematica*, 43(1):49–64, 2016.

[62] P. G. de Gennes and J. Prost. *The Physics of Liquid Crystals*. International Series of Monographs on Physics. Clarendon Press, 1995.

[63] J Den Hartog. *Mechanical Vibrations*. McGraw-Hill Book Company, Inc., New York, 1956.

[64] Orazio Descalzi, Marcel G Clerc, Stefania Residori, and Gaetano Assanto. *Localized states in physics: solitons and patterns*. Springer Science & Business Media, 2011.

[65] Ute Ebert and Wim van Saarloos. Front propagation into unstable states: universal algebraic convergence towards uniformly translating pulled fronts. *Physica D: Nonlinear Phenomena*, 146(1-4):1–99, 2000.

[66] Charles M Elliott and Zheng Songmu. On the cahn-hilliard equation. *Archive for Rational Mechanics and Analysis*, 96(4):339–357, 1986.

[67] JC Everts, MTJJM Punter, Sela Samin, PPAM van der Schoot, and René van Roij. A landau-de gennes theory for hard colloidal rods: Defects and tactoids. *The Journal of Chemical Physics*, 144(19), 2016.

[68] Michael Faraday. *Faraday's Chemical History of a Candle*. Chicago Review Press, 1861.

[69] A. L. Fetter and J.D. Walecka. *Theoretical mechanics of particles and continua*. Dover Publications, 2003.

[70] Jay Fineberg and Victor Steinberg. Vortex-front propagation in rayleigh-bénard convection. *Physical review letters*, 58(13):1332, 1987.

[71] Ronald Aylmer Fisher. The wave of advance of advantageous genes. *Annals of eugenics*, 7(4):355–369, 1937.

[72] Romain Fleury, Dimitrios L Sounas, Caleb F Sieck, Michael R Haberman, and Andrea Alù. Sound isolation and giant linear nonreciprocity in a compact acoustic circulator. *Science*, 343(6170):516–519, 2014.

[73] Ivar Fredholm. Sur une classe d'équations fonctionnelles. 1903.

[74] Jordi García-Ojalvo and José Sancho. *Noise in spatially extended systems*. Springer Science & Business Media, 2012.

[75] Crispin W Gardiner et al. *Handbook of stochastic methods*, volume 3. Springer Berlin, 1985.

[76] Robert Gilmore. *Catastrophe theory for scientists and engineers*. Courier Corporation, 1993.

[77] Francesco Ginelli, Fernando Peruani, Marie-Helène Pillot, Hugues Chaté, Guy Theraulaz, and Richard Bon. Intermittent collective dynamics emerge from conflicting imperatives in sheep herds. *Proceedings of the National Academy of Sciences*, 112(41):12729–12734, 2015.

[78] P Glansdorff and I Prigogine. Thermodynamic theory of structure, stability and fluctuations. *Wiley-Interscience, New York. Science*, 176(4042):1410–1420, 1972.

[79] Raymond E Goldstein, Gemunu H Gunaratne, L Gil, and P Coullet. Hydrodynamic and interfacial patterns with broken space-time symmetry. *Physical Review A*, 43(12):6700, 1991.

[80] László Gránásy, Tamás Pusztai, and Peter F James. Interfacial properties deduced from nucleation experiments: A cahn–hilliard analysis. *The Journal of chemical physics*, 117(13):6157–6168, 2002.

[81] John Guckenheimer and Philip Holmes. *Nonlinear oscillations, dynamical systems, and bifurcations of vector fields*, volume 42. Springer Science & Business Media, 2013.

[82] KP Hadeler and Franz Rothe. Travelling fronts in nonlinear diffusion equations. *Journal of Mathematical Biology*, 2(3):251–263, 1975.

[83] Aric Hagberg and Ehud Meron. From labyrinthine patterns to spiral turbulence. *Physical review letters*, 72(15):2494, 1994.

[84] Hermann Haken. *Advanced synergetics: Instability hierarchies of self-organizing systems and devices*, volume 20. Springer Science & Business Media, 2012.

[85] Frederick Duncan Michael Haldane and Srinivas Raghu. Possible realization of directional optical waveguides in photonic crystals with broken time-reversal symmetry. *Physical review letters*, 100(1):013904, 2008.

[86] A Hari and AA Nepomnyashchy. Nonpotential effects in dynamics of fronts between convection patterns. *Physical Review E*, 61(5):4835, 2000.

[87] F. Haudin, R. G. Elias, R. G. Rojas, U. Bortolozzo, M. G. Clerc, and S. Residori. Driven front propagation in 1d spatially periodic media. *Phys. Rev. Lett.*, 103(128003), 2009.

[88] F. Haudin, R. G. Elias, R. G. Rojas, U. Bortolozzo, M. G. Clerc, and S. Residori. *Phys. Rev. E*, 81(056203), 2010.

[89] Werner Horsthemke and Rene Lefever. *Noise induced transitions*. Springer, 1984.

[90] Brian R. Hunt and James A. Yorke. Maxwell on chaos. *Nonlinear Science Today*, 3(1):1–4, 1993.

[91] Gérard Iooss and Daniel D Joseph. *Elementary stability and bifurcation theory*. Springer Science & Business Media, 2012.

[92] E Atlee Jackson. *Perspectives of nonlinear dynamics*, volume 1. CUP Archive, 1992.

[93] Lishuai Jin, Romik Khajehtourian, Jochen Mueller, Ahmad Rafsanjani, Vincent Tournat, Katia Bertoldi, and Dennis M Kochmann. Guided transition waves in multistable mechanical metamaterials. *Proceedings of the National Academy of Sciences*, 117(5):2319–2325, 2020.

[94] Mehran Kardar, Giorgio Parisi, and Yi-Cheng Zhang. Dynamic scaling of growing interfaces. *Physical Review Letters*, 56(9):889, 1986.

[95] Kyozi Kawasaki and Takao Ohta. Kink dynamics in one-dimensional nonlinear systems. *Physica A: Statistical Mechanics and its Applications*, 116(3):573–593, 1982.

[96] Charles Kittel. *Introduction to solid state physics*. Wiley, 2005.

[97] A Kolmogorov, L Petrovsky, and N Piskunov. An investigation of the diffusion equation combined with an increase in mass and its application to a biological problem. *Bull Uni Moscow Ser Int A*, 1(6):1–26, 1937.

[98] Shigeru Kondo and Takashi Miura. Reaction-diffusion model as a framework for understanding biological pattern formation. *science*, 329(5999):1616–1620, 2010.

[99] Gregory Kozyreff and Mustapha Tlidi. Nonvariational real swift-hohenberg equation for biological, chemical, and optical systems. *Chaos: An Interdisciplinary Journal of Nonlinear Science*, 17(3), 2007.

[100] LD Landau and EM Lifshitz. *Statistical Physics: V. 5: Course of Theoretical Physics*. Pergamon Press, 1969.

[101] Lev D Landau and Evgenii Mikhailovich Lifshitz. *Course of theoretical physics*. Elsevier, 2013.

[102] J. Langer. *An introduction to the kinetics of first-order phase transition, In Solids Far from Equilibrium*. Cambridge University Press, Cambridge, 1992.

[103] Paul Langevin. Sur la théorie du mouvement brownien. *CR Acad. Sci. Paris*, 146(530-533):530, 1908.

[104] Olivier Lejeune, Mustapha Tlidi, and Pierre Couteron. Localized vegetation patches: a self-organized response to resource scarcity. *Physical Review E*, 66(1):010901, 2002.

[105] Stefano Lepri and Giulio Casati. Asymmetric wave propagation in nonlinear systems. *Physical review letters*, 106(16):164101, 2011.

[106] EM Lifschitz and LP Pitajewski. Physical kinetics. In *Textbook of theoretical physics. 10*. 1983.

[107] Hugo Lira, Zongfu Yu, Shanhui Fan, and Michal Lipson. Electrically driven nonreciprocity induced by interband photonic transition on a silicon chip. *Physical review letters*, 109(3):033901, 2012.

[108] David Lloyd and Björn Sandstede. Localized radial solutions of the swift–hohenberg equation. *Nonlinearity*, 22(2):485, 2009.

[109] David JB Lloyd, Björn Sandstede, Daniele Avitabile, and Alan R Champneys. Localized hexagon patterns of the planar swift–hohenberg equation. *SIAM Journal on Applied Dynamical Systems*, 7(3):1049–1100, 2008.

[110] R Luther. Räumliche ausbreitung chemischer reaktionen. *Zeitschrift für Elektrochemie*, 12:596–600, 1906.

[111] JE Macías, MG Clerc, C Falcón, and MA Garcia-Nustes. Spatially modulated kinks in shallow granular layers. *Physical Review E*, 88(2):020201, 2013.

[112] JE Macias, J. E.as and C Falcon. Dynamics of spatially modulated kinks in shallow granular layers. *New Journal of Physics*, 16(4):043032, 2014.

[113] Thomas Robert Malthus. *An essay on the principle of population: or, A view of its past and present effects on human happiness*. Reeves & Turner, 1888.

[114] Paul Mandel. *Theoretical problems in cavity nonlinear optics*, volume 21. Cambridge University Press, 2005.

[115] Nicholas Manton and Paul Sutcliffe. *Topological solitons*. Cambridge University Press, 2004.

[116] J Clerk Maxwell. L. on the calculation of the equilibrium and stiffness of frames. *The London, Edinburgh, and Dublin Philosophical Magazine and Journal of Science*, 27(182):294–299, 1864.

[117] Scott McCalla and Björn Sandstede. Snaking of radial solutions of the multi-dimensional swift–hohenberg equation: a numerical study. *Physica D: Nonlinear Phenomena*, 239(16):1581–1592, 2010.

[118] Baruch Meerson, Pavel V Sasorov, and Yitzhak Kaplan. Velocity fluctuations of population fronts propagating into metastable states. *Physical Review E*, 84(1):011147, 2011.

[119] Hilali M'F, Guy Dewel, and Pierre Borckmans. Subharmonic and strong resonances through coupling with a zero mode. *Physics Letters A*, 217(4-5):263–268, 1996.

[120] D Michaelis, U Peschel, F Lederer, DV Skryabin, and WJ Firth. Universal criterion and amplitude equation for a nonequilibrium ising-bloch transition. *Physical Review E*, 63(6):066602, 2001.

[121] Imran M Mirza, Wenchao Ge, and Hui Jing. Optical nonreciprocity and slow light in coupled spinning optomechanical resonators. *Optics express*, 27(18):25515–25530, 2019.

[122] Denis Mollison. Spatial contact models for ecological and epidemic spread. *Journal of the Royal Statistical Society. Series B (Methodological)*, pages 283–326, 1977.

[123] J. D. Murray. *Mathematical Biology*. Springer, Berlin Heidelberg,, 1989.

[124] James D Murray. *Mathematical Biology I: An Introduction, vol. 17 of Interdisciplinary Applied Mathematics*. Springer, New York, NY, USA,, 2002.

[125] James Dickson Murray. *Mathematical Biology. II Spatial Models and Biomedical Applications, Interdisciplinary Applied Mathematics V. 18*. Springer-Verlag New York Incorporated, 2001.

[126] Tomoyuki Nagaya and Jean-Marc Gilli. Experimental study of coarsening dynamics of the zigzag wall in a nematic liquid crystal with negative dielectric anisotropy. *Physical Review E*, 65(5):051708, 2002.

[127] Tomoyuki Nagaya and Jean-Marc Gilli. Experimental study of spinodal decomposition in a 1d conserved order parameter system. *Physical review letters*, 92(14):145504, 2004.

[128] Máté Nagy, Zsuzsa Ákos, Dora Biro, and Tamás Vicsek. Hierarchical group dynamics in pigeon flocks. *Nature*, 464(7290):890–893, 2010.

[129] G. Nicolis and I. Prigogine. *Self-Organization in Non Equilibrium Systems*. J. Wiley and Sons, New York, 1977.

[130] V Odent, MG Clerc, C Falcón, U Bortolozzo, E Louvergneaux, and S Residori. Photo-isomerization fronts in dye-doped nematic liquid crystals. *Optics letters*, 39(7):1861–1864, 2014.

[131] Arkady Pikovsky, Michael Rosenblum, and Jürgen Kurths. *Synchronization, A universal concept in nonlinear sciences*. Cambridge University Press, 2001.

[132] D Pinto-Ramos, K Alfaro-Bittner, MG Clerc, and RG Rojas. Nonreciprocal coupling induced self-assembled localized structures. *Physical Review Letters*, 126(19):194102, 2021.

[133] L. M. Pismen. *Patterns and Interfaces in Dissipative Dynamics*. Springer Series in Synergetics, Berlin Heidelberg, 2006.

[134] Henri Poincaré. *Les methodes nouvelles de la mecanique celeste*. Éditions Gauthiers-Villars, 1892.

[135] Yves Pomeau. Front motion, metastability and subcritical bifurcations in hydrodynamics. *Physica D: Nonlinear Phenomena*, 23(1):3–11, 1986.

[136] Thomas R Powers and Raymond E Goldstein. Pearling and pinching: propagation of rayleigh instabilities. *Physical review letters*, 78(13):2555, 1997.

[137] H-G Purwins, HU Bödeker, and Sh Amiranashvili. Dissipative solitons. *Advances in Physics*, 59(5):485–701, 2010.

[138] Alexander G Ramm. A simple proof of the fredholm alternative and a characterization of the fredholm operators. *The American Mathematical Monthly*, 108(9):855–860, 2001.

[139] Lorenz Ratke and Peter W Voorhees. *Growth and coarsening: Ostwald ripening in material processing*. Springer Science & Business Media, 2013.

[140] S. Residori. *Phys. Rep.*, 416(201), 2005.

[141] Stefania Residori, A Petrossian, Tomoyuki Nagaya, CS Riera, and MG Clerc. Fronts and localized structures in a liquid-crystal-light-valve with optical feedback. *Physica D: Nonlinear Phenomena*, 199(1):149–165, 2004.

[142] Jacobo Riccati. Animadversiones in aequationes differentiales secundi gradus. *Actorum Eruditorum Supplementa*, 8(1724):66–73, 1724.

[143] Wulf Rossmann. *Lie groups: an introduction through linear groups*, volume 5. Oxford University Press on Demand, 2002.

[144] Friedrich Schlögl. Chemical reaction models for non-equilibrium phase transitions. *Zeitschrift für physik*, 253(2):147–161, 1972.

[145] Arthur J Schwartz, John S Huang, and Walter I Goldburg. Spinodal decomposition in a binary liquid mixture near the critical point. *The Journal of Chemical Physics*, 62(5):1847–1852, 1975.

[146] Leonid Ivanovich Sedov. *Similarity and dimensional methods in mechanics*. CRC press, 1993.

[147] CA Smolders, JJ Van Aartsen, and A Steenbergen. Liquid-liquid phase separation in concentrated solutions of non-crystallizable polymers by spinodal decomposition. *Kolloid-Zeitschrift und Zeitschrift für Polymere*, 243(1):14–20, 1971.

[148] Dimitrios L Sounas, Christophe Caloz, and Andrea Alu. Giant non-reciprocity at the subwavelength scale using angular momentum-biased metamaterials. *Nature communications*, 4(1):2407, 2013.

[149] Norbert Stoop, Romain Lagrange, Denis Terwagne, Pedro M Reis, and Jörn Dunkel. Curvature-induced symmetry breaking determines elastic surface patterns. *Nature materials*, 14(3):337–342, 2015.

[150] S. H. Strogatz. *Nonlinear Dynamics and Chaos: with applications to Phyics, Biology, Chemistry and Engineering*. Westview Press, 2014.

[151] Ju Swift and Pierre C Hohenberg. Hydrodynamic fluctuations at the convective instability. *Physical Review A*, 15(1):319, 1977.

[152] Dirk Ter Haar. *Collected papers of LD Landau*. Elsevier, 2013.

[153] Mustapha Tlidi, Paul Mandel, and René Lefever. Localized structures and localized patterns in optical bistability. *Physical Review Letters*, 73(5):640, 1994.

[154] Enrique Trias, JJ Mazo, F Falo, and TP Orlando. Depinning of kinks in a josephson-junction ratchet array. *Physical Review E*, 61(3):2257, 2000.

[155] Laurette S Tuckerman and John Bechhoefer. Dynamical mechanism for the formation of metastable phases: The case of two nonconserved order parameters. *Physical Review A*, 46(6):3178, 1992.

[156] Alain M. Turing. The chemical basis of morphogenesis,. *Phil. Trans. R. Soc. Lond. B: Biol. Sci. 237, 37*, 1952.

[157] Tanmay Vachaspati. *Kinks and domain walls: An introduction to classical and quantum solitons*. Cambridge University Press, 2006.

[158] Nicolaas Godfried Van Kampen. *Stochastic processes in physics and chemistry*, volume 1. Elsevier, 1992.

[159] Wim Van Saarloos. Front propagation into unstable states. *Physics reports*, 386(2):29–222, 2003.

[160] Wim van Saarloos and PC Hohenberg. Fronts, pulses, sources and sinks in generalized complex ginzburg-landau equations. *Physica D: Nonlinear Phenomena*, 56(4):303–367, 1992.

[161] Pierre-François Verhulst. Notice sur la loi que la population suit dans son accroissement. *Corresp. Math. Phys.*, 10:113–126, 1838.

[162] N Verschueren, U Bortolozzo, MG Clerc, and Stefania Residori. Spatiotemporal chaotic localized state in liquid crystal light valve experiments<? format?> with optical feedback. *Physical review letters*, 110(10):104101, 2013.

[163] Ger Vertogen and Wim H Jeu. *Thermotropic liquid crystals, fundamentals*. Springer, Berlin Heidelberg, 1988.

[164] AG Vladimirov, René Lefever, and Mustapha Tlidi. Relative stability of multipeak localized patterns of cavity solitons. *Physical Review A*, 84(4):043848, 2011.

[165] Da-Wei Wang, Hai-Tao Zhou, Miao-Jun Guo, Jun-Xiang Zhang, Jörg Evers, and Shi-Yao Zhu. Optical diode made from a moving photonic crystal. *Physical review letters*, 110(9):093901, 2013.

[166] Zheng Wang, Yidong Chong, John D Joannopoulos, and Marin Soljačić. Observation of unidirectional backscattering-immune topological electromagnetic states. *Nature*, 461(7265):772–775, 2009.

[167] Pengfei Yang, Xiuwen Xia, Hai He, Shaokang Li, Xing Han, Peng Zhang, Gang Li, Pengfei Zhang, Jingping Xu, Yaping Yang, et al. Realization of nonlinear

optical nonreciprocity on a few-photon level based on atoms strongly coupled to an asymmetric cavity. *Physical review letters*, 123(23):233604, 2019.

[168] Anton Zettl. *Sturm-liouville theory*. Number 121. American Mathematical Soc., 2005.

[169] B Zinner, G Harris, and W Hudson. Traveling wavefronts for the discrete fisher equation. *Journal of differential equations*, 105(1):46–62, 1993.